How have terrestrial ecosystems responded to global environmental change?

Peter James Joyce

Submitted in accordance with the requirements for the degree of Doctor of Philosophy

The University of Leeds
School of Earth and Environment
School of Geography

January 2022

The candidate confirms that the work submitted is his own, except where work which has formed part of jointly authored publications has been included. The contribution of the candidate and the other authors to this work has been explicitly indicated below. The candidate confirms that appropriate credit has been given within the thesis where reference has been made to the work of others.

Chapter 2

Joyce, P., Brienen, R., Buermann, W., Wilson, C., Chipperfield, M.P., Claret, M. and Gloor, M., 2021. How robust is the apparent break-down of northern high-latitude temperature control on spring carbon uptake? Geophysical Research Letters, 48(7), p.e2020GL091601.

PJ (the candidate), WB, RB, and MG devised the manuscript. CW and MPC assisted PJ with setting up TOMCAT simulations. PJ conducted all statistical analyses and model simulations. MC produced net fluxes between the atmosphere and ocean. All authors gave critical feedback on a draft of the manuscript.

Chapter 3

Joyce, P., Brienen, R., Claret, M., Wilson, C., Chipperfield, M., Sonnerup, R., and Gloor, M., *In preparation*. What can atmospheric δ13C tell us about the carbon cycle?

PJ (the candidate), RB, and MG devised the manuscript. MC produced the ocean fluxes and uncertainties. PJ ran the CASA model and performed analyses. All authors gave critical feedback on a draft of the manuscript.

Chapter 4

Joyce, P., Wagner, F., Brienen, R., Gloor, M., *In preparation*. Cross calibration of Landsat 5 TM and Landsat 7 ETM+ using deep learning enhances tree cover Mapping consistency.

PJ (the candidate), FW, RB, and MG devised the manuscript. FW assisted PJ with setting up and training the ResNet model. PJ collected all data and trained the ResNet and random forests models. All authors gave critical feedback on a draft of the manuscript.

Acknowledgements

Firstly, I'd like to thank my primary supervisors Manuel and Roel for their help and support over the past few years. I have always felt that I could come to the both of them regardless of how big/small the issue was, for which I will always be grateful. Thank you also to Chris for volunteering many of his hours teaching me to use TOMCAT, as well as the hilarious (but sadly infrequent) emails about the football fantasy league. Thank you to Fabien for introducing me to the wonders of deep neural networks and remote sensing. Thank you to Wolfgang for choosing me for this project, Martyn for his supervision, and to NERC for funding my PhD and thus making it all possible in the first place.

Thank you to Lara for all your support during my PhD and the unexpected (to say the least) curveball thrown by the pandemic. Thank you also to the members of Geography tea club for the regular breaks in the working day for chit-chat and biscuits. Thank you to Andy, Michael, Jack, Becky, Rob, Max and all my other climbing partners for the good times on the wall to decompress after long days at the desk. Thank you to Nadir for making the office environment a little less serious and for the odd Spanish lesson! Thanks to Chris and Amy for the fun times at AGU and to Rob for the hilarious zoom calls during lockdown. Many thanks to the (too numerous to mention) members of LUU caving club for the fun times spelunking in the Yorkshire Dales. Thank you also to my LUU squash teammates Henry, Matty, Paul and Ben for the many good times on court.

Thank you to my mum and dad for their unwavering support over the years. Coming from a family of 7, I am still amazed to this day that they were able to dedicate enough time to each of us while working full-time jobs. Thank you to Helen, Ben, and Ewan for making me laugh and keeping me grounded over the years.

Abstract

In the past century, we have witnessed the most substantial rise in global surface temperatures for millennia. A considerable increase in the emission of carbon dioxide (CO_2) originating from human activities has been identified as the leading cause of this rapid climate change. The land and ocean sinks take up roughly one half of anthropogenic CO_2. In response to rising atmospheric CO_2 levels and global surface temperatures, an increasing quantity of CO_2 has been absorbed by land vegetation each year. This land sink is, however, highly variable and the precise mechanisms behind the recent positive trend in carbon uptake are poorly understood. Overall, this thesis aims to answer the question of to what extent has land vegetation functioning adapted in response to climate change over the past decades. This work focuses largely on northern boreal ecosystems, which have accounted for up to one half of the total land sink over recent years. First, atmospheric CO_2 records are compared with land surface temperature data, which was combined with an analysis of model simulations to determine the extent to which northern high-latitude vegetation uptake is still controlled by temperature. From this analysis, it is determined that high latitude spring carbon uptake remained strongly controlled by temperature during the 1979-2016 period, contrary to previous findings. Following on from this, the thesis analyses the carbon-13 (^{13}C) isotope record in the atmosphere, which is a key indicator of land vegetation functioning. A suite of simulations is then produced to determine the key driving factors behind the variation of ^{13}C in the atmosphere. Uncertainty in the oceans is determined to be the dominating factor over atmospheric ^{13}C, with vegetation productivity and soil turnover times also emerging as important players. Finally, shifts in the coverage of Alaskan forests are examined using remote sensing to detect changes over time. A deep learning model is trained with the aim of enhancing the consistency of the satellite record and hence improving the robustness of the estimated long-term trends of tree cover. This deep learning model is demonstrated to be more effective at enhancing the consistency of satellite data than classical means and allowing more accurate reconstructions of tree cover change over time.

Table of Contents

List of Figures

List of Tables

List of Appendices

List of Abbreviations

$\delta^{13}C$ – Index of ^{13}C isotope ratio to ^{12}C

$\delta^{13}C_{atm}$ – $\delta^{13}C$ in the atmosphere

^{12}C – Carbon-12

^{13}C – Carbon-13

$^{13}CO_2$ – Carbon dioxide with the ^{13}C isotope

^{14}C – Carbon-14

β – CO_2 fertilisation parameter

Δ – Isotopic discrimination parameter

Δ_{ref} – 17.8‰ is the global estimate of C3 discrimination in 1990

AO – Arctic Oscillation

API – Application Programming Interface

AVHRR – Advanced Very-High Resolution Radar

AZC – Autumn Zero Crossing

BLING – Biogeochemistry with Light Iron Nutrients and Gas

c_a – Ambient CO_2 concentration

c_i – CO_2 concentration within the stomatal cavity

CAM – Crassulacean acid metabolism

CASA – Carnegie-Ames-Stanford Approach

CCGCRV – Carbon Cycle Group CuRVe

CDIAC – Carbon Dioxide Information Analysis Center

CH4 – Methane

CO_2 – Carbon dioxide

DGVM – Dynamic Global Vegetation Model

DIC – Dissolved Inorganic Carbon

DL – Deep learning

ECMWF – European Centre for Medium-Range Weather Forecasts

ENSO – El Niño Southern Oscillation

ETM+ – Enhanced Thematic Mapper Plus

FACE – Free-Air CO_2 Enrichment

fAPAR – fraction of Absorbed Photosynthetically Active Radiation

FF – Fossil fuel emissions

FPAR – Fraction of Photosynthetically Active Radiation

GEE – Google Earth Engine

GFDL – Geophysical Fluid Dynamics Laboratory

GFED – Global Fire Emissions Database

GIMMS – Global Inventory Modelling and Mapping Studies

GML/ESRL – Global Monitoring Laboratory Earth System Research Laboratories

GtC – Gigatons of Carbon

GWP – Global warming potential

iWUE – Intrinsic water use efficiency

K_s – Solubility of CO_2 in seawater

L5 – Landsat 5

L7 – Landsat 7

LUE – Light use efficiency

LULCC – Land-use and land cover change

MAE – Mean absolute error

MOM5 – Modular Ocean Model version 5

MR – Multiple regression

MSE – Mean squared error

NDVI – Normalised Difference Vegetation Index

NOAA – National Oceanic and Atmospheric Administration

NEE – Net ecosystem exchange

NEP – Net ecosystem production

NIR – Near infrared

NPP – Net primary productivity

OCN – Net Ocean uptake

pCO_2 – Partial pressure of CO_2

PgC – Peta-grams of Carbon

ppm – Parts per million

PV – Piston velocity

Q10 – Increase in soil respiration in response to a warming of 10˚C

$\bar{r}$ – Mean correlation

ReLU – Rectified Linear Unit

ResNet – Residual Network deep neural network model

RGB – Red, green, blue

RMSE – Root mean squared error

RMSprop – Root Mean Squared propagation

R_{sample} – Abundance ratio of ^{13}C to ^{12}C in a sample

$R_{standard}$ – ^{13}C to ^{12}C ratio in the Pee-Dee Belemnite fossil commonly used as a standard, with a value of 0.0112372 mol mol^{-1}

SOC – Soil organic carbon

STL – Seasonal-Trend decomposition procedure based on Loess

SZC – Spring zero crossing

SCC – Spring carbon capture

SWIR – Short wave infra-red

TIR – Thermal infra-Red

TOA – Top of atmosphere

TM – Thematic Mapper

TOMCAT – Toulouse Off-line Model of Chemistry and Transport atmospheric chemistry model

USDI BLM – United States Department of the Interior Bureau of Land Management

VEG_{C3} – Fraction of vegetation that has C3 photosynthetic pathway

VEG_{C4} – Fraction of vegetation that has C4 photosynthetic pathway

WUE – Water use efficiency

1 Background

1.1 The global carbon cycle

In recent decades, we have witnessed unprecedented changes to the earth's climate. Global mean surface temperatures during 2010-2021 were 1.1˚C higher than the 1850-1900 average (Masson-Delmotte et al., 2021). This has been attributed to the greenhouse effect, which is the phenomenon in which outgoing longwave (infrared) terrestrial radiation is reflected back to the surface by gases in the atmosphere which causes a heating effect. We refer to gases that absorb radiation in the infrared range that are abundant in the atmosphere as greenhouse gases, and the overall impact of their effect is measured using a quantity known as radiative forcing. Radiative forcing is defined as the influence of a given climatic factor on the amount of downward-directed radiant energy impinging upon the Earth's surface. The radiative forcing of a greenhouse gas is a function of its build up in the atmosphere and of its capacity to absorb radiation, known as its global warming potential (GWP). CO_2 contributes the most to the earth's radiative forcing budget, due to its relatively large build up in the atmosphere since pre-industrial times, as well as its long lifetime. Methane (CH_4) is the second biggest contributor due to its high GWP and moderate increase in concentrations in the atmosphere since pre-industrial times (Figure 1.1). Radiative forcing has increased significantly over the past decades, driven largely by increases in atmospheric concentrations of CO_2 and CH_4 (Figure 1.1).

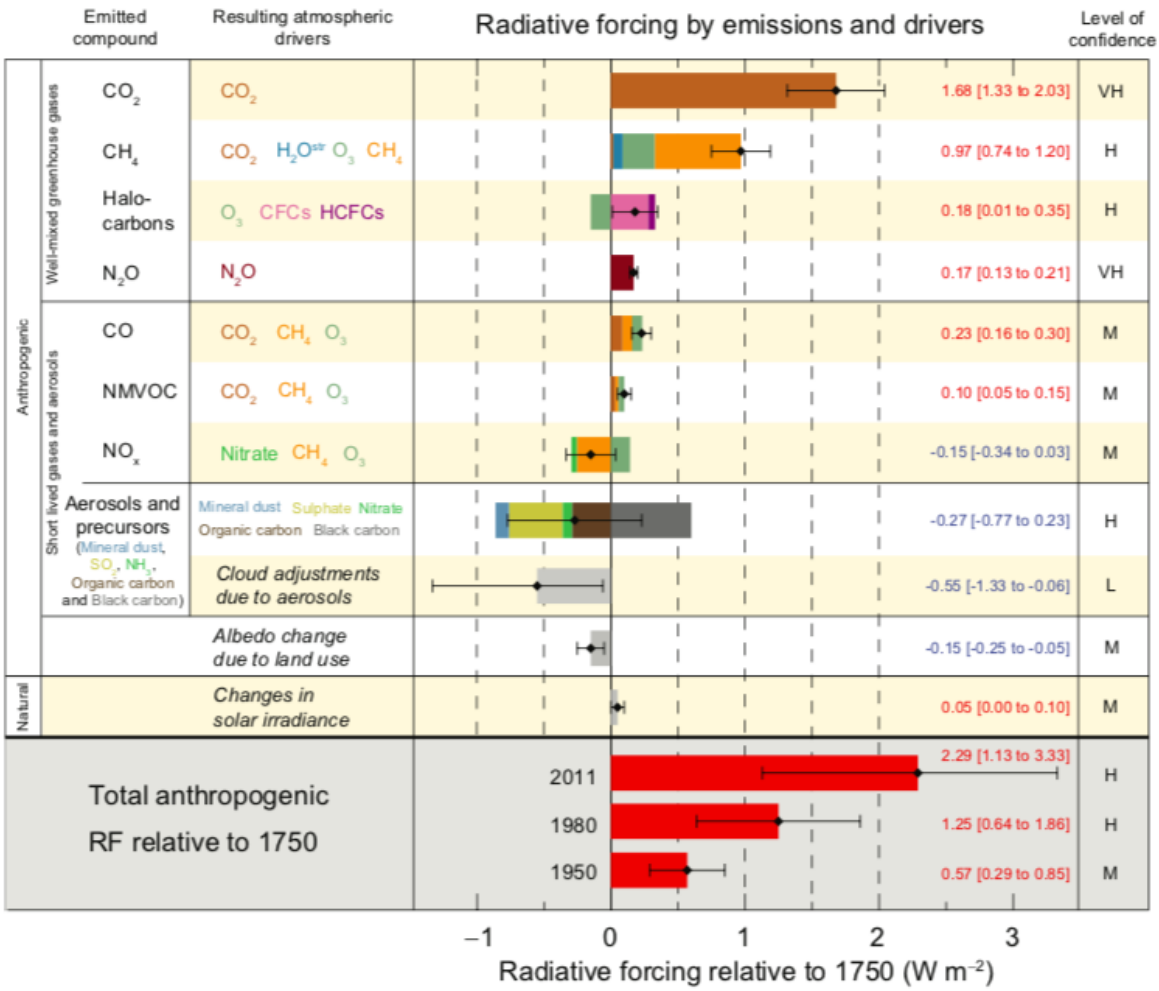

Figure 1.1. Radiative forcing of emitted compounds. The first column lists the substance being emitted; the second column lists the substance causing the radiative forcing. Bars indicate radiative forcing estimates relative to values before the industrial era and black whiskers indicate uncertainty of estimates (these values are also printed to the right of the plots) (Stocker et al., 2013).

The source of greenhouse gases comes primarily from the emission of fossil fuel burning during energy production, predominantly oil, coal, and gas. Other significant anthropogenic contributions include cement production and land-use change. Human activity in the industrial era (1751 to present) has caused large emissions of greenhouse gases into the atmosphere. Ice core data reveals that pre-industrial atmospheric CO_2 concentration stood at 280ppm, and, as of 2020, measurements taken from the longest-running CO_2 monitoring site at Mauna Loa in Hawaii reveal CO_2 concentrations to be 415ppm (Figure 1.2). Half of all fossil fuel emissions since 1751 have

remained in the atmosphere (Friedlingstein et al., 2020). This is because the land and oceans take up on average roughly half of all anthropogenic emissions.

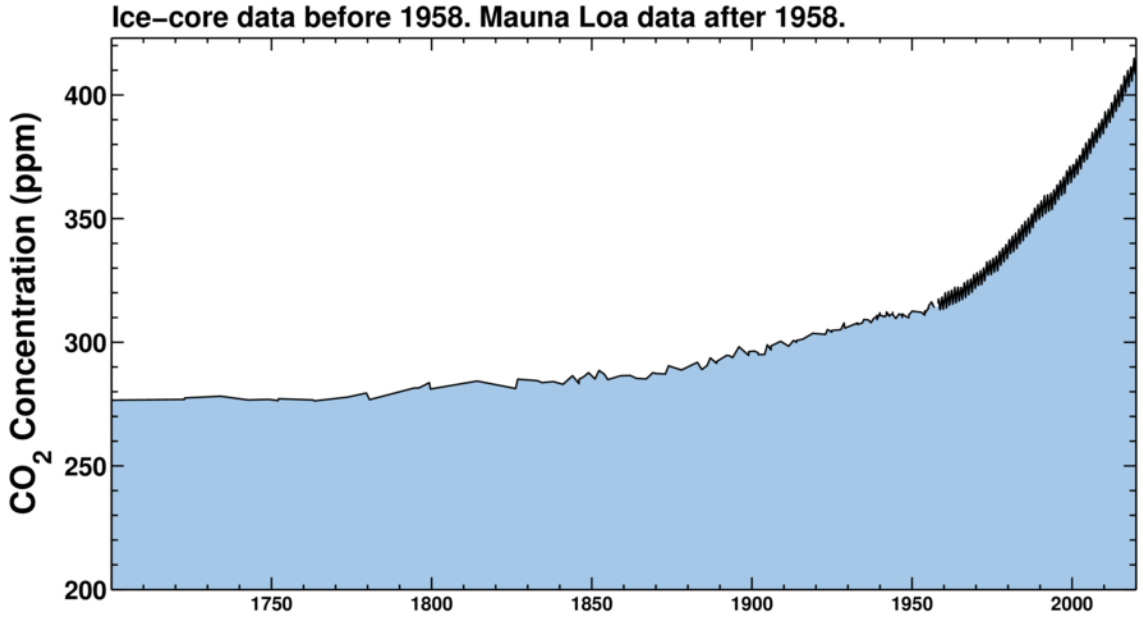

Figure 1.2. Atmospheric CO_2 concentration estimates during the industrial era. Data obtained from ice core data during 1700-1958 after which Mauna Loa site measurements are used. Figure taken from https://keelingcurve.ucsd.edu/

Carbon in the earth system is stored in several reservoirs on land and the ocean. There is a large degree of variability in the quantity of carbon stored in each of the earth's land biomes (Table 1.1). The total carbon in the soils is roughly 5 times larger than the sum of carbon in vegetation. Nearly half of all vegetation carbon is held in tropical forests, however, soil carbon is more evenly distributed around the biomes (Table 1.1). Boreal forests contain the largest amount of combined vegetation and soil carbon of all biomes, with 22% of the total carbon with only 9% of the land area.

Table 1.1. Global carbon stocks in vegetation and soil carbon pools down to a depth of 1m (Bolin et al., 2000). Mean NPP of ecosystems when dry, with the exception of wetland ecosystems (Colinvaux et al., 1973; Peregon et al., 2008).

Biome	**Area (10^9 ha)**	**Global Carbon Stocks (GtC)**			**NPP (g m^{-2} y^{-1})**
		Vegetation	**Soil**	**Total**	
Tropical forests	1.76	212	216	428	2000
Temperate forests	1.04	59	100	159	1300
Boreal forests	1.37	88	471	559	800
Tropical savannas	2.25	66	264	330	700
Temperate grasslands	1.25	9	295	304	500
Deserts and semideserts	4.55	8	191	199	70
Tundra	0.95	6	121	127	140
Wetlands	0.35	15	225	240	790
Croplands	1.6	3	128	131	650
Total	15.12	466	2011	2477	657

There is, however, considerable uncertainty in the quantification of global carbon stocks (Figure 1.3). Scharlemann et al. (2014) provided a summary of published global soil organic carbon (SOC) estimates and found a range of 504-3000 PgC between all 27 studies. Furthermore, they found significant variation within studies using similar methodologies. There was a range of 504-2469.5 PgC in the 7 spatially explicit studies and a range of 710-3000 PgC in the remaining 20 non-spatially explicit studies (Scharlemann et al., 2014).

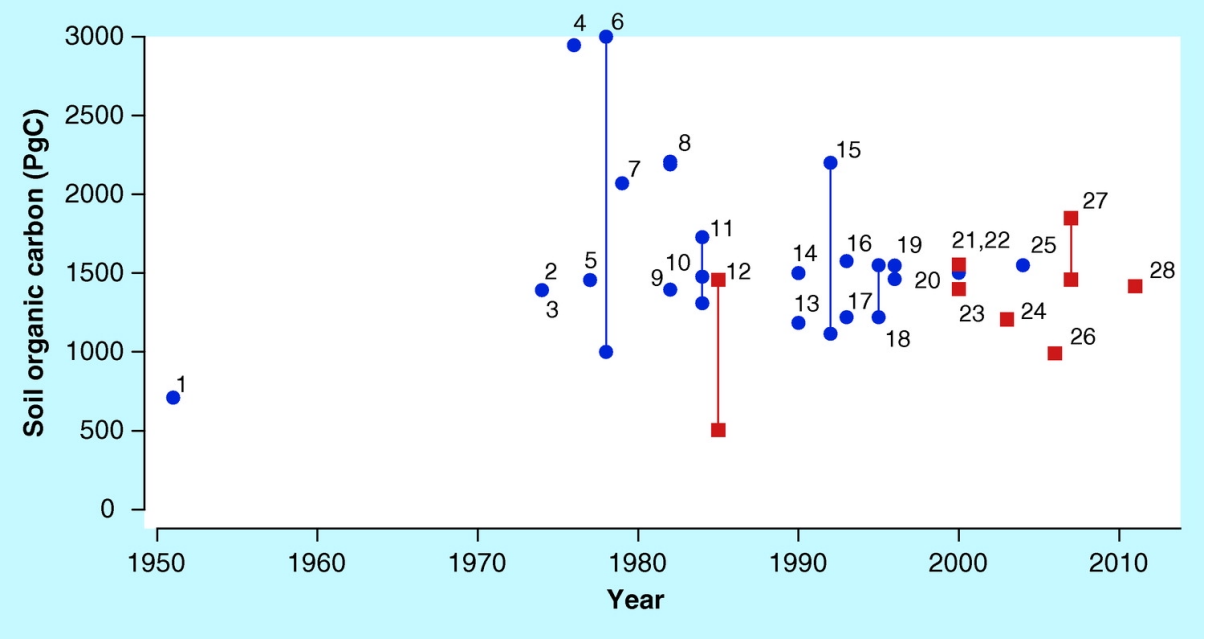

Figure 1.3. A summary of the estimates of global soil organic carbon stocks from the literature through time (Scharlemann et al., 2014). Labelled numbers indicate reference studies provided in the supplementary data of Scharlemann et al. (2014). Red (blue) points indicate spatially (non-spatially) explicit studies. Lines connect the minimum and maximum estimates of soil organic carbon within studies.

Large quantities of carbon are exchanged between the atmosphere and land vegetation and surface soils, as well as the shallow depths of the oceans (Figure 1.4). Far larger quantities of carbon are locked in the deep ocean and geosphere, but the timescales over which carbon is exchanged with the atmosphere are much longer when compared to the ocean and land.

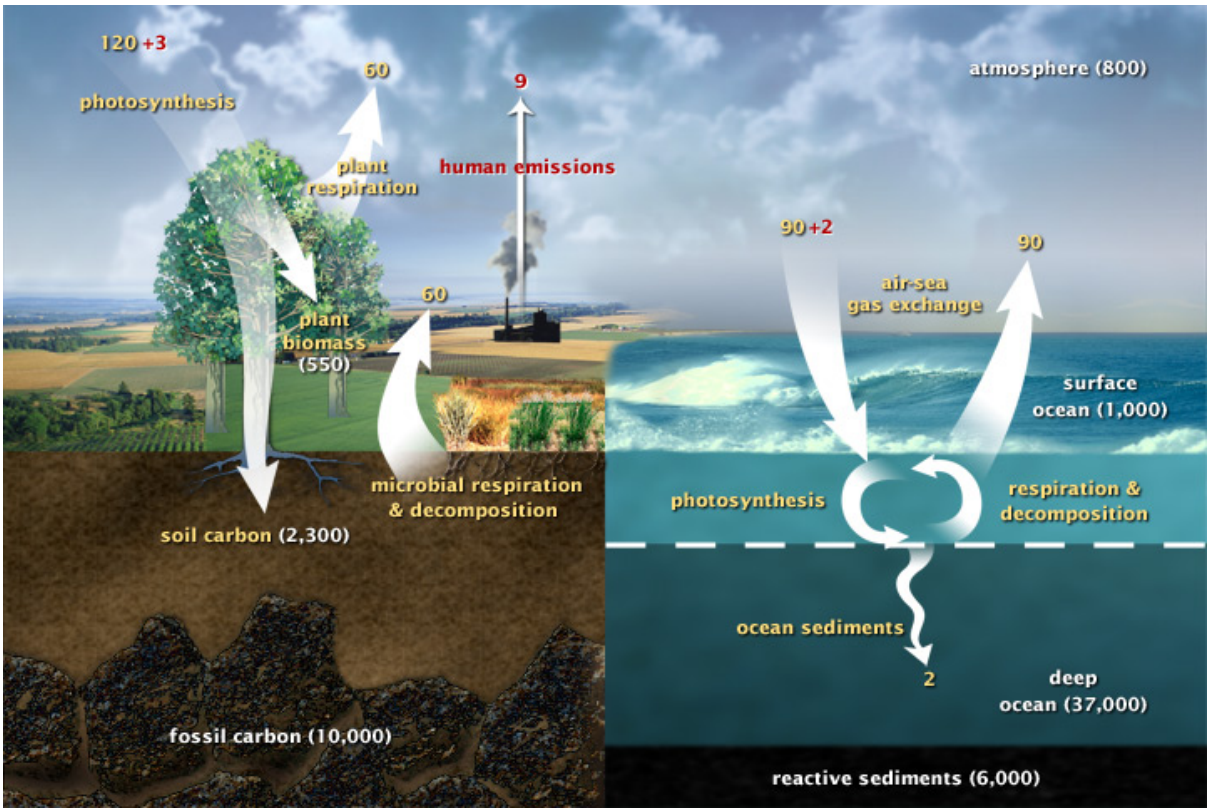

Figure 1.4. A diagram of fast carbon cycle processes between the land, atmosphere, and ocean. Arrows indicate the direction of the movement of carbon. Yellow numbers indicate natural fluxes and red are the human contributions (GtC yr^{-1}) at present day. White numbers indicate stored carbon. Figure taken from https://earthobservatory.nasa.gov/features/CarbonCycle.

A CO_2 sink is defined as a carbon pool that is a net absorber of carbon, whereas a CO_2 source is a net releaser of carbon. The land and oceans have historically been sinks of CO_2, thus removing CO_2 from the atmosphere overall. The magnitude of both the ocean and land carbon sink has grown in recent decades. The ocean sink increased from 1.0 ± 0.3 GtC yr^{-1} in the 1960s to 2.5 ± 0.6 GtC yr^{-1} during 2010-2019 (Friedlingstein et al., 2020). The ocean takes up carbon passively through the process of atmospheric CO_2 dissolving in the ocean. The land sink has increased by a similar magnitude, from 1.3 ± 0.4 GtC yr^{-1} in the 1960s to 3.4 ± 0.9GtC yr^{-1} during 2010-2019 (Friedlingstein et al., 2020) (Figure 1.5). Key drivers behind this increase in the land sink include climate changes leading to higher productivity and CO_2 fertilisation enhancing plant growth (see Section 1.2). The land sink has a far greater interannual variability than the ocean, with fluctuations

as high as 2 GtC yr^{-1} compared with the ocean which varies on the order of a few tenths of GtC yr^{-1} (Figure 1.5) (Friedlingstein et al., 2020). The exact mechanisms of the land carbon sink are poorly understood and estimates of the total land sink are subject to relatively large uncertainties.

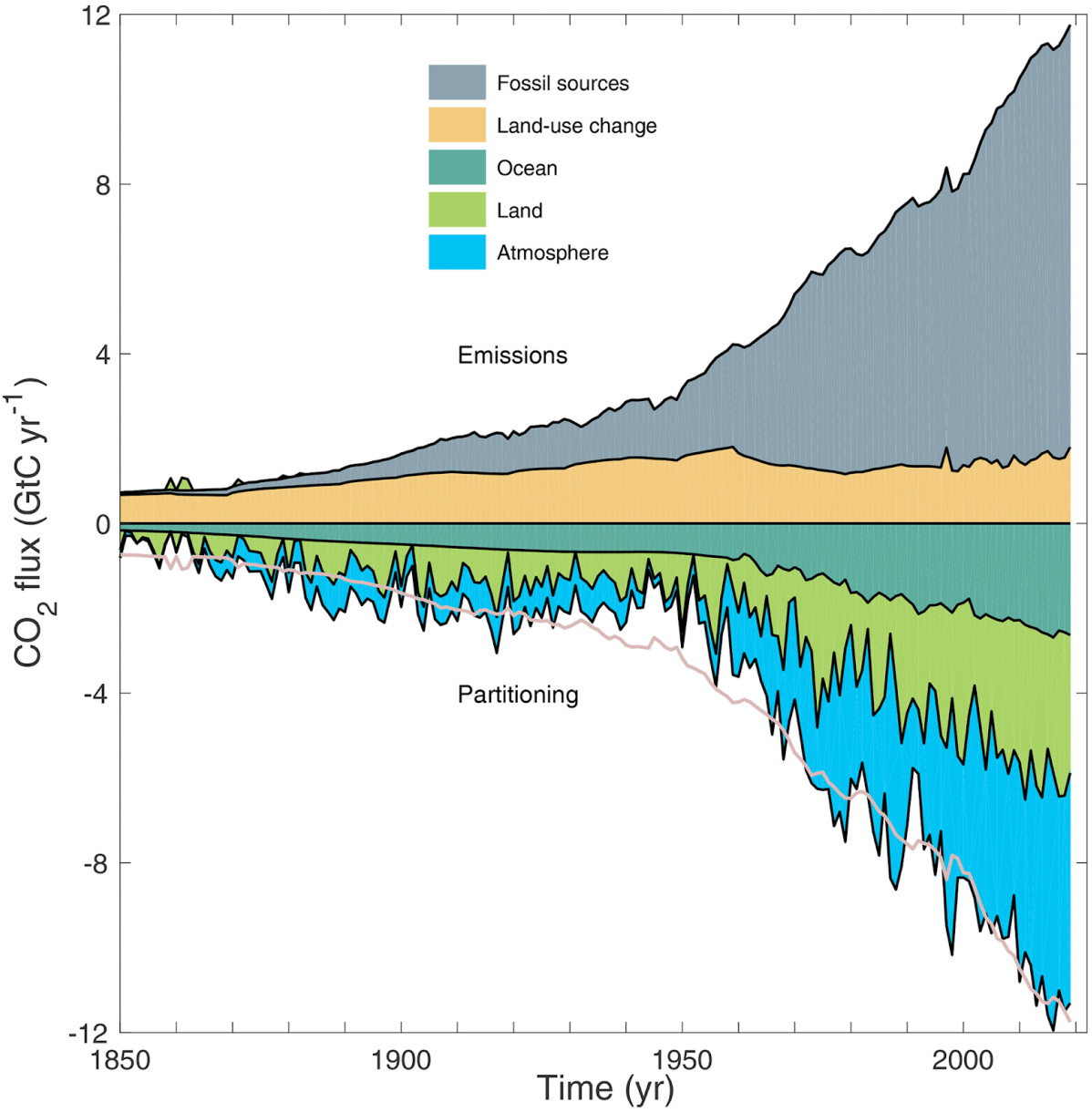

Figure 1.5. Historical sources and sinks in the Global Carbon Budget (Friedlingstein et al., 2020). Bottom grey line indicates the budget imbalance. Fossil fuel emission data relied on energy statistics and cement production data, land-use change data relied on a combination of bookkeeping and model estimates from the literature. Land and ocean sink data were calculated from the multi-model mean of estimates in the literature.

The oceans freely exchange carbon with the atmosphere due to CO_2 reacting with water to form carbonic acid and bicarbonate, leading to a phenomenon known as ocean acidification. The rate at which the ocean takes up carbon is affected by atmospheric CO_2 concentrations as well as the overturning circulation in which deep, carbon-rich ocean water flows upwards towards the surface waters (Sarmiento & Bryan, 1982). Observational data of the growth rates of surface water partial pressure of CO_2 (pCO_2) and atmospheric CO_2 are strongly correlated (Takahasi et al., 2006). Land vegetation takes up carbon through photosynthesis and releases it through plant and soil respiration, the controls of which are many and complex and discussed in Section 1.2. The high degree of interannual variability and uncertainty in the drivers behind the land sink emphasises the importance of understanding the uptake and release processes to predict the impact of future climate change on the land sink, as well as aiding our efforts to mitigate the damage to the earth's ecosystems.

1.2 Terrestrial carbon uptake processes

If the land sink were to maintain its current carbon absorption rate, atmospheric CO_2 is projected to reach 600ppm by 2050 for some fossil fuel emissions scenarios (Ciais et al., 2013), which would be nearly a 50% increase from current atmospheric concentrations. Projections for atmospheric CO_2 vary significantly between climate-carbon cycle models, with additional atmospheric CO_2 ranging from 20-200ppm (leading to an additional climate warming of 0.1-1.5˚C), with the strongest disagreement between models originating from the land sink and fossil fuel emission scenarios (Friedlingstein et al., 2006). The sink/source status of the land depends on the balance between photosynthesis, respiration, and disturbance. Land net carbon uptake is influenced by climate change, CO_2 fertilisation, nitrogen deposition, fire, and land-use/land cover changes (Bala et al., 2012; Devaraju et al., 2016; Piao et al., 2013; Shevliakova et al., 2013; Tharammal et al., 2019; Zhu et al., 2016).

1.2.1 Climate

Climate change has led to changes in surface temperature and precipitation patterns, both of which are inextricably linked with land vegetation functioning and hence its ability to sequester carbon. Interannual variations in the atmospheric CO_2 growth rate are significantly correlated with land

temperature (correlation coefficient r ranges from 0.5 - 0.7 depending on the method used), driven primarily by tropical ecosystem carbon uptake (Wang et al., 2013). Warming over the past decades has given rise to a lengthening of the growing season across northern ecosystems (Park et al., 2016), as well as an increase in summer productivity and greening (Barichivich et al., 2013; Xu et al., 2016). In high latitude regions, warmer springs have historically led to a greater uptake of carbon during springtime (Randerson et al., 1999), known as the warmer spring – larger carbon sink hypothesis.

Warming can lead to increased autumn respiration and carbon release which could cancel out additional gains during spring (Keenan et al., 2014; Piao et al., 2008). Furthermore, temperature rises can reduce net primary productivity (NPP) in certain ecosystems if the optimal temperature for photosynthesis is exceeded, leading to heat stress. Recent climate change has led to an increase in the frequency and severity of hot extremes and heatwaves (Masson-Delmotte et al., 2021) which have been shown to lead to substantial releases of carbon (Ciais et al., 2005). Warmer, drier conditions also lead to an increase in fire occurrence (see Section 1.2.4).

Changes in precipitation patterns can affect primary productivity and respiration due to changes in soil moisture availability but can also increase the incidence of droughts or floods. Tropical droughts in particular can be powerful, driving the interannual variability in the land sink during large drought events (Gatti et al., 2014). The interplay between precipitation and temperature is complex, with an increased temperature sensitivity of tropical regions in recent years, driven by changing moisture availability (Wang et al., 2014). The CO_2 growth rate is strongly sensitive to observed changes in terrestrial water storage, in which drier years are associated with a greater increase in atmospheric CO_2 (Humphrey et al., 2018). The El Niño Southern Oscillation (ENSO) is a mode of atmospheric variability strongly linked to precipitation patterns. ENSO has been linked as a key driver behind variations in the CO_2 growth rate (Bacastow, 1976; Bacastow, 1977; Humphrey et al., 2018).

There are various feedback mechanisms associated with climate and carbon uptake and release processes. Surface warming leads to the melting of permafrost, which causes an increase in CH_4 emissions (a greenhouse gas), therefore inducing further warming. Tipping points within the earth

system have been suggested, defined as a critical threshold where the movement of the system beyond would result in a qualitatively different mode of operation taking hold (Lenton et al., 2008). The threshold for boreal forest dieback due to increased water stress, peak summer heat stress and vulnerability to disease and fire is estimated at 3˚C above pre-industrial levels (Lucht et al., 2006; Joos et al., 2001). Furthermore, warmer temperatures are expected to lead to widespread compositional shifts in boreal forests (Anderson et al., 2011). The response of the Amazon rainforest to climate change is more complex, however, where a possible dieback has been theorised. The threshold for a dieback tipping point may be determined by a combination of land-use change and the responses of precipitation and ENSO to global environmental changes (Lenton et al., 2008). However, there is disagreement between some vegetation models that predict Amazon dieback (Li & Dickinson, 2006), and global climate models that do not predict it (Schaphoff et al., 2006). Thus, it is still an open question as to what the fate of the Amazon will be under future climate change and continuing deforestation in the Amazon.

1.2.2 CO_2 fertilisation

Experimental evidence shows an increase in leaf photosynthesis when plants are exposed to elevated CO_2 levels (Koerner, 2006). CO_2 is a key component in photosynthesis; therefore, elevated CO_2 fertilises primary productivity directly (Farquhar et al., 1980; Kimball et al., 1993). Furthermore, elevated CO_2 levels lead to a reduced stomatal opening and therefore reduced water loss hence further benefitting plant water use efficiency (Cowan & Farquhar, 1977; Field et al., 1995). CO_2 fertilisation was tested under controlled conditions using the free-air CO_2 enrichment (FACE) approach (Norby et al., 2005). Norby et al. measured a 23% increase in NPP after doubling CO_2 concentrations from pre-industrial levels. The growth in the land sink has been attributed primarily to the CO_2 fertilisation effect (Sitch et al., 2015), with 60% of the current sink attributed to it (Schimel et al., 2015). However, there are large uncertainties with estimates of the magnitude of the CO_2 fertilisation effect on land vegetation functioning (Friedlingstein et al., 2013; Friend et al., 2014). There are also additional uncertainties with respect to the longer-term dynamics of the response of forests to CO_2 fertilisation (Buggmann et al., 2020; Brienen et al 2020). Furthermore, a strong dependence is evident of CO_2 fertilisation on plant species as well as soil and air temperature, and availability of water and nutrients (Mcgrath & Lobell, 2013). Projections of the

future impacts of CO_2 fertilisation reveal a decrease in the sensitivity of terrestrial carbon storage to atmospheric CO_2 levels (Walker et al., 2020).

1.2.3 Nitrogen

Nitrogen limitations can dampen the CO_2 fertilisation effect because nitrogen is a major component in chlorophyll, which is essential for photosynthesis to occur. Projections of the future impacts of CO_2 fertilisation reveal a decrease in the sensitivity of terrestrial carbon storage to atmospheric CO_2 levels (Walker et al., 2020). Nitrogen deposition is caused by emissions of reactive nitrogen species into the atmosphere (Vitousek et al., 1997). Atmospheric nitrogen deposition originates from both biological and anthropogenic sources. However, anthropogenic emissions have increased substantially in recent years (Leonardi et al., 2012) and now dominate over biological sources in many regions (Galloway et al., 2008; Schlesinger et al., 2009). Nitrogen deposition can have damaging effects on human health due to ingestion of nitrites and nitrates in polluted drinking water, leading to a reduction in the oxygen-carrying capacity of haemoglobin (Camargo & Alonso, 2006). Furthermore, excessive nitrogen deposition can negatively impact growth (Liu et al., 2011) as well as reduce biodiversity (Bobbink et al., 2010) in terrestrial and aquatic ecosystems. However, increased nitrogen deposition has led to increases in nitrogen availability and leaf nitrogen (Hietz et al., 2011). An enhancement of the land carbon sink as a result of increased nitrogen inputs may be as high as 10% by 2030, although a more conservative estimate of 1-2% is more likely (Reay et al., 2008).

Most terrestrial ecosystems are somewhat limited by nitrogen availability (Vitousek & Howarth, 1991), with signs that when nitrogen is limiting, the influence of CO_2 fertilisation on plant productivity is reduced and the sign of the feedback between climate and carbon uptake can be reversed (Sokolov et al., 2008). An initial increase in plant growth due to CO_2 fertilisation leads to sequestration of nitrogen hence reducing soil mineral nitrogen and leading to nitrogen limitation on further growth (Luo et al., 2004). Increased nitrogen limitations on growth as a result of CO_2 fertilisation were confirmed using a terrestrial biosphere model (Bonan & Levis. 2010).

1.2.4 Fire

Estimates of total fire emissions range from 1.8 - 3.0 PgC yr^{-1} (Van der Werf et al., 2017), with 50% of global fire emissions originating from Africa. The next highest fire emissions originate from South America with 15% of global emissions. Roughly one-third of the variations in net land-atmosphere fluxes are caused by fire emissions (Keppel-Aleks et al., 2014, Prentice et al., 2011).

The climate is changing in regions with large quantities of organic carbon and where fires dominate the distribution of plants and soil carbon. Surface warming is associated with an increase in fire frequency, severity, and extent (Little et al., 2010; Skinner et al., 2006; Tymstra et al., 2007). Throughout the industrial era, human activity has had an increasing influence on fire occurrence (Bowman et al., 2011). A 2007 report linked 90% of fires directly or indirectly to human activities, power lines, or machinery (FAO, 2007). Deforestation zones have witnessed substantial increases in fire occurrence, however, intentional fire suppression techniques and conversion away from fire-prone landscapes (such as savannah to agriculture) has led to a reduction in fire activity (Andela & van der Werf, 2014; Bowman et al., 2009; Nowacki & Abrams, 2008).

Fires lead to losses in vegetation and soil carbon during the event, but also a legacy effect has been identified (Wan et al., 2014). Wan et al. found that fire size and severity had positive effects on aspen regeneration. However, high severity fires have been demonstrated to greatly reduce the resilience of forests to future fire events, when compared with low-to-moderate severity fires (Harris et al., 2020).

1.2.5 Land-use change

Land-use and land cover change (LULCC) is the process through which human activities transform the natural landscape. It encompasses any conversion between land cover types, for example, the conversion of forest to croplands. LULCC is nearly always associated with changing carbon stocks (Watson et al., 2000). This is because there is an equilibrium between inflows and outflows from the carbon pools that are disrupted by LULCC such that a new equilibrium is created which alters the carbon stocks available (Fearnside & Barbosa 1998).

Since 1850, cumulative LULCC has accounted for roughly one-third of total anthropogenic CO_2 emissions (Boden et al., 2013; Friedlingstein et al., 2020). Before 1940, when the land sink was not growing significantly, LULCC accounted for nearly the entire net terrestrial flux to the atmosphere (Houghton, 2013). Over the past 20 years, however, the net flux of LULCC emissions accounted for only 15% of anthropogenic carbon emissions (Friedlingstein et al., 2020). However, LULCC emissions have increased steadily over the past 20 years, accompanied by an increase in the spread between model estimates of LULCC (Friedlingstein et al., 2020). The uncertainty in LULCC is due to uncertainties in the rates of deforestation and afforestation, as well as uncertainties in the carbon density of land going through change (Houghton et al., 2012). Bookkeeping models have been used to estimate LULCC (Hansis et al., 2015), but they do not account for the effects of environmental changes on carbon stocks before and after LULCC occurs (Pongratz et al., 2014). Alternatively, dynamic global vegetation models (DGVMs) are utilised to estimate LULCC emissions and are able to estimate legacy carbon fluxes. However, estimates of LULCC differ significantly between different DGVMs, even when using the same inputs of land cover change data. Accurate forest cover maps, such as those produced by Hansen et al. (2013) can improve our understanding of how vegetation responds to disturbances, and greatly enhance the accuracy with which we estimate carbon loss (DeFries et al., 2002). The maps produced by Hansen et al. (2013) have global coverage and high resolution, but the first percentage tree cover estimates date back to 2000, thus they do not provide information on disturbance responses over longer timescales.

1.3 The high northern latitude carbon cycle

1.3.1 The high northern latitude sink

The high northern latitudes are significant sinks of carbon, accounting for up to 60% of the total land sink (Mcguire et al., 2009). The boreal zone has consistently been a net carbon sink for the past decades (Dolman et al., 2012). Boreal forests contain 88 GtC of vegetation carbon and 471GtC soil carbon and mean NPP of 800 g m^{-2} y^{-1} (Table 1.1). The relatively large soil carbon stocks present make the boreal zone an important region for the mitigation of climate change. However, the uncertainties of soil carbon stocks are very high (Figure 1.3).

Soil, sediment, or rock material that are continuously exposed to sub-zero temperatures are collectively referred to as permafrost. 24% of high northern latitude land is covered by permafrost, where vast quantities of carbon are stored (Zhang et al., 2000). Permafrost regions contain twice as much carbon as the total in the atmosphere (Tarnocai et al., 2009). The thawing of permafrost, and subsequent decomposition of the soils, may lead to large releases of CH_4 (in addition to CO_2) into the atmosphere, which is a concern for influencing future climate change due to the relatively large radiative forcing when compared with CO_2.

Estimates based on inventory data and process models indicate that forests across North America were near-neutral or small sinks of carbon (Balshi et al., 2007; Chen et al., 2000; Myneni et al., 2001). In contrast, forest inventory data show that Eurasian forests provide a larger net carbon sink than those in North America (Beer et al., 2006; Myneni et al., 2001). Due to the large uncertainties in estimating the land sink, the precise contribution from different regions is poorly understood and the sink or source status of the Arctic is unknown (Mcguire et al., 2012).

An increase in high latitude vegetation productivity has occurred over the past decades as a result of CO_2 fertilisation (Norby et al., 2005) and longer growing seasons (Piao et al., 2007). However, the effects of climate change in this region are not straightforward. Hayes et al. (2011) used the Terrestrial Ecosystem Model to show that warming-induced increases in soil organic matter decomposition and increases in fire emissions are potential mechanisms behind possible reductions in the high latitude land sink in recent decades. Boreal wildfires have increased in occurrence due to climate warming and drying (de Groot et al., 2013), and burning of legacy carbon threatens to change the sink-or-source status of the boreal zone (Walker et al., 2019).

1.3.2 Response to recent climate change

Northern lands have undergone substantial warming over the past decades (0.3˚C – 1.0˚C decade^{-1}), with clear implications on vegetation functioning (Walther et al., 2002). The responses of vegetation to temperature rise include increased height and coverage of shrubs but also a decrease

in biodiversity across tundra regions (Walker et al., 2006). Warming has led to a northern advance of the treeline, which enhances the high northern latitude sink, as well as causing shifts in species abundance (Macdonald et al., 2007). The northern treeline advance has been ubiquitous, but with significant variation between sites (Lloyd, 2005). Warming has been shown to have both positive and negative effects on aboveground biomass at the treeline. Drought stress has emerged as an additional limiting factor, effectively changing the sign of the influence of temperature on tree expansion (Wilmking et al., 2005).

Year-to-year variations in carbon uptake and release have historically been strongly controlled by temperature. Warmer springs have tended to result in earlier advancement of the growing season (Myneni et al., 1997; Menzel et al., 2006), leading to enhanced spring carbon uptake (Richardson et al., 2010; Randerson et al., 1999). Greater carbon release later in the year can be caused by earlier autumn senescence due to earlier springs (Keenan et al., 2015) and by warmer autumns (Piao et al., 2008). Buermann et al. (2018) confirmed the former hypothesis with an analysis of remotely sensed data, where they demonstrated significant adverse lagged effects of warmer springs on the accumulation of seasonal water deficits.

Permafrost ecosystems currently account for up to 7% of global CH_4 emissions (Kirschke et al., 2013). However, temperature rises are expected to lead to large releases of CO_2 from permafrost soils (Schuur & Abbott, 2011). As a result of rising temperatures driving permafrost thaw, tundra ecosystems have been predicted to transition from a sink to a source in the coming decade (Schuur et al., 2015), however, this has yet to occur in the years since this study.

1.4 Inference of the carbon cycle from atmospheric data

Land photosynthesis and respiration are the dominant controls over the seasonality of atmospheric CO_2. As a result, the CO_2 seasonal cycle is a useful tool in gaining insight into the workings of the terrestrial biosphere. Through analysis of the changes over time of the seasonal cycle, it is possible to infer changes in productivity, net carbon uptake or release during all times of the year, and the shifting or lengthening of the photosynthetic period.

In order to analyse the seasonal cycle, the long-term trend must be removed. Isolating the seasonal elements of the CO_2 data can be done using various smoothing procedures. The most common procedures are Carbon Cycle Group CuRVe (Thoning et al., 1989), HPSpline (Bacastow et al., 1985; Keeling et al., 1986; 1989) and Seasonal-Trend Decomposition Procedure Based on Loess (STL) (Cleveland et al. 1990). Each procedure has its own set of strengths and limitations for the type of analysis to be conducted (Pickers & Manning 2014). After detrending the time series and obtaining the seasonal cycle, there are a number of indices that are indicative of land vegetation functioning, which are discussed forthwith.

1.4.1 CO_2 amplitude

The CO_2 amplitude is calculated from the seasonal cycle yearly minima subtracted from the maxima. This is an indicator of seasonal variation in plant productivity and respiration. An increase in the amplitude implies that spring/summer productivity is increasing and/or winter release of carbon is increasing. The CO_2 amplitude has a strong latitudinal gradient, as northern high latitude regions experience the largest amplitudes, and the most southerly regions experience very small amplitudes (Figure 1.6). This is due primarily to the northern hemisphere containing far more land than the southern hemisphere and because of greater intra-annual variability in climate across the high latitudes, where net land carbon uptake varies significantly over the course of the year.

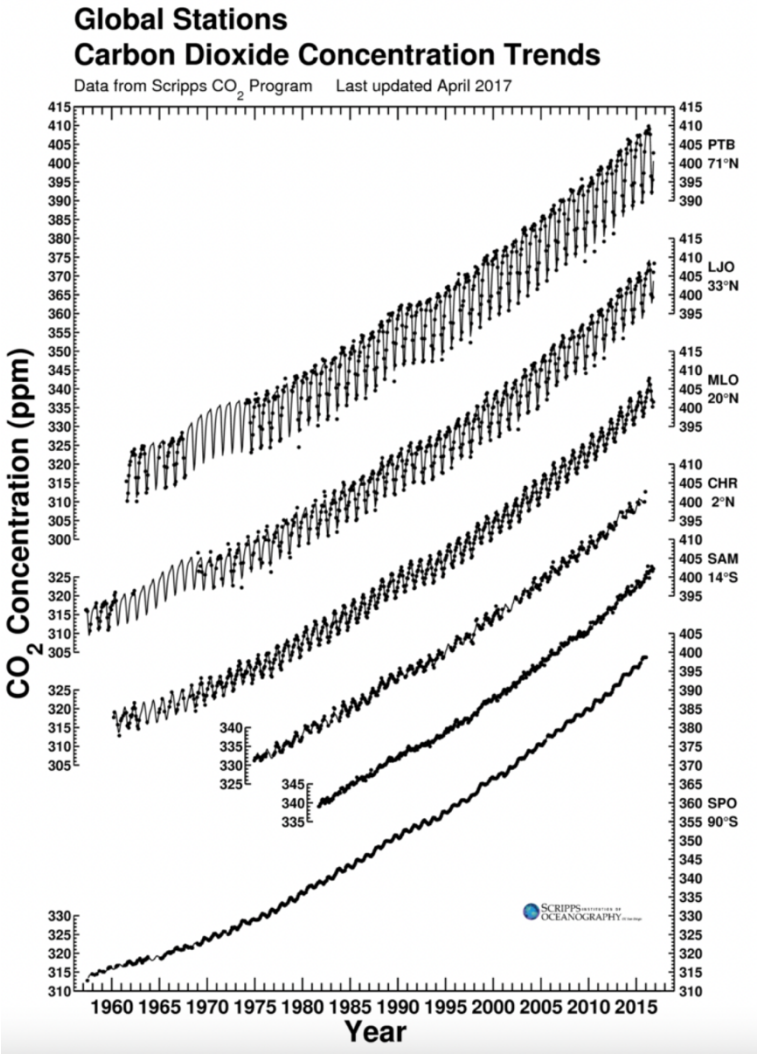

Figure 1.6. Variation in atmospheric CO_2 from measurement stations at a range of latitudes. Dots represent individual measurements from *in-situ* data and lines indicate the smoothed curve. Figure taken from Keeling et al. (2017).

The CO_2 amplitude has increased globally since the 1960s (Keeling et al., 1996), with amplitudes north of 45˚N increasing by 50% over the last 50 years, compared with less than 25% in the 10˚N to 45˚N region (Graven et al., 2013). The latitudinal gradient of CO_2 amplitude increase has been attributed to climate-driven increases in photosynthetic carbon uptake, mediated by changing land cover in northern ecosystems (Forkel et al., 2016). There is some evidence that the relationship between CO_2 amplitude and temperature is shifting. Yin et al. (2018) demonstrated that the correlation between detrended amplitude and detrended air temperature shifted from positive to negative around the year 2000 in the majority of northern hemisphere ground stations. The driver

behind this was suggested to be due to a breakdown in the warmer spring - larger carbon uptake and the warmer winter - larger carbon release hypotheses due to factors other than temperature controlling vegetation productivity, such as an increasing light limitation on spring growth.

1.4.2 Spring and autumn zero crossings

The spring zero crossing (SZC) is calculated from the day of the year when the CO_2 seasonal cycle passes downwards through the yearly mean (Figure 1.7). The SZC is a misnomer, due to the fact that the occurrence of the SZC is often during summer at most northern latitude CO_2 measurement sites. The SZC is indicative of the timing of spring vegetation green-up and is strongly associated with the mass of carbon that has been taken up by land vegetation during early spring. The SZC was correlated with the timing of spring thaw and the start of the thermal and photosynthetic growing seasons (Barichivich et al., 2013). More recently, Piao et al., (2017) showed that the SZC at the Barrow observatory was strongly correlated with land surface temperature averaged over vegetated land north of 50˚N during the 1979-1995 period, but the correlation broke down in the following years. From this, they deduced that the control of spring temperature on high northern latitude vegetation productivity has broken down. While intriguing, the analysis of Piao et al., (2017) did not account for several pertinent factors. Firstly, the comparison between the SZC at Barrow and spring temperature averaged over land north of 50˚N assumes that the air masses arriving at Barrow circulated uniformly across this region, with no significant year-to-year variability. Secondly, the factorial simulations conducted in the analysis did not include a run in which atmospheric transport was held constant. Rather, the influence of atmospheric transport was ascertained from the simulation in which net ecosystem exchange (NEP) fluxes were held constant, with atmospheric transport varying. The issue with this approach is that atmospheric transport and climate are inextricably linked, thus the full extent of the influence of atmospheric transport is not clear. A study by Murayama et al. (2007) demonstrated the powerful influence of atmospheric transport on the SZC at Barrow, hence ensuring the importance of re-examining the data from Piao et al. while probing deeper into the influence of atmospheric transport. The Autumn zero crossing (AZC) is calculated identically to the SZC, except it is the upward zero crossing later in the year (Figure 1.7). The AZC is indicative of the timing of autumn senescence, as well as a proxy for the release of carbon during autumn. Liu et al (2018) analysed the relationship between the AZC at Barrow and temperature averaged over the footprint region of Barrow. They found that warming

significantly enhanced net CO_2 release from the land throughout the entire record, but with attenuation emerging in the late 1990s. This was attributed to a reduction in the respiration response to temperature because of plant-derived carbon inputs to the soil being no longer controlled primarily by temperature variations due to limited radiation available during the dormant season.

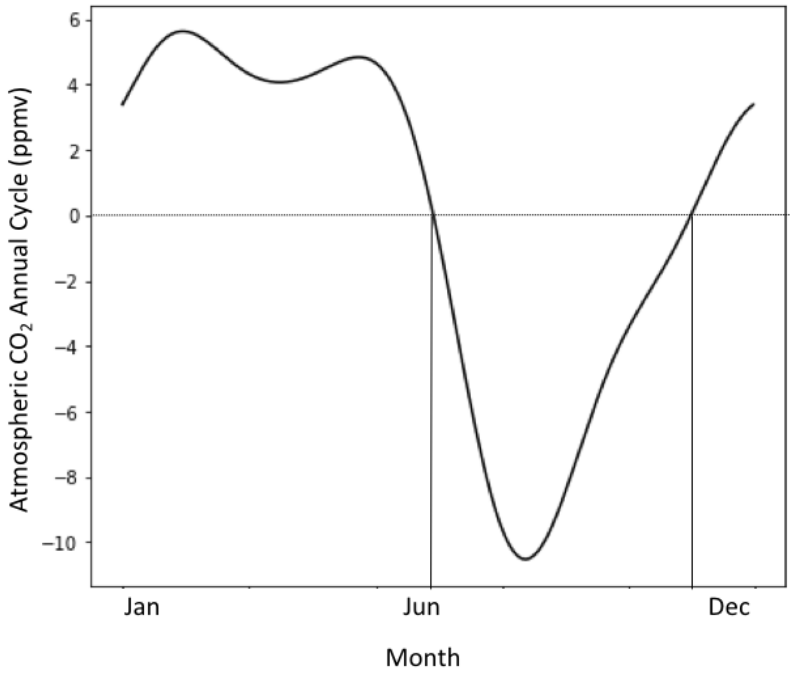

Figure 1.7. Depiction of the smoothed CO_2 seasonal cycle at the Barrow observatory (curved line). Horizontal line indicates the yearly mean of CO_2 concentrations (zero-centred). Vertical lines indicate the (left) SZC and (right) AZC.

1.4.3 Carbon-13 isotope

Discrimination of carbon-13 (^{13}C) during oxygen photosynthesis is a key indicator of water use efficiency in plants. ^{13}C makes up roughly 1% of the carbon in the earth system. The global increase in atmospheric CO_2 concentration throughout the industrial era has been accompanied by a corresponding decrease in the ratio between ^{13}C and ^{12}C. The depleted nature of fossil fuels is due to the carbon within it being originally fixed through photosynthesis, a process in which ^{12}C is preferentially taken up over ^{13}C, known as fractionation. C3 plants with higher water use efficiency will discriminate against $^{13}CO_2$ more strongly than a C4 plant with lower water use efficiency. In general, land vegetation fractionates against ^{13}C far more strongly than the oceans,

therefore having a greater effect on the isotopic composition of the atmosphere. Analysis of atmospheric ^{13}C records have been used to distinguish between oceanic and land sinks in the carbon budget (Keeling et al., 1995; Quay et al., 1992; Trudinger et al., 2005). This is not straightforward, however, because land fractionation can vary significantly depending on environmental conditions, as well as the photosynthetic pathway used (Farquhar et al., 1989). Van der Velde et al. (2013) identified a gap in the global $\delta^{13}C$ budget due to a discrepancy between modelled atmospheric $\delta^{13}C$ and observations. Keeling et al. (2017) demonstrated, using a simple box model, that the $\delta^{13}C$ budget could be closed with an increase in land C3 vegetation discrimination, leading to the conclusion that land vegetation has increased water-use efficiency in line with rising atmospheric CO_2 levels. Thus, analysis of atmospheric $\delta^{13}C$ levels can provide indications of land vegetation functioning at a global scale.

1.5 Modelling the carbon cycle

In order to better understand the mechanisms underlying carbon uptake and release processes, modelling procedures can be undertaken. Comparisons between modelled atmospheric CO_2 given prescribed fluxes and atmospheric concentration data can provide insights into the functioning of the land and ocean carbon sinks. Modelling the global average fluxes of carbon can be achieved using 'box models', where each reservoir of carbon is treated as a well-mixed zero-dimensional box. Box diffusion models include vertical diffusion of carbon in the ocean (Oeschger et al., 1975) and advective-diffusion models include convection of carbon in the ocean (Bacastow & Björkström, 1981). The advantages of box models lie in their simplicity and the ease with which results can be interpreted. To produce simulations of atmospheric CO_2 at a given location requires the production of gridded estimates of each of the significant sinks and sources of carbon in the earth system. These must then be fed into an atmospheric transport model so that CO_2 can be simulated at a given sample location. The land-atmosphere carbon flux with the lowest uncertainty comes from fossil fuels, where high-quality 2D gridded data is available from the Carbon Dioxide Information Analysis Center (Andres et al., 2016). This source provides fossil fuel CO_2 emissions, as well as $^{13}CO_2$ emissions (which are also gridded).

Simulating carbon uptake and release of the ocean can be done with various methods. The Geophysical Fluid Dynamics Laboratory (GFDL) Modular Ocean Model (MOM) is a level-

coordinate ocean model, in which the ocean is divided into boxes whose bottoms are located at fixed depths. This approach enables solving the equations of fluid motion in the model to be done efficiently, however, there are limitations with its ability to accurately model thin bottom boundary layers (Winton et al., 1998). Model setups with constant density layers can resolve this limitation but introduce new issues with representing the ocean mixed layer.

The Carnegie-Ames-Stanford Approach (CASA) model was initially developed to simulate long-term changes in vegetation carbon over a 2-dimensional grid (Potter et al., 1993). CASA estimates NPP using a light-use efficiency approach, a major component that incorporates satellite data estimating the fraction of photosynthetically active radiation (FPAR) at each grid cell. The carbon fixed via NPP is then split among the various vegetation, microbial, and soil pools in CASA, where a series of first-order differential equations are resolved at each time step to determine the flow of carbon between each of the pools and with the atmosphere. A more detailed description of CASA is given in Chapters 2 and 3.

Modelling the atmospheric transport of CO_2 accurately is an important process in order to accurately predict atmospheric concentrations given prescribed fluxes. TOMCAT is an atmospheric chemistry and transport model, which has been used to simulate the atmospheric chemistry of active atmospheric trace gases (Chipperfield et al., 1993). CO_2 emissions can be prescribed in TOMCAT simulations, which uses European Centre for Medium-Range Weather Forecasts (ECMWF) ERA-Interim meteorology (Dee et al., 2011), to produce gridded fields of simulated atmospheric CO_2. These simulations can then be compared with observational CO_2 data from the vast network of monitoring sites in the National Oceanic and Atmospheric Administration Global Monitoring Laboratory Earth System Research Laboratories (NOAA GML/ESRL) or Scripps programs (Keeling & Keeling, 2017).

1.6 Research Aims

The overall objective of this thesis is to better understand the response of land vegetation to recent climate change. As discussed in the preceding sections, there are various methods of measuring the response of vegetation functioning to climate change. This thesis employs the use of remotely

sensed satellite imagery of vegetation, *in-situ* CO_2 measurements, isotopic records in the earth system, and modelling procedures using classical and machine learning approaches. The variety of techniques utilised enables a wider net to be cast over the terrestrial biosphere and a fuller picture can be obtained of the underlying drivers behind global change. The specific aims that were constructed in order to achieve this are as follows:

Aim 1: *Investigate the temperature sensitivity of high northern latitude vegetation spring carbon uptake using atmospheric data.*

Aim 2: *Quantify the sensitivities of simulated global atmospheric $\delta^{13}C$ to uncertainties in the carbon cycle.*

Aim 3: *Evaluate the effect of disturbance on tree cover using a novel deep learning technique in remote sensing.*

The importance of the high northern latitude land sink is outlined in Section 1.3, with temperature emerging as a key limitation on plant growth. Spring carbon uptake has historically been strongly controlled by land surface temperature in the boreal zone, however, Piao et al. (2017) suggested that this control has broken down. However, there are numerous issues with their approach due to the fact that atmospheric transport was not explicitly accounted for (see Section 1.4.2). Addressing Aim 1 requires the use of data from the NOAA GML/ESRL program (Thoning et al., 2020), from which the SZC and SCC indices were derived from data retrieved from the Barrow observatory. The research employed the use of the HYSPLIT4 trajectory model in order to ascertain the footprint regions of Barrow. This enabled the attribution of regions of influence over Barrow during each month of the study period. Following on from this, the CASA land surface model was combined with the TOMCAT atmospheric chemistry model to perform factorial simulations to analyse the relative importance of changes in climate and atmospheric transport. Finally, the analyses are framed in the context of whether or not high latitude spring terrestrial carbon uptake remains controlled by temperature.

Changing water use efficiency is an important adaptation that plants may need to make in order to survive in a world with rapidly changing atmospheric CO_2 and moisture availability. In section 1.4.3 the importance of studying atmospheric $\delta^{13}C$ for understanding terrestrial carbon uptake was

outlined. Such analyses have the potential to pertain to information about soil turnover times and the partitioning between the ocean and land sinks. Addressing aim 2 involves a modified CASA model, in which $^{13}CO_2$ is modelled alongside $^{12}CO_2$. Ocean-atmosphere fluxes of ^{12}C and ^{13}C are obtained from GFDL ocean simulations (Claret et al., 2021), which are used alongside fossil fuel emissions obtained from CDIAC (Boden et al., 2009; Andres et al., 2016). Using this setup, an investigation is undertaken into the sensitivities of atmospheric $\delta^{13}C$ to various uncertainties of land and ocean uptake.

The effects of climate and CO_2 fertilisation on the functioning of vegetation were discussed in detail in Section 1.2. There, the importance of high-quality tree cover mapping was laid out as a key tool to further our understanding of the response of vegetation to disturbance events. Accurate mapping of forest growth over the past decades would further provide an indicator of the sensitivity of tree cover expansion to atmospheric CO_2 (among other factors). However, without a consistent satellite record, it is difficult to apply tree cover estimation algorithms beyond the current generation of satellites. To address Aim 3, a deep neural network is trained to emulate Landsat 7 imagery using Landsat 5 images. This is then combined with a tree cover random forests model to produce a continuous map of tree cover in a region in eastern Alaska. This study is one of the first to train a deep neural network model for remote sensing purposes, entirely using cloud-based resources.

1.7 Layout of this thesis

As detailed in section 1.6, this thesis aims to better understand the response of terrestrial ecosystems to environmental change in the past decades. Chapter 1 has laid out an overview of the literature to motivate the work carried out in this thesis and then outlined the primary research questions that are to be addressed. The remainder of this thesis consists of three research chapters and a synthesis chapter.

Chapter 2 is a study of the temperature sensitivity of high northern-latitude lands using the CO_2 measurements at the Barrow observatory in Alaska alongside modelling of atmospheric CO_2 using the land surface model CASA and the atmospheric chemistry model TOMCAT. Chapter 3 is an

analysis of the sensitivities of atmospheric $\delta^{13}C$ using CASA, alongside simulations from the ocean GFDL model. Estimates of uncertainty of land and ocean processes are obtained from the literature, as well as the ocean simulations themselves. Chapter 4 is an exploration into the use of deep neural network techniques to improve the consistency of satellite data to enhance estimates of tree cover and quantify the effect of environmental change on tree cover.

The key findings from Chapters 2-4 are synthesised and discussed in Chapter 5. This section lays out a more in-depth analysis of the results, in which the methodologies are criticised. This is then followed by a discussion on the implications for further research as a result of the work carried out in this thesis. Finally, concluding statements are made about the extent to which the aims set out in the opening chapter have been achieved.

References

Andela, N. and Van Der Werf, G.R., 2014. Recent trends in African fires driven by cropland expansion and El Niño to La Niña transition. Nature Climate Change, 4(9), pp.791-795.

Anderson, J.B., Warny, S., Askin, R.A., Wellner, J.S., Bohaty, S.M., Kirshner, A.E., Livsey, D.N., Simms, A.R., Smith, T.R., Ehrmann, W. and Lawver, L.A., 2011. Progressive Cenozoic cooling and the demise of Antarctica's last refugium. Proceedings of the National Academy of Sciences, 108(28), pp.11356-11360.

Andres, R.J., Boden, T.A. and Higdon, D.M., 2016. Gridded uncertainty in fossil fuel carbon dioxide emission maps, a CDIAC example. *Atmospheric Chemistry and Physics*, *16*(23), pp.14979-14995.

Bacastow, R.B., 1976. Modulation of atmospheric carbon dioxide by the Southern Oscillation. Nature, 261(5556), pp.116-118.

Bacastow, R.B., 1977. Influence of the southern oscillation on atmospheric carbon dioxide. The fate of fossil fuel CO, 2, pp.33-43.

Bala, G., Krishna, S., Narayanappa, D., Cao, L., Caldeira, K. and Nemani, R., 2013. An estimate of equilibrium sensitivity of global terrestrial carbon cycle using NCAR CCSM4. Climate dynamics, 40(7-8), pp.1671-1686.

Bacastow, R.B., 1981. Comparison of ocean models for the carbon cycle. *Carbon cycle modelling*, *16*, pp.29-79.

Bacastow, R.B., Keeling, C. and Whorf, T.P., 1985. Seasonal amplitude increase in atmospheric CO2 concentration at Mauna Loa, Hawaii, 1959–1982. *Journal of Geophysical Research: Atmospheres*, *90*(D6), pp.10529-10540.

Balshi, M.S., McGuire, A.D., Zhuang, Q., Melillo, J., Kicklighter, D.W., Kasischke, E., Wirth, C., Flannigan, M., Harden, J., Clein, J.S. and Burnside, T.J., 2007. The role of historical fire disturbance in the carbon dynamics of the pan-boreal region: A process-based analysis. *Journal of Geophysical Research: Biogeosciences*, *112*(G2).

Barichivich, J., Briffa, K.R., Myneni, R.B., Osborn, T.J., Melvin, T.M., Ciais, P., Piao, S. and Tucker, C., 2013. Large-scale variations in the vegetation growing season and annual cycle of atmospheric CO2 at high northern latitudes from 1950 to 2011. *Global change biology*, *19*(10), pp.3167-3183.

Beer, C., Lucht, W., Schmullius, C. and Shvidenko, A., 2006. Small net carbon dioxide uptake by Russian forests during 1981–1999. *Geophysical Research Letters*, *33*(15).

Bobbink, R., Hicks, K., Galloway, J., Spranger, T., Alkemade, R., Ashmore, M., Bustamante, M., Cinderby, S., Davidson, E., Dentener, F. and Emmett, B., 2010. Global assessment of nitrogen deposition effects on terrestrial plant diversity: a synthesis. Ecological applications, 20(1), pp.30-59.

Boden, T.A., Marland, G. and Andres, R.J., 2009. *Global, Regional, and National Fossil-Fuel CO2 Emissions, 1751-2006 (published 2009)*. Environmental System Science Data Infrastructure for a Virtual Ecosystem; Carbon Dioxide Information Analysis Center (CDIAC), Oak Ridge National Laboratory (ORNL), Oak Ridge, TN (United States).

Bolin, B., Sukumar, R., Ciais, P., Cramer, W., Jarvis, P., Kheshgi, H., Nobre, C., Semenov, S. and Steffen, W., 2000. Global Perspective. In land Use, Land-Use change and Forestry, RT Watson, IR Noble, B Bolin, NH Ravindranath, DJ Verardo, DJ Dokken (eds.) A Special Report of the IPCC.

Bonan, G.B. and Levis, S., 2010. Quantifying carbon-nitrogen feedbacks in the Community Land Model (CLM4). *Geophysical Research Letters*, *37*(7).

Bowman, D.M., Balch, J.K., Artaxo, P., Bond, W.J., Carlson, J.M., Cochrane, M.A., D'Antonio, C.M., DeFries, R.S., Doyle, J.C., Harrison, S.P. and Johnston, F.H., 2009. Fire in the Earth system. science, 324(5926), pp.481-484.

Bowman, D.M., Balch, J., Artaxo, P., Bond, W.J., Cochrane, M.A., D'antonio, C.M., DeFries, R., Johnston, F.H., Keeley, J.E., Krawchuk, M.A. and Kull, C.A., 2011. The human dimension of fire regimes on Earth. Journal of biogeography, 38(12), pp.2223-2236.

Brienen, R.J., Caldwell, L., Duchesne, L., Voelker, S., Barichivich, J., Baliva, M., Ceccantini, G., Di Filippo, A., Helama, S., Locosselli, G.M. and Lopez, L., 2020. Forest carbon sink neutralized by pervasive growth-lifespan trade-offs. Nature communications, 11(1), pp.1-10.

Buermann, W., Forkel, M., O'sullivan, M., Sitch, S., Friedlingstein, P., Haverd, V., Jain, A.K., Kato, E., Kautz, M., Lienert, S. and Lombardozzi, D., 2018. Widespread seasonal compensation effects of spring warming on northern plant productivity. *Nature*, *562*(7725), pp.110-114.

Bugmann, H. and Bigler, C., 2011. Will the CO 2 fertilization effect in forests be offset by reduced tree longevity?. Oecologia, 165(2), pp.533-544.

Camargo, J.A. and Alonso, Á., 2006. Ecological and toxicological effects of inorganic nitrogen pollution in aquatic ecosystems: a global assessment. Environment international, 32(6), pp.831-849.

Claret, M., Sonnerup, R.E. and Quay, P.D., 2021. A next generation ocean carbon isotope model for climate studies I: Steady state controls on ocean 13C. Global Biogeochemical Cycles, 35(4), p.e2020GB006757.

Cleveland, R.B., Cleveland, W.S., McRae, J.E. and Terpenning, I., 1990. STL: A seasonal-trend decomposition. *Journal of official statistics*, *6*(1), pp.3-73.

Chen, J., Chen, W., Liu, J., Cihlar, J. and Gray, S., 2000. Annual carbon balance of Canada's forests during 1895–1996. *Global Biogeochemical Cycles*, *14*(3), pp.839-849.

Chipperfield, M.P., 1999. Multiannual simulations with a three-dimensional chemical transport model. *Journal of Geophysical Research: Atmospheres*, *104*(D1), pp.1781-1805.

Ciais, P., Reichstein, M., Viovy, N., Granier, A., Ogée, J., Allard, V., Aubinet, M., Buchmann, N., Bernhofer, C., Carrara, A. and Chevallier, F., 2005. Europe-wide reduction in primary productivity caused by the heat and drought in 2003. Nature, 437(7058), pp.529-533.

Ciais, P., Sabine, C., Bala, G., Bopp, L., Brovkin, V., Canadell, J., Chhabra, A., DeFries, R., Galloway, J., Heimann, M. and Jones, C., 2014. Carbon and other biogeochemical cycles. In *Climate change 2013: the physical science basis. Contribution of Working Group I to the Fifth Assessment Report of the Intergovernmental Panel on Climate Change* (pp. 465-570). Cambridge University Press.

Colinvaux, P.A., 1973. Introduction to ecology. John wiley & sons.

Cowan, I.R., Farquhar, G.D. and Jennings, D.H., 1977. Integration of activity in the higher plant. Stomatal function in relation to leaf metabolism and environment. Cambridge Univ Press, Cambridge, pp.471-505.

de Groot, W.J., Flannigan, M.D. and Cantin, A.S., 2013. Climate change impacts on future boreal fire regimes. *Forest Ecology and Management*, *294*, pp.35-44.

Dee, D.P., Uppala, S.M., Simmons, A.J., Berrisford, P., Poli, P., Kobayashi, S., Andrae, U., Balmaseda, M.A., Balsamo, G., Bauer, D.P. and Bechtold, P., 2011. The ERA-Interim reanalysis: Configuration and performance of the data assimilation system. *Quarterly Journal of the royal meteorological society*, *137*(656), pp.553-597.

DeFries, R.S., Houghton, R.A., Hansen, M.C., Field, C.B., Skole, D. and Townshend, J., 2002. Carbon emissions from tropical deforestation and regrowth based on satellite observations for the 1980s and 1990s. Proceedings of the National Academy of Sciences, 99(22), pp.14256-14261.

Devaraju, N., Bala, G., Caldeira, K. and Nemani, R., 2016. A model based investigation of the relative importance of CO 2-fertilization, climate warming, nitrogen deposition and land use change on the global terrestrial carbon uptake in the historical period. *Climate Dynamics*, *47*(1), pp.173-190.

Dolman, A.J., Shvidenko, A., Schepaschenko, D., Ciais, P., Tchebakova, N., Chen, T., Van Der Molen, M.K., Belelli Marchesini, L., Maximov, T.C., Maksyutov, S. and Schulze, E.D., 2012. An estimate of the terrestrial carbon budget of Russia using inventory-based, eddy covariance and inversion methods. *Biogeosciences*, *9*(12), pp.5323-5340.

FAO (2007) Fire management global assessment 2006. A thematic study prepared in the framework of the Global Forest Resources Assessment 2005. Food and Agriculture Organization of the United Nations, Forestry Paper 151. (Rome, Italy).

Farquhar, G.D., von Caemmerer, S.V. and Berry, J.A., 1980. A biochemical model of photosynthetic CO 2 assimilation in leaves of C 3 species. *Planta*, *149*(1), pp.78-90.

Farquhar, G.D., Ehleringer, J.R. and Hubick, K.T., 1989. Carbon isotope discrimination and photosynthesis. *Annual review of plant biology*, *40*(1), pp.503-537.

Fearnside, P.M. and Barbosa, R.I., 1998. Soil carbon changes from conversion of forest to pasture in Brazilian Amazonia. *Forest ecology and management*, *108*(1-2), pp.147-166.

Field, C.B., Jackson, R.B. and Mooney, H.A., 1995. Stomatal responses to increased CO2: implications from the plant to the global scale. *Plant, Cell & Environment*, *18*(10), pp.1214-1225.

Friedlingstein, P., Cox, P., Betts, R., Bopp, L., von Bloh, W., Brovkin, V., Cadule, P., Doney, S., Eby, M., Fung, I. and Bala, G., 2006. Climate–carbon cycle feedback analysis: results from the C4MIP model intercomparison. Journal of climate, 19(14), pp.3337-3353.

Friedlingstein, P., Meinshausen, M., Arora, V.K., Jones, C.D., Anav, A., Liddicoat, S.K. and Knutti, R., 2014. Uncertainties in CMIP5 climate projections due to carbon cycle feedbacks. *Journal of Climate*, *27*(2), pp.511-526.

Friedlingstein, P., O'Sullivan, M., Jones, M.W., Andrew, R.M., Hauck, J., Olsen, A., Peters, G.P., Peters, W., Pongratz, J., Sitch, S. and Le Quéré, C., 2020. Global carbon budget 2020. *Earth System Science Data*, *12*(4), pp.3269-3340.

Friend, A.D., Lucht, W., Rademacher, T.T., Keribin, R., Betts, R., Cadule, P., Ciais, P., Clark, D.B., Dankers, R., Falloon, P.D. and Ito, A., 2014. Carbon residence time dominates uncertainty in terrestrial vegetation responses to future climate and atmospheric CO2. *Proceedings of the National Academy of Sciences*, *111*(9), pp.3280-3285.

Galloway, J.N., Townsend, A.R., Erisman, J.W., Bekunda, M., Cai, Z., Freney, J.R., Martinelli, L.A., Seitzinger, S.P. and Sutton, M.A., 2008. Transformation of the nitrogen cycle: recent trends, questions, and potential solutions. *Science*, *320*(5878), pp.889-892.

Gatti, L.V., Gloor, M., Miller, J.B., Doughty, C.E., Malhi, Y., Domingues, L.G., Basso, L.S., Martinewski, A., Correia, C.S.C., Borges, V.F. and Freitas, S., 2014. Drought sensitivity of Amazonian carbon balance revealed by atmospheric measurements. *Nature*, *506*(7486), pp.76-80.

Hansen, M.C., Potapov, P.V., Moore, R., Hancher, M., Turubanova, S.A., Tyukavina, A., Thau, D., Stehman, S.V., Goetz, S.J., Loveland, T.R. and Kommareddy, A., 2013. High-resolution global maps of 21st-century forest cover change. science, 342(6160), pp.850-853.

Hansis, E., Davis, S.J. and Pongratz, J., 2015. Relevance of methodological choices for accounting of land use change carbon fluxes. *Global Biogeochemical Cycles*, *29*(8), pp.1230-1246.

Harris, L.B., Drury, S.A. and Taylor, A.H., 2020. Strong legacy effects of prior burn severity on forest resilience to a high-severity fire. Ecosystems, pp.1-14.

Hayes, D.J., McGuire, A.D., Kicklighter, D.W., Gurney, K.R., Burnside, T.J. and Melillo, J.M., 2011. Is the northern high-latitude land-based CO2 sink weakening?. *Global Biogeochemical Cycles*, *25*(3).

He, K., Zhang, X., Ren, S. and Sun, J., 2016. Deep residual learning for image recognition (2015). *arXiv preprint arXiv:1512.03385*.

Hietz, P., Wanek, W., Wania, R. and Nadkarni, N.M., 2002. Nitrogen-15 natural abundance in a montane cloud forest canopy as an indicator of nitrogen cycling and epiphyte nutrition. *Oecologia*, *131*(3), pp.350-355.

Houghton, R.A., House, J.I., Pongratz, J., Van Der Werf, G.R., DeFries, R.S., Hansen, M.C., Quéré, C.L. and Ramankutty, N., 2012. Carbon emissions from land use and land-cover change. *Biogeosciences*, *9*(12), pp.5125-5142.

Houghton, R.A., 2013. Role of forests and impact of deforestation in the global carbon cycle. *Global Forest Monitoring from Earth Observation, eds Achard F, Hansen MC (CRC Press, Boca Raton, Florida)*, pp.15-38.

Humphrey, V., Zscheischler, J., Ciais, P., Gudmundsson, L., Sitch, S. and Seneviratne, S.I., 2018. Sensitivity of atmospheric CO 2 growth rate to observed changes in terrestrial water storage. *Nature*, *560*(7720), pp.628-631.

Joos, F., Prentice, I.C., Sitch, S., Meyer, R., Hooss, G., Plattner, G.K., Gerber, S. and Hasselmann, K., 2001. Global warming feedbacks on terrestrial carbon uptake under the Intergovernmental Panel on Climate Change (IPCC) emission scenarios. Global Biogeochemical Cycles, 15(4), pp.891-907.

Keeling, C.D., Guenther, P.R. and Whorf, T.P., 1986. An Analysis of the Concentration of Atmospheric Carbon Dioxide at Fixed Land Stations and over the Oceans based on Discrete samples and Daily Averaged Continuous Measurements.

Keeling, C.D., Bacastow, R.B., Carter, A.F., Piper, S.C., Whorf, T.P., Heimann, M., Mook, W.G. and Roeloffzen, H., 1989. A three-dimensional model of atmospheric CO2 transport based on observed winds: 1. Analysis of observational data. *Aspects of climate variability in the Pacific and the Western Americas*, *55*, pp.165-236.

Keeling, C.D., Whorf, T.P., Wahlen, M. and Van der Plichtt, J., 1995. Interannual extremes in the rate of rise of atmospheric carbon dioxide since 1980. *Nature*, *375*(6533), pp.666-670.

Keeling, R.F. and Keeling, C.D., 2017. Atmospheric monthly in situ CO2 data—Mauna Loa Observatory, Hawaii. Scripps CO2 program data [Data set]. *San Diego, CA: University of*

California, San Diego Library Digital Collections. https://doi. org/10.6075/J08W3BHW [accessed on 16 November 2020].

Keenan, T.F., Gray, J., Friedl, M.A., Toomey, M., Bohrer, G., Hollinger, D.Y., Munger, J.W., O'Keefe, J., Schmid, H.P., Wing, I.S. and Yang, B., 2014. Net carbon uptake has increased through warming-induced changes in temperate forest phenology. Nature Climate Change, 4(7), pp.598-604.

Keenan, T.F. and Richardson, A.D., 2015. The timing of autumn senescence is affected by the timing of spring phenology: implications for predictive models. *Global change biology*, *21*(7), pp.2634-2641.

Keppel-Aleks, G., Wolf, A.S., Mu, M., Doney, S.C., Morton, D.C., Kasibhatla, P.S., Miller, J.B., Dlugokencky, E.J. and Randerson, J.T., 2014. Separating the influence of temperature, drought, and fire on interannual variability in atmospheric CO2. *Global biogeochemical cycles*, *28*(11), pp.1295-1310.

Kimball, B.A., Mauney, J.R., Nakayama, F.S. and Idso, S.B., 1993. Effects of increasing atmospheric CO 2 on vegetation. *Vegetatio*, *104*(1), pp.65-75.

Kirschke, S., Bousquet, P., Ciais, P., Saunois, M., Canadell, J.G., Dlugokencky, E.J., Bergamaschi, P., Bergmann, D., Blake, D.R., Bruhwiler, L. and Cameron-Smith, P., 2013. Three decades of global methane sources and sinks. *Nature geoscience*, *6*(10), pp.813-823.

Körner, C., 2006. Plant CO2 responses: an issue of definition, time and resource supply. New phytologist, 172(3), pp.393-411.

Leonardi, S., Gentilesca, T., Guerrieri, R., Ripullone, F., Magnani, F., Mencuccini, M., Noije, T.V. and Borghetti, M., 2012. Assessing the effects of nitrogen deposition and climate on carbon isotope discrimination and intrinsic water-use efficiency of angiosperm and conifer trees under rising CO 2 conditions. *Global Change Biology*, *18*(9), pp.2925-2944.

Lenton, T.M., Held, H., Kriegler, E., Hall, J.W., Lucht, W., Rahmstorf, S. and Schellnhuber, H.J., 2008. Tipping elements in the Earth's climate system. *Proceedings of the national Academy of Sciences*, *105*(6), pp.1786-1793.

Littell, J.S., Oneil, E.E., McKenzie, D., Hicke, J.A., Lutz, J.A., Norheim, R.A. and Elsner, M.M., 2010. Forest ecosystems, disturbance, and climatic change in Washington State, USA. Climatic change, 102(1), pp.129-158.

Liu, X., Duan, L., Mo, J., Du, E., Shen, J., Lu, X., Zhang, Y., Zhou, X., He, C. and Zhang, F., 2011. Nitrogen deposition and its ecological impact in China: an overview. Environmental pollution, 159(10), pp.2251-2264.

Liu, D., Piao, S., Wang, T., Wang, X., Wang, X., Ding, J., Ciais, P., Peñuelas, J. and Janssens, I., 2018. Decelerating autumn CO2 release with warming induced by attenuated temperature dependence of respiration in northern ecosystems. *Geophysical Research Letters*, *45*(11), pp.5562-5571.

Li, W., Fu, R. and Dickinson, R.E., 2006. Rainfall and its seasonality over the Amazon in the 21st century as assessed by the coupled models for the IPCC AR4. Journal of Geophysical Research: Atmospheres, 111(D2).

Lloyd, A.H., 2005. Ecological histories, ecological futures: what recent changes at treeline reveal about the future. *Ecology*, *86*, pp.1687-1695.

Lucht, W., Schaphoff, S., Erbrecht, T., Heyder, U. and Cramer, W., 2006. Terrestrial vegetation redistribution and carbon balance under climate change. Carbon Balance and Management 1: 6.

Luo, Y., Su, B.O., Currie, W.S., Dukes, J.S., Finzi, A., Hartwig, U., Hungate, B., McMurtrie, R.E., Oren, R.A.M., Parton, W.J. and Pataki, D.E., 2004. Progressive nitrogen limitation of ecosystem responses to rising atmospheric carbon dioxide. *Bioscience*, *54*(8), pp.731-739.

MacDonald, G.M., Kremenetski, K.V. and Beilman, D.W., 2008. Climate change and the northern Russian treeline zone. *Philosophical Transactions of the Royal Society B: Biological Sciences*, *363*(1501), pp.2283-2299.

McGrath, J.M. and Lobell, D.B., 2013. Regional disparities in the CO2 fertilization effect and implications for crop yields. *Environmental Research Letters*, *8*(1), p.014054.

McGuire, A.D., Christensen, T.R., Hayes, D., Heroult, A., Euskirchen, E., Kimball, J.S., Koven, C., Lafleur, P., Miller, P.A., Oechel, W. and Peylin, P., 2012. An assessment of the carbon balance of Arctic tundra: comparisons among observations, process models, and atmospheric inversions. *Biogeosciences*, *9*(8), pp.3185-3204.

McGuire, A.D., Anderson, L.G., Christensen, T.R., Dallimore, S., Guo, L., Hayes, D.J., Heimann, M., Lorenson, T.D., Macdonald, R.W. and Roulet, N., 2009. Sensitivity of the carbon cycle in the Arctic to climate change. *Ecological Monographs*, *79*(4), pp.523-555.

Menzel, A., Sparks, T.H., Estrella, N., Koch, E., Aasa, A., Ahas, R., Alm-Kübler, K., Bissolli, P., Braslavská, O.G., Briede, A. and Chmielewski, F.M., 2006. European phenological response to climate change matches the warming pattern. *Global change biology*, *12*(10), pp.1969-1976.

Murayama, S., Higuchi, K. and Taguchi, S., 2007. Influence of atmospheric transport on the inter-annual variation of the CO2 seasonal cycle downward zero-crossing. Geophysical research letters, 34(4).

Myneni, R.B., Keeling, C.D., Tucker, C.J., Asrar, G. and Nemani, R.R., 1997. Increased plant growth in the northern high latitudes from 1981 to 1991. *Nature*, *386*(6626), pp.698-702.

Myneni, R.B., Dong, J., Tucker, C.J., Kaufmann, R.K., Kauppi, P.E., Liski, J., Zhou, L., Alexeyev, V. and Hughes, M.K., 2001. A large carbon sink in the woody biomass of Northern forests. *Proceedings of the National Academy of Sciences*, *98*(26), pp.14784-14789.

Norby, R.J., DeLucia, E.H., Gielen, B., Calfapietra, C., Giardina, C.P., King, J.S., Ledford, J., McCarthy, H.R., Moore, D.J., Ceulemans, R. and De Angelis, P., 2005. Forest response to elevated CO2 is conserved across a broad range of productivity. *Proceedings of the National Academy of Sciences*, *102*(50), pp.18052-18056.

Nowacki, G.J. and Abrams, M.D., 2008. The demise of fire and "mesophication" of forests in the eastern United States. BioScience, 58(2), pp.123-138.

Oeschger, H., Siegenthaler, U., Schotterer, U. and Gugelmann, A., 1975. A box diffusion model to study the carbon dioxide exchange in nature. *Tellus*, *27*(2), pp.168-192.

Park, T., Ganguly, S., Tømmervik, H., Euskirchen, E.S., Høgda, K.A., Karlsen, S.R., Brovkin, V., Nemani, R.R. and Myneni, R.B., 2016. Changes in growing season duration and productivity of northern vegetation inferred from long-term remote sensing data. Environmental Research Letters, 11(8), p.084001.

Peregon, A., Maksyutov, S., Kosykh, N.P. and Mironycheva-Tokareva, N.P., 2008. Map-based inventory of wetland biomass and net primary production in western Siberia. Journal of Geophysical Research: Biogeosciences, 113(G1).

Piao, S., Friedlingstein, P., Ciais, P., Viovy, N. and Demarty, J., 2007. Growing season extension and its impact on terrestrial carbon cycle in the Northern Hemisphere over the past 2 decades. Global Biogeochemical Cycles, 21(3).

Piao, S., Sitch, S., Ciais, P., Friedlingstein, P., Peylin, P., Wang, X., Ahlström, A., Anav, A., Canadell, J.G., Cong, N. and Huntingford, C., 2013. Evaluation of terrestrial carbon cycle models for their response to climate variability and to CO2 trends. *Global change biology*, *19*(7), pp.2117-2132.

Piao, S., Ciais, P., Friedlingstein, P., Peylin, P., Reichstein, M., Luyssaert, S., Margolis, H., Fang, J., Barr, A., Chen, A. and Grelle, A., 2008. Net carbon dioxide losses of northern ecosystems in response to autumn warming. *Nature*, *451*(7174), pp.49-52.

Pongratz, J., Reick, C.H., Houghton, R.A. and House, J.I., 2014. Terminology as a key uncertainty in net land use and land cover change carbon flux estimates. *Earth System Dynamics*, *5*(1), pp.177-195.

Potter, C.S.R. and Field, C.B., 1993. Terrestrial ecosystem production: A process model based on global satellite and surface data. *Global Biogeochemical Cycles*, *7*(4), p.811.

Prentice, I.C., Kelley, D.I., Foster, P.N., Friedlingstein, P., Harrison, S.P. and Bartlein, P.J., 2011. Modeling fire and the terrestrial carbon balance. *Global Biogeochemical Cycles*, *25*(3).

Quay, P.D., Tilbrook, B. and Wong, C.S., 1992. Oceanic uptake of fossil fuel CO2: Carbon-13 evidence. *Science*, *256*(5053), pp.74-79.

Randerson, J.T., Field, C.B., Fung, I.Y. and Tans, P.P., 1999. Increases in early season ecosystem uptake explain recent changes in the seasonal cycle of atmospheric CO2 at high northern latitudes. *Geophysical research letters*, *26*(17), pp.2765-2768.

Richardson, A.D., Andy Black, T., Ciais, P., Delbart, N., Friedl, M.A., Gobron, N., Hollinger, D.Y., Kutsch, W.L., Longdoz, B., Luyssaert, S. and Migliavacca, M., 2010. Influence of spring and autumn phenological transitions on forest ecosystem productivity. *Philosophical Transactions of the Royal Society B: Biological Sciences*, *365*(1555), pp.3227-3246.

Sarmiento, J.L. and Bryan, K., 1982. An ocean transport model for the North Atlantic. Journal of Geophysical Research: Oceans, 87(C1), pp.394-408.

Schaphoff, S., Lucht, W., Gerten, D., Sitch, S., Cramer, W. and Prentice, I.C., 2006. Terrestrial biosphere carbon storage under alternative climate projections. Climatic Change, 74(1), pp.97-122.

Scharlemann, J.P., Tanner, E.V., Hiederer, R. and Kapos, V., 2014. Global soil carbon: understanding and managing the largest terrestrial carbon pool. Carbon Management, 5(1), pp.81-91.

Schimel, D., Stephens, B.B. and Fisher, J.B., 2015. Effect of increasing CO2 on the terrestrial carbon cycle. *Proceedings of the National Academy of Sciences*, *112*(2), pp.436-441.

Schlesinger, W.H., 2009. On the fate of anthropogenic nitrogen. *Proceedings of the National Academy of Sciences*, *106*(1), pp.203-208.

Schuur, E.A. and Abbott, B., 2011. High risk of permafrost thaw. *Nature*, *480*(7375), pp.32-33.

Schuur, E.A., McGuire, A.D., Schädel, C., Grosse, G., Harden, J.W., Hayes, D.J., Hugelius, G., Koven, C.D., Kuhry, P., Lawrence, D.M. and Natali, S.M., 2015. Climate change and the permafrost carbon feedback. *Nature*, *520*(7546), pp.171-179.

Sitch, S., Friedlingstein, P., Gruber, N., Jones, S.D., Murray-Tortarolo, G., Ahlström, A., Doney, S.C., Graven, H., Heinze, C., Huntingford, C. and Levis, S., 2015. Recent trends and drivers of regional sources and sinks of carbon dioxide. *Biogeosciences*, *12*(3), pp.653-679.

Shevliakova, E., Stouffer, R.J., Malyshev, S., Krasting, J.P., Hurtt, G.C. and Pacala, S.W., 2013. Historical warming reduced due to enhanced land carbon uptake. *Proceedings of the National Academy of Sciences*, *110*(42), pp.16730-16735.

Skinner, W.R., Shabbar, A., Flannigan, M.D. and Logan, K., 2006. Large forest fires in Canada and the relationship to global sea surface temperatures. Journal of Geophysical Research: Atmospheres, 111(D14).

Sokolov, A.P., Kicklighter, D.W., Melillo, J.M., Felzer, B.S., Schlosser, C.A. and Cronin, T.W., 2008. Consequences of considering carbon–nitrogen interactions on the feedbacks between climate and the terrestrial carbon cycle. *Journal of Climate*, *21*(15), pp.3776-3796.

Masson-Delmotte, V., Zhai, P., Pirani, A., Connors, S.L., Péan, C., Berger, S. and Zhou, B., 2021. Climate change 2021: the physical science basis. Working Group I contribution to the Sixth Assessment Report of the Intergovernmental Panel on Climate Change.

Stocker, T.F., Qin, D., Plattner, G.K., Tignor, M.M., Allen, S.K., Boschung, J., Nauels, A., Xia, Y., Bex, V. and Midgley, P.M., 2014. Climate Change 2013: The physical science basis. contribution of working group I to the fifth assessment report of IPCC the intergovernmental panel on climate change.

Takahashi, T., Sutherland, S.C., Feely, R.A. and Wanninkhof, R., 2006. Decadal change of the surface water pCO2 in the North Pacific: A synthesis of 35 years of observations. Journal of Geophysical Research: Oceans, 111(C7).

Tape, K.E.N., Sturm, M. and Racine, C., 2006. The evidence for shrub expansion in Northern Alaska and the Pan-Arctic. *Global Change Biology*, *12*(4), pp.686-702.

Tarnocai, C., Canadell, J.G., Schuur, E.A., Kuhry, P., Mazhitova, G. and Zimov, S., 2009. Soil organic carbon pools in the northern circumpolar permafrost region. *Global biogeochemical cycles*, *23*(2).

Taylor, P.C., Ellingson, R.G. and Cai, M., 2011. Geographical distribution of climate feedbacks in the NCAR CCSM3. 0. *Journal of climate*, *24*(11), pp.2737-2753.

Tharammal, T., Bala, G., Narayanappa, D. and Nemani, R., 2019. Potential roles of CO 2 fertilization, nitrogen deposition, climate change, and land use and land cover change on the global terrestrial carbon uptake in the twenty-first century. *Climate Dynamics*, *52*(7), pp.4393-4406.

Thoning, K.W., Tans, P.P. and Komhyr, W.D., 1989. Atmospheric carbon dioxide at Mauna Loa Observatory: 2. Analysis of the NOAA GMCC data, 1974–1985. *Journal of Geophysical Research: Atmospheres*, *94*(D6), pp.8549-8565.

Thoning, K.W., Crotwell, A.M. and Mund, J.W., 1973. Atmospheric Carbon Dioxide Dry Air Mole Fractions from continuous measurements at Mauna Loa. *Hawaii, Barrow, Alaska, American Samoa, and South Pole*, *2019*, pp.2020-08.

Trudinger, C., Enting, I., Etheridge, D., Francey, R. and Rayner, P., 2005. The carbon cycle over the past 1000 years inferred from the inversion of ice core data. In *A history of Atmospheric CO2 and its Effects on Plants, Animals, and Ecosystems* (pp. 329-349). Springer, New York, NY.

Tymstra, C., Flannigan, M.D., Armitage, O.B. and Logan, K., 2007. Impact of climate change on area burned in Alberta's boreal forest. International Journal of Wildland Fire, 16(2), pp.153-160.

Vitousek, P.M. and Howarth, R.W., 1991. Nitrogen limitation on land and in the sea: how can it occur?. Biogeochemistry, 13(2), pp.87-115.

Vitousek, P.M., Cassman, K.E.N., Cleveland, C., Crews, T., Field, C.B., Grimm, N.B., Howarth, R.W., Marino, R., Martinelli, L., Rastetter, E.B. and Sprent, J.I., 2002. Towards an ecological understanding of biological nitrogen fixation. In *The nitrogen cycle at regional to global scales* (pp. 1-45). Springer, Dordrecht.

Walker, X.J., Baltzer, J.L., Cumming, S.G., Day, N.J., Ebert, C., Goetz, S., Johnstone, J.F., Potter, S., Rogers, B.M., Schuur, E.A. and Turetsky, M.R., 2019. Increasing wildfires threaten historic carbon sink of boreal forest soils. *Nature*, *572*(7770), pp.520-523.

Walker, A.P., De Kauwe, M.G., Bastos, A., Belmecheri, S., Georgiou, K., Keeling, R., McMahon, S.M., Medlyn, B.E., Moore, D.J., Norby, R.J. and Zaehle, S., 2020. Integrating the evidence for a terrestrial carbon sink caused by increasing atmospheric CO2. *New Phytologist*.

Werf, G.R., Randerson, J.T., Giglio, L., Leeuwen, T.T.V., Chen, Y., Rogers, B.M., Mu, M., Van Marle, M.J., Morton, D.C., Collatz, G.J. and Yokelson, R.J., 2017. Global fire emissions estimates during 1997–2016. *Earth System Science Data*, *9*(2), pp.697-720.

Walker, M.D., Wahren, C.H., Hollister, R.D., Henry, G.H., Ahlquist, L.E., Alatalo, J.M., Bret-Harte, M.S., Calef, M.P., Callaghan, T.V., Carroll, A.B. and Epstein, H.E., 2006. Plant community responses to experimental warming across the tundra biome. *Proceedings of the National Academy of Sciences*, *103*(5), pp.1342-1346.

Walther, G.R., Post, E., Convey, P., Menzel, A., Parmesan, C., Beebee, T.J., Fromentin, J.M., Hoegh-Guldberg, O. and Bairlein, F., 2002. Ecological responses to recent climate change. *Nature*, *416*(6879), pp.389-395.

Wan, H.Y., Olson, A.C., Muncey, K.D. and Clair, S.B.S., 2014. Legacy effects of fire size and severity on forest regeneration, recruitment, and wildlife activity in aspen forests. Forest ecology and management, 329, pp.59-68.

Wang, W., Ciais, P., Nemani, R.R., Canadell, J.G., Piao, S., Sitch, S., White, M.A., Hashimoto, H., Milesi, C. and Myneni, R.B., 2013. Variations in atmospheric CO2 growth rates coupled with tropical temperature. *Proceedings of the National Academy of Sciences*, *110*(32), pp.13061-13066.

Wang, X., Piao, S., Ciais, P., Friedlingstein, P., Myneni, R.B., Cox, P., Heimann, M., Miller, J., Peng, S., Wang, T. and Yang, H., 2014. A two-fold increase of carbon cycle sensitivity to tropical temperature variations. *Nature*, *506*(7487), pp.212-215.

Watson, R.T., Noble, I.R., Bolin, B., Ravindranath, N.H., Verardo, D.J. and Dokken, D.J., 2000. *Land use, land-use change and forestry: a special report of the Intergovernmental Panel on Climate Change*. Cambridge University Press.

Wilmking, M. and Juday, G.P., 2005. Longitudinal variation of radial growth at Alaska's northern treeline—recent changes and possible scenarios for the 21st century. *Global and Planetary Change*, *47*(2-4), pp.282-300.

Winton, M., Hallberg, R. and Gnanadesikan, A., 1998. Simulation of density-driven frictional downslope flow in z-coordinate ocean models. *Journal of Physical Oceanography*, *28*(11), pp.2163-2174.

Yin, Y., Ciais, P., Chevallier, F., Li, W., Bastos, A., Piao, S., Wang, T. and Liu, H., 2018. Changes in the response of the Northern Hemisphere carbon uptake to temperature over the last three decades. *Geophysical Research Letters*, *45*(9), pp.4371-4380.

Zhang, T., Heginbottom, J.A., Barry, R.G. and Brown, J., 2000. Further statistics on the distribution of permafrost and ground ice in the Northern Hemisphere. *Polar geography*, *24*(2), pp.126-131.

Zhu, Z., Piao, S., Myneni, R.B., Huang, M., Zeng, Z., Canadell, J.G., Ciais, P., Sitch, S., Friedlingstein, P., Arneth, A. and Cao, C., 2016. Greening of the Earth and its drivers. *Nature climate change*, *6*(8), pp.791-795.

2 How robust is the apparent break-down of northern high-latitude temperature control on spring carbon uptake?

Abstract

Vegetation growth in northern high-latitudes during springtime is strongly temperature limited, and thus anomalously warm springs are expected to result in an increased drawdown of carbon dioxide (CO_2). However, a recent analysis of the relationship between spring temperature anomalies and atmospheric CO_2 anomalies at Point Barrow, Alaska, suggests that the link between spring carbon uptake by northern ecosystems and temperature anomalies has been weakening over recent decades due to a diminishing control of temperature on plant productivity. Upon further analysis, covering the 1982-2015 period, we found no significant change in the relationship between spring vegetation productivity derived from remote sensing data and air temperature. We showed that a reduction in spatial coherence of temperature anomalies, alongside a significant sensitivity to atmospheric transport, is likely responsible for the apparent weakening. Our results, therefore, suggest that spring temperature remains as an important control of northern high-latitude CO_2 uptake.

2.1 Introduction

Land vegetation has been a significant sink of atmospheric CO_2 over past decades, taking up roughly a quarter of emissions from fossil fuels and land-use change (Friedlingstein et al., 2019). Towards the end of the 20th century, the Arctic and boreal ecosystems took up between 0.3 and 0.6 PgC yr^{-1} – representing a significant fraction of the global land sink of 1.0 PgC yr^{-1} during this period based on top-down and bottom-up carbon budget estimates (McGuire et al., 2009). Previous studies also indicate that this northern carbon sink has also accelerated in recent decades (Wang et al., 2013; Ciais et al., 2019). In a warming world, it is important to understand how the relationship

between climate and carbon uptake in the northern high-latitudes is evolving if we are to understand the future behaviour of the land carbon sink.

A valuable metric for understanding the carbon cycle in the northern hemisphere is the atmospheric CO_2 seasonal cycle. This cycle exhibits a yearly maximum during the colder months when CO_2 release processes (respiration) dominate, and a yearly minimum during the warmer months when photosynthesis dominates. Keeling et al. (1996) noted that the amplitude of CO_2 seasonal cycle (defined as the difference between annual maximum and minimum) has been increasing over time and that the fastest changes were occurring in northern high latitudes. They also showed that the increase in the CO_2 seasonal amplitude was correlated with northern temperature anomalies and accompanied by a phase advance during the declining phase of the seasonal cycle of CO_2 giving rise to the hypothesis that longer growing seasons are associated with warmer temperatures. A more recent analysis of global CO_2 records confirms that this phenomenon is continuing, showing that the CO_2 seasonal amplitude at the Barrow (Nuvuk) Observatory in Alaska (hereafter referred to as Barrow) increased by 0.60% per year from 1961 to 2011 (Graven et al., 2013).

Respiration and photosynthesis are both strongly affected by temperature, and the competition between them is expected to lead to different responses of net carbon uptake to temperature throughout the year. Observational and model evidence suggest that warming during spring leads to increased carbon uptake while warming during autumn leads to decreased carbon uptake during each respective period (Randerson et al., 1999, Piao et al., 2008). This is explained by the stronger response of photosynthesis (relative to respiratory processes) to warming during springtime, whereas in fall the respiration sensitivity to warming exceeds that of photosynthesis (Piao et al., 2008).

Recently, Piao et al. (2017) (hereafter P2017) showed that the springtime relationship between northern high-latitude temperature and concurrent CO_2 uptake (inferred from atmospheric CO_2 data measured at Barrow) has substantially weakened since the mid-1990s. In their study, this phenomenon was attributed to a weakening of the temperature control on plant productivity based on factorial simulations with biospheric and atmospheric transport models (P2017). These results, therefore, challenge the *"warmer spring – larger carbon sink mechanism"*, and may be indicative

of approaching a new regime in which other climatic constraints, such as *"reduced chilling during dormancy"* and *"an emerging light limitation"*, play a more dominant role in determining spring carbon uptake across northern land (P2017).

While these results are intriguing, influences of atmospheric circulation patterns on findings that are based on single CO_2 monitoring stations cannot be ruled out. The Arctic Oscillation (AO), an atmospheric circulation regime which has a powerful influence over wind patterns and near-surface climate patterns in the high northern latitudes (Thompson et al., 1998), could play an important role here. In this regard, it is notable that the change in correlation between spring vegetation activity and temperature between the two focal periods 1982-1996 and 1997-2012 (which we refer to as the early/late period), as shown in Figure 3j of P2017, has a spatial pattern that strongly resembles an AO pattern (Figure S2.1). This led us to investigate further if the apparent weakening temperature control on spring carbon uptake (P2017) was influenced by large-scale atmospheric circulation patterns.

P2017 investigated the effect of holding land fluxes constant while atmospheric transport varies. They analysed the spring zero crossing (SZC), an indicator of the timing and magnitude of spring carbon uptake by land vegetation. P2017 found that the correlation between the SZC and temperature reduces significantly during the early period (when compared with the control), although there is still a clear difference in correlation between the two periods. However, there is no simulation in P2017 in which transport is held constant, so it is not possible to determine the strength of the interaction effect between land fluxes and transport.

We therefore aim to explore the role of atmospheric transport in the apparent weakening of the link between springtime northern temperatures and carbon uptake in more detail. Unlike P2017, we use interannually-varying footprints of Barrow during spring calculated with the HYSPLIT4 atmospheric trajectory model (Stein et al., 2015) to better understand corresponding influences. To gain additional information on the drivers of spring carbon uptake across northern land, we then performed factorial forward simulations combining modelled land-atmosphere carbon flux exchanges (based on the Carnegie-Ames-Stanford Approach (CASA) land-surface model (Potter

et al., 1993; Randerson et al., 1996)) and the TOMCAT atmospheric chemistry-transport model (Chipperfield, 2006).

2.2 Materials and Methods

2.2.1 Atmospheric CO_2 and analysis of SZC

We analysed the daily *in-situ* CO_2 record at the Barrow Observatory, Alaska (71˚N, 156˚W) from the National Oceanic and Atmospheric Administration (NOAA) Earth Research Laboratory/Global Monitoring Division program (Thoning et al., 2020). The raw CO_2 data were smoothed using the Carbon Cycle Group CuRVe (CCGCRV) routine (Thoning et al., 1989), from which we obtained the detrended smoothed seasonal cycle (see Text S2). The SZC is defined as the day of the year when the CO_2 levels pass through zero in the detrended smoothed seasonal cycle. Similarly, an additional metric for spring carbon uptake known as spring carbon capture (SCC) is calculated from the difference between the first week of May and last week of June in the detrended smoothed seasonal cycle. Our definition of early and late period shifts to 1979-1995 and 1996-2012, respectively, when analysing SZC and SCC due to the availability of data during the 1979-1981 period.

2.2.2 Climate and vegetation data

Satellite NDVI (or greenness) data were used as a proxy for vegetation productivity. Monthly data were obtained from the Global Inventory Modelling and Mapping Studies (GIMMS) Version 3g Advanced Very-High Resolution Radar (AVHRR) dataset (Pinzon and Tucker 2014) over the 1982-2015 period, means-aggregated to a spatial resolution of 0.25˚ (from their native resolution of 8km). An additional satellite product used as a proxy for productivity is the Fraction of Photosynthetically Active Radiation (FPAR) (Zhu et al. (2013). Monthly 0.5˚ resolution air temperature, precipitation and cloud cover data were taken from the Climatic Research Unit TS 4.01 datasets (https://crudata.uea.ac.uk/cru/data/hrg/; Harris et al., 2014), during the 1979-2016 period, with spatial averages calculated over vegetated land, indicated by an NDVI value greater than 0.1. During years in which no NDVI data were available (1979-1981 and 2016), the NDVI > 0.1 mask was calculated from averages taken of the 3 chronologically closest years. For calculating

the detrended spatial average of NDVI and climate data, we detrended the data at each pixel, then summed over the region of interest. The AO dataset was obtained from December to March averages taken from the NOAA teleconnections dataset. More information is available from https://www.cpc.ncep.noaa.gov/products/precip/CWlink/daily_ao_index/ao.shtml

2.2.3 HYSPLIT4 footprints

Back trajectories, calculated using National Centers for Environmental Prediction meteorological data, were used to track the source of the springtime CO_2 signal. Trajectories starting at Barrow during the March-June period were computed every 6 hours. Each back trajectory was extended 30 days backwards in time with locations sampled every hour. For footprint-weighting of temperature and NDVI, we multiplied the temperature and NDVI respectively by the monthly average footprint (units of hours), before averaging the March-June value for each year.

2.2.4 Factorial simulations

We used an observation-based modelling approach to simulate atmospheric CO_2 at Barrow with the CASA land-surface model feeding Net Ecosystem Exchange (NEE) fluxes into the TOMCAT atmospheric chemistry model.

CASA uses a simple light-use efficiency approach to estimate Net Primary Productivity (NPP) as follows:

$$NPP_{tot} = FPAR \cdot SLR \cdot LUE_{max} \cdot f_{temp} \cdot f_{moist} \cdot SC \quad \textbf{[2.1]}$$

where *FPAR* is the fraction of photosynthetically active radiation, *SLR* is ECMWF ERA-Interim 1D solar radiation (Dee et al., 2011), LUE_{max} is the maximum light use efficiency which is based on estimated values for each biome type, the temperature and moisture scalars (f_{temp} and f_{moist} respectively) reduce NPP proportional to their deviation from optimal values, and solar conversion (*SC*) converts to solar units. NPP of herbaceous and woody vegetation is calculated separately with different moisture scalars. CASA uses a series of first-order, linear differential equations to

calculate heterotrophic respiration and the flow of carbon between each of the soil and vegetation pools.

The NEE fluxes from CASA were applied as surface boundary conditions in TOMCAT, as well as fossil fuel emissions from the Carbon Dioxide Information Analysis Center (Andres et al., 2016) and monthly air-sea CO_2 gas fluxes from an ice-ocean-biogeochemical coupled model of the NOAA Geophysical Fluid Dynamics Laboratory forced with COREv2 normal year atmospheric forcing and historical CO_2 atmospheric concentrations (Claret et al., 2021). TOMCAT used ECMWF ERA-Interim meteorology (Dee et al., 2011), running on a 2.8˚ horizontal grid with 60 vertical levels up to 0.1hPa to simulate transport and mixing of atmospheric CO_2. Simulated CO_2 concentrations were then sampled at the locations of the measurement sites every 6 hours, after which, daily averages were taken, and the simulated daily CO_2 time series treated identically to the observed CO_2 data outlined in Section 2.2.1.

We conducted several experiments where we changed components of the CASA model. Specifically, we performed simulations in which we kept the following CASA driver variables at their climatological mean values (with their referenced names in parentheses): Temperature scalar (*TMP*), temperature and moisture scalars (*TMO*), solar radiation (*SLR*), the fraction of absorbed photosynthetically active radiation (a satellite product indicative of assimilation of CO_2 by vegetation - see Section 2.2.2) (*FPAR*), all of those previously mentioned (*ALL*). We then repeated these experiments with atmospheric transport repeating itself every year (using 2006 meteorology). The runs using annually repeating transport fields are referred to with the '*AT,*' prefix, e.g. *AT,TMP* is the run with annually-repeating transport and temperature. It should be noted that the temperature variable in CASA only influences NPP through temperature stress (the *temp_scalar* term from equation (1)), with the positive effects of temperature on productivity being modulated through FPAR. Similarly, the moisture scalars only relate to moisture stress in NPP.

2.3 Results and Discussion

2.3.1 Temperature Sensitivity of SZC and NDVI

In a first step, we reproduced and extended the analysis of P2017 by 4 years up to 2016 and compared the timing of the detrended CO_2 spring zero crossing (SZC) of the seasonal cycle of atmospheric CO_2 at Barrow with the spatially averaged (all vegetated land north of 50˚N) detrended spring temperature. Our results are consistent with those from P2017 and show for the 1979-1995 time-period the strong correlation between detrended SZC at Barrow and spring March-June temperature (Figure 2.1a). However, and as pointed out by P2017, after 1996 this relationship weakens substantially (Figure 2.1a, 2.1b). P2017 repeated their analyses with SCC and obtained the same result. We also repeated this analysis with SCC (Text S1), confirming their conclusion.

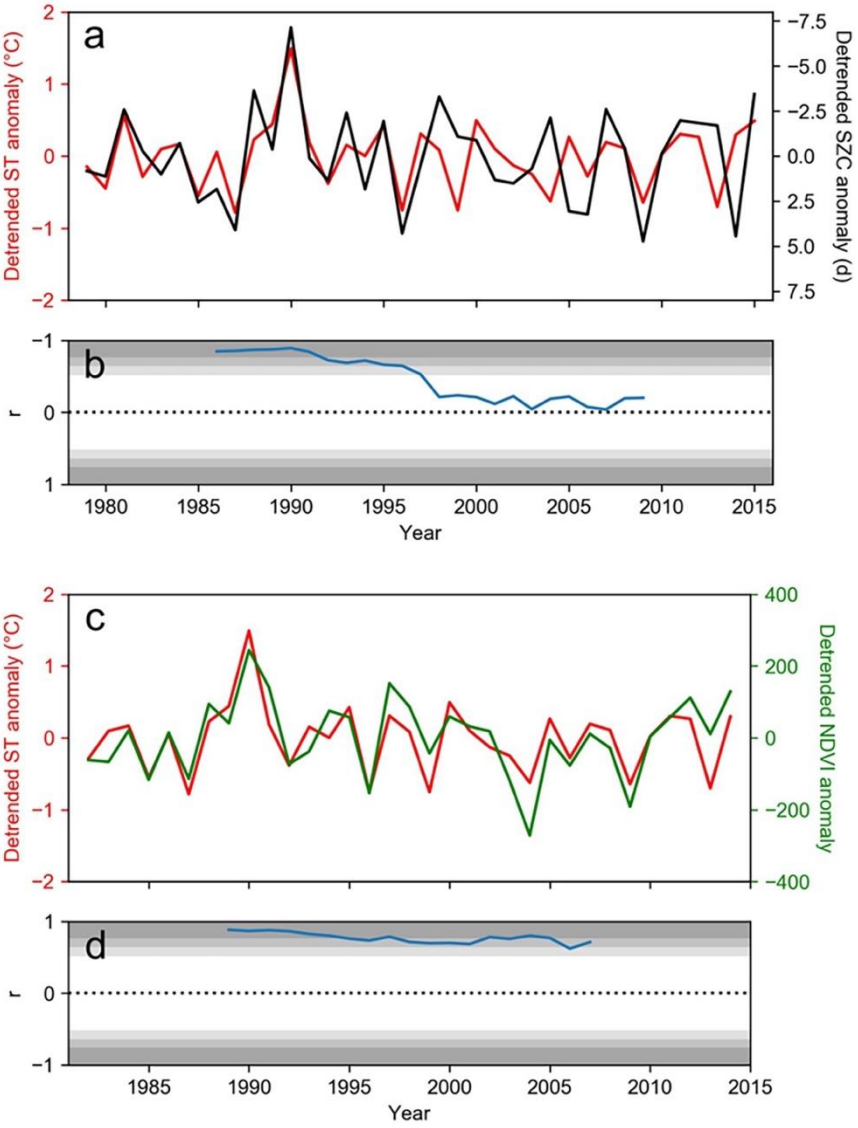

Figure 2.1. Time series of the anomaly (˚C) in detrended spring (March to June) temperature (ST) averaged across vegetated land north of 50˚N along with (a) detrended SZC (days) at Barrow and (c) detrended spring NDVI (March to June) averaged over vegetated land north of 50˚N. Panels (b) and (d) show corresponding moving window (15 yr) partial correlations (accounting for precipitation and radiation). Shaded regions depict 5%, 1% and 0.1% significance levels (n=15).

We next analysed a similar relationship between springtime temperature and NDVI, a satellite-based proxy of photosynthetic activity (Pinzon and Tucker 2014). In contrast to the SZC-temperature relationship, we found that the correlation between the 50˚N spatial average of springtime NDVI and temperature does not weaken significantly over time (Figure 2.1c, 2.1d).

The relationship between spring vegetation productivity and satellite-based NDVI (or greenness) is not straightforward with actual onset of photosynthesis potentially lagging spring green up (estimated from NDVI) depending on land cover type (Walther et al. 2016). However, these results do not support the hypothesised weakening of the temperature control of high latitude plant productivity during springtime put forward by P2017, opening the door for alternative explanations for the breakdown of the SZC-temperature relationship.

One possible explanation is that interannually-varying atmospheric transport contributes to the decoupling of detrended SZC and spring temperature. This is because the CO_2 signal recorded at Barrow has a spatial footprint representative of a limited region of influence, whereas the relationship between detrended NDVI anomalies and detrended temperature anomalies is based on the entire region above 50˚N. In the P2017 analysis, the temperature record used is a zonal average across vegetated lands north of 50˚N, which assumes that the atmospheric footprint of Barrow is influenced uniformly and exclusively by land in this zonal band for all years in the study period. This is despite their footprint analysis of Barrow demonstrating significantly larger contributions from fluxes in Alaska and Eastern Eurasia to the Barrow record than other high-northern latitude regions (P2017).

2.3.2 Footprint of Barrow

In a next step, we analysed the influence of variations in atmospheric transport on CO_2 concentrations at Barrow using the HYSPLIT4 trajectory model (hereafter referred to as 'Hysplit'). Hysplit footprints revealed strong spatial variation in the origin of the air arriving at Barrow (Figure S2.2). We found disproportionately large contributions from Alaska and up to 10% of the signal coming from vegetated land south of 50˚N. This suggests potential pitfalls with relating CO_2 data at Barrow to temperature data averaged uniformly over land north of 50˚N.

We also observed significant interannual variability in the regions influencing Barrow (Figure S2.3), with contributions from Eurasia ranging from 30% to 65% of the total land footprint. These results suggest that atmospheric transport may have a strong influence on the variability of CO_2 sampled at Barrow. These findings are also in line with previous studies highlighting the necessity

to account for changing circulation patterns when inferring carbon dynamics from single-site analyses (Buermann et al., 2007; Wang et al., 2020).

Nonetheless, when we weighted the temperature, precipitation, and cloud cover (a proxy for solar radiation) data using interannually-varying Barrow footprints (see Section 2.2.3), we found that the strong decoupling of the springtime temperature-SZC relationship after 1995 is retained (Figure S2.4a). Furthermore, we found that the springtime temperature sensitivity of vegetation productivity has weakened slightly more inside the footprint of Barrow than across the high latitudes as a whole (Figures S2.4c and 2.1b) although this weakened relationship inside the Barrow footprint occurs only from 2003 onwards and is also statistically not very robust (Figure S2.4b).

2.3.3 Spatial variability of temperature

An ensuing analysis of the influence of atmospheric transport on the temperature-SZC relationship showed that the method for averaging temperature (Barrow footprint-weighted vs all vegetated land above 50˚N) is unimportant in the early period 1979-1995 (corresponding temperature time series correlate strongly), but during the later period, these temperature time series diverge (Figure S2.5). This result points towards greater spatial variability in the temperature signal and thus an increase in the importance of atmospheric transport in the later period.

To understand the reason for this behaviour, we looked at the spatial distribution of spring temperature anomalies. To do so, we compared the anomalies in the detrended large-scale mean spatial average temperature (across all vegetated regions above 50˚N) with the detrended spring temperatures at each pixel. Temperature anomalies for the period 1979-1995 generally agreed well with the spatial mean (mean correlation averaged over all pixels, $\underline{r} = 0.37$), but there was a shift in the second period towards less coherent temperature correlation pattern ($\underline{r} = 0.27$) (Figure S2.5). If the correlations are weighted by the time-varying Barrow footprint, the correlation is even stronger in the early period ($\underline{r} = 0.42$) and breaks down more significantly in the later period ($\underline{r} = 0.21$).

These results suggest that during the later period, the high latitude temperature anomalies are less coherent across large spatial scales and the footprint as seen by Barrow is less representative of the entirety of the high northern latitudes (Figure S2.6; Figure S2.5). The strong agreement in large-scale temperature anomalies in the early period (before the mid-1990s) may be due to the strong activity of the AO. During 1979-1995, the AO index maintained prolonged periods in its negative and positive phase, which promoted large-scale temperature coherence especially in footprint regions of Barrow (Figure S2.1; Figure S2.2). In contrast, during the later period, such extended periods of persistent AO phases were absent. Another indication for a strong AO influence during the early period is that the spatial pattern of correlations between local and large-scale springtime temperature signals in the early period (Figure S2.5) is to a large extent reminiscent of the correlation pattern between spring temperature and the AO index (Figure S2.1b).

The strong spatial coherence of temperature in the early period minimises the influence of transport on CO_2 sampled at Barrow. In contrast, during the later period, transport will have been more important provided the CO_2 signal (as a result of land NEE) was more spatially variable as indicated by greater spatial variability in spring temperature (Figure S2.5).

The springtime temperature sensitivity of vegetation green-up exhibits significant nonlinear behaviour across the high latitudes (Park et al., 2015). Across the same region, there is also significant variability in the temperature sensitivity of spring productivity, as indicated by a regression between spring NDVI and temperature (Figure S2.7). The sensitivity of NDVI to temperature during springtime is more spatially variable in the later period (standard deviation of the sensitivity, $\sigma = 95.5^{\circ}C^{-1}$) than the early period ($\sigma = 78.1^{\circ}C^{-1}$) (Figure S2.6), hence exacerbating the effects of the reduced spatial coherence in temperature (Figure S2.5). As a result, in the later period when temperature coherence is reduced, the correlation between temperature averaged over Barrow footprints and SZC at Barrow would decrease, independently from a decrease in temperature sensitivity of vegetation.

2.3.4 Factorial simulations

To further examine the relative influence of vegetation productivity (NPP) and atmospheric transport on the link between detrended SZC and spring temperatures, we conducted factorial forward simulations with land-based carbon NEE fluxes (based on the CASA model) feeding into the TOMCAT atmospheric chemistry-transport model (see Methods). Results based on a control run (hereafter referred to as CTR) in which all model drivers (e.g., climate, vegetation state (FPAR), and atmospheric transport) vary, showed that the observed seasonal amplitude and trend in atmospheric CO_2 are well reproduced with our CASA_TOMCAT framework, albeit with a bias in the trend in recent years (Figure S2.8). In terms of SZC, while the modelled trend and magnitude show some bias (Figure S2.9a), its interannual variability is reproduced with fairly high accuracy ($r=0.74$, $P<0.1\%$) (Figure S2.9b). The trend biases in recent years suggest limitations in our model framework, however, the interannual variability of simulated SZC is well reproduced, which is the focus of this work. Thus, we can further investigate within our model framework what could cause a breakdown using factorial simulations where the respective model driver of interest was held constant.

The influence of each model driver was assessed by comparing the SZC obtained from that respective factorial simulation (SZC from the SLR simulation is denoted SZC_{SLR}) with the SZC from the CTR simulation (SZC_{CTR}). The SZC obtained from factorial simulations with constant climate drivers (SZC_{TMP}, SZC_{TMO} and SZC_{SLR}) show nearly perfect correlations with SZC_{CTR}, whereas keeping FPAR constant (SZC_{FPAR}) leads to a significant reduction in correlation with SZC_{CTR}, particularly in the later period (Table 2.1). SZC_{ALL} (climate and FPAR held constant) has very similar correlations with SZC_{CTR} as SZC_{FPAR}. These results show that NPP through FPAR is the most dominant CASA factor in controlling SZC variability, with an increase in influence in the later period.

Table 2.1. Correlations between simulated SZC from factorial simulations with observed SZC and spring temperature. The notations *, ** and *** indicate significance at 5%, 1% and 0.1% levels, respectively. Values over the 1997-2012 period are taken from the median correlation value after systematically removing each year from the chronology. Partial correlations take precipitation and cloud cover into account. The constant transport runs are referred to with the '*AT*' prefix. Detailed plots on each of the simulations in supplementary materials (Figures S2.10-20).

Simulation	**Correlation of simulated SZC with complete model, and model with variables held constant**		**Partial correlation of simulated SZC with footprint-averaged observed spring temperature**		**Partial correlation of simulated SZC with 50˚N-averaged observed spring temperature**	
	1982-1996	**1997-2012**	**1982-1996**	**1997-2012**	**1982-1996**	**1997-2012**
Control Run (CTRL)	N/A	N/A	-0.83***	-0.47	-0.85***	-0.16
Variable(s) held constant						
Temperature scalar (TMP)	0.95***	0.92***	-0.74**	-0.53*	-0.69**	-0.05
Temperature and Moisture scalars (TMO)	0.95***	0.92***	-0.75*	-0.51*	-0.70**	-0.12
Solar Radiation (SLR)	0.89***	0.95***	-0.87***	-0.32	-0.82***	-0.12
FPAR	0.82***	0.67**	-0.54*	-0.05	-0.54*	-0.08
TMO, SLR and FPAR (ALL)	0.82***	0.70**	-0.74**	-0.07	-0.63*	0.00
Transport (AT,CTRL)	0.74**	0.43	-0.55*	-0.50	-0.50	-0.18
Transport and Temperature scalar (AT,TMP)	0.75**	0.33	-0.55*	-0.61*	-0.54*	-0.27
Transport and Temperature and Moisture scalars (AT,TMO)	0.75**	0.44	-0.58*	-0.62*	-0.49	-0.29
Transport and Solar Radiation (AT,SLR)	0.67**	0.39	-0.73**	-0.25	-0.73**	-0.02
Transport and FPAR (AT,FPAR)	0.06	-0.07	0.03	-0.05	0.18	0.00
Transport, TMO, SLR and FPAR (AT,ALL)	0.22	-0.15	-0.24	0.07	-0.01	0.24

In the case of constant transport simulations (denoted by prefix '*AT,*') the correlations with SZC_{CTR} underwent a greater reduction during both periods than SZC_{FPAR} (Table 2.1). This shows that atmospheric transport had the largest influence on SZC variability throughout the study period, with an increase in dominance in the later period. Simulations that combine interannually non-varying transport with constant climate ($SZC_{AT,TMP}$, $SZC_{AT,TMO}$ and $SZC_{AT,SLR}$) show no significant deviation from $SZC_{AT,CTR}$ regarding correlations with SZC_{CTR}. $SZC_{AT,FPAR}$ and $SZC_{AT,ALL}$ demonstrate near full absence of the correlation with SZC_{CTR}, further indicating that NPP (through FPAR) and atmospheric transport are the two most important factors controlling interannual variability in SZC at Barrow (Table 2.1).

In regard to correlations between simulated SZC at Barrow and footprint-weighted spring temperature, we first confirm that simulated SZC shows a breakdown with temperature similar to the observed breakdown (Table 2.1). We then determine the influence of each variable in CASA, as well as atmospheric transport in TOMCAT, on the SZC temperature sensitivity by holding the respective variables constant (while maintaining seasonal variations). If those simulations still show the breakdown, then we can conclude that this variable did not cause the breakdown between the two periods. According to this logic, we find for all CASA variables tested that the breakdown is still strong. The only simulations where we do not find a breakdown is when atmospheric transport is held constant. As we only observe a breakdown from the 1st to the 2nd period with varying transport simulations, but no breakdown when transport is held constant, we can conclude that temperature sensitivity has remained constant throughout the study period, and that atmospheric transport is a driving force behind the breakdown in temperature sensitivity of SZC. The correlations between simulated SZC and temperature averaged over 50˚N differ to a large extent from correlations between footprint-weighted temperature and simulated SZC (Table 2.1) which further indicates the importance of accounting for interannually-varying footprints.

Our model reproduced interannual variations in SCC slightly better than SZC (Figure S2.23), although there was a similar bias in the trend and magnitude (Figure S2.24). Analysis of SCC from our factorial simulations yielded similar results to those obtained from SZC analysis, albeit with even greater dominance of atmospheric transport over temperature sensitivity, revealed by

consistent correlation between SCC_{ATCTR} and footprint-weighted spring temperature ($r = 0.68$, $P < 0.01$) during both periods (Table S2.1).

Based on their process-based factorial simulation results, P2017 concluded that transport played no significant role in interannual correlations between SZC and temperature, and that net ecosystem productivity in boreal regions is the dominating factor. Our analysis differs from that of P2017 in that we also compare simulated SZC with the control run (in which all variables vary), as well as simulated SZC with footprint-averaged temperature. We found that atmospheric transport controls a significant proportion of SZC variability, particularly in the later period, which is consistent with our finding that the spatial coherence of temperature anomalies decreased significantly in the late period (Figure S2.5). Furthermore, when holding atmospheric transport constant (ATCTR), there was no breakdown in temperature sensitivity of SZC (Table 2.1), whereas when holding NEE constant (ALL), we did witness a breakdown. This illustrates that, contrary to the conclusions of P2017, atmospheric transport is the key driver behind the breakdown in temperature sensitivity of spring carbon uptake. We also compared the simulated SZC with 50˚N averaged temperature and found differing results, which highlights the sensitivity of temperature to the footprint. Therefore, this suggests 50˚N is not an accurate representation of the air masses seen by Point Barrow, as used by P2017.

2.4 Conclusions

We are witnessing a phase of changing CO_2 levels and climate to which land vegetation is exposed and is adapting. Over the past decades, atmospheric records and fossil fuel emission inventories indicate that the land carbon sink has been growing, taking up approximately 25% of CO_2 entering the atmosphere as a result of fossil fuel burning and land-use change (Friedlingstein et al., 2019). Other indicators of changes in terrestrial carbon cycling include (amongst others) increasing trends in the seasonal amplitude of atmospheric CO_2 exchanges in the northern high latitudes (Graven et al. 2013). In this regard, a weakening relationship between atmospheric CO_2 drawdown measured at Barrow and above 50˚N land surface temperature during Boreal spring have been interpreted as a shift from spring temperature as the main control over plant productivity and consequently spring carbon uptake towards other controls, such as light limitation (P2017). This conclusion is based

on the breakdown of the correlation between SZC anomalies and spring temperature anomalies averaged over vegetated land north of 50˚N after 1995. Somewhat surprisingly, however, our analysis of NDVI (a proxy for plant productivity) does not indicate a similar breakdown of spring temperature controls on NDVI after 1995. We, therefore, have attempted to understand why these analyses come to different conclusions.

One aspect which has not been studied in great detail so far is the role of site-specific regions of influence of atmospheric signals, as well as the interplay between the interannual variation of site-specific regions of influence and homogeneity of temperature anomalies. We find that regions of influence are quite localised and vary substantially at an interannual timescale. For the Barrow site, the influence of fluxes from Eurasia versus North America varies interannually, contributing between 30% and 65% of the total land signal (Figure S2.3). Simulations of the CO_2 signals at high-latitude sites for interannually varying land-atmosphere carbon exchange flux simulated with a data-driven model reveal that anomalies of CO_2 drawdown signals can be very well reproduced when using site-specific regions of influence but not when using above 50˚N average surface temperature anomalies. This suggests a major role played by varying atmospheric transport when attempting to properly represent the influence of temperature on SZC anomalies. Furthermore, our factorial simulations reveal that atmospheric transport is strongly influential over SZC variability, particularly in the later period, playing a dominant role in the breakdown of the correlations between SZC and temperature. Thus, the breakdown in correlation between SZC and temperature is not indicative of a breakdown in the temperature sensitivity of spring carbon uptake, and thus is in agreement with the consistent correlation between NDVI and temperature anomalies (Figure 2.1c).

We furthermore investigated the extent to which the homogeneity of temperature anomalies has changed over the study period. We find a significant shift towards greater spatial heterogeneity in anomalies (Figure S2.5), likely driven by a sustained, strong Arctic Oscillation during the 1979-1995 period becoming comparatively inactive in the 1996-2012 period (Figure S2.1). The trend towards greater heterogeneity in the spring temperature anomalies across the northern latitudes in the later period (Figure S2.5) may explain the increased role of transport in the later period (Figure

2.1) and may also provide an alternative explanation for the breakdown in the correlations between SZC at Barrow and average northern high latitude spring temperatures as noted by P2017.

Together, these findings suggest that the temperature sensitivity of vegetation during springtime has not changed as significantly across the high latitudes as previously suggested (P2017) and that the increased importance of atmospheric transport due to a change in spatial coherence of the temperature signal is the main factor responsible for the breakdown in correlation between SZC and spring temperature. We found that after accounting for atmospheric transport, the weakening of the temperature sensitivity of spring carbon uptake in the high northern latitudes is substantially smaller than previously asserted. Based on the atmospheric CO_2 data and satellite vegetation data we thus conclude that temperature remains an important control of spring plant carbon uptake above 50 N. Improved understanding of the controls of carbon uptake and release of boreal and arctic ecosystems, primarily forests, helps to forecast how these ecosystems may evolve over coming decades.

2.5 Additional information

2.5.1 Repeating analyses with SCC

The SZC and SCC are closely related, with strong correlation (r=, P<0.1%). Overall, we draw the same conclusions from using the SCC as with the SZC. We found a significant breakdown in correlation between SCC and spring temperature averaged over vegetated land north of 50°N (Figure S2.20), and when averaging the temperature over Hysplit footprints (Figure S2.21). Our CASA-TOMCAT model simulates SCC with fairly high accuracy on interannual timescales (r=0.78, P<0.1%) (Figure S2.22), however the modelled trend and magnitude show some bias (Figure S2.23), similar to the simulated SZC. The factorial simulations yield similar results to those carried out with the SZC, however there appears to be a lower influence of FPAR and a higher influence of transport. The former is evidenced from the FPR run, in which the correlations between the simulated SCC and of the control are higher than seen in the SZC simulations (Table S2.1). Similarly, the ATCTR run produced SCC values that correlated lower with the control than seen in the SZC simulations (Table S2.1). Furthermore, the ATCTR simulations of SCC consistently correlated with Hysplit-averaged temperature at higher levels than in the SZC runs

(Table S2.1), further demonstrating the role of transport in the breakdown in control of temperature on spring carbon uptake.

2.5.2 Snow melt

A reviewer expressed the concern that snow melt may have been responsible for the consistent NDVI-Temperature relationship. Thus, we produced an NDVI time series in which regions where temperature was below zero were omitted from the NDVI and temperature reconstruction (Figure S2.25).

References

Andres, R.J., Boden, T.A. and Higdon, D.M., 2016. Gridded uncertainty in fossil fuel carbon dioxide emission maps, a CDIAC example. Atmospheric Chemistry and Physics, 16(23), pp.14979-14995.

Buermann, W., Lintner, B.R., Koven, C.D., Angert, A., Pinzon, J.E., Tucker, C.J. and Fung, I.Y., 2007. The changing carbon cycle at Mauna Loa Observatory. Proceedings of the National Academy of Sciences, 104(11), pp.4249-4254.

Chipperfield, M.P., 2006. New version of the TOMCAT/SLIMCAT off-line chemical transport model: Intercomparison of stratospheric tracer experiments. Quarterly Journal of the Royal Meteorological Society: A journal of the atmospheric sciences, applied meteorology and physical oceanography, 132(617), pp.1179-1203.

Ciais, P., Tan, J., Wang, X., Roedenbeck, C., Chevallier, F., Piao, S.L., Moriarty, R., Broquet, G., Le Quéré, C., Canadell, J.G. and Peng, S., 2019. Five decades of northern land carbon uptake revealed by the interhemispheric CO 2 gradient. Nature, 568(7751), pp.221-225.

Claret, M., Sonnerup, R., & Quay, P. (2021). Next generation global ice-ocean-biogeochemistry coupled model with 13C-cycling (GFDL-MOM5-BLING13C) [Data set]. Zenodo. http://doi.org/10.5281/zenodo.4458981

Cleland, E.E., Chuine, I. and Menzel, A., 2007. Mooney, HA & Schwartz, MD (2007). Shifting plant phenology in response to global change. Trends in Ecology and Evolution, 22(7), pp.357-365.

Dee, D.P., Uppala, S.M., Simmons, A.J., Berrisford, P., Poli, P., Kobayashi, S., Andrae, U. and Vitart, F., The ERA-Interim reanalysis: Configuration and performance of the data assimilation system (2011) Quarterly Journal of the Royal Meteorological Society, 137 (656).

Friedlingstein, P., Jones, M.W., O'Sullivan, M., Andrew, R.M., Hauck, J., Peters, G.P., Peters, W., Pongratz, J., Sitch, S., Le Quéré, C. and Bakker, D.C.E., 2019. Global Carbon Budget 2019, Earth Syst. Sci. Data, 11, 1783–1838.

Graven, H.D., Keeling, R.F., Piper, S.C., Patra, P.K., Stephens, B.B., Wofsy, S.C., Welp, L.R., Sweeney, C., Tans, P.P., Kelley, J.J. and Daube, B.C., 2013. Enhanced seasonal exchange of CO2 by northern ecosystems since 1960. Science, 341(6150), pp.1085-1089.

Harris, I.P.D.J., Jones, P.D., Osborn, T.J. and Lister, D.H., 2014. Updated high-resolution grids of monthly climatic observations–the CRU TS3. 10 Dataset. International journal of climatology, 34(3), pp.623-642.

Keeling, C.D., Chin, J.F.S. and Whorf, T.P., 1996. Increased activity of northern vegetation inferred from atmospheric CO 2 measurements. Nature, 382(6587), pp.146-149.

Keenan, T.F. and Riley, W.J., 2018. Greening of the land surface in the world's cold regions consistent with recent warming. Nature climate change, 8(9), pp.825-828.

Liu, Z., Kimball, J.S., Parazoo, N.C., Ballantyne, A.P., Wang, W.J., Madani, N., Pan, C.G., Watts, J.D., Reichle, R.H., Sonnentag, O. and Marsh, P., 2020. Increased high-latitude photosynthetic carbon gain offset by respiration carbon loss during an anomalous warm winter to spring transition. Global change biology, 26(2), pp.682-696.

McGuire, A.D., Anderson, L.G., Christensen, T.R., Dallimore, S., Guo, L., Hayes, D.J., Heimann, M., Lorenson, T.D., Macdonald, R.W. and Roulet, N., 2009. Sensitivity of the carbon cycle in the Arctic to climate change. Ecological Monographs, 79(4), pp.523-555.

Park, H., Jeong, S.J., Ho, C.H., Kim, J., Brown, M.E. and Schaepman, M.E., 2015. Nonlinear response of vegetation green-up to local temperature variations in temperate and boreal forests in the Northern Hemisphere. Remote Sensing of Environment, 165, pp.100-108.

Piao, S., Ciais, P., Friedlingstein, P., Peylin, P., Reichstein, M., Luyssaert, S., Margolis, H., Fang, J., Barr, A., Chen, A. and Grelle, A., 2008. Net carbon dioxide losses of northern ecosystems in response to autumn warming. Nature, 451(7174), pp.49-52.

Piao, S., Liu, Z., Wang, T., Peng, S., Ciais, P., Huang, M., Ahlstrom, A., Burkhart, J.F., Chevallier, F., Janssens, I.A. and Jeong, S.J., 2017. Weakening temperature control on the interannual variations of spring carbon uptake across northern lands. Nature Climate Change, 7(5), pp.359-363.

Pinzon, J.E. and Tucker, C.J., 2014. A non-stationary 1981–2012 AVHRR NDVI3g time series. Remote sensing, 6(8), pp.6929-6960.

Polgar, C.A. and Primack, R.B., 2011. Leaf-out phenology of temperate woody plants: from trees to ecosystems. New phytologist, 191(4), pp.926-941.

Potter, C.S., Randerson, J.T., Field, C.B., Matson, P.A., Vitousek, P.M., Mooney, H.A. and Klooster, S.A., 1993. Terrestrial ecosystem production: a process model based on global satellite and surface data. Global Biogeochemical Cycles, 7(4), pp.811-841.

Randerson, J.T., Thompson, M.V., Malmstrom, C.M., Field, C.B. and Fung, I.Y., 1996. Substrate limitations for heterotrophs: Implications for models that estimate the seasonal cycle of atmospheric CO2. Global Biogeochemical Cycles, 10(4), pp.585-602.

Randerson, J.T., Field, C.B., Fung, I.Y. and Tans, P.P., 1999. Increases in early season ecosystem uptake explain recent changes in the seasonal cycle of atmospheric CO2 at high northern latitudes. Geophysical research letters, 26(17), pp.2765-2768.

Reed, B.C., Brown, J.F., VanderZee, D., Loveland, T.R., Merchant, J.W. and Ohlen, D.O., 1994. Measuring phenological variability from satellite imagery. Journal of vegetation science, 5(5), pp.703-714.

Stein, A.F., Draxler, R.R., Rolph, G.D., Stunder, B.J., Cohen, M.D. and Ngan, F., 2015. NOAA's HYSPLIT atmospheric transport and dispersion modeling system. Bulletin of the American Meteorological Society, 96(12), pp.2059-2077.

Stocker, T.F., Qin, D., Plattner, G.K., Tignor, M.M., Allen, S.K., Boschung, J., Nauels, A., Xia, Y., Bex, V. and Midgley, P.M., 2014. Climate Change 2013: The physical science basis. contribution of working group I to the fifth assessment report of IPCC the intergovernmental panel on climate change.

Thoning, K.W., Tans, P.P. and Komhyr, W.D., 1989. Atmospheric carbon dioxide at Mauna Loa Observatory: 2. Analysis of the NOAA GMCC data, 1974–1985. Journal of Geophysical Research: Atmospheres, 94(D6), pp.8549-8565.

Thoning, K., Crotwell, A. and Mund, J., 2020. Atmospheric Carbon Dioxide Dry Air Mole Fractions from continuous measurements at Mauna Loa, Hawaii, Barrow, Alaska, American Samoa and South Pole. 1973-2019. National Oceanic and Atmospheric Administration (NOAA), Global Monitoring Laboratory (GML), Boulder, Colorado, USA, doi: https://doi. org/10.15138/yaf1-bk21.

Walther, S., Voigt, M., Thum, T., Gonsamo, A., Zhang, Y., Köhler, P., Jung, M., Varlagin, A. and Guanter, L., 2016. Satellite chlorophyll fluorescence measurements reveal large-scale decoupling

of photosynthesis and greenness dynamics in boreal evergreen forests. Global change biology, 22(9), pp.2979-2996.

Wang, Y., Li, M. and Shen, L., 2013. Accelerating carbon uptake in the Northern Hemisphere: evidence from the interhemispheric difference of atmospheric CO2 concentrations. Tellus B: Chemical and Physical Meteorology, 65(1), p.20334.

Wang, K., Wang, Y., Wang, X., He, Y., Li, X., Keeling, R.F., Ciais, P., Heimann, M., Peng, S., Chevallier, F. and Friedlingstein, P., 2020. Causes of slowing-down seasonal CO2 amplitude at Mauna Loa. Global change biology, 26(8), pp.4462-4477.

Zhu, Z., Bi, J., Pan, Y., Ganguly, S., Anav, A., Xu, L., Samanta, A., Piao, S., Nemani, R.R. and Myneni, R.B., 2013. Global data sets of vegetation leaf area index (LAI) 3g and fraction of photosynthetically active radiation (FPAR) 3g derived from global inventory modeling and mapping studies (GIMMS) normalized difference vegetation index (NDVI3g) for the period 1981 to 2011. Remote sensing, 5(2), pp.927-948.

3 What can atmospheric $\delta^{13}C$ tell us about the carbon cycle?

Abstract

Trends in the atmospheric ^{13}C to ^{12}C ratio, expressed as $\delta^{13}C_{atm}$, are the result of uptake and release of carbon between the atmosphere, biosphere, and oceans, as well as fossil fuel emissions. Thus, the $\delta^{13}C_{atm}$ trend holds information about these processes. The record shows a decrease in $\delta^{13}C_{atm}$ due to fossil fuel emissions, also known as the Suess effect. The observed atmospheric decrease, however, is shallower than expected from fossil fuel emissions, which is due to a net uptake of CO_2 by land vegetation and plant discrimination against heavier ^{13}C. Atmospheric ^{13}C records are thus affected by various factors, including land and ocean carbon uptake and changes therein, as well as by possible changes in plant isotope discrimination due to CO_2 fertilisation. However, it is still unclear what the sensitivity of $\delta^{13}C_{atm}$ is to these various drivers, and thus how it can be used to improve our understanding of the earth carbon cycle. Here we estimate the sensitivity of $\delta^{13}C_{atm}$ to uncertainties in parameterisations involving processes in the land biosphere, as well as uncertainties of ocean and fossil fuel emissions using the global land surface model (CASA) along with air-sea ^{12}C and ^{13}C exchanges from the GFDL ocean model. The default values of net primary productivity (NPP), ocean uptake and C3 discrimination led to an overestimate of the decline of $\delta^{13}C_{atm}$ when compared to the observed trend. Uncertainties are large for soil turnover times, NPP, and ocean uptake and we find that $\delta^{13}C_{atm}$ is most sensitive to ocean uptake, followed by NPP. Our results thus show that uncertainty of ocean uptake strongly affects $\delta^{13}C_{atm}$ trends and that without better constraints on ocean net uptake, we cannot infer much about changes in plant isotope discrimination.

3.1 Introduction

Atmospheric CO_2 has increased throughout the industrial era from 280ppm to over 415 ppm by end of 2021 and continues to increase. This has been accompanied by a global rise in earth surface temperature of approximately 1˚C, with temperature currently increasing at a rate of 0.2˚C per decade (Arias et al., 2021). Atmospheric CO_2 records and estimates of fossil fuel and land-use change emissions reveal that on average 44% of fossil fuel and land-use change emissions

accumulate in the atmosphere over the past 6 decades (Friedlingstein et al., 2020) while the rest is taken up by oceans and processes on land. Models and data analysis to partition these fluxes suggest that processes on land cause a substantial net uptake of carbon roughly equivalent to 30% of fossil fuel emissions (Friedlingstein et al., 2020). Surface warming and CO_2 fertilisation are key drivers behind this land vegetation carbon sink (Schimel et al., 2015; Sitch et al., 2015; Zhu et al., 2016; Keenan et al. 2021). Nonetheless, the spread of estimates of ocean uptake is quite large, and thus substantial uncertainties of land versus ocean carbon uptake remain. Model-based estimates of ocean uptake over the period from 1982 to 2012 summarised by Friedlingstein et al. (2020) range from 1.72 to 2.51 PgC yr^{-1} where the mean of all models is 2.00 PgC yr^{-1}, while data-based estimates range from 1.48 – 1.85 PgC yr^{-1} and a mean of 1.64 PgC yr^{-1}.

Understanding the responses of land vegetation sinks and soil carbon pools to increasing CO_2, changes in nutrient deposition, and environmental change are also incomplete (Walker et al., 2021). The spread of land sink estimates in the global carbon budget across 17 models is between 1.36 and 4.25 PgC yr^{-1} during the period 1982-2012, with a multi-model mean of 2.65 PgC yr^{-1}. The average budget imbalance in the global carbon budget is 0.61 PgC yr^{-1}, which is thought to be primarily a result of uncertainty related to land processes (Friedlingstein et al., 2020). There is clear evidence that climate change and elevated atmospheric CO_2 affects vegetation functioning (Stocker et al., 2013). For example, early season carbon uptake at high latitudes is strongly positively correlated with positive temperature anomalies (Randerson et al. 1999) (see Chapter 2), driven partially by longer growing seasons (Park et al., 2016). Vegetation productivity is further stimulated due to increased atmospheric CO_2 concentration, i.e., CO_2 fertilisation (Farquhar et al., 1980; Kimball et al., 1993). This effect is often described as follows (Friedlingstein et al., 1995):

$$\beta = \frac{\left(NPP(t) - NPP\left(t_0\right)\right) \cdot c_a\left(t_0\right)}{\left(c_a(t) - c_a\left(t_0\right)\right) \cdot NPP\left(t_0\right)}$$

[3.1]

Where *NPP* is net primary productivity, c_a is the ambient CO_2 concentration is t_0 is the reference time (pre-industrial commonly used). Experimental evidence shows indeed an increase in leaf photosynthesis when plants are exposed to elevated CO_2 levels under controlled conditions (Körner, 2006). However, under natural conditions, the effect of CO_2 fertilisation on terrestrial productivity does not only depend on atmospheric CO_2 alone. For example, when nitrogen is limiting, the effect of CO_2 fertilisation on plant growth is significantly reduced (Sokolov et al., 2008). Indeed, some larger-scale free-air CO_2 enrichment (FACE) studies do not show a significant growth stimulation effect caused by elevated CO_2 (Norby et al., 2004; Norby et al., 2005).

However, bottom-up estimates of the land carbon sink agree with modelling studies which suggest that CO_2 fertilisation may have given rise to significant growth in the net land sink over past decades (Sitch et al., 2015), with some of these studies attributing 60% of the current sink attributed to the effect of CO_2 on photosynthesis (Schimel et al., 2015). Nonetheless, a meta-analysis of the effect of CO_2 on vegetation shows that most studies agree that CO_2 increases resulted in increases in productivity, but there is still high uncertainty regarding the precise value of β due to diverging estimates based on different approaches (Walker et al. 2021). Elevated CO_2 levels are not only expected to cause growth stimulation but also lead to reduced stomatal opening and therefore reduced water loss and hence an increased plant water use efficiency (WUE) (Cowan & Farquhar, 1977; Field et al., 1995). 98% of the variation in high latitude tree WUE has been attributed to atmospheric CO_2 levels (Wang & Feng, 2012). Meta-analyses of laboratory and FACE plots suggest that the stomatal response to rising CO_2 concentrations varies by plant type (Curtis & Wang, 1998; Medlyn et al., 2001; Brodribb et al., 2009).

Other elements of the global carbon cycle (relevant on timescales of the human perturbation of atmospheric CO_2) are the size of soil carbon pools, their turnover times, and possible changes in turnover times. Estimates of total soil carbon stocks vary considerably (Raich & Schlesinger, 1992; Scharlemann et al., 2014; Jackson et al., 2017), and turnover times of soil carbon are well known to have significant uncertainties associated with them in general and across biomes (Trumbore, 2000; Carvalhais et al., 2014). Furthermore, the response of soil respiration to temperature is poorly known and subject to significant spatial variation (Zhou et al., 2009). Studies on the response of soil microbial respiration to surface warming have yielded significant decreases (Bradford et al., 2008; Bradford et al., 2010; Crowther et al., 2013) and increases (Hartley et al., 2008; Nie et al., 2013) in soil carbon losses due to warming.

One compound which is involved in and holds information about all these processes is carbon-13 (^{13}C). Due to the difference in the degree to which ^{12}C is preferentially taken up over ^{13}C by vegetation and oceans, the atmospheric ^{13}C record has been used to apportion between oceanic and land sinks in the carbon budget (Tans et al., 1993; Keeling et al., 1995; Quay et al., 1992; Trudinger et al., 2005; Heimann & Maier-Reimer, 1996).

^{13}C makes up roughly 1% of the carbon in the earth system. The global increase in atmospheric CO_2 concentration throughout the industrial era has been accompanied by a corresponding

decrease in the ratio between ^{13}C and ^{12}C in the atmosphere. This ratio is often presented as $\delta^{13}C$, with units per mille (‰), defined as follows:

$$\delta^{13}C = \left(\frac{R_{sample}}{R_{standard}} - 1 \right) \cdot 1000‰$$

[3.2]

R_{sample} is the abundance ratio of ^{13}C to ^{12}C in a sample, $R_{standard}$ is the ^{13}C to ^{12}C ratio in the Pee-Dee Belemnite fossil commonly used as a standard, with a value of 0.0112372 (mol mol^{-1}) (Craig et al., 1957). ^{13}C parallels all ^{12}C flux processes but at subtly differing rates varying with different flux processes. This process is called fractionation, and the resulting difference between the atmosphere ($\delta^{13}C_{atm}$) and other pools (e.g., $\delta^{13}C_{plant}$) is called discrimination (Δ) and is calculated as:

$$\Delta = (\delta^{13}C_{atm} - \delta^{13}C_{plant}) \; / \left(1 + \frac{\delta^{13}C_{plant}}{1000} \right)$$

[3.3]

In general, land vegetation carbon uptake discriminates against ^{13}C far more strongly (i.e., Δ ~18‰) than air-sea gas exchange (Δ ~ 7-10‰) (Vogel et al., 1980). Therefore, land vegetation is generally thought to have a greater effect on the isotopic composition of the atmosphere (Figure 3.1). However, discrimination, by land vegetation can vary considerably depending on environmental conditions, as well as the photosynthetic pathway used (Vogel, 1980; Farquhar, 1989). The $\delta^{13}C$ composition of C3 plants is between -20 and -37 ‰ (Vogel, 1980; Kohn, 2010), whereas C4 plants are in the range of -12 to -16 ‰ (O'Leary et al., 1988), and thus C3 plants discriminate far more strongly against ^{13}C than C4 plants.

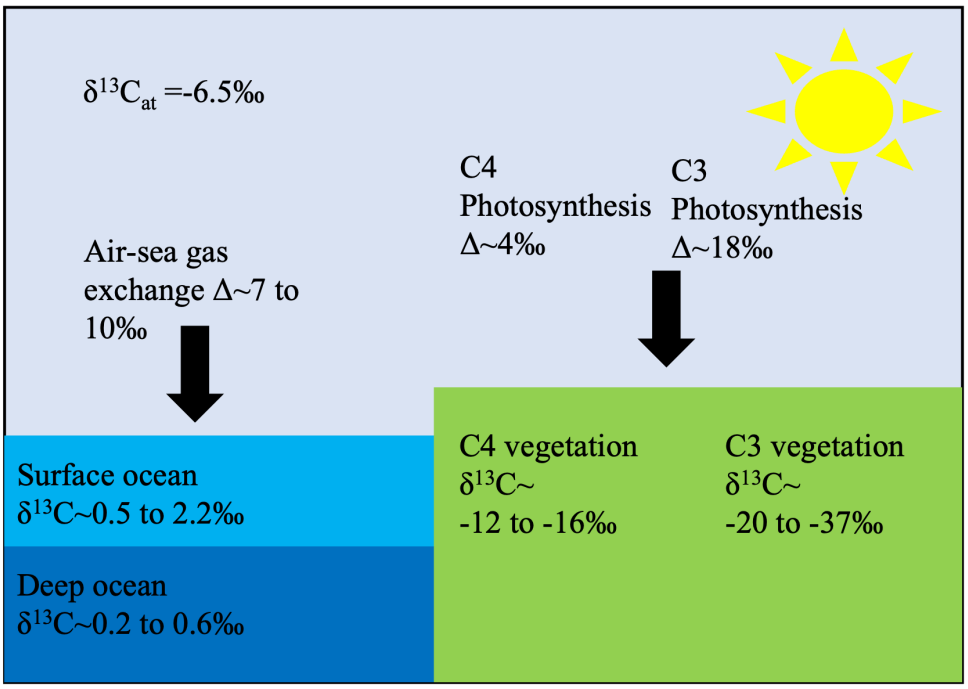

Figure 3.1. Mean preindustrial $\delta^{13}C$ distribution (‰) in the land, ocean, and atmosphere as well as the discrimination factors during land vegetation and ocean uptake (Δ). Arrows indicate net fluxes of carbon.

The decrease in $\delta^{13}C_{atm}$ throughout the industrial era is known as the 'carbon-13 Suess effect' (Figure 3.2) and is due to vast emissions of fossil fuels with a low $\delta^{13}C$ signature. Fossil fuels have a low value of $\delta^{13}C$ as the carbon has been fixed through photosynthesis. The decrease in $\delta^{13}C_{atm}$ caused by fossil fuel emissions is counteracted by plant photosynthesis and ocean uptake which leaves relatively heavy ^{13}C in the atmosphere, and thus has helped constrain land and ocean carbon uptake (Tans et al., 1993; Keeling et al., 1995; Quay et al., 1992; Trudinger et al., 2005; Heimann & Maier-Reimer, 1996) (Figure 3.2).

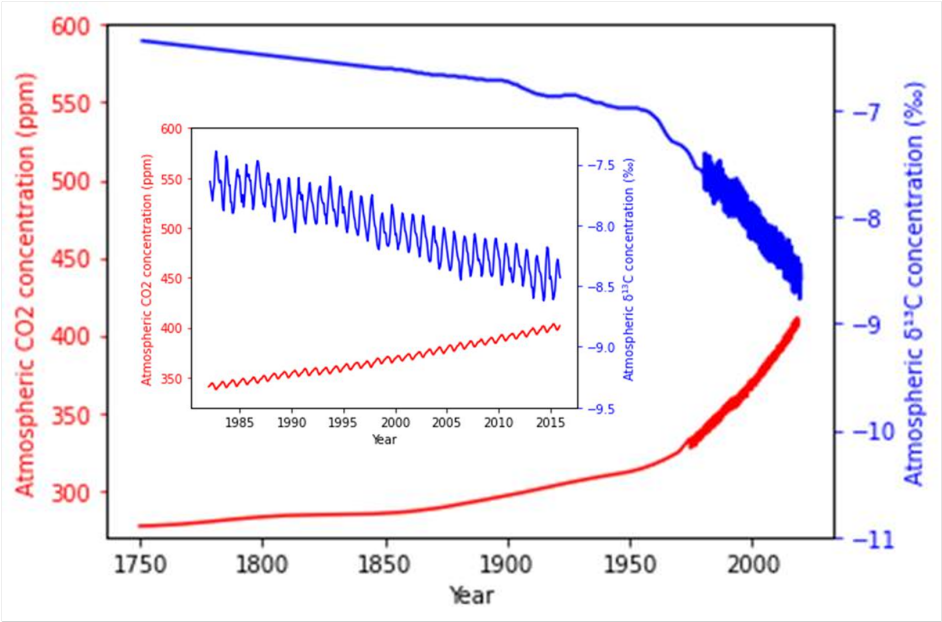

Figure 3.2. Atmospheric CO_2 (red) and $\delta^{13}C$ (blue) are from a combination of the ice-core datasets (Etheridge et al., 1998; Graven et al., 2017) and Scripps (Keeling & Keeling, 2017) *in-situ* measurements at the Mauna Loa observatory. Inset image depicts the atmospheric records during the 1982-2016 period.

One additional possible application of trends in $\delta^{13}C_{atm}$ is to provide insight on changes in vegetation discrimination, and thus its functioning, at the global scale (Keeling et al. 2017). The magnitude of discrimination is related to the ratio of the CO_2 concentration within the stomatal cavities (c_i) to the ambient CO_2 (c_a) according to the plant isotope discrimination model of Farquhar et al. (1982). Thus, changes in discrimination can be related to changes in c_i/c_a, which in turn allow inferring the so-called intrinsic water use efficiency (iWUE) (Ehleringer et al. 1993). iWUE of plants is expected to increase in response to atmospheric CO_2, as plants tend to reduce stomatal conductance (g_s) and increase their assimilation (A), allowing greater carbon uptake for the same amount of water (Ainsworth & Long 2005; Van der Sleen et al., 2015). iWUE is a measure of photosynthesis per unit stomatal conductance, and is given by the following:

$$iWUE = \frac{A}{g_s} = \frac{c_a}{1.6} \cdot \left(1 - \frac{c_i}{c_a}\right) \quad \textbf{[3.4]}$$

Quantification of changes in discrimination from $\delta^{13}C$ in the atmosphere could thus shed light on the debate regarding the strength of increases in plant iWUE (Keeling et al 2017).

Modelling efforts that use most up to date estimates of ocean and terrestrial carbon exchange show that decreases of $\delta^{13}C_{atm}$ are too rapid when compared with observations (Van der Velde et al., 2013), which has been suggested to be due to a global increase in C3 discrimination over time (Keeling et al., 2017). Keeling et al. (2017) modelled the land biosphere as consisting of three boxes and an ocean interior as a one-dimensional diffusive system and find that a simulation with C3 discrimination increases of 0.014 ‰ ppm^{-1} are most consistent with observations of $\delta^{13}C_{atm}$. This would translate to a 20% increase in iWUE of earth vegetation for the 20th century. However, soil turnover times and air-sea exchange also affect $\delta^{13}C_{atm}$, and while fluxes were tuned in the model to match estimates of atmospheric ^{14}C they still carry significant uncertainties (Keeling et al, 2017). Comparing the discrimination trend estimates from Keeling et al. (2017) with the experimental and tree ring derived estimates of discrimination responses to CO_2, yields mixed results. While some experimental data (e.g., Schubert & Jahren (2013)) compare well, tree ring data show a range of responses, some agreeing with Keeling's estimates (e.g., Schubert & Jahren, 2015; Voelker et al. 2016), and others showing opposite (negative) trends (Adams et al. 2020). It should be noted however that tree ring data are limited because isotopic discrimination trends can be confounded with ontogenetic trends (Vadeboncoeur et al., 2020; Brienen et al., 2017).

In all, while $\delta^{13}C_{atm}$ has been used to constrain ocean and land uptake, as well as their discrimination trends, it is unclear how sensitive such estimates are to various components of the earth carbon cycle, such as soil turnover, plant productivity, and ocean uptake. Despite large efforts to constrain these fluxes, they still have relatively large uncertainties and their effect on trends in $\delta^{13}C_{atm}$ are poorly quantified. Thus, the power of $\delta^{13}C_{atm}$ to inform us about changes in plant functioning is reduced, as well as its use in partitioning between the land and ocean sinks. We here use a spatially explicit model to better understand to what extent the shallower than expected decreasing trend in $\delta^{13}C_{atm}$ can tell us about various poorly constrained aspects of the carbon cycle.

In this study, we adapted the Carnegie Ames Stanford Approach (CASA) Global Fire Emissions Database (GFED) land surface model (Potter et al., 1993; Randerson et al., 2018) to simulate land-atmospheric ^{13}C and ^{12}C fluxes. This was done in concert with ocean-atmosphere ^{12}C and ^{13}C simulations from the Geophysical Fluid Dynamics Laboratory (GFDL) simulations (Claret et al., 2021). These simulations use the Biogeochemistry with Light Iron Nutrients and Gas (BLING) (Galbraith et al., 2010) model with the Modular Ocean Model version 5 (MOM5) (Griffies, 2012).

In the default model setup, we found that the trend in $\delta^{13}C_{atm}$ was far steeper than observations. As a result, we investigated the sensitivities of $\delta^{13}C_{atm}$ to perturbing a range of parameters in the model. Furthermore, we were interested in how well $\delta^{13}C_{atm}$ can be used to constrain the large-scale global change in vegetation discrimination. For this to be possible, it was first necessary to determine the uncertainties of each of the major components of the model setup. We then assessed the sensitivity of the simulated $\delta^{13}C_{atm}$ to all relevant drivers in the model. This study presents the first comprehensive analysis of the sensitivities of atmospheric CO_2 and $\delta^{13}C_{atm}$ using a land surface model with spatial variability in the land-atmosphere fluxes of CO_2 and $^{13}CO_2$.

3.2 Materials and Methods

3.2.1 Fossil fuel emissions and ocean fluxes

Yearly mean emissions of CO_2 and the corresponding $\delta^{13}C$ signature of fossil fuel emissions were obtained from the Carbon Dioxide Information Analysis Center (Andres et al., 2016). Coal, oil, and gas have different $\delta^{13}C$ signatures, thus the $\delta^{13}C$ signature of fossil fuel emissions varied year-to-year due to differing masses of coal, oil, and gas being burned each year. Monthly air-sea ^{12}C and ^{13}C gas fluxes were obtained from an ice-ocean-biogeochemical coupled earth system model of the NOAA Geophysical Fluid Dynamics Laboratory forced with COREv2 normal year atmospheric forcing and historical CO_2 atmospheric concentrations (Claret et al., 2021). The ocean emissions were then summed into global total emissions at monthly resolution.

3.2.2 CASA model setup

We used an observation-based modelling approach using remotely sensed satellite observations to construct 2D grids of productivity to simulate global averages of atmospheric CO_2 and $\delta^{13}C_{atm}$ with the CASA land-surface model operating at 0.25˚ resolution on a monthly timescale. The total carbon ($^{12}C + ^{13}C$) stored in land vegetation and soils was modelled at the same time as the ^{13}C.

3.2.2.1 Calculation of Net Primary Productivity

We henceforth differentiate between pools and fluxes of total carbon, ^{12}C and ^{13}C variables using ‘tot’, 12 and 13 respectively as the subscript following the variable in question. The Net Primary Productivity of total carbon (NPP_{tot}) (g/month) was calculated in CASA using a simple light-use efficiency approach whereby the amount of carbon that is fixed during photosynthesis per

incoming photons in the frequency range that can be absorbed by chlorophyll is calculated as follows:

$$NPP_{tot} = FPAR \cdot SLR \cdot LUE_{max} \cdot f_{temp} \cdot f_{moist} \cdot SC$$

[3.5]

where *FPAR* is the fraction of photosynthetically active radiation estimated using satellite data, *SLR* is ECMWF ERA-Interim 1D solar radiation (Dee et al., 2011), LUE_{max} is the maximum light use efficiency which is based on estimated values for each biome type, and the temperature and moisture scalars (f_{temp} and f_{moist} respectively) reduce NPP_{tot} proportional to the deviations of temperature and moisture optimal values, and solar conversion (*SC*) converts to the units of NPP (gC/month). NPP_{tot} of herbaceous and woody vegetation were calculated separately using this formulation with different moisture scalars. NPP_{13} (gC/month), is related to NPP_{12} as follows:

$$NPP_{13} = NPP_{12} \cdot R_{at} \cdot MRWR \cdot \alpha$$

[3.6]

where *MRWR* = 13/12 (g/mol)/(g/mol), the conversion between molar ratio and mass ratio, R_{at} is the atmospheric abundance ratio of ^{13}C to ^{12}C (mol/mol), and α is the fractionation factor during uptake of carbon by plants (see section 3.2.2.3). CASA operates with total carbon rather than ^{12}C, using

$$NPP_{TOT} = NPP_{12} + NPP_{13} = NPP_{12} \cdot \left(1 + \alpha \cdot R_{at} \cdot MRWR\right)$$

[3.7]

[3.6] thus translates into:

$$NPP_{13} = NPP_{12} \cdot \alpha \cdot R_{at} \cdot MRWR = NPP_{TOT} \cdot \frac{\alpha \cdot R_{at} \cdot MRWR}{1 + \left(\alpha \cdot R_{at} \cdot MRWR\right)}$$

[3.8]

CASA time-steps a series of first-order, linear differential equations to calculate the flow of carbon between each of the soil and vegetation pools and heterotrophic respiration (Figure 3.3). To include ^{13}C in CASA, we introduced a series of ^{13}C pools which mirrored the 'total carbon' pools in CASA with identical respiration processes and no additional discrimination occurring during respiration.

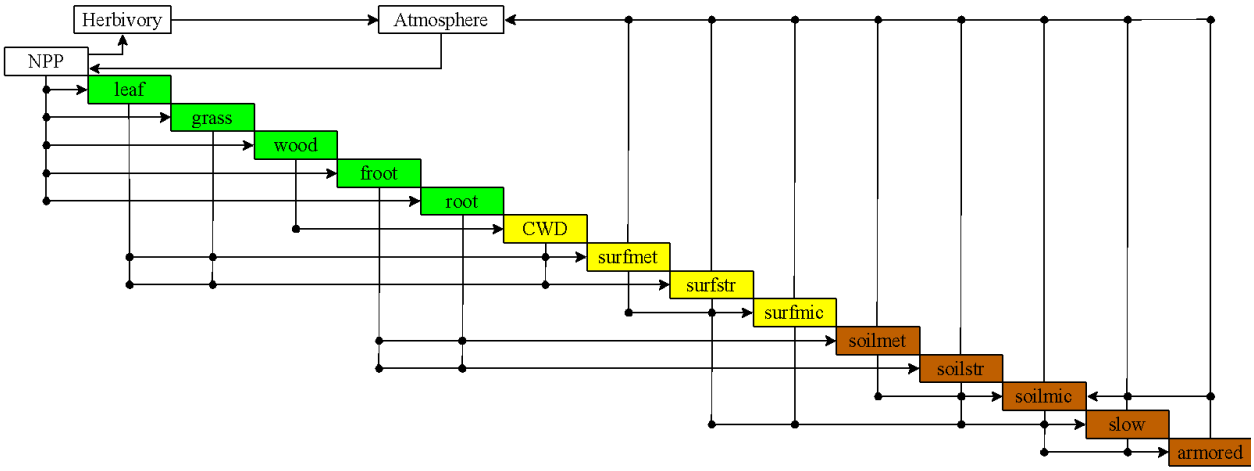

Figure 3.3. Schematic of the direction of atmosphere-land carbon inputs via NPP and outputs via respiration in CASA. Green boxes are the alive pools, yellow are the surface and litter pools, and brown boxes are the soil pools. Adapted from Schaefer et al. (2008) to include additional pools.

3.2.2.2 Spin up and transition interannually-varying climatology

The model runs began with a 1000-year spinup in which climatological and FPAR forcing data were kept at 1981 estimates, with intra-annual variability maintained throughout the year. This spinup allowed the soil pools to fill with carbon until reaching an equilibrium before 1982 when the model began using interannually-varying climatology based on satellite observations. During the spinup, R_{at} varied according to observational data of atmospheric CO_2 and $\delta^{13}C_{atm}$ from a combination of ice core (Etheridge et al., 1998; Graven et al., 2017) and Scripps *in-situ* measurements at the Mauna Loa observatory (Keeling & Keeling, 2017). A linear interpolation was calculated between 1750 and 1850 for the $\delta^{13}C_{atm}$ time series between the known pre-industrial value of -6.35, and the first data point in the ice core data. From 1982 onwards, R_{at} began to vary as follows:

$$\frac{d^{12}M_{at}}{dt} = FF_{12} - OCN_{12} - NEE_{12}$$

[3.9]

$$\frac{d^{13}M_{at}}{dt} = FF_{13} - OCN_{13} - NEE_{13}$$

[3.10]

$$R_{at} = \frac{^{13}M_{at}}{^{12}M_{at} \cdot MRWR}$$

[3.11]

Where M_{at} is the mass of carbon in the atmosphere (PgC), *FF* is fossil fuel emissions, *OCN* is the net ocean uptake, and *NEE* is the net land uptake (net ecosystem exchange).

3.2.2.3 Discrimination of carbon-13 from Net Primary Productivity

The discrimination constant, α in equation **[3.8]** varied spatially and was calculated as follows:

$$\alpha = \left(\alpha_{C3} \cdot VEG_{C3}\right) + \left(\alpha_{C4} \cdot VEG_{C4}\right)$$

[3.12]

Where VEG_{C3} and VEG_{C4} are the fractions of vegetation inside each cell, derived from maps of the fraction of C4 vegetation (Still et al., 2003). The variables α_{C3} and α_{C4} are related to discrimination as follows:

$$\alpha_{C3} = \frac{\Delta_{C3}}{1000} + 1$$
$$\alpha_{C4} = \frac{\Delta_{C4}}{1000} + 1$$

[3.13]

where Δ_{C3}, Δ_{C4} are the discrimination of C3 and C4 vegetation expressed in ‰ which is the difference in $\delta^{13}C$ between the atmosphere and the plant. We did not include estimates for vegetation with the crassulacean acid metabolism (CAM) pathway due to the low prevalence of CAM vegetation (roughly 7%), coupled with relatively low growth rates when compared with C3 and C4 plants. We thus assumed that all vegetated land had either C3 or C4 metabolic pathways. Farquhar et al. (1989) describe C3 and C4 discrimination as follows:

$$\Delta_{C4} = a + \left(b_4 + \left(b_3 \cdot \phi\right) - a\right) \frac{c_i}{c_a}$$

[3.14]

$$\left(b_4 + \left(b_3 \cdot \phi\right) - a\right) \approx 0$$

[3.15]

$$\Delta_{C3} = a + (b - a) \cdot \frac{c_i}{c_a} - \frac{\left(b - a_m\right)\left(\frac{A}{c_a}\right)}{g_i} - \frac{f\Gamma^*}{c_a}$$

[3.16]

where a = 4.4‰ is the discrimination occurring due to diffusion in air, b = 30‰, a_m = 1.8‰, A is leaf-level gross photosynthesis, g_i is mesophyll conductance, f is the discrimination due to photorespiration, and Γ* is the CO_2 compensation point in the absence of day respiration (Farquhar et al., 1982; Cernusak et al., 2013; Seibt et al., 2008). Note that the final two terms in **[3.15]** are often neglected as they are close to zero.

Experimental evidence supports the simplification equation **[3.14]**, thus short term C4 discrimination varies little due to variations in c_i/c_a (Farquhar et al., 1989). We, therefore, assumed that Δ_{C4} would remain constant at 4.4‰. In our attempts to understand changes in global C3 discrimination, we increased Δ_{C3} as a function of atmospheric CO_2 as follows:

$$\Delta_{C3} = \Delta_{ref} - K \cdot \left(C_{cur} - C_{ref} \right)$$

[3.17]

Where Δ_{ref} = 17.8‰ is the global estimation of C3 discrimination in 1990 (Lloyd & Farquhar, 1994), C_{ref} is the atmospheric CO_2 average in 1990, C_{cur} is the atmospheric CO_2 variable in CASA, C_{pre} is atmospheric CO_2 pre-industrial concentration, K is the sensitivity of C3 discrimination to atmospheric CO_2. Keeling et al. (2017) estimated K to be equal to 0.014 ± 0.007 ‰ ppm^{-1}.

3.2.2.4 Pool turnover times

In CASA, there are 14 gridded pools that turnover at varying rates with vastly different masses and $\delta^{13}C$ signatures. Each of these pools and their turnover rate, mass and $\delta^{13}C$ in the default model are summarised in Table 3.1.

Table 3.1. Summary of soil and vegetation pools in CASA at the end of spinup. In the pools column, the long-form name and shortened version are provided in brackets, where applicable.

Pool	Turnover times (yr)	Mass (PgC)	$\delta^{13}C$ (‰)
Leaf	0.37*	4.7	-24.3
Wood	40	253.8	-22.8
Grass	0.33	9.9	-21.9
Root	40	63.3	-22.8
Fine root (froot)	0.5	14.3	-21.4
Course woody debris (cwd)	4	65.7	-23.2
Surface metabolic (surfmet)	0.06	6.0	-22.7
Surface structural (surfstr)	0.15	37.2	-23.4
Surface microbial (surfmic)	0.10	4.7	-23.1
Soil metabolic (soilmet)	0.05	3.9	-21.8
Soil structural (soilstr)	0.2	31.5	-22.8
Soil microbial (soilmic)	0.14	11.9	-22.1
Slow	13.16*	752.4	-27.8
Armored	1000*	592.2	-31.1

*Turnover is spatially variable, so the value presented is the global mean.

3.2.3 Sensitivity analyses to uncertainties

We here lay out the key elements in the carbon cycle for which the trend in $\delta^{13}C_{atm}$ may be sensitive.

3.2.3.1 Isotopic discrimination

There were considerable uncertainties in various elements in the model setup. Estimates of long-term change in plant isotope discrimination most consistent with $\delta^{13}C_{atm}$ indicate a C3 discrimination trend of 0.014 ± 0.007 ‰ ppm^{-1} (Keeling et al., 2017).

Contrary to Keeling's result, studies of the isotopic composition of tree rings do not support an increase in C3 discrimination. In general, a decrease in discrimination is apparent from the available studies (Adams et al. 2020). However, due to the biases present in all studies par one (Van der Sleen et al., 2015), it is impossible to fully disentangle the actual response of plant discrimination to CO_2 from the change in discrimination due to increases in tree height and crown light environment (Vadeboncoeur et al., 2020; Brienen et al., 2017; Brienen et al., 2021).

3.2.3.2 Land uptake

In general, soil respiration is known to increase with surface temperature, and the factor by which soil respiration increases for every 10˚C temperature rise is known as Q10. A Q10 value of 2 is commonly used in land surface models, the likely uncertainty range of Q10 is between 1.43 and 2.03 (Zhou et al., 2009). C3 vegetation maps were obtained from Still et al. (2003), where approximately 75% of gross primary production were C3. We here test the magnitude of the sensitivity of $\delta^{13}C_{atm}$ to estimates of C3 vegetation cover by increasing C3 cover to 100% as no alternative uncertainty is available.

Soil turnover times and total soil carbon stocks are well known to have significant uncertainties related with them. Carvalhais et al. (2014) estimated that carbon resides in vegetation and soil on average for 15 years close at tropical latitudes, and 255 years at high latitudes. However, Trumbore (2000) estimated soil turnover times to be 3 and 30 years for tropical and high latitude regions respectively. Lastly, Raich and Schlesinger (1992) estimated soil turnover times to be 10 and 500 years for tropical savannah and tundra or peaty wetlands respectively. Estimates of total global soil organic carbon (SOC) differ considerably, with estimates ranging from 504-3000 PgC (Scharlemann et al., 2014). A more recent analysis estimated SOC at depths 2 and 3 m to be between 2270 and 2770 PgC (Jackson et al., 2017). This could also be a gross underestimate because soils can be far deeper than 3 m (particularly in the tropics). The rate of soil respiration in response to warming is also subject to considerable uncertainty. The Q10 index is defined as the factor by which soil respiration would be expected to rise as a result of 10˚C of warming. The value of Q10 varies between biomes, and the global average Q10 likely lies between 1.43 and 2.03 (Zhou et al., 2009).

Within CASA, soil turnover is inextricably linked with the total mass of soils (longer turnover times led to larger pools of soil carbon). When comparing estimates from the literature with the CASA model, it is evident that tropical soil turnover (25˚S - 25˚N) is on the upper end of the estimates at 14.6 years (24.2 years if the armored pool is included). However, high latitude (<50˚S, >50˚N) soil turnover is relatively low compared with the estimates in the literature at 62.5 years (120.3 years if the armored pool is included). Total soil carbon in CASA is 1392.2 PgC, which is within the uncertainty range of Scharlemann et al., (2014), but lower than the range from Jackson et al. (2017). The high northern latitudes contain 530.9 PgC in CASA, and a fourfold increase in turnover time would cause a corresponding increase in soil carbon of roughly 1500 PgC, which

would be close to the upper estimate of Scharlemann et al. (2014). Thus, we test the sensitivity of $\delta^{13}C_{atm}$ to increasing the turnover time across the high latitude regions by 4 times.

Calculated NPP in CASA from the light use efficiency model varies between 59.5 and 67.1 PgC depending on the year. Estimates of NPP range from 10.3 to 149 PgC based on 251 estimates from a range of estimates with differing methodologies (Ito, 2011). However, the vast majority of the estimates lie in the 30 to 90 PgC range, which is the uncertainty we utilised in this study.

3.2.3.3 Ocean uptake uncertainty

The ocean CO_2 flux uncertainty was calculated by constructing a monthly time series between the years 1982 and 2012 of observation-based and modelled sea-air CO_2 partial pressure (ΔpCO_2) - the difference between sea surface pCO_2 (pCO_2^{sea}) and atmospheric pCO_2 (pCO_2^{air}). The ΔpCO_2 data (Landschützer et al. 2020) are based on pCO_2^{sea} from Surface Ocean CO_2 Atlas version 2 (SOCATv2) observations interpolated into a 1˚ x 1˚ grid using a neural network method (Landschützer et al. 2016) and on pCO_2^{air} derived from *GLOBALVIEW-CO2* data. The modelled ΔpCO_2 output comes from GFDL MOM5-BLING^{13}C, which also has a nominal lateral resolution of 1˚ x 1˚. Both time series (observational-based and modelled) were constructed by performing a spatial average weighted by the cell grid area, the modelled piston velocity (PV), and the modelled CO_2 solubility in seawater (K_s). The final uncertainty was obtained by computing the root mean squared error (RMSE) between the two ΔpCO_2 time series (ΔpCO_2^{RMSE}) and propagating it to a sea-air CO_2 flux (F) using the conventional formula:

$$F = PV \cdot K_s \cdot \Delta pCO_2 \quad \textbf{[3.18]}$$

That is, the sea-air CO_2 flux uncertainty is as follows:

$$\left| PV^{AVE} \cdot K_s^{AVE} \right| \cdot \Delta pCO_2^{RMSE} \quad \textbf{[3.19]}$$

In this expression, PV^{AVE} and K_s^{AVE} were averaged in space, weighted by the area and by PV for K_s, and in time. The uncertainty is based on the RMSE of ΔpCO_2 instead of F because ΔpCO_2 is directly measurable while F depends on wind speed versus gas exchange parameterisations. Moreover, ΔpCO_2 is a function of many processes, including the CO_2 gas transfer velocity and phenomena influencing the sea surface temperature on which the pCO_2^{sea} solubility depends (e.g., the sea-air heat exchange and the ocean circulation). Therefore, ΔpCO_2^{RMSE} between model and

observational-based products is a metric that already contains model uncertainties in PV^{AVE} and K_s^{AVE}.

The $^{13}CO_2$ ocean flux uncertainty was computed applying the same rationale. Monthly time series of observed and modelled ^{13}C sea-air disequilibrium (R_{dis}) were constructed spanning over the same period as those of ΔpCO_2. Here R_{dis} is defined as:

$$R_{dis} = \frac{R_{DIC}}{R_{CO2}^{air} \cdot \alpha_{DIC \leftarrow g}}$$

[3.20]

where R_{DIC} and R_{CO2}^{air} are the $^{13}C/^{12}C$ ratios of dissolved inorganic carbon in seawater (DIC) and pCO_2^{air} respectively, and $\alpha_{DIC\square g}$ the isotopic fractionation from dissolved gas to DIC (Zhang et al. 1995). This definition is consistent with the $^{13}CO_2$ air-sea flux formulation of Quay et al. (2007, equation 3), based on Zhang et al. (1995), which can be rearranged in terms of a sea-air $^{13}CO_2$ flux as:

$$F^{13C} = PV \cdot K_s \cdot \alpha_k \cdot \alpha_{aq \leftarrow g} \cdot R_{CO2}^{air} \cdot \left(R_{dis} \cdot \left(\Delta pCO_2 + pCO_2^{air} \right) - pCO_2^{air} \right)$$

[3.21]

where α_k and α_{aqpg} are the isotopic fractionations during air-sea CO_2 gas exchange and from gas to dissolved gas respectively. Observed R_{dis} data were computed from point observations of sea surface ^{13}C of DIC ($DI^{13}C$) (Quay et al. 2003; Quay et al. 2007; Quay et al. 2017) and atmospheric $p^{13}CO_2$ ($p^{13}CO_2^{air}$) from Graven et al. (2017) at the same time. R_{dis} data were then binned over 5º x 2º longitude x latitude bands and spatially averaged, weighting by the area and the modelled PV, K_s, and R_{CO2}^{air} – all three properties binned over the same longitude and latitude bands. Modelled R_{dis} was computed analogously by extracting sea surface $DI^{13}C$ and $p^{13}CO_2^{air}$ output for the same location and/or time than point observations. Using these time series, the RMSE of R_{dis} (R_{dis}^{RMSE}) was computed between observations and model, weighting it by the number of observations over a given month in each bin. The model bias in R_{dis} was finally expressed in terms of a sea-air $^{13}CO_2$ flux by propagating the RMSEs of ΔpCO_2 and R_{dis} using the equation for F^{13C} **[3.21]** with averaged values of modelled PV, K_s, R_{CO2}^{air}, and pCO_2^{air} appropriately weighted, and constant values α_k= 0.99915 and $\alpha_{aq\leftarrow g}$=0.99876 (Zhang et al., 1995).

During 1982-2017, the estimated global mean ocean sink was 2.323 PgC yr^{-1} and the corresponding uncertainty in the estimate was 1.02 PgC yr^{-1} (Claret et al., 2021). The estimated ocean sink from the global carbon budget is 2.08 PgC (Friedlingstein et al., 2020). Individual models vary between 1.82 and 2.60 PgC, and observation-based estimates range from 1.58 to 2.28 PgC (Friedlingstein et al., 2020). Thus, the uncertainty estimated here is relatively high, but testing a lower bound of 1.6 - 1.8 PgC is within the bounds of the estimates.

3.2.3.3 Fossil Fuel emission uncertainty

The total ($^{12}C + {}^{13}C$) fossil fuel emissions have an uncertainty of 5% (Friedlingstein et al., 2020), whereas the $\delta^{13}C$ signature of fossil fuels have an uncertainty of 0.6‰ (Popa et al., 2014). As with the ocean emissions, we combine these uncertainties to estimate the sensitivity of $\delta^{13}C_{atm}$ to overall fossil fuel emission uncertainty.

3.2.3.3 Overview of sensitivity analyses

We conducted a number of sensitivity analyses to examine the relative influence of each of these parameters over $\delta^{13}C_{atm}$ in the CASA model (Table 3.2). All analyses were conducted as perturbations from the default CASA setup with discrimination as in Keeling et al. (2017) (unless otherwise stated).

Table 3.2 Summary of sensitivity analyses conducted in this chapter.

Parameter	Default value in model	Minimum value(s) tested	Maximum value(s) tested	Reference for default value	Reference for uncertainty range
C3 discrimination trend (‰ ppm^{-1})	0.014	0.007	0.021	Keeling et al. (2017)	Keeling et al. (2017)
C3 vegetation distribution (%)	75	75	100	Still et al. (2003)	N/A
Q10	2	1.43	2	Potter et al., 1993; Randerson et al., 2018	Zhou et al. (2009)
Turnover times of fast soils in high latitudes (years)	120	120	500	Potter et al., 1993; Randerson et al., 2018	Raich & Schelsinger (1992); Carvalhais (2014)
NPP (PgC yr^{-1})	60*	30*	90*	Potter et al., 1993; Randerson et al., 2018	Ito (2011)
Ocean ^{12}C uptake (PgC yr^{-1})	2.28*	1.26*	3.30*	Claret et al. (2021)	Claret et al. (2021)
Ocean ^{13}C uptake (PgC yr^{-1})	0.0269	0.0145	0.0393	Claret et al. (2021)	Claret et al. (2021)
Fossil fuel ^{12}C emissions (PgC yr^{-1})	9.67*	10.15*	9.19*	Boden et al. (2009)	Friedlingstein et al. (2020)
Fossil fuel ^{13}C signature (‰)	-27.8*	-28.4*	-27.2*	Andres et al. (1996)	Popa et al. (2014)

*Indicates a value that varies from year to year, so the mean value is presented.

3.3 Results and discussion

3.3.1 Default CASA model

Running the model setup with the default conditions in CASA and the calculated ocean uptake and fossil fuel emissions led to an estimate of atmospheric CO_2 that had a slightly steeper trend than observed values (Figure 3.4a). We thus added a slight CO_2 fertilisation effect, whereby the land vegetation NPP calculated in **[3.5]** was then modified as follows:

$$NPP_{fert}(t) = NPP(t) \cdot \left(\frac{CO_2(t)}{CO_2(t_{ref})} \right)^{\beta}$$

[3.22]

where β is an additional CO_2 fertilisation parameter in addition to the already built-in response of vegetation to changing environmental conditions derived from FPAR calculated from satellite observations. After iteratively running the model with different values of β, 0.15 was found to be the optimal value to enable atmospheric CO_2 to be well fitted to observations. However, the modelled trend in $\delta^{13}C_{atm}$ is far steeper than the observed trend (Figure 3.4b).

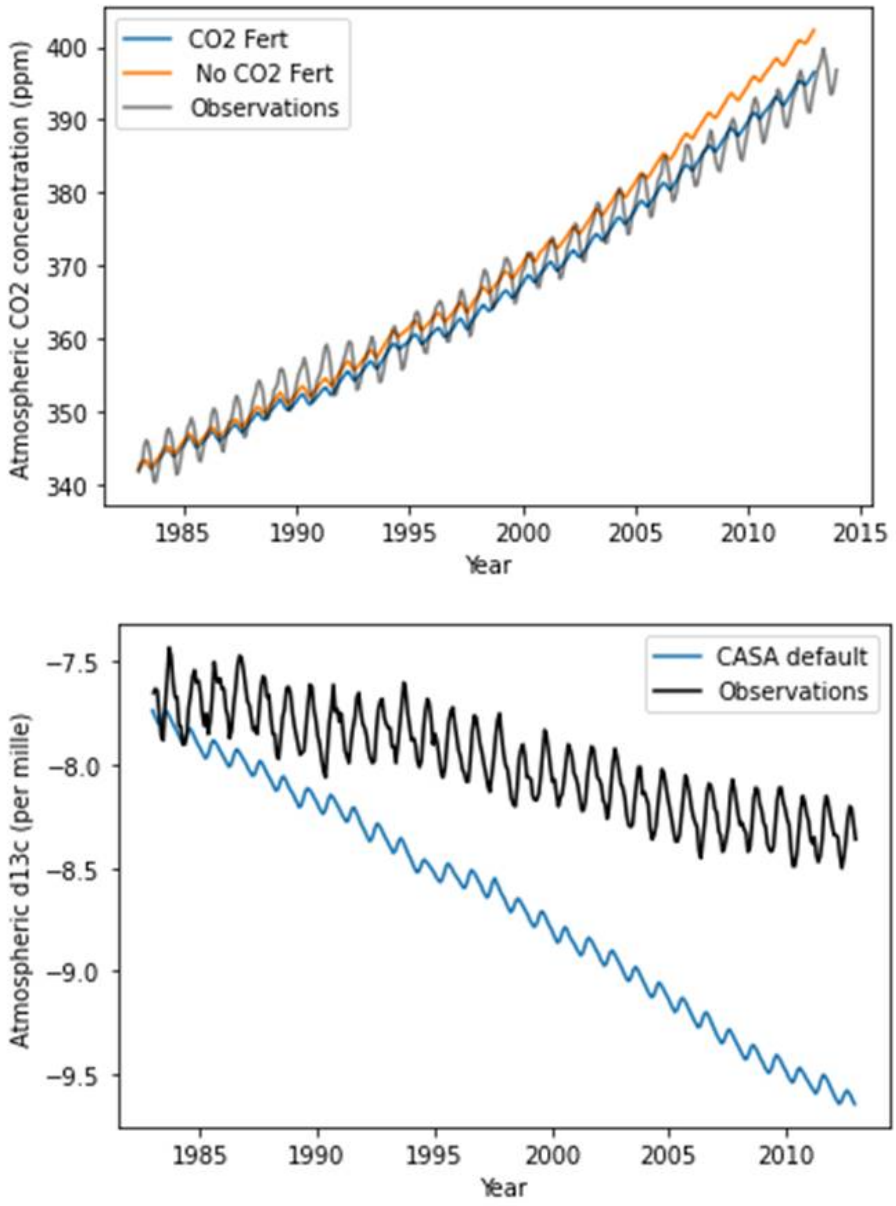

Figure 3.4. Default simulation of (a) atmospheric CO_2 with and without CO_2 fertilisation, and (b) $\delta^{13}C_{atm}$ with CO_2 fertilisation. The CO_2 fertilisation parameter in the 'CO_2 fert' model run was 0.15.

Comparing the value of β directly with estimates from other studies would not be appropriate because CASA includes some stimulatory effect on vegetation due to the trends in temperature and FPAR obtained from satellite data. Thus, we analyse the total increase in NPP compared with the spinup NPP as a result of the combination of CO_2 fertilisation and environmental effects which will serve as an upper bound on the total CO_2 fertilisation effect. Using the CASA-calculated NPP and modelled atmospheric CO_2, β_{tot} was calculated as follows:

$$\beta_{tot} = \frac{\log(NPP) - \log\left(NPP\left(t_{ref}\right)\right)}{\log\left(CO_2(t)\right) - \log\left(CO_2\left(t_{ref}\right)\right)}$$

[3.23]

3.3.2 Sensitivity Analyses

We then tested the sensitivities of $\delta^{13}C_{atm}$ and CO_2 (where appropriate) to each of the uncertainty ranges presented in Table 3.2. In each run, the β parameter was adjusted such that atmospheric CO_2 was fitted to observed values (within an error of 1% of the default CO_2 trend). The reasoning for this adjustment is that $\delta^{13}C_{atm}$ is calculated from atmospheric ^{12}C and ^{13}C **[3.2]**, thus if the trend in ^{12}C changes between simulations, $\delta^{13}C$ will be affected in ways unrelated to the land and ocean processes we are interested in studying. In each set of runs, unless otherwise stated, all other parameters were held at their default values.

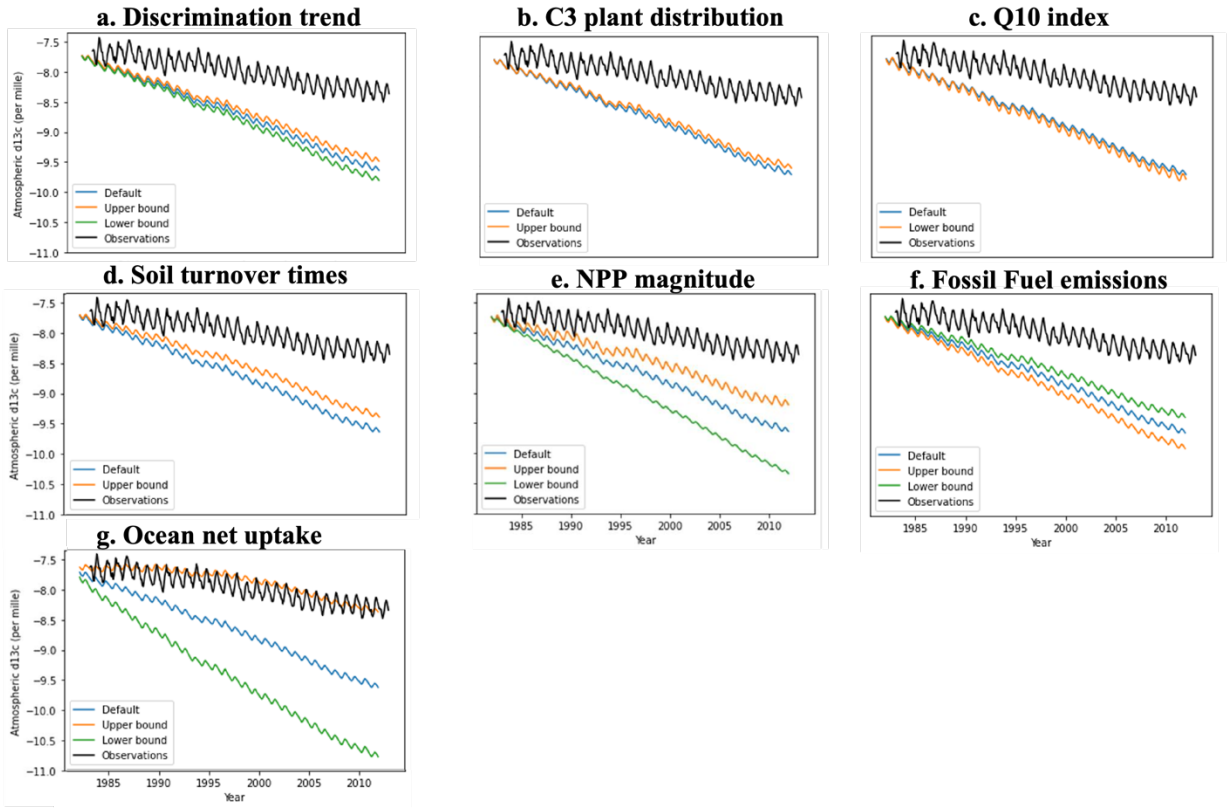

Figure 3.5. Modelled $\delta^{13}C_{atm}$ as (a) the trend of C3 discrimination, (b) soil turnover times, (c) ocean uptake, (d) C3 plant distribution, (e) Q10 index, (f) fossil fuel emissions, (g) NPP magnitude vary according to the upper and lower bounds from Table 3.2. Note that for the ocean uptake, the bounds are in terms of fluxes into the atmosphere and thus the upper bound is where the ocean-atmosphere flux is highest.

3.3.2.1 C3 discrimination

We first tested the upper and lower bounds of the discrimination of C3 vegetation between the 0.014 ± 0.007 ‰ ppm^{-1} bounds estimated by Keeling et al. (2017). The upper bound led to a small reduction in the steepness of the trend in $\delta^{13}C_{atm}$, with a corresponding increase in the steepness with the lower bound in the discrimination trend (Figure 3.5a). Furthermore, increasing the coverage of C3 vegetation had very little impact on $\delta^{13}C_{atm}$ (Figure 3.5b).

3.3.2.2 Soil respiration and turnover

Next, we tested the effect of varying the Q10 parameter within CASA and found that there was very little sensitivity of the trend in atmospheric CO_2 and $\delta^{13}C_{atm}$. However, the seasonal amplitude was strongly influenced by Q10, where the lower Q10 value led to greater seasonal amplitude in

$\delta^{13}C$ (Figure 3.5c). Slowing down soil turnover times over the high latitudes in CASA had little influence on the modelled trend in $\delta^{13}C_{atm}$ (Figure 3.5d).

3.3.2.3 Net primary productivity

Altering NPP from the default values calculated in CASA via multiplication by a scalar throughout the entire model simulation (including the spinup phase) led to significant shifts in $\delta^{13}C_{atm}$ with very little impact on atmospheric CO_2 levels (Figure 3.5e), due to increased pool sizes after spinup and hence larger respiration during the 1982-2012 period.

3.3.2.4 Fossil fuel and ocean uncertainties

As discussed in section 3.2.3, the uncertainties in ocean uptake and fossil fuel emissions were evaluated by combining the upper and lower bounds of the total emissions and $\delta^{13}C$ signature.
The uncertainty range due to fossil fuel emission uncertainty was moderate for atmospheric CO_2 and $\delta^{13}C$ (Figure 3.5f). However, the uncertainty range in ocean emissions led to a large uncertainty in $\delta^{13}C_{atm}$ (Figure 3.5g). The lower bound of ocean emissions alone reduced the trend in $\delta^{13}C_{atm}$ to nearly be in line with observed values.

3.3.4 Summary of runs

We present here a summary of all runs depicted in the preceding sections (Table 3.3).

Table 3.3. Key figures for each of the simulations presented in this study and observed values. Trends in atmospheric CO_2 and $\delta 13C_{atm}$ were obtained from a 12-month moving average of the respective time series. βtot was calculated from **[3.23]** where the mean of all years was calculated during 1982-2012. N/A values present in the 'Observed' row when no estimate exists for the given quantity during the 1982-2012 period.

Run	Trend in atmospheric CO_2 (ppm yr^{-1})	Trend in $\delta^{13}C_{atm}$ (‰)	Mean land sink (PgC yr^{-1}) *	Mean ocean sink (PgC yr^{-1})	Mean ^{13}C ocean sink (PgC yr^{-1})	Mean land NPP (PgC yr^{-1})	Mean $\delta^{13}C$ of land NPP (‰)	β	β_{TOT}
Observed	1.72	-0.0253	1.36-4.25	1.48-2.51	N/A	30 - 90	N/A	N/A	N/A
Default	1.78	-0.0636	3.26	2.28	0.0269	63.47	-22.95	0.15	0.30
Upper bound discrimination trend	1.77	-0.0588	3.26	2.28	0.0269	63.47	-22.93	0.15	0.30
Lower bound discrimination trend	1.77	-0.0688	3.26	2.28	0.0269	63.47	-22.98	0.15	0.30
Upper bound C3 distribution	1.78	-0.0600	3.26	2.28	0.0269	63.47	-26.35	0.15	0.30
Lower bound Q10	1.73	-0.0659	3.04	2.28	0.0269	63.47	-23.00	0.15	0.30
Slower Soil Turnover	1.88	-0.0558	3.23	2.28	0.0269	60.05	-22.79	0.3	-0.10
Upper bound NPP	1.76	-0.0492	4.36	2.28	0.0269	93.90	-22.73	0.05	0.20
Lower bound NPP	1.91	-0.0865	1.88	2.28	0.0269	32.22	-23.3	0.3	0.40
Upper bound FF	1.93	-0.0716	3.56	2.28	0.0269	64.38	-23.05	0.25	0.30
Lower bound FF	1.63	-0.0557	2.83	2.28	0.0269	62.17	-22.89	0	0.31
Upper bound Ocean	1.71	-0.0246	2.29	3.30	0.0313	60.55	-22.18	-0.2	-0.04
Lower bound Ocean	1.79	-0.0991	4.35	1.26	0.0145	66.74	-23.68	0.6	0.65

3.4 Discussion

We here present an exploration into modelling $\delta^{13}C_{atm}$ using the CASA 2D land-surface model alongside ocean GFDL emissions and CDIAC fossil fuel data. We found in the default model setup that the increase in atmospheric CO_2 was close to observations, but there was a large discrepancy between modelled and observed $\delta^{13}C_{atm}$ decreased with the model results showing an almost 2 times stronger decrease. This is a steeper trend than was found by Van der Velde et al. (2013). Our series of sensitivity analyses within estimated uncertainties revealed significant sensitivity of $\delta^{13}C_{atm}$ to (in order of importance): Ocean uptake, NPP, the trend in C3 discrimination, and soil turnover time. The source of the uncertainty in ocean emissions originates from the uncertainties in ocean circulation, productivity, and gas exchange. Our study differs from other analyses that try to use $\delta^{13}C_{atm}$ to partition between ocean and land because we tested the uncertainties of each of the major components of the land biosphere, as well as the uncertainties of ocean uptake and fossil fuel emissions. This study has not touched on various other uncertainties of the land functioning, such as parameters involved with the carbon uptake and release of peat, as well as fire mortality of vegetation**.**

The use of CASA in this study is justified by the accuracy of many elements within the model when compared with estimates from the literature. Firstly, the soil turnover times and total soil carbon stocks in CASA lie close to the estimates from the literature and within the uncertainty bounds (see section 3.2.3.2). Furthermore, the global NPP sum is very close to the majority of estimates in the literature (Ito, 2011). In our simulations, we modified the CO_2 fertilisation parameter to fit the simulations to atmospheric CO_2 observations. This was because the other components of our model setup are more tightly constrained than the terrestrial sink. Estimates for the terrestrial sink range from 1.36-4.25PgC yr^{-1} during 1982-2012, thus making it far more uncertain than all the major sinks/sources in the carbon budget (Friedlingstein et al., 2020). This compares with the uncertainty calculated from this study of 1.88-4.36PgC yr^{-1} (Table 3.3). The difference in the seasonal cycle of atmospheric CO_2 and $\delta^{13}C$ between CASA and the observations (Figure 3.4) is expected because the observed values come from the mean of data from the South Pole and Mauna Loa observatories. The data from these observatories are affected by regional variations in uptake and release processes by vegetation (which are the dominating factors behind CO_2 amplitude). Whereas the CASA atmospheric record is a global mean, thus is not subject to this phenomenon. The estimates of the ocean fluxes are slightly higher than the multi-model mean

from the global carbon project (Friedlingstein et al., 2020), however, they lie well within the model range of 1.78-2.59. Most of the uncertainty of the ^{13}C ocean net uptake originated from the uncertainty in the ^{12}C net uptake, which we have demonstrated is large.

Our study suggests that ocean (land) uptake is on the lower (upper) end of the range of model estimates from the global carbon budget (Friedlingstein et al., 2020) (Table 3.3). Estimates of the precise value of the CO_2 fertilisation parameter β vary significantly between studies (Walker et al., 2021). Keenan et al., (2021) found that gross primary productivity (GPP) estimated from only the fraction of absorbed photosynthetically active radiation (fAPAR) underestimates the CO_2 fertilisation effect, thus justifying the inclusion of an additional CO_2 fertilisation effect in this study. In their study, they estimated that the CO_2 fertilisation effect on gross primary productivity (β_{GPP}) to be 0.54 ± 0.03. This compares with the upper bound estimated in this study of 0.65 (Table 3.3), however, the β estimated here is calculated from NPP, thus not directly comparable with the estimate of Keenan et al. (2021).

Estimates of C3 discrimination from experimental data Schubert & Jahren (2013) as well as discrimination changes over long (glacial-interglacial) time scales (Schubert & Jahren, 2015; Voelker et al. 2016) fell inside the uncertainty range estimated by Keeling et al. (2017). Adams et al. (2020) compiled tree ring studies with $\delta^{13}C$ measurements across multiple decades and sites. Contrary to the finding of Keeling et al. (2017), the overall trend in tree ring $\delta^{13}C$ demonstrates a decrease over time (after accounting for changing $\delta^{13}C_{atm}$). However, this is not necessarily indicative of changes (or lack thereof) in C3 discrimination. This is because, as previously discussed, there is a significant influence of plant size on isotopic discrimination (Vadeboncoeur et al., 2020; Brienen et al., 2017; Brienen et al., 2021), thus size must be accounted for when deriving time trends of discrimination from tree ring isotopes. For all datasets included in Adams et al. (2020), bar one (Van der Sleen et al., 2015), the size effect on plant discrimination was not accounted for. The sensitivity of discrimination from Van der Sleen et al. (2015) was 0.0056‰ ppm^{-1}, which is slightly below the lower bound estimated by Keeling et al. (2017) of 0.007‰. However, due to the lack of spatial and species coverage from a single study, it is not possible to generalise to a global scale from this estimate alone. We here find that we cannot use modelled $\delta^{13}C_{atm}$ to provide additional constraints on C3 discrimination due to the low sensitivity of $\delta^{13}C_{atm}$ to varying discrimination trends (Figure 3.5).

3.5 Conclusion

Rising atmospheric CO_2 concentrations and the accompanying surface warming of the earth is causing rapid changes to the biological landscape. Careful analysis of the $\delta^{13}C_{atm}$ signature has been used to estimate the ratio between the land and ocean sinks (Tans et al., 1993; Keeling et al., 1995; Quay et al., 1992; Trudinger et al., 2005; Heimann & Maier-Reimer, 1996). The magnitudes of the land and ocean sinks are still poorly understood. Thus, understanding the sensitivity of $\delta^{13}C_{atm}$ to various parameters within the earth system would help characterise the robustness of any studies that analyse model simulations of $\delta^{13}C_{atm}$ to infer information about land and ocean uptake processes. $\delta^{13}C_{atm}$ has also been used to estimate the trend in C3 discrimination as a result of rising atmospheric CO_2 concentrations (Keeling et al., 2017). The reported trend from Keeling et al. (2017) of C3 discrimination was estimated by running the model many times and choosing the trend where $\delta^{13}C_{atm}$ levels matched observations. In their study, they acknowledged the sensitivity of $\delta^{13}C_{atm}$ to the turnover of carbon in the land biosphere and air-sea gas exchange. The parameters strongly influencing both processes were tuned by modelling atmospheric ^{14}C and fitted the model to match the atmospheric record.

Our study has demonstrated that the significant uncertainties of the functioning of land and ocean processes lead to vastly different effects on $\delta^{13}C_{atm}$. $\delta^{13}C_{atm}$ was found to be far more sensitive to ocean net carbon uptake (i.e., ocean sink) than any of the land uncertainties. Furthermore, because of the reduced ocean uptake, land uptake must have been larger. C3 discrimination was not found to influence $\delta^{13}C_{atm}$ as strongly when varying within the uncertainty bounds, thus we cannot make a strong argument about the extent to which that has changed over the past decades.

This study differs from other analyses that try to use $\delta^{13}C_{atm}$ to partition between ocean and land because we tested the uncertainties of each of the major components of the land biosphere, as well as the uncertainties of ocean uptake and fossil fuel emissions. We have provided important insight into the sensitivities of $\delta^{13}C_{atm}$ to a range of parameters within the land and ocean sinks. We thus conclude that more work is needed in improving the robustness of estimates of vegetation productivity and global soil turnover over land, as well as circulation, productivity, and gas exchange in the oceans.

References

Adams, M.A., Buckley, T.N. and Turnbull, T.L., 2020. Diminishing CO 2-driven gains in water-use efficiency of global forests. Nature Climate Change, 10(5), pp.466-471.

Ainsworth, E.A. and Long, S.P., 2005. What have we learned from 15 years of free-air CO2 enrichment (FACE)? A meta-analytic review of the responses of photosynthesis, canopy properties and plant production to rising CO2. New phytologist, 165(2), pp.351-372.

Andres, R.J., Boden, T.A. and Marland, G., 1996. Annual Fossil-Fuel CO2 Emissions: Global Stable Carbon Isotopic Signature (1751-2008) (DB1013 V. 2011) (No. DB-1013). Environmental System Science Data Infrastructure for a Virtual Ecosystem; Carbon Dioxide Information Analysis Center (CDIAC), Oak Ridge National Laboratory (ORNL), Oak Ridge, TN (USA).

Arias, P., Bellouin, N., Coppola, E., Jones, R., Krinner, G., Marotzke, J., Naik, V., Palmer, M., Plattner, G.K., Rogelj, J. and Rojas, M., 2021. Climate Change 2021: The Physical Science Basis. Contribution of Working Group14 I to the Sixth Assessment Report of the Intergovernmental Panel on Climate Change; Technical Summary.

Bala, G., Krishna, S., Narayanappa, D., Cao, L., Caldeira, K. and Nemani, R., 2013. An estimate of equilibrium sensitivity of global terrestrial carbon cycle using NCAR CCSM4. Climate dynamics, 40(7-8), pp.1671-1686.

Batjes, N.H., 1996. Total carbon and nitrogen in the soils of the world. European journal of soil science, 47(2), pp.151-163.

Boden, T.A., Marland, G. and Andres, R.J., 2009. Global, Regional, and National Fossil-Fuel CO2 Emissions, 1751-2006 (published 2009). Environmental System Science Data Infrastructure for a Virtual Ecosystem; Carbon Dioxide Information Analysis Center (CDIAC), Oak Ridge National Laboratory (ORNL), Oak Ridge, TN (United States).

Bradford, M.A., Davies, C.A., Frey, S.D., Maddox, T.R., Melillo, J.M., Mohan, J.E., Reynolds, J.F., Treseder, K.K. and Wallenstein, M.D., 2008. Thermal adaptation of soil microbial respiration to elevated temperature. Ecology letters, 11(12), pp.1316-1327.

Bradford, M.A., Watts, B.W. and Davies, C.A., 2010. Thermal adaptation of heterotrophic soil respiration in laboratory microcosms. Global Change Biology, 16(5), pp.1576-1588.

Brienen, R.J.W., Gloor, E., Clerici, S., Newton, R., Arppe, L., Boom, A., Bottrell, S., Callaghan, M., Heaton, T., Helama, S. and Helle, G., 2017. Tree height strongly affects estimates of water-use efficiency responses to climate and CO 2 using isotopes. Nature Communications, 8(1), pp.1-10.

Brienen, R., Helle, G., Pons, T., Boom, A., Gloor, M., Groenendijk, P., Clerici, S., Leng, M. and Jones, C., 2021. Paired analysis of tree ring width and carbon isotopes indicate when controls on tropical tree growth change from light to water limitations. Tree Physiology.

Brodribb, T.J., McAdam, S.A., Jordan, G.J. and Feild, T.S., 2009. Evolution of stomatal responsiveness to CO2 and optimization of water-use efficiency among land plants. New Phytologist, 183(3), pp.839-847.

Carvalhais, N., Forkel, M., Khomik, M., Bellarby, J., Jung, M., Migliavacca, M., Saatchi, S., Santoro, M., Thurner, M., Weber, U. and Ahrens, B., 2014. Global covariation of carbon turnover times with climate in terrestrial ecosystems. Nature, 514(7521), pp.213-217.

Cernusak, L.A., Ubierna, N., Winter, K., Holtum, J.A., Marshall, J.D. and Farquhar, G.D., 2013. Environmental and physiological determinants of carbon isotope discrimination in terrestrial plants. New Phytologist, 200(4), pp.950-965.

Claret, M., Sonnerup, R.E. and Quay, P.D., 2021. A next generation ocean carbon isotope model for climate studies I: Steady state controls on ocean 13C. Global Biogeochemical Cycles, 35(4), p.e2020GB006757.

Cowan, I.R. and GD, F., 1977. Stomatal function in relation to leaf metabolism and environment.

Craig, H., 1957. Isotopic standards for carbon and oxygen and correction factors for mass-spectrometric analysis of carbon dioxide. Geochimica et cosmochimica acta, 12(1-2), pp.133-149.

Crowther, T.W. and Bradford, M.A., 2013. Thermal acclimation in widespread heterotrophic soil microbes. Ecology letters, 16(4), pp.469-477.

Curtis, P.S. and Wang, X., 1998. A meta-analysis of elevated CO 2 effects on woody plant mass, form, and physiology. Oecologia, 113(3), pp.299-313.

Dee, D.P., Uppala, S.M., Simmons, A.J., Berrisford, P., Poli, P., Kobayashi, S., Andrae, U., Balmaseda, M.A., Balsamo, G., Bauer, D.P. and Bechtold, P., 2011. The ERA-Interim reanalysis: Configuration and performance of the data assimilation system. Quarterly Journal of the royal meteorological society, 137(656), pp.553-597.

Devaraju, N., Bala, G., Caldeira, K. and Nemani, R., 2016. A model based investigation of the relative importance of CO 2-fertilization, climate warming, nitrogen deposition and land use change on the global terrestrial carbon uptake in the historical period. Climate Dynamics, 47(1), pp.173-190.

Etheridge, D.M., Steele, L.P., Langenfelds, R.L., Francey, R.J., Barnola, J.M. and Morgan, V.I., 1998. Historical CO2 records from the Law Dome DE08, DE08-2, and DSS ice cores. Trends: a compendium of data on global change, pp.351-364.

Farquhar, G.D., Ehleringer, J.R. and Hubick, K.T., 1989. Carbon isotope discrimination and photosynthesis. Annual review of plant biology, 40(1), pp.503-537.

Farquhar, G.D., O'Leary, M.H. and Berry, J.A., 1982. On the relationship between carbon isotope discrimination and the intercellular carbon dioxide concentration in leaves. Functional Plant Biology, 9(2), pp.121-137.

Farquhar, G.D., von Caemmerer, S.V. and Berry, J.A., 1980. A biochemical model of photosynthetic CO 2 assimilation in leaves of C 3 species. Planta, 149(1), pp.78-90.

Field, C.B., Jackson, R.B. and Mooney, H.A., 1995. Stomatal responses to increased CO2: implications from the plant to the global scale. Plant, Cell & Environment, 18(10), pp.1214-1225.

Friedlingstein, P., Fung, I., Holland, E., John, J., Brasseur, G., Erickson, D. and Schimel, D., 1995. On the contribution of CO2 fertilization to the missing biospheric sink. Global Biogeochemical Cycles, 9(4), pp.541-556.

Friedlingstein, P., O'sullivan, M., Jones, M.W., Andrew, R.M., Hauck, J., Olsen, A., Peters, G.P., Peters, W., Pongratz, J., Sitch, S. and Le Quéré, C., 2020. Global carbon budget 2020. Earth System Science Data, 12(4), pp.3269-3340.

Galbraith, E.D., Gnanadesikan, A., Dunne, J.P. and Hiscock, M.R., 2010. Regional impacts of iron-light colimitation in a global biogeochemical model. Biogeosciences, 7(3), pp.1043-1064.

Graven, H., Allison, C.E., Etheridge, D.M., Hammer, S., Keeling, R.F., Levin, I., Meijer, H.A., Rubino, M., Tans, P.P., Trudinger, C.M. and Vaughn, B.H., 2017. Compiled records of carbon isotopes in atmospheric CO 2 for historical simulations in CMIP6. Geoscientific Model Development, 10(12), pp.4405-4417.

Griffies, S.M., 2012. Elements of the modular ocean model (MOM). GFDL Ocean Group Tech. Rep, 7(620), p.47.

Hartley, I.P., Hopkins, D.W., Garnett, M.H., Sommerkorn, M. and Wookey, P.A., 2008. Soil microbial respiration in arctic soil does not acclimate to temperature. Ecology letters, 11(10), pp.1092-1100.

Heimann, M. and Maier-Reimer, E., 1996. On the relations between the oceanic uptake of CO2 and its carbon isotopes. Global Biogeochemical Cycles, 10(1), pp.89-110.

Ito, A., 2011. A historical meta-analysis of global terrestrial net primary productivity: are estimates converging?. Global Change Biology, 17(10), pp.3161-3175.

Jackson, R.B., Lajtha, K., Crow, S.E., Hugelius, G., Kramer, M.G. and Piñeiro, G., 2017. The ecology of soil carbon: pools, vulnerabilities, and biotic and abiotic controls. Annual Review of Ecology, Evolution, and Systematics, 48, pp.419-445.

Kallenbach, C.M., Frey, S.D. and Grandy, A.S., 2016. Direct evidence for microbial-derived soil organic matter formation and its ecophysiological controls. Nature communications, 7(1), pp.1-10.

Keeling, C.D., Whorf, T.P., Wahlen, M. and Van der Plichtt, J., 1995. Interannual extremes in the rate of rise of atmospheric carbon dioxide since 1980. Nature, 375(6533), pp.666-670.

Keeling, R.F., Graven, H.D., Welp, L.R., Resplandy, L., Bi, J., Piper, S.C., Sun, Y., Bollenbacher, A. and Meijer, H.A., 2017. Atmospheric evidence for a global secular increase in carbon isotopic discrimination of land photosynthesis. Proceedings of the National Academy of Sciences, 114(39), pp.10361-10366.

Keeling, R.F. and Keeling, C.D., 2017. Atmospheric monthly in situ CO2 data-mauna loa observatory, Hawaii. Scripps CO2 program data.

Keenan, T.F., Luo, X., De Kauwe, M.G., Medlyn, B.E., Prentice, I.C., Stocker, B.D., Smith, N.G., Terrer, C., Wang, H., Zhang, Y. and Zhou, S., 2021. A constraint on historic growth in global photosynthesis due to increasing CO2. Nature, 600(7888), pp.253-258.

Kimball, B.A., Mauney, J.R., Nakayama, F.S. and Idso, S.B., 1993. Effects of increasing atmospheric CO 2 on vegetation. Vegetatio, 104(1), pp.65-75.

Kohn, M.J., 2010. Carbon isotope compositions of terrestrial C3 plants as indicators of (paleo) ecology and (paleo) climate. Proceedings of the National Academy of Sciences, 107(46), pp.19691-19695.

Körner, C., 2006. Plant CO2 responses: an issue of definition, time and resource supply. New phytologist, 172(3), pp.393-411.

Landschützer, P., Gruber, N. and Bakker, D.C.E., 2016. Decadal variations and trends of the global ocean carbon sink, Global Biogeochemical Cy-25 cles, 30, 1396–1417.

Landschützer, P; Gruber & N; Bakker, D. C. E. 2020. An observation-based global monthly gridded sea surface pCO2 product from 1982 onward and its monthly climatology (NCEI Accession 0160558). Version 5.5. NOAA National Centers for Environmental Information. Dataset.

Lloyd, J. and Farquhar, G.D., 1994. 13 C discrimination during CO 2 assimilation by the terrestrial biosphere. Oecologia, 99(3), pp.201-215.

McCarroll, D., Gagen, M.H., Loader, N.J., Robertson, I., Anchukaitis, K.J., Los, S., Young, G.H., Jalkanen, R., Kirchhefer, A. and Waterhouse, J.S., 2009. Correction of tree ring stable carbon isotope chronologies for changes in the carbon dioxide content of the atmosphere. Geochimica et Cosmochimica Acta, 73(6), pp.1539-1547.

McGuire, A.D., Anderson, L.G., Christensen, T.R., Dallimore, S., Guo, L., Hayes, D.J., Heimann, M., Lorenson, T.D., Macdonald, R.W. and Roulet, N., 2009. Sensitivity of the carbon cycle in the Arctic to climate change. Ecological Monographs, 79(4), pp.523-555.

Medlyn, B.E., Barton, C.V.M., Broadmeadow, M.S.J., Ceulemans, R., De Angelis, P., Forstreuter, M., Freeman, M., Jackson, S.B., Kellomäki, S., Laitat, E. and Rey, A., 2001. Stomatal conductance of forest species after long-term exposure to elevated CO2 concentration: a synthesis. New Phytologist, 149(2), pp.247-264.

Menviel, L., Mouchet, A., Meissner, K.J., Joos, F. and England, M.H., 2015. Impact of oceanic circulation changes on atmospheric δ13CO2. Global Biogeochemical Cycles, 29(11), pp.1944-1961.

Nie, M., Pendall, E., Bell, C., Gasch, C.K., Raut, S., Tamang, S. and Wallenstein, M.D., 2013. Positive climate feedbacks of soil microbial communities in a semi-arid grassland. Ecology letters, 16(2), pp.234-241.

Norby, R.J., Cotrufo, M.F., Ineson, P., O'Neill, E.G. and Canadell, J.G., 2001. Elevated CO 2, litter chemistry, and decomposition: a synthesis. Oecologia, 127(2), pp.153-165.

Norby, R.J., Ledford, J., Reilly, C.D., Miller, N.E. and O'Neill, E.G., 2004. Fine-root production dominates response of a deciduous forest to atmospheric CO2 enrichment. Proceedings of the national Academy of Sciences, 101(26), pp.9689-9693.

Norby, R.J., DeLucia, E.H., Gielen, B., Calfapietra, C., Giardina, C.P., King, J.S., Ledford, J., McCarthy, H.R., Moore, D.J., Ceulemans, R. and De Angelis, P., 2005. Forest response to elevated CO2 is conserved across a broad range of productivity. Proceedings of the National Academy of Sciences, 102(50), pp.18052-18056.

O'Leary, M.H., 1988. Carbon isotopes in photosynthesis. Bioscience, 38(5), pp.328-336.

Oeschger, H., Siegenthaler, U., Schotterer, U. and Gugelmann, A., 1975. A box diffusion model to study the carbon dioxide exchange in nature. Tellus, 27(2), pp.168-192.

Park, T., Ganguly, S., Tømmervik, H., Euskirchen, E.S., Høgda, K.A., Karlsen, S.R., Brovkin, V., Nemani, R.R. and Myneni, R.B., 2016. Changes in growing season duration and productivity of northern vegetation inferred from long-term remote sensing data. Environmental Research Letters, 11(8), p.084001.

Popa, M.E., Vollmer, M.K., Jordan, A., Brand, W.A., Pathirana, S.L., Rothe, M. and Röckmann, T., 2014. Vehicle emissions of greenhouse gases and related tracers from a tunnel study: CO: CO 2, N 2 O: CO 2, CH 4: CO 2, O 2: CO 2 ratios, and the stable isotopes 13 C and 18 O in CO 2 and CO. Atmospheric Chemistry and Physics, 14(4), pp.2105-2123.

Potter, C.S., Randerson, J.T., Field, C.B., Matson, P.A., Vitousek, P.M., Mooney, H.A. and Klooster, S.A., 1993. Terrestrial ecosystem production: a process model based on global satellite and surface data. Global Biogeochemical Cycles, 7(4), pp.811-841.

Quay, P.D., Tilbrook, B. and Wong, C.S., 1992. Oceanic uptake of fossil fuel CO2: Carbon-13 evidence. Science, 256(5053), pp.74-79.

Quay, P., Sonnerup, R., Westby, T., Stutsman, J. and McNichol, A., 2003. Changes in the 13C/12C of dissolved inorganic carbon in the ocean as a tracer of anthropogenic CO2 uptake. Global Biogeochemical Cycles, 17(1), pp.4-1.

Quay, P., Sonnerup, R., Stutsman, J., Maurer, J., Körtzinger, A., Padin, X.A. and Robinson, C., 2007. Anthropogenic CO2 accumulation rates in the North Atlantic Ocean from changes in the 13C/12C of dissolved inorganic carbon. Global biogeochemical cycles, 21(1).

Quay, P., Sonnerup, R., Munro, D. and Sweeney, C., 2017. Anthropogenic CO2 accumulation and uptake rates in the Pacific Ocean based on changes in the 13C/12C of dissolved inorganic carbon. Global Biogeochemical Cycles, 31(1), pp.59-80.

Raich, J.W. and Schlesinger, W.H., 1992. The global carbon dioxide flux in soil respiration and its relationship to vegetation and climate. Tellus B, 44(2), pp.81-99.

Randerson, J.T., Field, C.B., Fung, I.Y. and Tans, P.P., 1999. Increases in early season ecosystem uptake explain recent changes in the seasonal cycle of atmospheric CO2 at high northern latitudes. Geophysical research letters, 26(17), pp.2765-2768.

Randerson, J.T., Van Der Werf, G.R., Giglio, L., Collatz, G.J. and Kasibhatla, P.S., 2018. Global Fire Emissions Database, Version 4,(GFEDv4), ORNL DAAC, Oak Ridge, Tennessee, USA.

Rao, Z., Guo, W., Cao, J., Shi, F., Jiang, H. and Li, C., 2017. Relationship between the stable carbon isotopic composition of modern plants and surface soils and climate: A global review. Earth-Science Reviews, 165, pp.110-119.

Saurer, M., Siegwolf, R.T. and Schweingruber, F.H., 2004. Carbon isotope discrimination indicates improving water-use efficiency of trees in northern Eurasia over the last 100 years. Global Change Biology, 10(12), pp.2109-2120.

Schaefer, K., Collatz, G.J., Tans, P., Denning, A.S., Baker, I., Berry, J., Prihodko, L., Suits, N. and Philpott, A., 2008. Combined simple biosphere/Carnegie-Ames-Stanford approach terrestrial carbon cycle model. Journal of Geophysical Research: Biogeosciences, 113(G3).

Scharlemann, J.P., Tanner, E.V., Hiederer, R. and Kapos, V., 2014. Global soil carbon: understanding and managing the largest terrestrial carbon pool. Carbon Management, 5(1), pp.81-91.

Schimel, D.S., House, J.I., Hibbard, K.A., Bousquet, P., Ciais, P., Peylin, P., Braswell, B.H., Apps, M.J., Baker, D., Bondeau, A. and Canadell, J., 2001. Recent patterns and mechanisms of carbon exchange by terrestrial ecosystems. Nature, 414(6860), pp.169-172.

Schimel, D., Stephens, B.B. and Fisher, J.B., 2015. Effect of increasing CO2 on the terrestrial carbon cycle. Proceedings of the National Academy of Sciences, 112(2), pp.436-441.

Schubert, B.A. and Jahren, A.H., 2012. The effect of atmospheric CO2 concentration on carbon isotope fractionation in C3 land plants. Geochimica et Cosmochimica Acta, 96, pp.29-43.

Schubert, B.A. and Jahren, A.H., 2013. Reconciliation of marine and terrestrial carbon isotope excursions based on changing atmospheric CO 2 levels. Nature Communications, 4(1), pp.1-6.

Schubert, B.A. and Jahren, A.H., 2015. Global increase in plant carbon isotope fractionation following the Last Glacial Maximum caused by increase in atmospheric p CO2. Geology, 43(5), pp.435-438.

Seibt, U., Rajabi, A., Griffiths, H. and Berry, J.A., 2008. Carbon isotopes and water use efficiency: sense and sensitivity. Oecologia, 155(3), pp.441-454.

Sitch, S., Friedlingstein, P., Gruber, N., Jones, S.D., Murray-Tortarolo, G., Ahlström, A., Doney, S.C., Graven, H., Heinze, C., Huntingford, C. and Levis, S., 2015. Recent trends and drivers of regional sources and sinks of carbon dioxide. Biogeosciences, 12(3), pp.653-679.

Shevliakova, E., Stouffer, R.J., Malyshev, S., Krasting, J.P., Hurtt, G.C. and Pacala, S.W., 2013. Historical warming reduced due to enhanced land carbon uptake. Proceedings of the National Academy of Sciences, 110(42), pp.16730-16735.

Sokolov, A.P., Kicklighter, D.W., Melillo, J.M., Felzer, B.S., Schlosser, C.A. and Cronin, T.W., 2008. Consequences of considering carbon–nitrogen interactions on the feedbacks between climate and the terrestrial carbon cycle. Journal of Climate, 21(15), pp.3776-3796.

Still, C.J., Berry, J.A., Collatz, G.J. and DeFries, R.S., 2003. Global distribution of C3 and C4 vegetation: carbon cycle implications. Global biogeochemical cycles, 17(1), pp.6-1.

Tans, P.P., Berry, J.A. and Keeling, R.F., 1993. Oceanic 13C/12C observations: a new window on ocean CO2 uptake. Global Biogeochemical Cycles, 7(2), pp.353-368.

Tharammal, T., Bala, G., Narayanappa, D. and Nemani, R., 2019. Potential roles of CO 2 fertilization, nitrogen deposition, climate change, and land use and land cover change on the global terrestrial carbon uptake in the twenty-first century. Climate Dynamics, 52(7), pp.4393-4406.

Treydte, K.S., Frank, D.C., Saurer, M., Helle, G., Schleser, G.H. and Esper, J., 2009. Impact of climate and CO2 on a millennium-long tree-ring carbon isotope record. Geochimica et Cosmochimica Acta, 73(16), pp.4635-4647.

Trudinger, C., Enting, I., Etheridge, D., Francey, R. and Rayner, P., 2005. The carbon cycle over the past 1000 years inferred from the inversion of ice core data. In A history of Atmospheric CO2 and its Effects on Plants, Animals, and Ecosystems (pp. 329-349). Springer, New York, NY.

Trumbore, S., 2000. Age of soil organic matter and soil respiration: radiocarbon constraints on belowground C dynamics. Ecological applications, 10(2), pp.399-411.

Vadeboncoeur, M.A., Jennings, K.A., Ouimette, A.P. and Asbjornsen, H., 2020. Correcting tree-ring δ 13C time series for tree-size effects in eight temperate tree species. Tree physiology, 40(3), pp.333-349.

Van Der Sleen, P., Groenendijk, P., Vlam, M., Anten, N.P., Boom, A., Bongers, F., Pons, T.L., Terburg, G. and Zuidema, P.A., 2015. No growth stimulation of tropical trees by 150 years of CO 2 fertilization but water-use efficiency increased. Nature geoscience, 8(1), pp.24-28.

Voelker, S.L., Brooks, J.R., Meinzer, F.C., Anderson, R., Bader, M.K.F., Battipaglia, G., Becklin, K.M., Beerling, D., Bert, D., Betancourt, J.L. and Dawson, T.E., 2016. A dynamic leaf gas-exchange strategy is conserved in woody plants under changing ambient CO2: evidence from carbon isotope discrimination in paleo and CO2 enrichment studies. Global Change Biology, 22(2), pp.889-902.

Vogel, J.C., 1980. Fractionation of the carbon isotopes during photosynthesis. In Fractionation of the Carbon Isotopes During Photosynthesis (pp. 5-29). Springer, Berlin, Heidelberg.

Walker, A.P., De Kauwe, M.G., Bastos, A., Belmecheri, S., Georgiou, K., Keeling, R.F., McMahon, S.M., Medlyn, B.E., Moore, D.J., Norby, R.J. and Zaehle, S., 2021. Integrating the evidence for a terrestrial carbon sink caused by increasing atmospheric CO2. New Phytologist, 229(5), pp.2413-2445.

Wang, C., Houlton, B.Z., Liu, D., Hou, J., Cheng, W. and Bai, E., 2018. Stable isotopic constraints on global soil organic carbon turnover. Biogeosciences, 15(4), pp.987-995.

Wang, G. and Feng, X., 2012. Response of plants' water use efficiency to increasing atmospheric CO2 concentration. Environmental science & technology, 46(16), pp.8610-8620.

Wang, W., Ciais, P., Nemani, R.R., Canadell, J.G., Piao, S., Sitch, S., White, M.A., Hashimoto, H., Milesi, C. and Myneni, R.B., 2013. Variations in atmospheric CO2 growth rates coupled with tropical temperature. Proceedings of the National Academy of Sciences, 110(32), pp.13061-13066.

Wong, S.C., Cowan, I.R. and Farquhar, G.D., 1979. Stomatal conductance correlates with photosynthetic capacity. Nature, 282(5737), pp.424-426.

Zhang, J., Quay, P.D. and Wilbur, D.O., 1995. Carbon isotope fractionation during gas-water exchange and dissolution of CO2. Geochimica et Cosmochimica Acta, 59(1), pp.107-114.

Zhou, T., Shi, P., Hui, D. and Luo, Y., 2009. Global pattern of temperature sensitivity of soil heterotrophic respiration (Q10) and its implications for carbon-climate feedback. Journal of Geophysical Research: Biogeosciences, 114(G2).

Zhu, Z., Piao, S., Myneni, R.B., Huang, M., Zeng, Z., Canadell, J.G., Ciais, P., Sitch, S., Friedlingstein, P., Arneth, A. and Cao, C., 2016. Greening of the Earth and its drivers. Nature climate change, 6(8), pp.791-795.

4 Cross calibration of Landsat 5 TM and Landsat 7 ETM+ using deep learning enhances tree cover mapping consistency

Abstract

To quantify ecosystem responses over large areas, long-term and continuous satellite data are essential. However, the longest-running remote sensing data, from the Landsat program, suffer from switches in sensors between successive satellite generations. Therefore, it remains difficult to use Landsat data to assess long-term shifts in land cover over periods longer than the lifetime of a single generation of satellites. We here aim to emulate reflectance values of Landsat 7 Enhanced Thematic Mapper Plus (ETM+) with Landsat 5 Thematic Mapper (TM) using a deep learning model to produce a consistent Landsat time series from 1985-2021. Our approach uses open-source cloud-based resources that enable our Tensorflow deep learning model to be trained and run using Google Collaboratory and Google Earth Engine entirely on the cloud. Our model successfully emulates Landsat 7 imagery, with greater similarity to the Landsat 7 ETM+ image than the original Landsat 5 TM (up to 40% reduction in squared error). We then applied a random forests model to estimate tree cover from the emulated images and provide a continuous record of tree coverage in a region in eastern Alaska from 1985 to 2021. Regions unaffected by fires showed a general increase in tree cover, whereas widespread reduction in tree cover was found following wildfires, followed by a recovery period. We thus conclude that our deep learning model is effective at emulating satellite data to improve the continuity of the satellite data record, hence enabling improved applications to remote sensing of vegetation using Landsat data.

4.1 Introduction

The Earth's land vegetation is a significant sink of atmospheric CO_2 (Friedlingstein et al., 2020), a large part of which is due to northern ecosystems. Towards the end of the 20th century, the Arctic and boreal ecosystems took up between 0.3 and 0.6 Pg C yr^{-1}, which makes up a significant fraction of the 1.0 Pg C yr^{-1} net land sink estimated during the 1990s (Mcguire et al., 2009). The primary drivers behind the increase of the northern CO_2 sink are thought to be a stimulation of plant productivity due to warming and CO_2 fertilisation (Wang et al., 2013; Cias et al., 2019). Global average surface temperatures increased by 1.1˚C during the 1880-2021 period (Masson-Delmotte et al., 2021), and high latitude regions have warmed twice as fast due to various climate feedbacks (Screen et al., 2010; Jeong et al., 2012). Atmospheric CO_2 concentrations have increased from 280 ppm pre-1751 to over 400 ppm present day, and the ensuing CO_2 fertilisation of plants is thought to have contributed towards 60% of the current land sink (Schimel et al., 2015).

The global carbon budget has significant uncertainties, largely attributed to poor quantification of the land carbon sink, which fluctuates on the order of several GtC from year to year (Friedlingstein et al., 2020). Climate-carbon cycle models disagree strongly on the magnitude of the future land sink when compared to other sinks and sources in the earth system (Friedlingstein et al., 2006). One of the largest uncertainties regarding predictions for the future carbon sink is the response of boreal forests to climate change (Friedlingstein et al., 2020). There is evidence of boreal forest expansion and greater seasonal uptake and release of CO_2 (Graven et al., 2013), but also evidence for large-scale increases in disturbances, such as fire (de Groot et al., 2013) and insect outbreaks (Kurz et al., 2008). The ability to measure the summer photosynthetic uptake of carbon by the land depends heavily on accurate measurements of the changes in aboveground biomass (Houghton, 2005). Greater accuracy in quantifying the land sink can be achieved with better estimates of carbon stock changes (Harris et al., 2021) and forest cover (Bonan et al., 2002; DeFries et al., 2002).

Natural disturbances, such as fire and insect outbreaks, disrupt vegetation functioning and can change the future composition of an ecosystem (White et al., 1985). Climate has emerged as the dominant driver behind disturbance regime change (Seidl et al., 2011). Climate change has caused increases in fire (Pechony & Shindell, 2010; Westerling, 2016), insect outbreaks (Paritsis &

Veblen, 2011) and drought (Constance & Stephenson, 2025), potentially paving the way for large-scale forest dieback. Furthermore, changes in disturbance regimes are soon predicted to be one of the most significant effects of climate change on the land biosphere (Lindner et al. 2010). Thus, it is of interest to document and understand the effect of past forest ecosystem disturbance to accurately predict and mitigate against future changes. One of the only methods of gaining insight into these systems over a large scale is with remote sensing.

One of the most widely used satellite observations is from the Landsat program. This program began in 1972 and is still operational to this day, making it the longest continuous satellite record of moderate resolution at a global scale. However, over the course of the program, nine different satellites have been used, each containing onboard sensors with characteristics that have not been consistent from satellite to satellite. The number of bands, wavelengths of bands and image quality have varied significantly throughout Landsat's history, making it difficult to combine imagery from successive satellites without introducing bias. This hinders the use of Landsat data in long-term analyses. Consequently, remote sensing products from Landsat data, such as global high-resolution percentage tree cover maps (Hansen et al., 2013) only cover a short period from 2000 to 2019. As large-scale shifts in forest dynamics tend to occur over multi-decadal timescales, reconstruction of longer chronologies of, for example, tree cover would be advantageous. Longer timescales have been analysed in the Mapbiomas project, where they made detections of land cover across the Amazon from 1985 to present-day (Souza et al., 2020). Their method analysed changes in land cover classes to date the apparition of secondary forest (Heinrich et al., 2021), but the value of tree cover per pixel is still lacking. We here aim to emulate Landsat imagery to provide consistent characteristics of the data and produce 30 years of continuous estimates of percentage tree cover maps.

The longest-running satellite of the Landsat mission currently in operation is Landsat 7 (L7), which shares a 14-year overlap with Landsat 5 (L5), which was launched in 1984. Together, these satellites provide uninterrupted satellite imagery from 1984 to present-day. L5 and L7 both have 8-bit radiometric resolution with an identical spatial resolution of 30m and near-identical spectral resolution. L7 additionally has a pansharpened band (520-900nm) at 15m spatial resolution (see L7 user guide: https://www.usgs.gov/media/files/landsat-7-data-users-handbook for more details). Land cover studies have utilised data from a combination of Landsat generations, including L5

and L7 (Gong et al., 2013; Liu et al., 2018; Murray et al., 2019; Gong et al., 2020). However, 'tandem' orbits where nearly coincident imagery was collected from L5 and L7 (Teillet et al., 2001) show there are significant differences between spectral data obtained from these two satellites. Specifically, they found a difference in spectral response on the order of 2%, except in the short-wave infrared (SWIR) bands, where the difference was 3-7% depending on the band and region. Previous work has neglected these disparities between successive Landsat products, which suggests an additional error in calculations as a result of the change in satellites. This effect is particularly significant when there is a nonlinear dependence, or simply a high sensitivity of land cover class to the spectral signature.

The long temporal overlap in which imagery for both satellites is available (1999-2013) ensures their suitability for training a deep learning (DL) model to enable cross-calibration (Chander et al., 2005). We aim to emulate L7 images from L5 images for Alaska during the 1985-1999 period to obtain a continuous satellite record from 1985 to present-day with consistent spectral characteristics at a spatial resolution of 30m. Additionally, we will predict the L7 pansharpened band at 15 m resolution from the emulated 30 m resolution bands to further improve the accuracy of the emulated bands. This will enable greater precision of the mapping of areas for the period before L7 was launched. Improving the resolution of an image is known as image super-resolution (Dong et al., 2015), a technique that is still rarely used to supplement remote sensing techniques (Pouliot et al., 2018). We choose to do this for Alaska as its good quality coverage of Landsat images throughout the study period provides us with a suitable quantity of training data. Alaska is also important as it hosts the two largest national forests in the USA. Alaska contains ~77 PgC of soil organic carbon (Mishra et al., 2012), which makes up nearly 4% of global soil carbon (Bolin et al., 2000).

Working with large-scale time-series images has been greatly improved with the development of the Google Earth Engine (GEE) platform. One of the first scientific works with the platform was the global tree cover dataset (Hansen et al., 2013), which was followed by the addition of large quantities of satellite data onto GEE. More recently, GEE has incorporated the capability to load deep learning models onto the platform, which we take advantage of in this study. After deploying the DL model onto GEE, a random forests model will be used to predict tree cover percentage at a 15m scale in a region in east Alaska as a proof of concept. These maps will provide a continuous

estimate of tree cover spanning more than 3 decades. This technique will enable the possibility of providing land cover maps before 1999 with greater detail than was previously possible at a large scale. The primary advantage of these maps is that they will enjoy greater continuity during the transition from L5 to L7 data.

In summary, our objectives are to emulate L7 images from L5 images using a deep learning model, which will be compared with a classical regression model, as well as the original L5 images. Then, we will use a tree cover model computed with the emulated L7 images from L5 (1985-1994) and on the L7 images (2002-2021) to produce percentage tree cover maps spanning from 1985 to present-day.

4.2 Materials and Methods

4.2.1 Experimental Design

The overall methodology and workflow are shown in Figure 4.1. We first trained a percentage tree cover model (Section 4.3.1) and then emulated L7 images from L5 images using a deep neural network model and a regression model (Section 4.3.2 – 4.3.4). We then used these emulated L7 images from these two approaches to produce continuous maps of percentage tree cover from 1985-2021 using the tree cover random forests model (Section 4.4) (Figure 4.1).

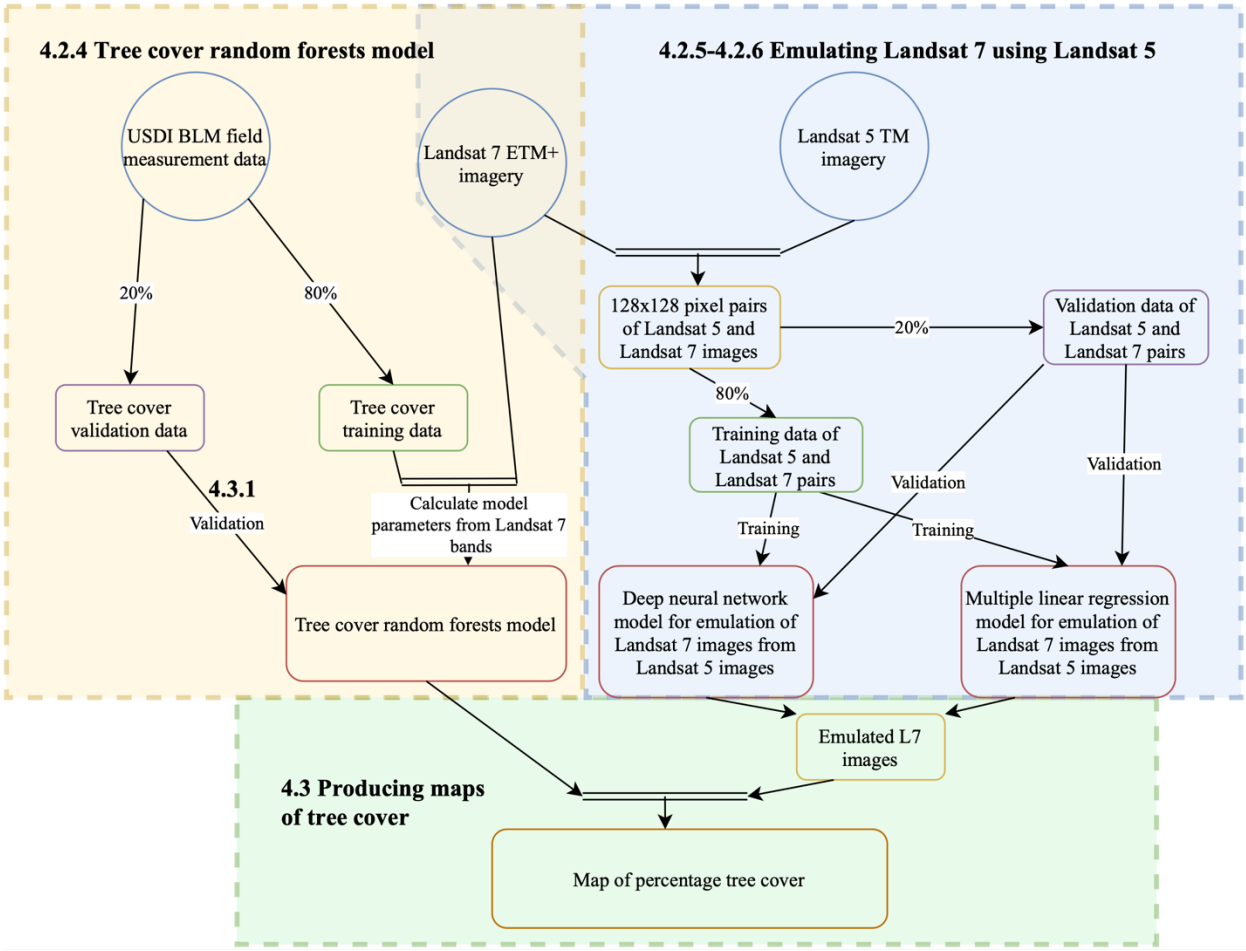

Figure 4.1. The methodology presented in this chapter. Each coloured box is labelled with reference to the section in this study being depicted. Circle boxes indicate data origin, square boxes indicate stages of the methodology. 3 large, coloured backgrounds indicate stages of the methodology with labels of the sections of the paper pertaining to them.

4.2.2 Study site and training data pre-processing

The study area in this Chapter is located on the eastern edge of Alaska, United States of America (Figure 4.2). For this region, we used L5 Thematic Mapper (TM) and L7 Enhanced Thematic Mapper Plus (ETM+) ortho-rectified top-of-the-atmosphere (TOA) images in the GEE cloud computing platform. We chose to use the TOA images rather than surface reflectance products because of the availability of an additional pansharpened band with a greater spatial resolution of 15m (instead of 30 m).

4.2.2.1 Training and testing data for L7 emulation

Our training data consisted of 120 pairs of overlapping L5 and L7 images in Alaska and western Canada (Figure 4.2 middle panel) with a low probability of cloud cover (<10%) during the 1999-2013 period. The maximum time separating the collection of each image in each pair was 2 days, and a maximum of 1-hour difference in the time of day of collection. This is because the conditions under which the pairs of L5 and L7 images were obtained needed to be as similar as possible in order to accurately train the DL and MR models.

Each image was taken during the June to September period and located within or very close to the US state of Alaska. We used all the overlapping area of images taken before 2003, but due to failure of the scan line corrector (SLC) onboard Landsat 7 in 2003, we were only able to use the central strip of the L7 images for training thereafter (see Table S4.1 for a list of the L5 and L7 image pairs used in training the model).

The training images were imported onto Google Colab using the GEE Python application programming interface (API). We used the '*simpleCloudScore'* GEE function to mask any pixels where there was a likelihood of 10% or higher of a cloud being present in that pixel. We then retiled the images into 128x128 pixels images for each of the 30m bands (and 256x256 for the 15m pansharpened band). For each pair of images, the mean squared error (MSE) was calculated between the L5 and L7 images and all images with MSE greater than 2 standard deviations from the mean were examined visually for clouds or shadows. After removal of the poor-quality image pairs, 32119 pairs remained, 20% of which were set aside for validation. The images analysed in the study region in section 4.3.2 were also subject to the same set of restrictions in order to minimise the effects of differences in lighting, atmospheric conditions, and surface features.

4.2.2.2 Data for random forests model and final percentage tree cover maps

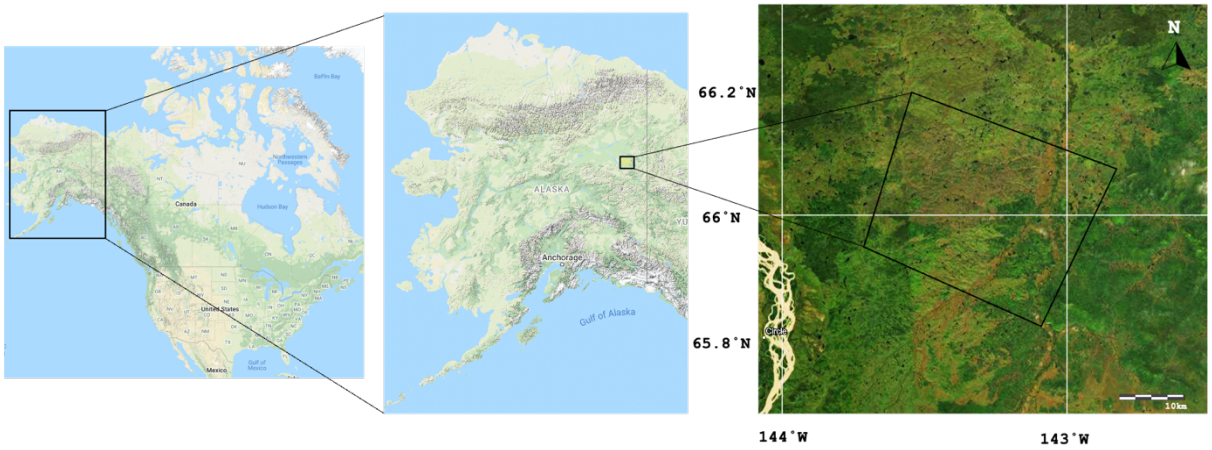

Figure 4.2. Map showing the location of the region in Alaska, USA analysed in this study. Middle panel depicts the area used to collect training data for the models used in this chapter.

4.2.3 Fire data

The region of interest experienced three major fire events during the study period (1993, 1997 and 2009). The 1993 fires lasted 58 days and 94 days respectively, the 1997 fire lasted 81 days and the 2009 fire 100 days (Figure 4.3). The fire data were obtained from the Alaska Bureau of Land Management (data available here: https://fire.ak.blm.gov/predsvcs/maps.php).

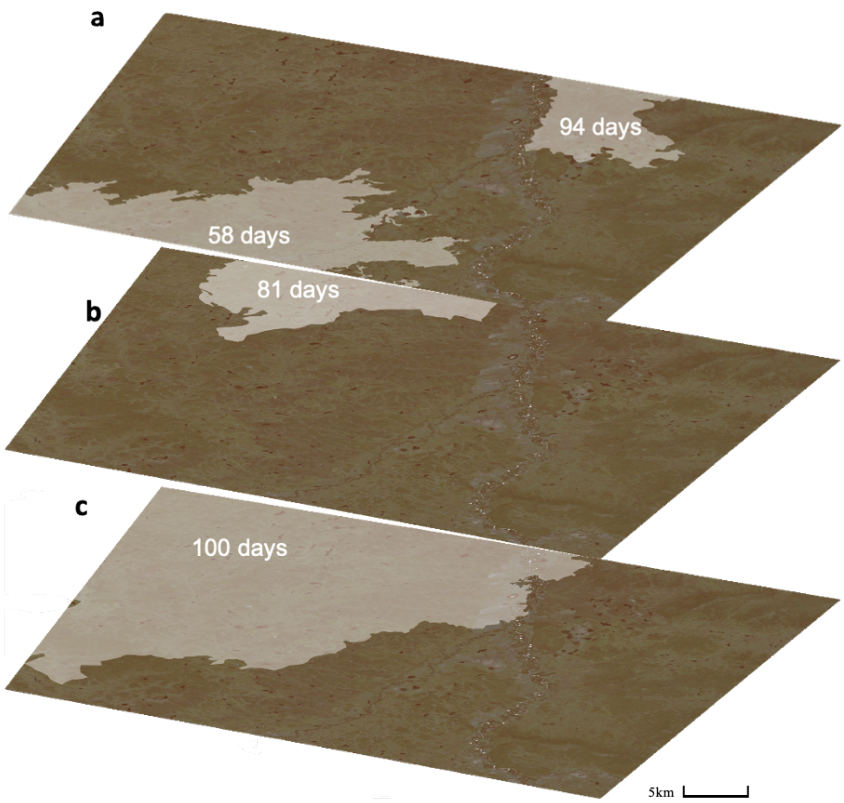

Figure 4.3. Fires occurring in the study region in lighter colour during **(a)** 1993, **(b)** 1997, and **(c)** 2009 overlaid on an RGB L7 image of the study region. Annotated on each fire geometry is the duration of the fire. This data is available here: https://fire.ak.blm.gov/predsvcs/maps.php.

4.2.4 Tree cover random forests model

To estimate tree cover, we used terrestrial field measurement data from the United States Department of the Interior Bureau of Land Management (USDI BLM) (https://landscape.blm.gov/geoportal/catalog/AIM/AIM.page). From this dataset, we obtained 18998 data points across the contiguous United States and Alaska. Each data point contained information on percentage tree cover, location, and date of measurement. We then set aside 10% of this data for cross-validation and a further 10% for testing. The remaining 80% of the data was used to train a random forests model.

The random forests model was tested using all the L7 bands, as well the normalised difference vegetation index (NDVI) which is calculated with the near-infrared band (NIR) and red band (Red) of the Landsat images as follows:

$$NDVI = \frac{NIR - Red}{NIR + Red}$$

[4.1]

Tuning of various parameters in the training of the random forests model was undertaken by assessing the accuracy of predictions in the cross-validation dataset. The highest accuracy was achieved by using NDVI as well as all the L7 bands, except for the high gain and low gain B6 bands. Using 100 decision trees achieved a high degree of accuracy, with no measurable improvement when increasing this further. This optimal model obtained a root mean squared error (RMSE) of 8.2% tree cover.

4.2.5 Deep learning model architecture

We trained a deep learning neural network model with a structure similar to a residual neural network (Res-Net) (He et al., 2016) (Figure 4.4). Res-Net models are typically implemented with double-layer skip connections Rectified Linear Unit (ReLU) activation functions and batch normalisation in between (He et al., 2016). We disaggregated the L5 input bands to 15m resolution and implemented six two-dimensional convolutional layers. We then applied a sigmoid activation function to produce an output image containing emulations of the L7 bands disaggregated at 15m resolution (Figure 4.4). Next, we up-sampled the image (increase the spatial resolution by repeating each element) and applied three more convolutional layers and another sigmoid activation function to produce an emulation of the L7 15m resolution pansharpened band (Figure 4.4). We chose to emulate the pansharpened band in order to improve the predictive power of the model (Wagner et al., 2021). We chose to emulate also the 15m band because deep learning models are capable of utilising spatial and spectral information to infer image characteristics at a higher spatial resolution (Dong et al., 2015). To ensure the model trained each band with equal importance, we weighted the error in the training such that each of the 30m bands had equivalent weights to the pansharpened band. Our model was initialised with random weights, after which, adjustments were made to the weights based on a standard batch gradient descent algorithm that aimed to minimise the cost function, for which we used MSE. The gradient descent algorithm was implemented after each pass through the entire dataset, defined as one epoch. Updating the weights takes the following form:

$$\theta_j := \theta_j - \alpha \frac{\partial}{\partial \theta_j} J(\theta)$$

[4.2]

Here θ_j is a given weight, α is the learning rate (between 0 and 1), $J(\theta)$ is the cost function (a function of all the weights), and $:=$ is the assignment operator. The accuracy of the model was evaluated by calculating the mean absolute error (MAE) from the test dataset, and the RMSprop optimiser was used for calculating the gradient of the descent ($\partial J/(\partial \theta_j)$) (Chollet et al., 2015). We did not apply any data augmentation techniques.

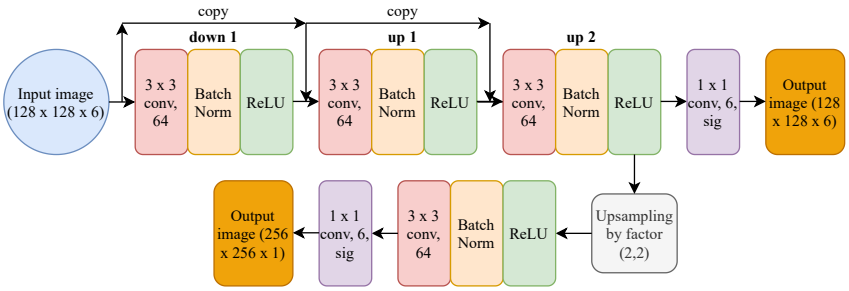

Figure 4.4. Deep learning model architecture. In convolutional (conv) layers, the kernel size and number of filters are indicated. 'sig' refers to the sigmoid activation function. Arrows labelled with 'copy' refer to the tensors from the start of the arrow being concatenated with the tensors at the end of the arrow to then be inputted into the next layer. 'down1', 'up1', 'up2' refer to the 3 stages of the ResNet model.

4.2.6 Training models to emulate L7

Preliminary training resulted in a model which had difficulty in accurately emulating the TIR band. The TIR band is subject to significant variability in surface reflectiveness, therefore we excluded it from the final model, which performed far better (see Section 4.3.4). Training of the deep learning model was coded in the Python programming language using the Keras API (Chollet, 2015) and the Tensorflow package (Abadi et al., 2016) on Google Colab.

We trained the deep learning model for 250 epochs using the maximum batch size available on Google Colab of 64 images and started with a learning rate of 0.001, which we reduced by a factor of 10 whenever there was no improvement in validation MAE for more than 10 epochs. Leading up to the 250th epoch, the MAE of the validation dataset had stopped decreasing, at which point the optimal value of MAE had reached 0.0058 for predicting the 30m resolution bands, and 0.0074

for predicting the 15m resolution pansharpened band. We then uploaded the model onto GEE through the Google Cloud Platform to make predictions in the study region (Figure 4.2). For every 128x128 pixel prediction, the model included an overlap of 8 pixels. This was done in order to remove an effect whereby the borders of each prediction box were distorted (a known effect from regression-based deep neural networks (Wagner et al., 2021). The DL model took 20 hours to train on Google Colab, which (at time of writing) is a freely available service, although this study made use of the Colab Pro service (£8.10 per month) which allows longer running times of the GPUs while fine-tuning the model.

In order to compare our DL model with classical methods of satellite cross-calibration, we then trained a multiple linear regression model (MR), in which each L7 band was emulated using a linear function of the L5 bands, as follows:

$$L7_{BN} = k_{N0} + \sum_{i=1}^{7} k_{Ni} L5_{Bi} \quad \textbf{[4.3]}$$

$L7_{BN}$, $L5_{Bi}$ are bands of Landsat 7 and Landsat 5 respectively and the coefficients k_{Ni} are constants calculated from linear least squares regression between the L5 and L7 images in the same dataset used to train the deep learning model. Note that the k coefficients are different for each band of Landsat 7.

4.2.7 Statistical Analysis: Validating predictions from L7 emulations

After training, we tested the two models on the images that were held back for validation by calculating the error based on the MSE between the L7 image and its L5/MR/DL counterpart. The RGB images of the DL-emulated and MR-emulated images show a visible increase in similarity to the L7 image than the L5 image (Figure 4.5). The MSE from the L7 images is lower for the emulated images (MR and DL MSE) than the original (L5 MSE) for all bands save one (Table 4.1). The MR model also produces an improvement on the L5 images, with lower MSE than the L5 images for nearly all bands. The DL model outperforms the MR model for half of the bands and has lower overall MSE (6.7e-5 vs 6.9e-5). In order to accurately model tree cover, we first tested the sensitivity of tree cover estimates to the time of year that the L7 satellite image was taken in 10-day increments. We used the region of interest for this sensitivity analysis, as well as all other regions in Alaska inside a similar latitude band (64.8˚N – 66.5˚N). There was little variability (range = 2.5%) in tree cover estimates in the 180th – 230th days of the year. Outside

this range, calculated tree cover started to decrease substantially, therefore we made sure to only use imagery during this period in order that seasonal variations in vegetation greenness and atmospheric conditions did not influence the results.

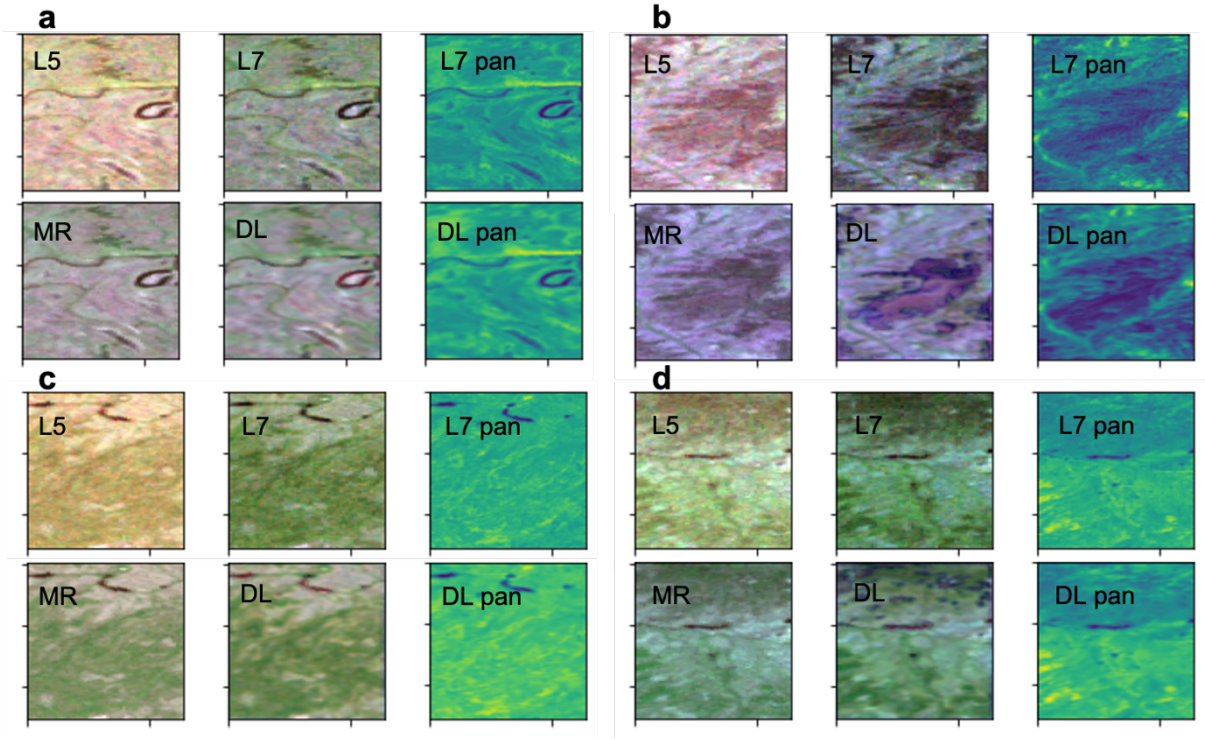

Figure 4.5. RGB images from the validation dataset not seen during training of the MR and DL models. Each box depicts a 128x128 pixel scene where each pixel has dimensions 30m x 30m. **(a)**, **(b)**, **(c)** and **(d)** each depict a different scene from the validation dataset from different regions in Alaska.

Table 4.1. Summary of the bands used in training and their wavelengths and spatial resolutions from the Landsat 5 and Landsat 7 satellites. The 3 rightmost columns contain the mean squared error (MSE) of the validation images held back during training. DL refers to the deep learning model and MR refers to the multiple regression model. Improvements on the L5 image underlined for the MR MSE and DL MSE columns. The lowest MSE for each respective row is indicated in bold. No available Panchromatic MSE for L5 and MR because L5 images do not contain this band.

Band	**L5 wavelength (µm)**	**L7 wavelength (µm)**	**Resolution**	**L5 MSE**	**MR MSE**	**DL MSE**
Blue	0.45-0.52	0.45-0.52	30m	6.06e-5	**4.91e-5**	5.08e-5
Green	0.52-0.60	0.52-0.60	30m	5.41e-5	**2.85e-5**	3.25e-5
Red	0.63-0.69	0.63-0.69	30m	5.20e-5	4.15e-5	**3.74e-5**
Near Infrared	0.76-0.90	0.77-0.90	30m	1.11e-4	1.12e-4	**1.05e-4**
Shortwave infrared 1	1.55-1.75	1.55-1.75	30m	1.21e-4	**1.20e-4**	1.25e-4
Shortwave infrared 2	2.08-2.35	2.08-2.35	30m	7.07e-5	6.33e-5	**5.02e-5**
Panchromatic	N/A	0.52-0.90	15m	N/A	N/A	**8.55e-4**

For the red, blue, and green bands, the DL-emulated L5 images are visibly closer to the 1:1 line than the original L5 image (Figure 4.6). The difference is less clear in the SWIR1, SWIR2 and NIR plots, however, it is evident that the band values in the DL-emulated images change more smoothly than the L5 (Figure 4.6). Note that the striping effect visible in Figure 4.6 is due to the radiometric resolution limitations of L5 and L7 imagery.

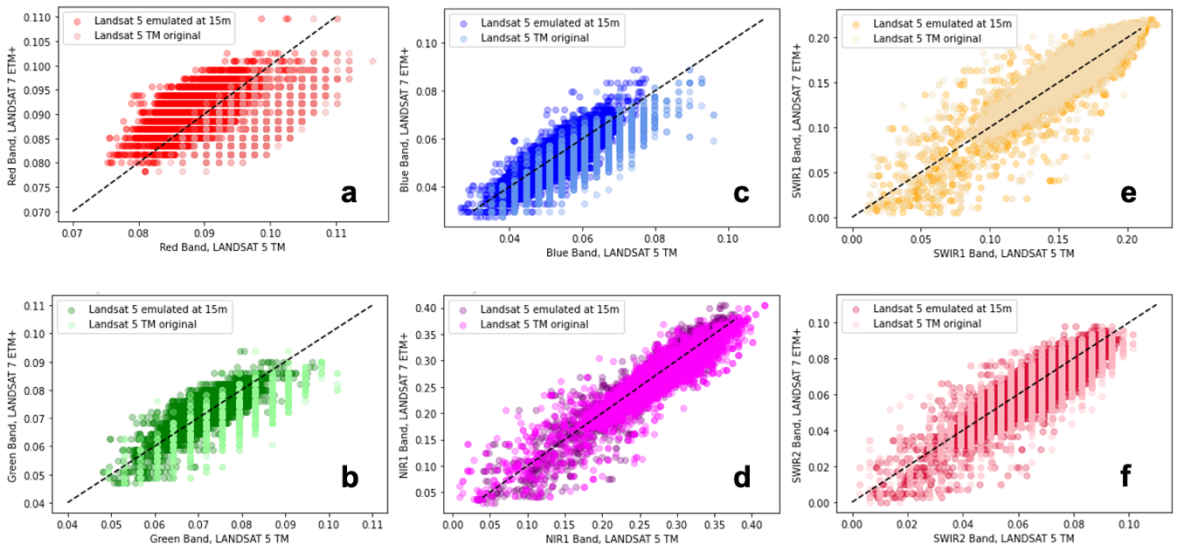

Figure 4.6. Scatterplots of the **(a)** red, **(b)** green), **(c)** blue, **(d)** NIR, **(e)** SWIR1, **(f)** SWIR2 bands from a random sample of images in the validation dataset. Band values for each of the L5 bands used in training are plotted against their corresponding L7 band values. Darker points indicate the DL-emulated images, and lighter points indicate the original L5 images.

Thus, the DL model has the lowest error and is less subject to variability in the accuracy of its estimates. Therefore, we have shown that the model enables us to perform (in part) a cross-calibration between L5 TM and L7 ETM+. This effectively allows an improvement of the consistency of percentage tree cover estimates during the study period.

4.3 Results

4.3.1 Tree cover error in the validation dataset

We first applied the tree cover model to the validation dataset to test the difference in estimates of tree cover using L7 with tree cover estimated from the L5, DL-emulated, and MR-emulated images. The error was greater for regions with higher tree cover, and the DL model produced lower error than the L5 images for all tree cover intervals (Table 4.2). The MR-emulated images produced similar or slightly higher error than the L5 images.

Table 4.2. Summary of RMSE in percentage tree cover estimates in the training dataset for each interval of tree cover. Each RMSE column depicts RMSE in calculated tree cover between the L7 and each respective image type. Underlined values indicate RMSE lower than obtained by using the original L5 image. Bold values indicate the lowest RMSE obtained for that row.

Tree cover	**L5 RMSE (% tree cover)**	**MR RMSE (% tree cover)**	**DL RMSE (% tree cover)**
0-10%	2.2	<u>2.1</u>	**1.9**
10-20%	2.5	2.6	**2.3**
20-30%	9.3	10.0	**8.5**
>30%	7.9	8.5	**6.9**

4.3.2 Tree cover error in the study region

We tested the error of the DL-emulated, MR-emulated and L5 tree cover estimates in the images across the entire study region during the overlap period with the L7 images. We found that the overall error was lower for the DL-emulated images (RMSE=8.1% tree cover) than the MR-emulated images (RMSE=9.6% tree cover) and the original L5 images (RMSE=12.9% tree cover) averaged over all 4 images (Table 4.3). Furthermore, the DL-emulated images produced lower error than the MR-emulated and original L5 images in all images (Table 4.3; Figure S4.1-4.4).

Table 4.3: Summary of RMSE in percentage tree cover estimates in the study region for each of the years in which low cloud cover L5 and L7 imagery exist. Each RMSE column depicts RMSE in calculated tree cover between the L7 and each respective image type. Underlined values indicate RMSE lower than obtained by using the original L5 image. Bold values indicate the lowest RMSE obtained for that row. The 'All' row indicates the overall RMSE from all 4 years.

Image year	L5 RMSE (% tree cover)	MR RMSE (% tree cover)	DL RMSE (% tree cover)
2003	8.5	7.8	**6.8**
2004	7.8	7.3	**6.5**
2005	23.2	14.0	**10.7**
2006	12.0	9.0	**8.2**
All	12.9	9.6	**8.1**

4.3.3 Mapping tree cover during 1985-2019

As the DL-emulated images produced lower error compared with the MR-emulated and L5 images, we here present the time series of tree cover from 1985 to 2021 using the DL-emulated images (1985-1994) combined with the L7 images (2002-2021) (Figure 4.7). The years where full composite images were available to produce this time series were: 1985, 1989, 1990, 1994, 2001-2002, 2006-2007, 2010-2011, 2012-2013, 2014-2015, 2016-2017, and 2020-2021. We split up the study region depending on the existence of a fire during the study period. We found that in the region with no fires, the mean tree cover did not change significantly (slope=-1.6% tree cover decade^{-1}, P=0.12) (Figure 4.7a). In the region with fires in 1993, mean tree cover dropped from 43.3% to 30.1% between the 1990 and 1994 images, thereafter, tree cover further decreased in 2002 to 20.7%, after which it increased significantly throughout the remainder of the study period (slope=5.8% decade^{-1}, P=0.001) (Figure 4.7b). In the region with a fire in 1997, the fire resulted in a drop in tree cover from 43.4% to 17.6% between 1994 and 2002, although the immediate loss was likely to have been greater, no images are available 1995-2001. Following the fire, tree cover increased by 5.9% decade^{-1} (P=5.9e-5) (Figure 4.7c). Finally, the region containing a fire in 2009 showed a steady decline in tree cover pre-fire (slope=-5.7% decade^{-1}, P=0.003), after which, the fire led to a reduction in tree cover from 37.6% to 27.1%, without having time to recover in the ensuing years (Figure 4.7d).

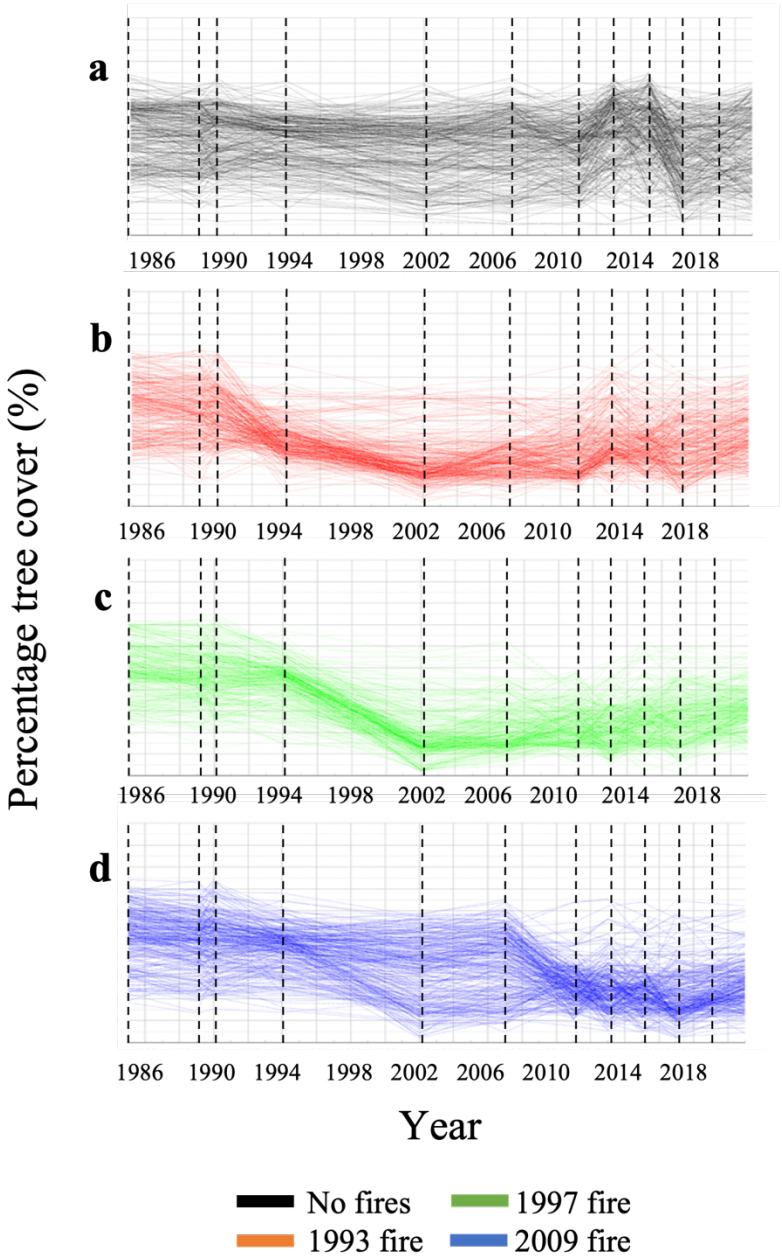

Figure 4.7. Time series of a sample of 300 points inside the study region with **(a)** no fires occurring, **(b)** a fire in 1993, **(c)** a fire in 1997, **(d)** a fire in 2009. The timing of each fire is depicted on the corresponding plot with a dotted line. The year value on the x-axis is the later year in the 2-year composite, when applicable. Vertical dotted lines indicate data points available during 1985, 1989, 1990, 1994, 2002, 2007, 2011, 2013, 2015, 2017, and 2021. Legend indicates fires corresponding to each time series.

The overall change in tree cover during the study period reveals domination by the fire in 2009, due largely to the recency of the event to the final data point (Figure 4.8). The majority of regions unaffected by the 2009 fire have experienced increases in tree cover over the study period, with

the exception of the region in the northwest affected by the 1993 fire lasting 94 days. The region in the southwest was affected also by a fire in 1993 but lasting only 58 days largely experienced an increase in tree cover, hence demonstrating the importance of the duration of fires on the recovery of tree growth.

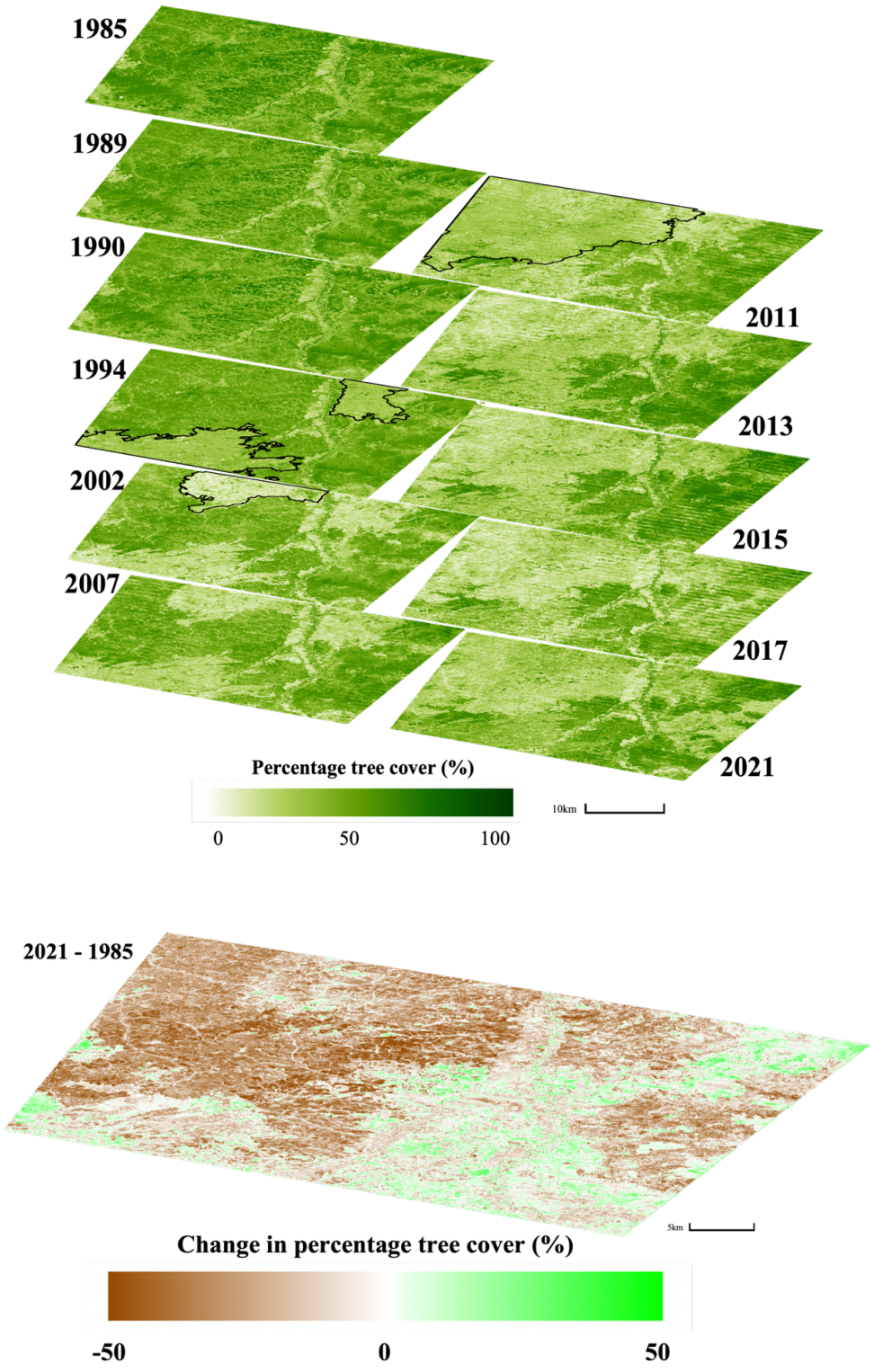

Figure 4.8. (top) Percentage tree cover at the beginning and end of the study period, and after each fire event. Years labelling plots are the later year in the 2-year composite, when applicable. (bottom) The difference in percentage tree cover between the 2021 and 1985 images. Grey areas indicate masked regions due to scan line corrector failure or cloud cover.

4.4 Discussion

In this study, we aimed to demonstrate a technique with the capability of estimating pixel-level resolution of percentage tree cover over a multi-decadal timescale. This was achieved by training a deep neural network model to emulate L7 images from L5 images with a reduction in error of predictions when compared with a classical regression approach to emulation. Our deep learning model has been successful in emulating L7 ETM+ imagery using only L5 TM images as input for the period 1985-2006 (Figure 4.5; Figure 4.6; Table 4.1; Table 4.2). The emulated images showed band values with a 15% reduction in MSE with the L7 images compared with the original L5 (Figure 4.6; Table 4.1) and were thus deemed to give improved estimations of percentage tree cover. Using this same dataset, the calculated tree cover was 8-15% closer to the L7 estimates using the DL-emulated images than with the L5 images using a tree cover random forests model. The tree cover estimated from the DL-emulated images is closest to the L7 images estimates across all ranges of tree cover when looking at the RMSE in each tree cover percentage interval (Table 4.3). This improvement is greatest in regions with higher tree cover. This could indicate that the model can recover the spectral information and spatial of the forests. However, for the regions with low tree cover, there could be more diversity in land cover types, explaining why the model is not so efficient and thus a larger volume of training data would likely be required to accurately emulate L7 imagery in such regions.

In the study region, the DL-emulated images enabled a more accurate (37.2% decrease in RMSE) chronology of tree cover (Table 4.3; Figure S4.1-4.4) for the past 3 decades. This is a greater improvement than the average from the training data (Table 4.2), however, it is within one standard deviation of the errors derived from this dataset. Our percentage tree cover estimates were largely consistent from year to year, with much of the change caused by fires occurring in 1993, 1997, and 2009 (Figure 4.7). The DL model was trained only with data covering Alaska and western Canada (Figure 4.2). The capabilities of the model to emulate L7 imagery in new locations relies on the model being trained with a wide variety of atmospheric conditions and land types.

4.5 Conclusions

Determining how forest disturbance history has changed over the past decades is of significant interest to the wider research community. Landsat presents the most suitable satellite dataset for carrying out long term analysis. However, there are differences in the band information collected by different satellites (Teillet et al., 2001) and changes in the wavelengths monitored by successive satellites. Here, we have demonstrated a method through which greater consistency can be achieved in long-term studies of land cover change using a deep neural network model to cross calibrate the Landsat satellites. Hence, we have illustrated the potential of these methods to open the door to vast improvements in the reconstruction of disturbance history over the past four decades.

The spatiotemporal changes in tree cover over the boreal zone are still poorly quantified. This hinders our understanding of the drivers of large-scale disturbances. Remote sensing techniques can address questions such as whether disturbance rates are increasing over time, what the main drivers of disturbances are, and whether boreal forests are expanding in size. The approach presented in this Chapter could be transferred to, for example, regions in Siberia to assess the impact of recent unprecedented droughts (Lin et al., 2020) on forestry dynamics. Furthermore, this model framework can emulate satellite imagery in any region with sufficient training images (as little as 4000 images have previously been used to train such models (Wagner et al., 2021)). The potential for deep learning techniques in cross-validation of satellite images is high and an algorithm emulating L7 images at a global scale would have wide-ranging implications. Lastly, we recommend that future work should focus on validating remotely sensed estimates of forest cover with ground plot measurements to improve confidence in the techniques applied.

References

Abadi, M., Agarwal, A., Barham, P., Brevdo, E., Chen, Z., Citro, C., Corrado, G.S., Davis, A., Dean, J., Devin, M. and Ghemawat, S., 2016. Tensorflow: Large-scale machine learning on heterogeneous distributed systems. arXiv preprint arXiv:1603.04467.

Bolin, B., Sukumar, R., Ciais, P., Cramer, W., Jarvis, P., Kheshgi, H., Nobre, C., Semenov, S. and Steffen, W., 2000. Global Perspective. In land Use, Land-Use change and Forestry, RT Watson, IR Noble, B Bolin, NH Ravindranath, DJ Verardo, DJ Dokken (eds.) A Special Report of the IPCC.

Bonan, G.B., Levis, S., Kergoat, L. and Oleson, K.W., 2002. Landscapes as patches of plant functional types: An integrating concept for climate and ecosystem models. Global Biogeochemical Cycles, 16(2), pp.5-1.

Chander, G., Markham, B.L., Micijevic, E., Teillet, P.M. and Helder, D.L., 2005, August. Improvement in absolute calibration accuracy of Landsat-5 TM with Landsat-7 ETM+ data. In Earth Observing Systems X (Vol. 5882, p. 588209). International Society for Optics and Photonics.

Chollet, F. et al. Keras. 2015, https:/keras.io

Ciais, P., Tan, J., Wang, X., Roedenbeck, C., Chevallier, F., Piao, S.L., Moriarty, R., Broquet, G., Le Quéré, C., Canadell, J.G. and Peng, S., 2019. Five decades of northern land carbon uptake revealed by the interhemispheric CO 2 gradient. Nature, 568(7751), pp.221-225.

de Groot, W.J., Flannigan, M.D. and Cantin, A.S., 2013. Climate change impacts on future boreal fire regimes. Forest Ecology and Management, 294, pp.35-44.

DeFries, R.S., Houghton, R.A., Hansen, M.C., Field, C.B., Skole, D. and Townshend, J., 2002. Carbon emissions from tropical deforestation and regrowth based on satellite observations for the 1980s and 1990s. Proceedings of the National Academy of Sciences, 99(22), pp.14256-14261.

Dong, C., Loy, C.C., He, K. and Tang, X., 2015. Image super-resolution using deep convolutional networks. IEEE transactions on pattern analysis and machine intelligence, 38(2), pp.295-307.

Friedlingstein, P., Cox, P., Betts, R., Bopp, L., von Bloh, W., Brovkin, V., Cadule, P., Doney, S., Eby, M., Fung, I. and Bala, G., 2006. Climate–carbon cycle feedback analysis: results from the C4MIP model intercomparison. Journal of climate, 19(14), pp.3337-3353.

Friedlingstein, P., O'sullivan, M., Jones, M.W., Andrew, R.M., Hauck, J., Olsen, A., Peters, G.P., Peters, W., Pongratz, J., Sitch, S. and Le Quéré, C., 2020. Global carbon budget 2020. Earth System Science Data, 12(4), pp.3269-3340.

Gong, P., Wang, J., Yu, L., Zhao, Y., Zhao, Y., Liang, L., Niu, Z., Huang, X., Fu, H., Liu, S. and Li, C., 2013. Finer resolution observation and monitoring of global land cover: First mapping results with Landsat TM and ETM+ data. International Journal of Remote Sensing, 34(7), pp.2607-2654.

Gong, P., Li, X., Wang, J., Bai, Y., Chen, B., Hu, T., Liu, X., Xu, B., Yang, J., Zhang, W. and Zhou, Y., 2020. Annual maps of global artificial impervious area (GAIA) between 1985 and 2018. Remote Sensing of Environment, 236, p.111510.

Gorelick, N., Hancher, M., Dixon, M., Ilyushchenko, S., Thau, D. and Moore, R., 2017. Google Earth Engine: Planetary-scale geospatial analysis for everyone. Remote sensing of Environment, 202, pp.18-27.

Graven, H.D., Keeling, R.F., Piper, S.C., Patra, P.K., Stephens, B.B., Wofsy, S.C., Welp, L.R., Sweeney, C., Tans, P.P., Kelley, J.J. and Daube, B.C., 2013. Enhanced seasonal exchange of CO2 by northern ecosystems since 1960. Science, 341(6150), pp.1085-1089.

Hansen, M.C., Potapov, P.V., Moore, R., Hancher, M., Turubanova, S.A., Tyukavina, A., Thau, D., Stehman, S.V., Goetz, S.J., Loveland, T.R. and Kommareddy, A., 2013. High-resolution global maps of 21st-century forest cover change. science, 342(6160), pp.850-853.

Harris, N.L., Gibbs, D.A., Baccini, A., Birdsey, R.A., De Bruin, S., Farina, M., Fatoyinbo, L., Hansen, M.C., Herold, M., Houghton, R.A. and Potapov, P.V., 2021. Global maps of twenty-first century forest carbon fluxes. Nature Climate Change, 11(3), pp.234-240.

He, K., Zhang, X., Ren, S. and Sun, J., 2016. Deep residual learning for image recognition. In Proceedings of the IEEE conference on computer vision and pattern recognition (pp. 770-778).

Heinrich, V.H., Dalagnol, R., Cassol, H.L., Rosan, T.M., de Almeida, C.T., Junior, C.H.S., Campanharo, W.A., House, J.I., Sitch, S., Hales, T.C. and Adami, M., 2021. Large carbon sink potential of secondary forests in the Brazilian Amazon to mitigate climate change. Nature communications, 12(1), pp.1-11.

Houghton, R.A., 2005. Aboveground forest biomass and the global carbon balance. Global change biology, 11(6), pp.945-958.

Jeong, J.H., Kug, J.S., Kim, B.M., Min, S.K., Linderholm, H.W., Ho, C.H., Rayner, D., Chen, D. and Jun, S.Y., 2012. Greening in the circumpolar high-latitude may amplify warming in the growing season. Climate dynamics, 38(7), pp.1421-1431.

Kurz, W.A., Dymond, C.C., Stinson, G., Rampley, G.J., Neilson, E.T., Carroll, A.L., Ebata, T. and Safranyik, L., 2008. Mountain pine beetle and forest carbon feedback to climate change. Nature, 452(7190), pp.987-990.

Lin, X., Rogers, B.M., Sweeney, C., Chevallier, F., Arshinov, M., Dlugokencky, E., Machida, T., Sasakawa, M., Tans, P. and Keppel-Aleks, G., 2020. Siberian and temperate ecosystems shape Northern Hemisphere atmospheric CO2 seasonal amplification. Proceedings of the National Academy of Sciences, 117(35), pp.21079-21087.

Lindner, M., Maroschek, M., Netherer, S., Kremer, A., Barbati, A., Garcia-Gonzalo, J., Seidl, R., Delzon, S., Corona, P., Kolström, M. and Lexer, M.J., 2010. Climate change impacts, adaptive capacity, and vulnerability of European forest ecosystems. Forest ecology and management, 259(4), pp.698-709.

Liu, X., Hu, G., Chen, Y., Li, X., Xu, X., Li, S., Pei, F. and Wang, S., 2018. High-resolution multi-temporal mapping of global urban land using Landsat images based on the Google Earth Engine Platform. Remote sensing of environment, 209, pp.227-239.

Masson-Delmotte, V., Zhai, P., Pirani, A., Connors, S.L., Péan, C., Berger, S. and Zhou, B., 2021. Climate change 2021: the physical science basis. Working Group I contribution to the Sixth Assessment Report of the Intergovernmental Panel on Climate Change.

McGuire, A.D., Anderson, L.G., Christensen, T.R., Dallimore, S., Guo, L., Hayes, D.J., Heimann, M., Lorenson, T.D., Macdonald, R.W. and Roulet, N., 2009. Sensitivity of the carbon cycle in the Arctic to climate change. Ecological Monographs, 79(4), pp.523-555.

Millar, C.I. and Stephenson, N.L., 2015. Temperate forest health in an era of emerging megadisturbance. Science, 349(6250), pp.823-826.

Mishra, U. and Riley, W.J., 2012. Alaskan soil carbon stocks: spatial variability and dependence on environmental factors. Biogeosciences, 9(9), pp.3637-3645.

Murray, N.J., Phinn, S.R., DeWitt, M., Ferrari, R., Johnston, R., Lyons, M.B., Clinton, N., Thau, D. and Fuller, R.A., 2019. The global distribution and trajectory of tidal flats. Nature, 565(7738), pp.222-225.

Paritsis, J. and Veblen, T.T., 2011. Dendroecological analysis of defoliator outbreaks on Nothofagus pumilio and their relation to climate variability in the Patagonian Andes. Global Change Biology, 17(1), pp.239-253.

Pechony, O. and Shindell, D.T., 2010. Driving forces of global wildfires over the past millennium and the forthcoming century. Proceedings of the National Academy of Sciences, 107(45), pp.19167-19170.

Pouliot, D., Latifovic, R., Pasher, J. and Duffe, J., 2018. Landsat super-resolution enhancement using convolution neural networks and Sentinel-2 for training. Remote Sensing, 10(3), p.394.

Schimel, D., Stephens, B.B. and Fisher, J.B., 2015. Effect of increasing CO2 on the terrestrial carbon cycle. Proceedings of the National Academy of Sciences, 112(2), pp.436-441.

Screen, J.A. and Simmonds, I., 2010. The central role of diminishing sea ice in recent Arctic temperature amplification. Nature, 464(7293), pp.1334-1337.

Seidl, R., SCHELHAAS, M.J. and Lexer, M.J., 2011. Unraveling the drivers of intensifying forest disturbance regimes in Europe. Global Change Biology, 17(9), pp.2842-2852.

Souza, C.M., Z Shimbo, J., Rosa, M.R., Parente, L.L., A Alencar, A., Rudorff, B.F., Hasenack, H., Matsumoto, M., G Ferreira, L., Souza-Filho, P.W. and de Oliveira, S.W., 2020. Reconstructing three decades of land use and land cover changes in brazilian biomes with landsat archive and earth engine. Remote Sensing, 12(17), p.2735.

Teillet, P.M., Barker, J.L., Markham, B.L., Irish, R.R., Fedosejevs, G. and Storey, J.C., 2001. Radiometric cross-calibration of the Landsat-7 ETM+ and Landsat-5 TM sensors based on tandem data sets. Remote sensing of Environment, 78(1-2), pp.39-54.

Wagner, F.H., Joyce, P., Brienen, R. and Gloor, E., 2021, July. Increasing Landsat 5 TM Spatial Resolution to 15 M Using a Super-Resolution Deep Learning Model Trained with Pan-Sharpened Landsat 7 ETM+ DATA. In 2021 IEEE International Geoscience and Remote Sensing Symposium IGARSS (pp. 3877-3880). IEEE.

Wang, Y., Li, M. and Shen, L., 2013. Accelerating carbon uptake in the Northern Hemisphere: evidence from the interhemispheric difference of atmospheric CO2 concentrations. Tellus B: Chemical and Physical Meteorology, 65(1), p.20334.

Westerling, A.L., 2016. Increasing western US forest wildfire activity: sensitivity to changes in the timing of spring. Philosophical Transactions of the Royal Society B: Biological Sciences, 371(1696), p.20150178.

White, P.S., 1985. Natural disturbance and patch dynamics: an introduction. Natural disturbance and patch dynamics, pp.3-13.

5 Discussion

In this chapter I will first provide a summary of the aims and key methodologies of the work carried out in this thesis and present the key findings from Chapters 2-4. Following on from this, a critical analysis is undertaken of the quality of the research. Finally, the implications of the research will be discussed alongside suggestions for future work that can advance understanding of the earth system.

5.1 Aims and methods

Land vegetation from across the globe is impacted by recent climate change. Northern high latitude regions have experienced one of the strongest rates of warming, the Arctic has warmed more than twice as much as the global average (Masson-Delmotte et al., 2021). High latitude ecosystems take up a significant proportion of the net land sink (Mcguire et al., 2009), and their response to climate change plays an important role in atmospheric CO_2 concentrations. Surface warming has resulted in considerable vegetation responses across a wide range of northern ecosystems (Walther et al., 2002). Furthermore, uncertainties are high regarding the effects of climate change on the overall carbon sink or source status of high latitude lands, as well as regional differences in the response (Mcguire et al., 2009). Thus, it is important that a better understanding is gained of the response of vegetation in these regions, as well as globally, to changing climate and disturbance regimes.

In this thesis, three different methods were utilised: the analysis of high latitude CO_2 records, atmospheric $\delta^{13}C$, and remote sensing. All of these were combined with modelling to study the response of vegetation to climate change and rising atmospheric CO_2 concentrations and determine the drivers behind such changes. The following specific aims were addressed:

Aim 1: *Investigate the temperature sensitivity of high northern latitude vegetation spring carbon uptake using atmospheric data.* **(Chapter 2)**

Aim 2: *Quantify the sensitivities of simulated global atmospheric $\delta^{13}C$ to uncertainties in the carbon cycle.* **(Chapter 3)**

Aim 3: *Evaluate the effect of disturbance on tree cover using a novel deep learning technique in remote sensing.* **(Chapter 4)**

5.1.1 How robust is the apparent breakdown of northern high-latitude temperature control on spring carbon uptake? (Chapter 2)

Chapter 2 studied the temperature sensitivity of spring carbon uptake in northern high latitudes during the past 3 decades. The dominant limitations on plant productivity vary substantially across space, however, high latitude ecosystems have been thought to be limited by temperature during 1982-1999 based on climate data and satellite observations (Nemani et al., 2003). Careful analysis of the seasonality of atmospheric CO_2 concentrations at the Barrow observatory (73˚N) has been used to evaluate the timing (Barichivich et al., 2013), and length (Keeling et al., 1996) of the photosynthetic growing season and autumn release (Piao et al., 2008) by land vegetation in these high latitudes. Furthermore, a strong correlation between spring temperatures and spring CO_2 drawdown at four high northern latitude stations (55-76˚N) was found by Randerson et al. (1999). These studies used the Barrow observatory (73˚N) and thus provide insight into the northern high latitude region due to the limited footprint of this CO_2 measurement site. Keeling et al. (1996) also analysed CO_2 data at the Mauna Loa observatory (19˚N), which is a site that is often used in global analyses of CO_2 uptake and release processes. In their study, the CO_2 amplitude at Mauna Loa was demonstrated to be strongly controlled by land temperature in the 30˚N to 80˚N latitude range due to the dominance of the high latitude regions over the global CO_2 amplitude.

The investigation in Chapter 2 was prompted by an analysis of work by Piao et al. (2017). In their study, they demonstrated that the correlation between the spring zero crossing (SZC) at the Barrow observatory and the spatial average in spring temperature north of 50˚N reduced significantly around 1995. This was an intriguing result for several reasons: Firstly, the difference between SZC and spring temperature anomalies was only high for 4 years in the 1996-2012 period, which is not consistent with an overall loss in temperature sensitivity. Secondly, analysis of the temperature sensitivity of NDVI revealed no significant decoupling over the 1982-2012 period, which is also not consistent with a reduction in the temperature sensitivity of vegetation productivity. Lastly, a time series of the CO_2 flux footprint of Barrow revealed strong interannual variability in the origin of air arriving at Barrow. Previous work has highlighted the influence of atmospheric transport on the SZC. Murayama et al., (2007) found significant changes to modelled SZC can be obtained by year-to-year changes in the atmospheric transport alone. In this thesis, the drivers behind the

change in correlation between surface spring temperatures north of 50˚N and SZC were further investigated. This was supplemented by the utilisation of a trajectory model to estimate the footprint of Barrow which was used to weigh the temperature data. Following on from this was a series of factorial simulations of atmospheric CO_2 using the CASA-TOMCAT framework (Potter et al., 1993; Randerson et al., 1996; Chipperfield, 2006) to attribute specific drivers to the change in SZC-temperature correlation. The factorial simulations were composed of runs in which different climate variables in CASA were held constant, as well as runs in which atmospheric transport in TOMCAT did not vary from year to year. These runs enabled precise testing of the extent to which temperature sensitivity had broken down in the high northern latitude region.

The main findings from this study are:

a) The normalised difference vegetation index (NDVI) is a satellite-based product that is a measure of primary productivity and greenness of vegetation. During the 1982-2015 period, there was no significant change in the overall temperature sensitivity of spring vegetation greenness. This result was consistent whether averaging temperature and NDVI over the entire region north of 50˚N or averaging over the footprint of Barrow. Thus, if greenness is a good measure of productivity, then this analysis indicates that there has been no weakening of the temperature sensitivity of vegetation.
b) Analysis of the output from factorial simulations revealed that atmospheric transport has strong control over SZC variability. There was a simulated breakdown of temperature sensitivity of SZC when atmospheric transport varied, however, when holding transport constant, there was no significant drop in temperature sensitivity of SZC, contrary to the findings of Piao et al. (2017).
c) The spatial coherence of temperature anomalies significantly reduced during the 1979-2012 study period, hence providing a mechanism explaining the greater influence of atmospheric transport in the latter part of the study period.

This thesis aimed to better understand high latitude vegetation temperature sensitivity, which was done by determining the robustness of the results from Piao et al. (2017). Accurate footprint analyses are critical when inferring information from site-specific data (Murayama et al., 2007). This analysis led to the conclusion that temperature sensitivity remained strong contrary to the findings from Piao et al., (2017), which directly addresses the primary aim of the chapter.

The research carried out by Piao et al., (2017) and in Chapter 2 both heavily relied on the CO_2 data from a single measurement site. This was necessitated by the fact that the Barrow observatory is the only high northern latitude site with data extending from the early 1980s to present-day. As was demonstrated in the footprint analyses, Barrow shows very non-uniform, and inter-annually varying coverage of the high northern latitudes. Thus, the extent to which statements can be made about the functioning of the high northern latitudes as a whole is limited. Overall, while there are drawbacks with the research approach and methodology, the study presented in Chapter 2 provides important insights into the functioning of high northern latitude land vegetation.

Implications for further work

The influence of large-scale atmospheric modes of variability on site-specific measurements of atmospheric CO_2 was demonstrated in this chapter. This work also illustrates the importance of accounting for atmospheric footprints when analysing site-level CO_2 data. One area of further research could involve a more comprehensive analysis combining estimates of the climate sensitivity of all high-latitude CO_2 sites. The inclusion of the atmospheric footprint of each site would provide a fuller picture of the response of spring carbon uptake across the high latitudes and the relative impact of atmospheric transport on the data retrieved from each site. The results from this analysis would additionally indicate spatial variations in climate sensitivity, which could be attributed based on the atmospheric footprint of each site. One additional possibility would be to use a dimensionality reduction technique, such as a principal component analysis (Hotelling, 1933) on the CO_2 uptake indices. Following on from this, a similar analysis to that conducted in this chapter would enable the overall climate sensitivity of the high northern latitudes to be evaluated over the past decades. This was an approach taken by Russell & Wallace (2004), which could be improved upon with atmospheric footprint analyses and a more sophisticated index of CO_2 uptake by vegetation, such as the SZC or SCC. The work in Chapter 2 also highlights the effectiveness of the CASA-TOMCAT setup to simulate atmospheric CO_2, in particular, the model could reproduce seasonal cycle indices accurately, such as the SZC, SCC, and amplitude. Thus, this setup could be utilised further to examine the relative contributions of climatological drivers on uptake and release processes by the terrestrial biosphere.

5.1.2 What can atmospheric $\delta^{13}C$ tell us about the carbon cycle? (Chapter 3)

Chapter 3 explored the sensitivities of $\delta^{13}C_{atm}$ to uncertainties in the size of the land and ocean sinks, as well as soil and vegetation carbon stocks. Measurements of $\delta^{13}C_{atm}$ can provide additional clues about large-scale land vegetation functioning. The $\delta^{13}C_{atm}$ signature is influenced by the relative proportions of the land and ocean carbon uptake due to the far stronger fractionation of land vegetation compared with that of the ocean (Vogel et al., 1980). As a result, $\delta^{13}C_{atm}$ measurements have been proposed to allow partitioning of the ocean and land sinks (Tans et al., 1993; Keeling et al., 1995; Quay et al., 1992; Trudinger et al., 2005; Heimann & Maier-Reimer, 1996). $\delta^{13}C_{atm}$ is strongly influenced by the extent to which land plants discriminate against $^{13}CO_2$ during photosynthesis. This varies depending on plant type and water-use efficiency (Farquhar, 1989). Therefore, careful analysis of $\delta^{13}C_{atm}$ can reveal changes in vegetation composition and functioning in response to global environmental change (Keeling et al., 2017). To better understand future land sink behaviour, it is important that a firm understanding is gained of the response of land vegetation to changes in environmental conditions up to present-day.

Previous efforts to accurately model ^{13}C have yielded a gap between the observed and modelled $\delta^{13}C_{atm}$ levels (Van der Velde et al., 2013). However, Keeling et al., (2017) were able to close the budget with the assertion that land C3 discrimination has increased as a function of atmospheric CO_2 throughout the industrial era. Thus, their study illustrated the sensitivity of $\delta^{13}C_{atm}$ to isotopic C3 discrimination. What was missing, however, was a comprehensive analysis of the primary sensitivities of $\delta^{13}C_{atm}$ to uncertainties of land and ocean functioning.

For this purpose, ^{13}C was added to the Carnegie Ames-Stanford Approach (CASA) model (Potter et al., 1993) to simulate ^{13}C alongside ^{12}C fluxes between vegetation and soil pools. Ocean emissions from the Geophysical Fluid Dynamics Laboratory (GFDL) and fossil fuel emissions from the Carbon Dioxide Information Analysis Center (CDIAC) were used for ^{12}C and ^{13}C alongside the CASA model to simulate changes in atmospheric CO_2 and $\delta^{13}C$ for the 1982-2016 period. The default CASA setup produced simulated atmospheric CO_2 with only a slight bias in trend (+0.1 ppm yr^{-1}), however, the trend in $\delta^{13}C_{atm}$ was roughly twice that of the observed values. To understand this discrepancy, an investigation was performed into the various sensitivities of $\delta^{13}C_{atm}$ to uncertainties in the ocean, soil, and vegetation functioning. An increase in NPP was

implemented as a function of atmospheric CO_2 to account for CO_2 fertilisation that was not included in the standard CASA model.

The main findings from this study are:

a) The modelled atmospheric CO_2 trend best matched the observed trend when explicitly adding an additional CO_2 fertilisation effect on top of the growth stimulation present in the model from FPAR.
b) Large uncertainties in ocean net uptake had a strong effect on modelled $\delta^{13}C_{atm}$
c) $\delta^{13}C_{atm}$ was also sensitive to the magnitude of global NPP, as well as soil turnover, and the trend of C3 discrimination.
d) The response of soil respiration to temperature (Q10), and distribution of C3 vegetation has little effect on atmospheric $\delta^{13}C$.

The ocean uptake, soil turnover, and C3 discrimination by earth vegetation have previously been identified as having a large effect on $\delta^{13}C_{atm}$ (Keeling et al., 2017). As such, each of these (among others) were explored systematically using the most appropriate uncertainty bounds indicated by previous research. While many factors were considered in the uncertainty analysis, it is not an exhaustive list. For example, uncertainties regarding peat and land-use change emissions were not considered. In particular, the $\delta^{13}C$ signature of peat is known to vary significantly depending on environmental conditions (Royles et al., 2016), and depth (Drollinger et al., 2019).

The uncertainty in ocean net uptake had the greatest effect on $\delta^{13}C_{atm}$, from which, it was inferred that a greater understanding of ocean processes and better constraint of ocean net fluxes are necessary to utilise $\delta^{13}C_{atm}$ to constrain the response of land vegetation to CO_2 and climate. The estimated upper and lower uncertainty bounds of the ocean uptake as estimated by GFDL were found to be within the spread of estimates in the global carbon budget (Friedlingstein et al., 2020). Other studies that attempted to model $\delta^{13}C_{atm}$ (Van de Velde et al., 2013; Keeling et al., 2017) did not report the size of the uncertainties of ocean ^{12}C and ^{13}C uptake. If the uncertainty ranges are similarly large as in this study, then $\delta^{13}C_{atm}$ cannot realistically be used as a tool to constrain land vegetation functioning.

Implications for further work

$\delta^{13}C_{atm}$ has been used to constrain trends in discrimination (Keeling et al., 2017). However, the study presented here shows that $\delta^{13}C_{atm}$ trends are most sensitive to ocean uncertainty. If $\delta^{13}C_{atm}$ is to be used as an indicator for land vegetation functioning, then uncertainty must be significantly reduced for ocean uptake. Trends in $\delta^{13}C_{atm}$ were also found to be sensitive to other factors, such as NPP magnitude and soil turnover, which are both subject to considerable uncertainties (Raich & Schelsinger, 1992; Trumbore, 2000; Ito, 2011; Carvalhais, 2014). In addition, there are large uncertainties in estimates of total soil organic carbon stocks (Scharlemann et al., 2014; Jackson et al., 2017). In CASA, total soil organic carbon stocks are inextricably linked to soil turnover times, thus, both these uncertainties were tested simultaneously. The uncertainty of the trend in C3 discrimination estimated by Keeling et al (2017) is equal to one half of the trend itself. Thus, greater accuracy of this estimate is pertinent to understanding the response of terrestrial vegetation to environmental changes. However, the comparably low sensitivity of $\delta^{13}C_{atm}$ to C3 discrimination trend implies it may be difficult to further constrain discrimination trends using the $\delta^{13}C_{atm}$ record alone.

Continuous, and consistent measurements of the $\delta^{13}C$ signature of tree rings would provide strong observation-based evidence of the trend of plant discrimination. Tree rings also intrinsically record changes in discrimination due to other factors such as a change in tree height and light as trees grow (Brienen et al., 2017; Vadeboncoeur et al. 2020) and thus do not purely reflect plant physiological responses to CO_2. Hence, it is essential that these biases are accounted for when using tree rings to infer changing isotopic discrimination of trees. There are strong variations in the responses of plant isotope discrimination to increasing atmospheric CO_2 across environmental conditions and species (Saurer et al., 2004), requiring a wide variety of regions and plant types to be sampled (whilst accounting for the aforementioned biases) to obtain a representative global picture. Tree rings are increasingly being used in carbon cycle research, with many tree ring isotopes studies having been collected by Adams et al. (2020). Extension of this dataset may enable greater confidence of the estimated trend in C3 discrimination and hence the adaptation of land vegetation to enhanced ambient atmospheric CO_2 concentrations.

The CASA setup outlined in Chapter 3 could be used to produce net ecosystem exchange (NEE) fluxes, which could be combined with 2-dimensional net ocean uptake data and fossil fuel emissions to be inputted into an atmospheric transport model. Thus, such an analysis could provide

additional constraints on land vegetation functioning by comparing the seasonal cycles of the simulated and observed atmospheric CO_2 and $\delta^{13}C$ (similar to the analysis of Chapter 2). The seasonality of CO_2 and $\delta^{13}C$ fluxes are strongly controlled by vegetation functioning and allow a greater capability for constraining CO_2 uptake and release processes. Furthermore, there are many sites with long-term data for CO_2 and $\delta^{13}C$, thus it may be possible for significant constraints to be made on regional ocean uptake and land vegetation processes.

5.1.3 Cross calibration of Landsat 5 TM and Landsat 7 ETM+ using deep learning enhances tree cover mapping consistency (Chapter 4)

Chapter 4 presents a method through which the Landsat 7 ETM+ and Landsat 5 TM satellites can be cross calibrated using a novel deep learning technique. High-quality, consistently retrieved satellite data is one useful data source that can be analysed to monitor vegetation growth and mortality in response to climate change and disturbance events (Hansen et al., 2013; Guay et al., 2014; Zhang et al., 2009). A primary benefit of this approach is that responses of individual regions are comparatively easier to tease out than with atmospheric data. However, far greater computational costs are necessary, and data quality and consistency vary considerably by decade and region. Using remote sensing to infer the responses of land vegetation to climate change often uses various indices of vegetation growth, such as the Normalised Difference Vegetation Index (NDVI) (Pinzon & Tucker, 2014), or by utilising the complete spectral signature obtained from satellite data and using a model trained by ground-truthing data (Souza et al., 2020). Furthermore, these data can be used as input for land-surface models and terrestrial ecosystem models. One limitation of such products is the limited lifetime of each generation of satellites, which can lead to artefacts in the data when crossing between satellites (Claverie et al., 2015).

Improving the consistency of the Landsat record implies greater confidence with which vegetation can be analysed over multi-decadal timescales. This study was motivated by an observation that the tree cover maps of Hansen et al. (2013) only extended back as far as 2000, whereas consistent, global coverage of satellite data began in the Landsat programme in 1974. A longer analysis of satellite data is used in the Mapbiomas project (Souza et al., 2020), however, their analysis did not examine trends in percentage tree cover and was limited to the Amazon region.

The study presented a novel approach using a deep learning model to cross calibrate successive generations of Landsat satellites to reduce the error created when changing between satellites for

image data. Simulated satellite data was used to estimate percentage tree cover over the 1985-2016 period, which was combined with spatial data of fire events during this period to analyse the effect of the fire events on changes in tree cover. The study was thus successful in outlining the effectiveness of applying deep learning techniques to supplement remote sensing techniques over long timescales.

A deep neural network model was trained using pairs of Landsat 5 TM and Landsat 7 ETM+ images across Alaska. The aim was to predict the 30m bands of Landsat 7 as well as the higher resolution 15m pansharpened band. The model converged to reach a high degree of accuracy at predicting images from the validation dataset. Using the same set of training and validation data, a classical multiple regression model was produced with the same aim of emulating Landsat 7 imagery from Landsat 5. A random forests tree cover model was then trained using forestry data, which was then applied to Landsat 5, Landsat 7, and emulated Landsat 7 images from the deep learning and multiple regression models. The accuracy of all approaches was evaluated, and the percentage tree cover was mapped out across a region in Alaska from 1985 to present-day.

The main findings from this study are:

a) The deep learning model effectively emulated Landsat 7 ETM+ imagery, with evidence of greater spatial resolution achieved than the Landsat 5 TM original image. The error of the deep learning-emulated images was significantly reduced when compared with the original Landsat 5 images and performed better than producing emulated images using the classical multiple regression model.
b) The emulated images produced lower error when the tree cover model was applied, with closer estimates to the Landsat 7 estimates than the original Landsat 5 and multiple regression model.
c) The higher accuracy in tree cover estimates from the deep learning approach gave greater confidence in the predictions of tree cover pre-1999 when no Landsat 7 imagery existed.
d) The legacy effects of fires early in the study period were now possible to analyse with higher accuracy due to the lower error in the predicted tree cover.

This study was successful at improving the consistency of the satellite record during the study period. This method led to more accurate trends to be identified from the data in the study region. The improvement of consistency between satellite products was considerable but not as great as

that achieved by Wagner et al., (2021), possibly as a result of the high degree of variability of topography across the study region.

Due to the large amount of processing power and memory required to perform the analysis, the study region was relatively small, and thus it was not possible to make generalisations about how the response of vegetation to disturbance has evolved at a large scale. Furthermore, when collecting Landsat tiles for this analysis, it was apparent that there were not sufficiently many images covering a large spatial range to analyse the response of global or even high northern latitude vegetation functioning since the 1980s. However, this study does provide a glimpse into the potential for deep learning to be used to enhance the consistency of more recent satellite imagery that vary in characteristics over successive generations.

A key advantage of the approach used in this study is that the deep neural network model could feasibly be transferred to be trained on any pair of satellite products for cross-calibration with very little adjustment of the model architecture. The model training process can take a considerable amount of time, but once this has been completed, model predictions are near-instantaneous, thus can be included in larger-scale analyses without significantly increasing prediction time.

Implications for further work

The effectiveness of using deep neural networks to simulate satellite data and elongate the record of continuous satellite coverage was demonstrated here. This process enabled more accurate remote sensing data analysis techniques to be applied and thus provide greater confidence in the trends in vegetation cover and response to disturbance events. The Landsat programme has been running since the mid-1970s; however, few studies are able to effectively utilise the full extent of the period over which imagery is available. Thus, applying this type of deep learning model to accurately simulate Landsat data would be invaluable to studies on the long-term behaviour of land ecosystems. The model produced in this study was trained on Landsat data within the Alaskan region, however, it is unlikely to be accurate in predicting imagery in most other regions on the earth. Thus, training a model on a dataset with imagery from a wide variety of land cover types, altitude and latitude ranges would be invaluable in producing a generalised model for cross-calibration of Landsat imagery. Furthermore, a cross-calibration with the earliest generations of Landsat could further extend the usable satellite record further back to 1972 and allow an even

longer analysis of land cover changes. However, the spectral signatures of the scanners onboard Landsat 1-4 differed more from Landsat 7 than Landsat 5, thus more errors will propagate through.

More research around cross-calibration between different satellite programs, such as Landsat and Sentinel (Zhang et al., 2021) enables an additional improvement in spectral information available during certain periods. Another area in which more work would be effective is in the collection of forestry-based ground truthing data to validate land cover classifications. For example, measurements of basal area and tree species distribution would be essential in remote sensing techniques to estimate land cover classification.

Machine learning methods have existed for decades, but their applications were limited until recent developments in general-purpose GPUs and neural network frameworks that could operate on them (Raina et al., 2009). This has led to their widespread use within data science practices in the private sector and academia. The frameworks in which machine learning models can be trained and deployed have improved vastly with application programming interfaces (APIs) such as Keras (Chollet et al., 2015). These APIs allow users to train and deploy deep neural networks without the need for extensive training in deep neural networks. This is supplemented by the growing ubiquity and shrinking costs of cloud computing servers, hence enabling machine learning models to be trained cheaply and quickly. Machine learning use is growing in the academic community, but the adaptation has been slow in general. It can be the only option for modelling relationships between variables that are too complex to do so with classical means. Thus, greater confidence and understanding of machine learning methods would greatly enhance the quality of research. Furthermore, developing more effective and efficient machine learning architectures is important if we are to continue to expand the utility of such models in science.

5.2 Synthesis of research chapters

In each research chapter of this thesis, one of the aims laid out in Chapter 1 were addressed. It was clear in each chapter that the land biosphere is changing rapidly in response to environmental change.

A consistent theme in Chapters 2-4 was an emphasis on the importance of the necessary attention to detail that is necessary in order to successfully analyse the terrestrial biosphere using the tools we have available. In Chapter 2, it was made clear that one cannot directly compare the CO_2 data

at a single site to infer changes in land vegetation functioning across a latitude range without careful analysis of the footprint of the site. In Chapter 3, it was demonstrated that significant uncertainties remain in the ocean emissions, and thus care must be taken when inferring changes in land vegetation functioning using the $\delta^{13}C_{atm}$ signature alone. Chapter 4 showed that the shift from Landsat 5 to Landsat 7 led to greater error in satellite retrievals and hence less certainty in the long-term trends in vegetation activity. A key focus of Chapters 2 and 4 was to remedy these issues and provide a method with which to work around these limitations.

All the models developed in this thesis were demonstrated to be effective and were used successfully to supplement observational analyses. The CASA model simulating land processes well and hence is effective as a tool in carbon cycle research. However, the direct implications of the model output on understanding of the carbon cycle were less obvious. Some of the conclusions from the CASA-TOMCAT model simulations in Chapter 2 rely on correlational analyses that are not trivial to interpret. However, when combining the findings from the satellite NDVI and model simulations, they consistently demonstrate a sustained control of temperature over vegetation productivity. In Chapter 3, the considerable uncertainties present in net ocean uptake demonstrate that more research is needed to constrain the net ocean uptake if $\delta^{13}C$ can be effectively used to constrain land carbon uptake processes. As a result, the model output cannot be used to determine, for example, to what extent C3 discrimination has changed. The effect of disturbance on tree cover in Alaska was analysed in Chapter 4, however, large scale application of these techniques over larger land surface areas is needed to determine the precise impact on the carbon cycle on a biome scale. For example, a terrestrial ecosystem model could be used in concert with the satellite data to determine the reduction in the land sink as a result of each disturbance event.

While each model was validated when compared with observational data, it is not always clear how well they fit in with other modelling efforts. Previous attempts at modelling $\delta^{13}C_{atm}$ did not explicitly calculate the uncertainty of oceanic uptake (Van der Velde et al., 2013; Keeling et al., 2017). Thus, these previous studies may have been subject to the same issues as a result of the high uncertainty of net ocean uptake. The modelled cross-calibration of the Landsat 5 & 7 satellites in Chapter 4 did not retrieve an error as low as that achieved by Wagner et al., (2021), the reasons for which are not certain. Lastly, the correlation between modelled and observed carbon uptake was high for the CASA-TOMCAT model in Chapter 2, however, the only other study in which this was simulated (Piao et al., 2017) did not report this correlation.

Each of the three chapters involved the development of a model and in each case, the model was able to provide important information about the state of terrestrial ecosystem research. Thus, continuing research involving the use of the models developed in this thesis would be beneficial. The models could be effective in investigating the functioning of the land biosphere over a larger spatial range. For example, the CASA-TOMCAT model developed in Chapter 2 could be employed to analyse the CO_2 seasonal cycle in the tropics. Furthermore, the deep neural network developed in Chapter 4 could be employed in any region with sufficient satellite data coverage to improve the consistency of satellite data over successive satellite generations.

It is clear that much work remains to be done to fully understand the changes in the functioning of the terrestrial biosphere. All three of the research chapters highlighted the value of high quality, consistently measured *in-situ* data. These include measurements of atmospheric CO_2 and $\delta^{13}C$ at ground measurement sites, as well as species information included as part of forestry data collection schemes. With more of such data being made available, reduced uncertainty can be achieved, and analyses can be undertaken at a wider range of locations in order to gain a more complete understanding of the response of the land carbon sink to climate change.

5.3 Conclusions

Evidence from atmospheric and satellite data indicates the expansion of terrestrial vegetation and a growing land carbon sink. In particular, the consistent increasing trend of CO_2 amplitude, as well as the strong relationship between climate and the atmospheric growth rate are key indicators of increases in land CO_2 sequestration. The primary aim of this thesis was to develop a deeper understanding of terrestrial carbon uptake processes and their response to recent climate change. Throughout the course of the research carried out in this thesis, the state of knowledge in this field has been expanded. The temperature sensitivity of high latitude lands was reanalysed using observed atmospheric CO_2 data alongside model simulations. From this, it was revealed that atmospheric transport played a key role in the variability of CO_2 uptake indices at a ground measurement site. As a result, it was concluded that the temperature sensitivity of high latitude lands remained strong during the study period, contrary to previous research suggesting otherwise. Simulations of $\delta^{13}C_{atm}$ were undertaken through a combination of land-surface and ocean uptake modelling. Following on from this, an analysis of the uncertainties present in land and ocean uptake processes was undertaken. Ocean uncertainty emerged as the most significant influence on

$\delta^{13}C_{atm}$ and thus presented the greatest limiting factor on using atmospheric isotopic analyses to determine changes in plant functioning. It was concluded that it was not possible to infer changes in isotopic discrimination from the atmospheric record alone due to the high ocean uncertainty. Finally, an attempt was made to improve the long-term consistency of percentage tree cover estimates from Landsat satellite data using a deep neural network model. The model produced significantly lower error when compared with the original data and with a classical approach. As a proof-of-concept, the improved satellite record was used to analyse the response of percentage tree cover to disturbance events. Overall, these results provide an important step forward in our understanding of the responses of the terrestrial biosphere to climate change that will enable more appropriate adaptations in the future.

References

Adams, M.A., Buckley, T.N. and Turnbull, T.L., 2020. Diminishing CO 2-driven gains in water-use efficiency of global forests. Nature Climate Change, 10(5), pp.466-471.

Brienen, R. J. W., Gloor, E., Clerici, S., Newton, R., Arppe, L., Boom, A., ... & Timonen, M. (2017). Tree height strongly affects estimates of water-use efficiency responses to climate and CO 2 using isotopes. Nature Communications, 8(1), 1-10.

Carvalhais, N., Forkel, M., Khomik, M., Bellarby, J., Jung, M., Migliavacca, M., Saatchi, S., Santoro, M., Thurner, M., Weber, U. and Ahrens, B., 2014. Global covariation of carbon turnover times with climate in terrestrial ecosystems. Nature, 514(7521), pp.213-217.

Chipperfield, M.P., 2006. New version of the TOMCAT/SLIMCAT off-line chemical transport model: Intercomparison of stratospheric tracer experiments. Quarterly Journal of the Royal Meteorological Society: A journal of the atmospheric sciences, applied meteorology and physical oceanography, 132(617), pp.1179-1203.

Chollet, F. et al. Keras. 2015, https:/keras.io

Claverie, M., Vermote, E.F., Franch, B. and Masek, J.G., 2015. Evaluation of the Landsat-5 TM and Landsat-7 ETM+ surface reflectance products. Remote Sensing of Environment, 169, pp.390-403.

Drollinger, S., Kuzyakov, Y. and Glatzel, S., 2019. Effects of peat decomposition on δ13C and δ15N depth profiles of Alpine bogs. Catena, 178, pp.1-10.

Farquhar, G.D., Ehleringer, J.R. and Hubick, K.T., 1989. Carbon isotope discrimination and photosynthesis. Annual review of plant biology, 40(1), pp.503-537.

Guay, K.C., Beck, P.S., Berner, L.T., Goetz, S.J., Baccini, A. and Buermann, W., 2014. Vegetation productivity patterns at high northern latitudes: A multi-sensor satellite data assessment. Global Change Biology, 20(10), pp.3147-3158.

Hansen, M.C., Potapov, P.V., Moore, R., Hancher, M., Turubanova, S.A., Tyukavina, A., Thau, D., Stehman, S.V., Goetz, S.J., Loveland, T.R. and Kommareddy, A., 2013. High-resolution global maps of 21st-century forest cover change. science, 342(6160), pp.850-853.

Heimann, M. and Maier-Reimer, E., 1996. On the relations between the oceanic uptake of CO2 and its carbon isotopes. Global Biogeochemical Cycles, 10(1), pp.89-110.

Hotelling, H., 1933. Analysis of a complex of statistical variables into principal components. Journal of educational psychology, 24(6), p.417.

Ito, A., 2011. A historical meta-analysis of global terrestrial net primary productivity: are estimates converging?. Global Change Biology, 17(10), pp.3161-3175.

Jackson, R.B., Lajtha, K., Crow, S.E., Hugelius, G., Kramer, M.G. and Piñeiro, G., 2017. The ecology of soil carbon: pools, vulnerabilities, and biotic and abiotic controls. Annual Review of Ecology, Evolution, and Systematics, 48, pp.419-445.

Keeling CD, Whorf TP, Wahlen M, Vanderplicht J (1995) Interannual extremes in the rate of rise of atmospheric carbon-dioxide since 1980. Nature 375:666–670.

Keeling, C.D., Chin, J.F.S. and Whorf, T.P., 1996. Increased activity of northern vegetation inferred from atmospheric CO 2 measurements. Nature, 382(6587), pp.146-149.

Keeling, R. F. et al. Atmospheric evidence for a global secular increase in carbon isotopic discrimination of land photosynthesis. Proc. Natl Acad. Sci. USA 114, 10361–10366 (2017).

Keeling, R. F., & Keeling, C. D. (2017). Atmospheric monthly in situ CO2 data-mauna loa observatory, Hawaii. Scripps CO2 program data.

Masson-Delmotte, V., Zhai, P., Pirani, A., Connors, S.L., Péan, C., Berger, S. and Zhou, B., 2021. Climate change 2021: the physical science basis. Working Group I contribution to the Sixth Assessment Report of the Intergovernmental Panel on Climate Change.

McGuire, A.D., Anderson, L.G., Christensen, T.R., Dallimore, S., Guo, L., Hayes, D.J., Heimann, M., Lorenson, T.D., Macdonald, R.W. and Roulet, N., 2009. Sensitivity of the carbon cycle in the Arctic to climate change. Ecological Monographs, 79(4), pp.523-555.

McGuire, A.D., Christensen, T.R., Hayes, D., Heroult, A., Euskirchen, E., Kimball, J.S., Koven, C., Lafleur, P., Miller, P.A., Oechel, W. and Peylin, P., 2012. An assessment of the carbon balance of Arctic tundra: comparisons among observations, process models, and atmospheric inversions. Biogeosciences, 9(8), pp.3185-3204.

Murayama, S., Higuchi, K. and Taguchi, S., 2007. Influence of atmospheric transport on the inter-annual variation of the CO2 seasonal cycle downward zero-crossing. Geophysical research letters, 34(4).

Nemani, R.R., Keeling, C.D., Hashimoto, H., Jolly, W.M., Piper, S.C., Tucker, C.J., Myneni, R.B. and Running, S.W., 2003. Climate-driven increases in global terrestrial net primary production from 1982 to 1999. science, 300(5625), pp.1560-1563.

Piao, S., Ciais, P., Friedlingstein, P., Peylin, P., Reichstein, M., Luyssaert, S., Margolis, H., Fang, J., Barr, A., Chen, A. and Grelle, A., 2008. Net carbon dioxide losses of northern ecosystems in response to autumn warming. Nature, 451(7174), pp.49-52.

Piao, S., Liu, Z., Wang, T., Peng, S., Ciais, P., Huang, M., Ahlstrom, A., Burkhart, J.F., Chevallier, F., Janssens, I.A. and Jeong, S.J., 2017. Weakening temperature control on the interannual

variations of spring carbon uptake across northern lands. Nature Climate Change, 7(5), pp.359-363.

Pinzon, J.E. and Tucker, C.J., 2014. A non-stationary 1981–2012 AVHRR NDVI3g time series. Remote sensing, 6(8), pp.6929-6960.

Potter, C.S.R. and Field, C.B., 1993. Terrestrial ecosystem production: A process model based on global satellite and surface data. Global Biogeochemical Cycles, 7(4), p.811.

Quay PD, Tilbrook B, Wong CS (1992) Oceanic uptake of fossil-fuel CO2: Carbon-13 evidence. Science 256:74–79.

Raich, J.W. and Schlesinger, W.H., 1992. The global carbon dioxide flux in soil respiration and its relationship to vegetation and climate. Tellus B, 44(2), pp.81-99.

Raina, R., Madhavan, A. and Ng, A.Y., 2009, June. Large-scale deep unsupervised learning using graphics processors. In Proceedings of the 26th annual international conference on machine learning (pp. 873-880).

Randerson, J.T., Thompson, M.V., Malmstrom, C.M., Field, C.B. and Fung, I.Y., 1996. Substrate limitations for heterotrophs: Implications for models that estimate the seasonal cycle of atmospheric CO2. Global Biogeochemical Cycles, 10(4), pp.585-602.

Randerson, J.T., Field, C.B., Fung, I.Y. and Tans, P.P., 1999. Increases in early season ecosystem uptake explain recent changes in the seasonal cycle of atmospheric CO2 at high northern latitudes. Geophysical research letters, 26(17), pp.2765-2768.

Royles, J., Amesbury, M.J., Roland, T.P., Jones, G.D., Convey, P., Griffiths, H., Hodgson, D.A. and Charman, D.J., 2016. Moss stable isotopes (carbon-13, oxygen-18) and testate amoebae reflect environmental inputs and microclimate along a latitudinal gradient on the Antarctic Peninsula. Oecologia, 181(3), pp.931-945.

Russell, J.L. and Wallace, J.M., 2004. Annual carbon dioxide drawdown and the Northern Annular Mode. Global biogeochemical cycles, 18(1).

Saurer, M., Siegwolf, R. T., & Schweingruber, F. H. (2004). Carbon isotope discrimination indicates improving water-use efficiency of trees in northern Eurasia over the last 100 years. Global Change Biology, 10(12), 2109-2120.

Scharlemann, J.P., Tanner, E.V., Hiederer, R. and Kapos, V., 2014. Global soil carbon: understanding and managing the largest terrestrial carbon pool. Carbon Management, 5(1), pp.81-91.

Souza, C.M., Z Shimbo, J., Rosa, M.R., Parente, L.L., A Alencar, A., Rudorff, B.F., Hasenack, H., Matsumoto, M., G Ferreira, L., Souza-Filho, P.W. and de Oliveira, S.W., 2020. Reconstructing three decades of land use and land cover changes in brazilian biomes with landsat archive and earth engine. Remote Sensing, 12(17), p.2735.

Tans, P.P., Berry, J.A. and Keeling, R.F., 1993. Oceanic 13C/12C observations: a new window on ocean CO2 uptake. Global Biogeochemical Cycles, 7(2), pp.353-368.

Thoning, K.W., Tans, P.P. and Komhyr, W.D., 1989. Atmospheric carbon dioxide at Mauna Loa Observatory: 2. Analysis of the NOAA GMCC data, 1974–1985. Journal of Geophysical Research: Atmospheres, 94(D6), pp.8549-8565.

Trudinger C, Enting I, Etheridge D, Francey R, Rayner P (2005) The carbon cycle over the past 1000 years inferred from the inversion of ice core data. A History of Atmospheric CO2 and Its Effects on Plants, Animals, and Ecosystems, eds Ehleringer JR, Cerling TE, Dearing MD (Springer, New York), pp 329–349.

Trumbore, S., 2000. Age of soil organic matter and soil respiration: radiocarbon constraints on belowground C dynamics. Ecological applications, 10(2), pp.399-411.

Vadeboncoeur, M. A., Jennings, K. A., Ouimette, A. P., & Asbjornsen, H. (2020). Correcting tree-ring δ 13C time series for tree-size effects in eight temperate tree species. Tree physiology, 40(3), 333-349.

Van der Velde, I.R., Miller, J.B., Schaefer, K., Masarie, K.A., Denning, S., White, J.W.C., Tans, P.P., Krol, M.C. and Peters, W., 2013. Biosphere model simulations of interannual variability in terrestrial 13C/12C exchange. Global biogeochemical cycles, 27(3), pp.637-649.

Vogel, J.C., 1980. Fractionation of the carbon isotopes during photosynthesis. In Fractionation of the Carbon Isotopes During Photosynthesis (pp. 5-29). Springer, Berlin, Heidelberg.

Wagner, F.H., Joyce, P., Brienen, R. and Gloor, E., 2021, July. Increasing Landsat 5 TM Spatial Resolution to 15 M Using a Super-Resolution Deep Learning Model Trained with Pan-Sharpened Landsat 7 ETM+ DATA. In 2021 IEEE International Geoscience and Remote Sensing Symposium IGARSS (pp. 3877-3880). IEEE.

Walther, G.R., Post, E., Convey, P., Menzel, A., Parmesan, C., Beebee, T.J., Fromentin, J.M., Hoegh-Guldberg, O. and Bairlein, F., 2002. Ecological responses to recent climate change. Nature, 416(6879), pp.389-395.

Zhang, X., Friedl, M.A. and Schaaf, C.B., 2009. Sensitivity of vegetation phenology detection to the temporal resolution of satellite data. International Journal of Remote Sensing, 30(8), pp.2061-2074.

Zhang, Y., Ling, F., Wang, X., Foody, G.M., Boyd, D.S., Li, X., Du, Y. and Atkinson, P.M., 2021. Tracking small-scale tropical forest disturbances: Fusing the Landsat and Sentinel-2 data record. Remote Sensing of Environment, 261, p.112470.

Appendices

Text S2.1. Repeating analyses with SCC

The SZC and SCC are closely related, with strong correlation (r=, P<0.1%). Overall, we draw the same conclusions from using the SCC as with the SZC. We found a significant breakdown in correlation between SCC and spring temperature averaged over vegetated land north of 50°N (Figure S2.20), and when averaging the temperature over Hysplit footprints (Figure S2.21). Our CASA-TOMCAT model simulates SCC with fairly high accuracy on interannual timescales (r=0.78, P<0.1%) (Figure S2.22), however the modelled trend and magnitude show some bias (Figure S2.23), similar to the simulated SZC. The factorial simulations yield similar results to those carried out with the SZC, however there appears to be a lower influence of FPAR and a higher influence of transport. The former is evidenced from the FPR run, in which the correlations between the simulated SCC and of the control are higher than seen in the SZC simulations (Table S2.1). Similarly, the ATCTR run produced SCC values that correlated lower with the control than seen in the SZC simulations (Table S2.1). Furthermore, the ATCTR simulations of SCC consistently correlated with Hysplit-averaged temperature at higher levels than in the SZC runs (Table S2.1), further demonstrating the role of transport in the breakdown in control of temperature on spring carbon uptake.

Text S2.2. Description of CCGCRV routine

In order to extract the seasonal cycle from the raw CO_2 data, we applied the Carbon Cycle Group CuRVe (CCGCRV) routine to the data (Thoning et al., 1989). The routine fitted a polynomial (quadratic) function for the long-term trend and a harmonic term (4 per year) for the annual cycle. We then calculated the residuals from this function fit and oscillations with periods shorter than 45 days were removed using a Full Width at Half Maximum (FWHM) low-pass filter. We then added the filtered residuals to the fitted function. This process was repeated to remove oscillations with periods longer than 390 days using an FWHM high-pass filter, which were then added to the polynomial function. The CO_2 seasonal cycle was obtained by subtracting the long-term trend from the smooth curve. We computed the residuals between this function fit and the data points and removed data that fell outside 5 standard deviations of the residuals. We then repeated the above steps until all residuals resided within 5 standard deviations. This is identical to the smoothing method employed in Piao et al. (2017) as we aimed to reproduce their results as closely as possible.

Text S2.3. Description of temperature and NDVI masks to eliminate the snow melt influence

In order to remove the effects of snow melt timing on the NDVI and temperature time series, we imposed a constraint on all temperature and NDVI data points where the spring temperature must be greater than 0 and NDVI must be greater than 0.1 for each pixel used in the spatial average. Utilising these masks for the 50°N spatial average and the footprint-weighted average yields consistent and significant positive correlations between NDVI and temperature (Figure S2.24). Therefore, we demonstrated that snow melt timing is not the cause for the consistent NDVI-temperature relationship.

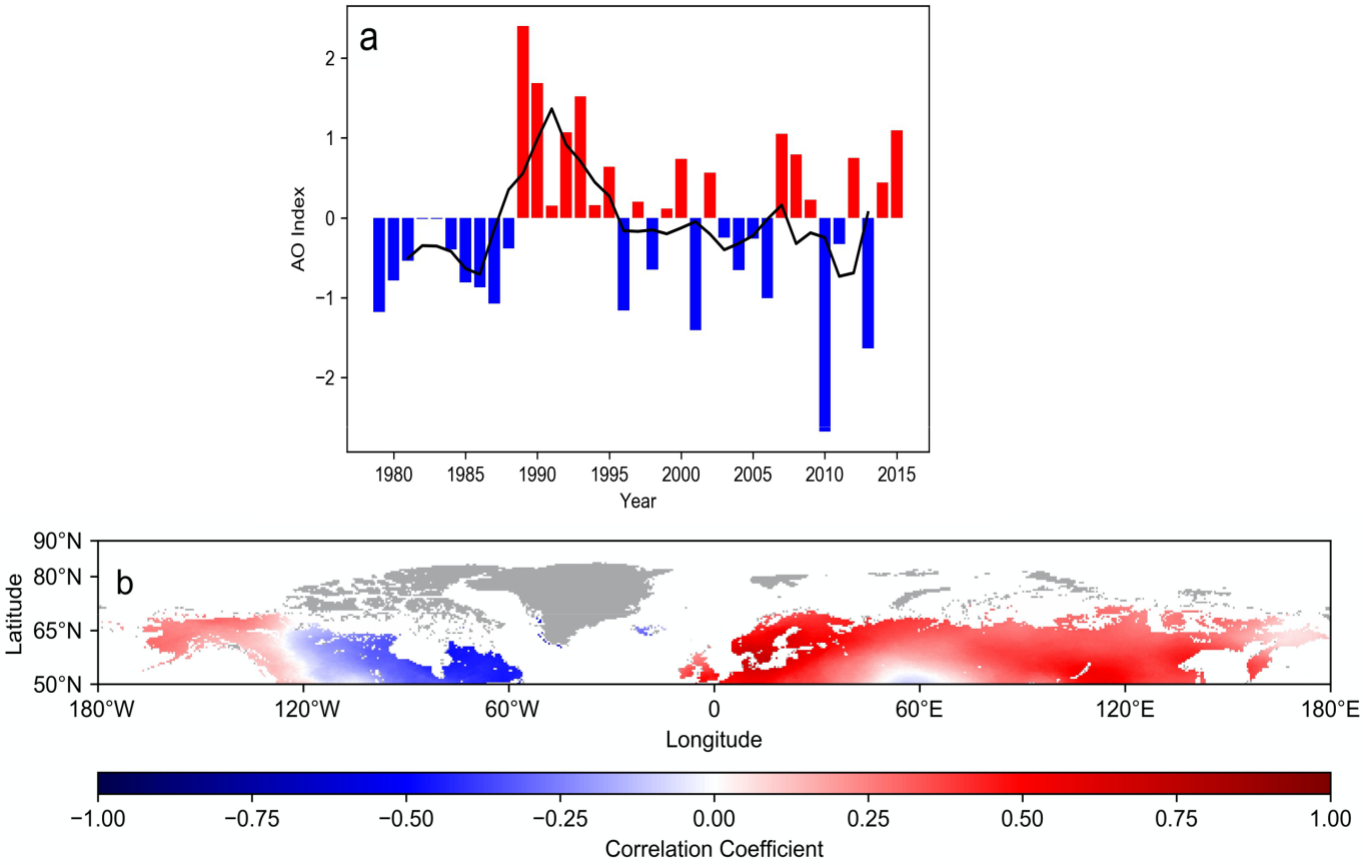

Figure S2.1. (a) December to March average Arctic Oscillation (AO) index time series. Negative values are blue and positive values are red, black line indicates 5-year moving average. (b) Spatial correlation between AO index time series and detrended spring temperature spatio-temporal fields over the 1979-2016 period.

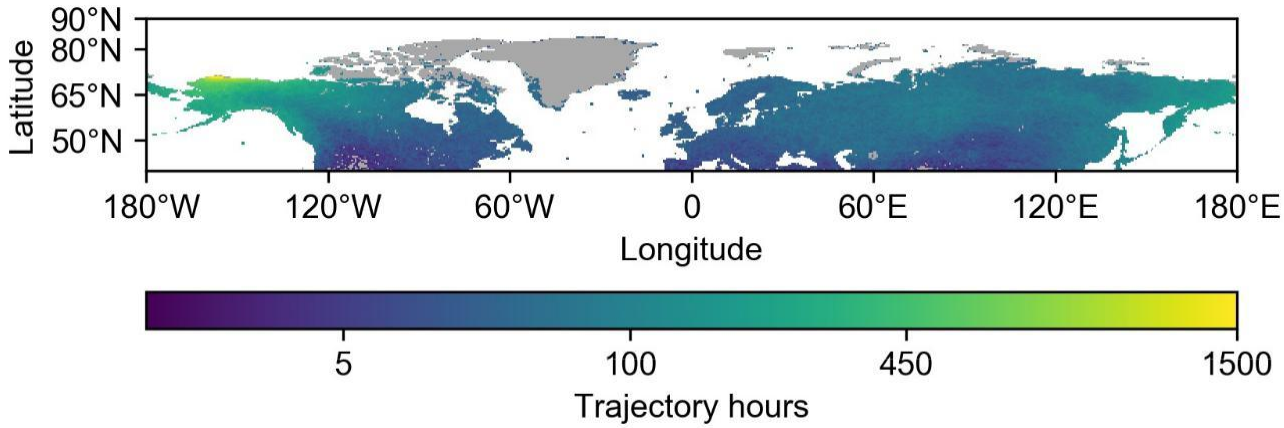

Figure S2.2. Hysplit 30-day March-June footprints of Barrow summed over the 1979-2016 period. Units expressed as trajectory hours, calculated as the amount of time an air mass trajectory spends within the boundary layer (0 to 2 km above ground level) over a specified region. Colour scale is logarithmic to ensure a wide range in magnitudes of footprint is visible.

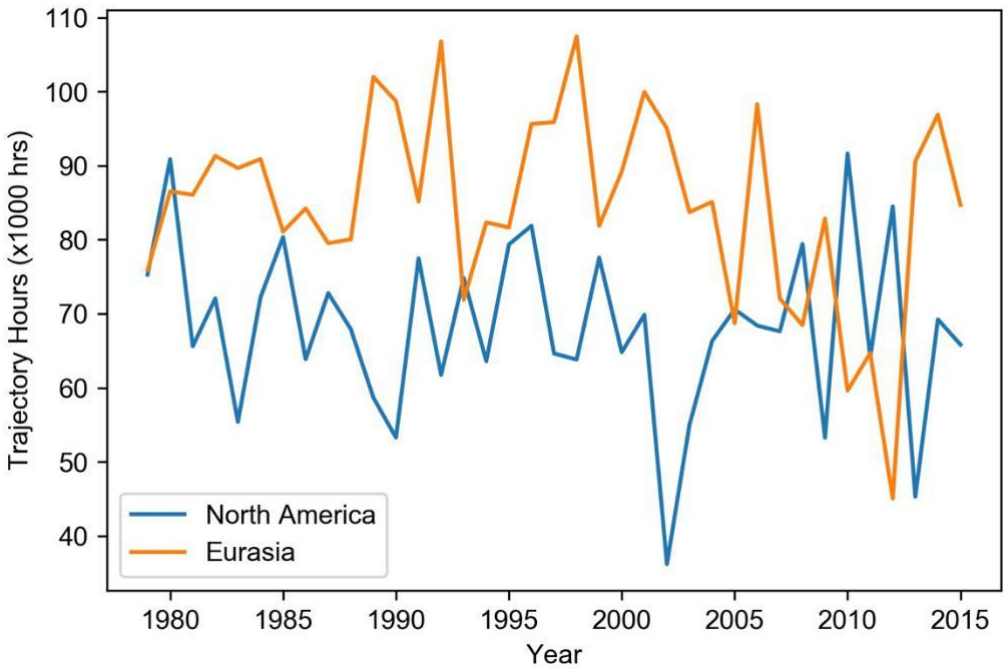

Figure S2.3. Hysplit 30-day March-June footprints of Barrow detailing the contribution of Eurasia and North America. Units expressed as trajectory hours, calculated as the amount of time an air mass trajectory spends within the boundary layer (0 to 2 km above ground level) over vegetated land (NDVI > 0.1) inside the specified region. Eurasia and North America defined as 12˚W-190˚E, 30˚N-78˚N and 168˚W-52˚W, 30˚N-78˚N, respectively.

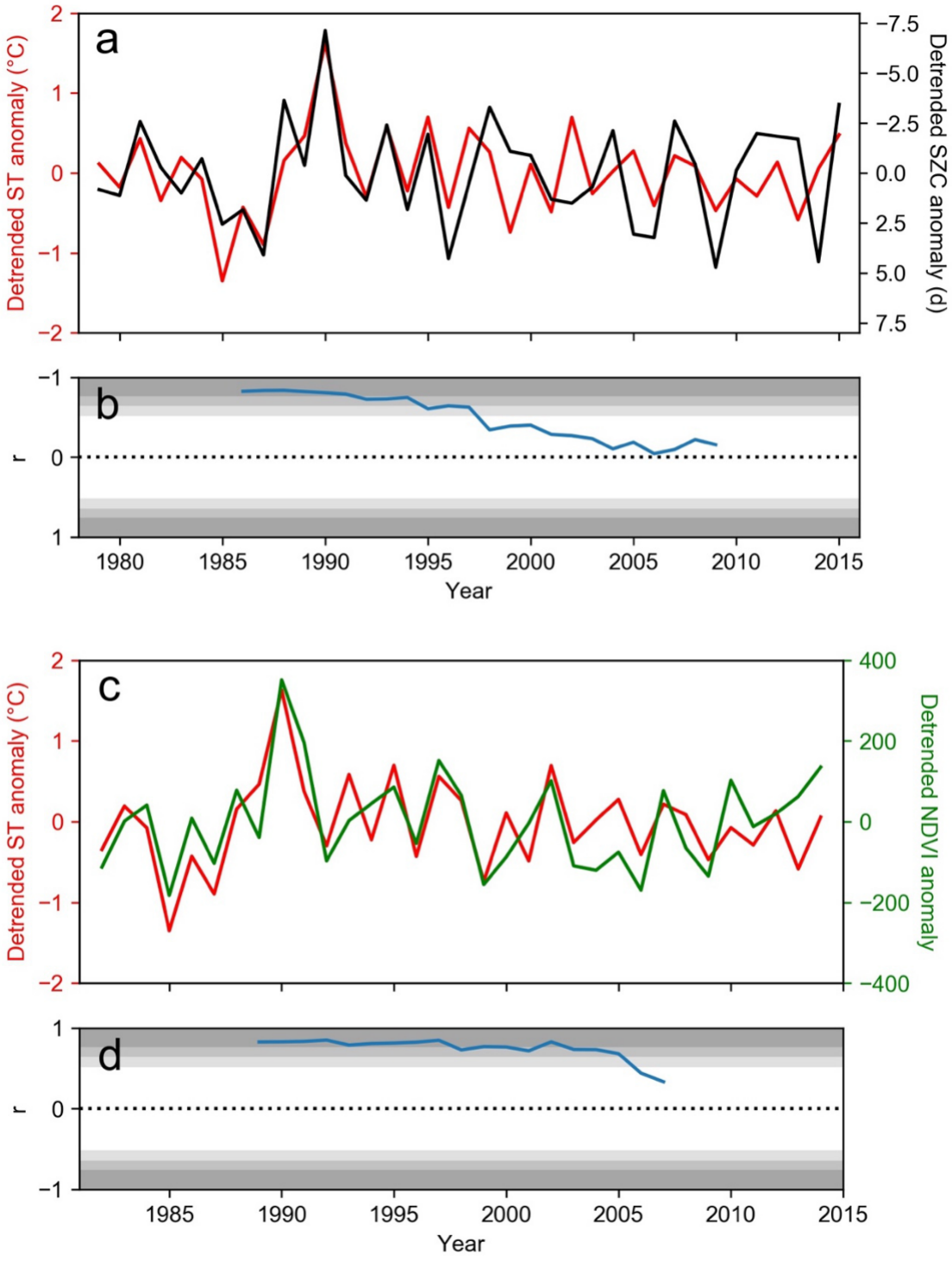

Figure S2.4. Times series of anomalies in detrended spring temperature (ST) weighed by footprints along with (a) detrended SZC at Barrow and (b) detrended NDVI averaged over footprints. Corresponding moving window (15 yr) partial correlations (accounting for precipitation and radiation) are also shown. Shaded regions depict 5%, 1% and .1% significance levels (n=15).

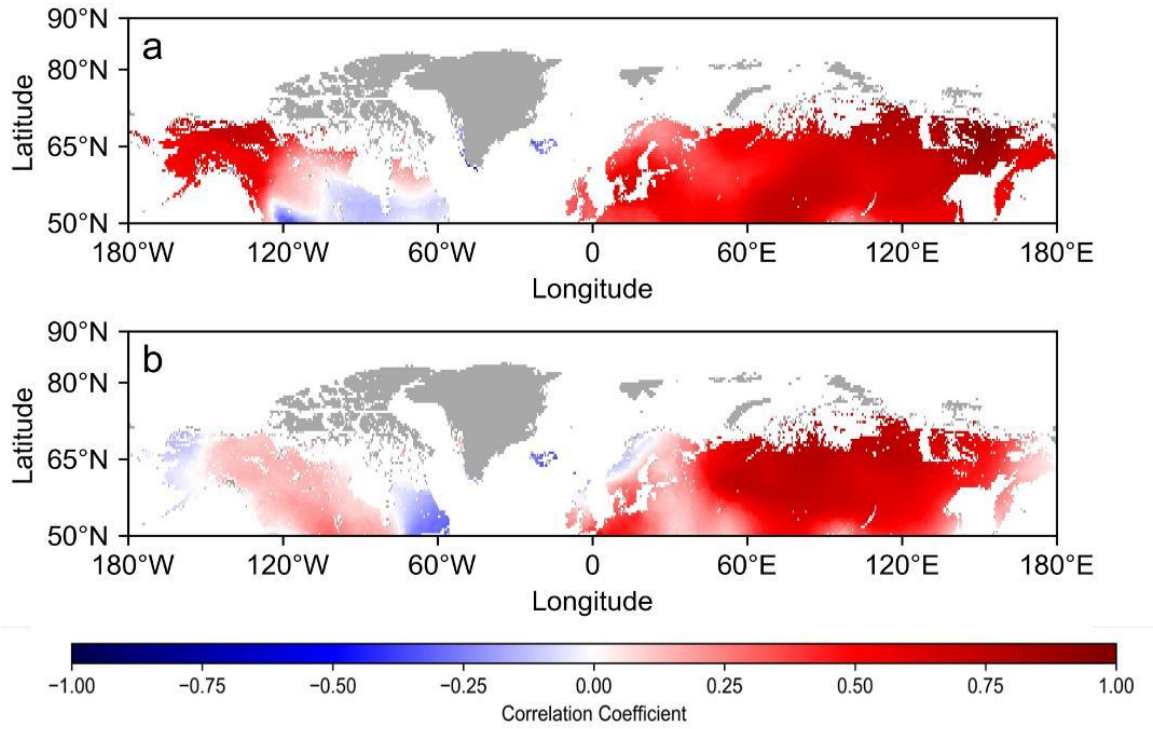

Figure S2.5. Spatial correlation between the time series of detrended spring (March-June) temperature at each pixel and the detrended spatially averaged temperature of vegetated land north of 50˚N during the (a) 1979-1995 and (b) 1996-2012 periods. The Barrow observatory is located at 71˚N, 156˚W.

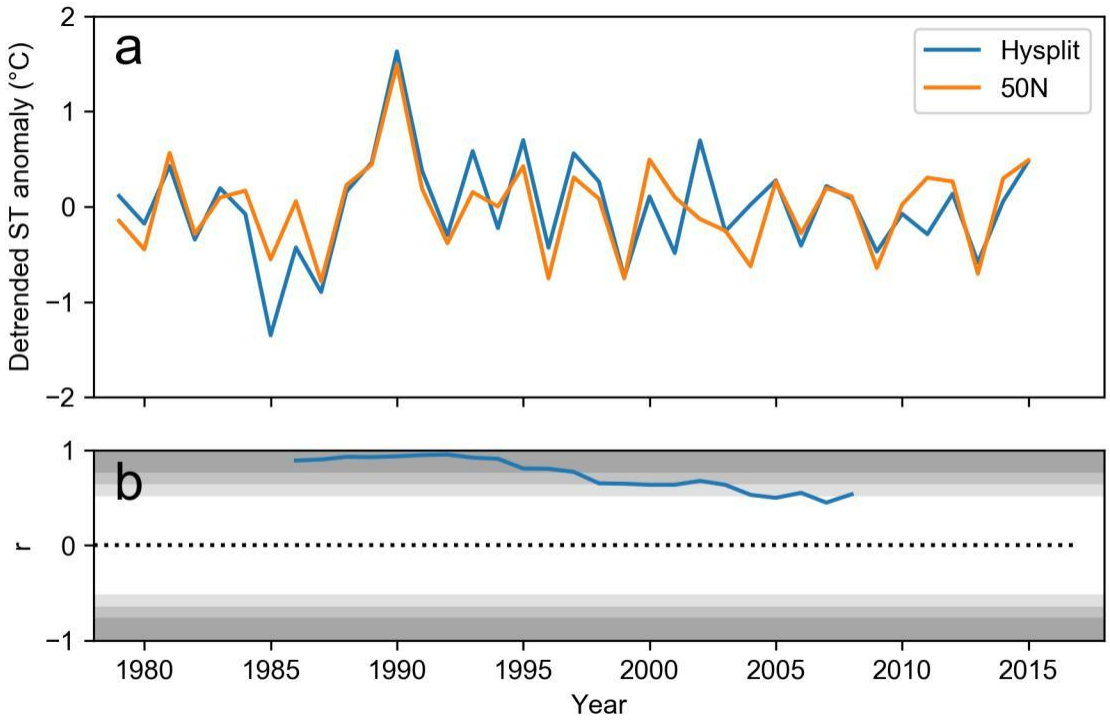

Figure S2.6. (a) Detrended spring temperature (ST) averaged over: all land north of 50˚N (orange) and Hysplit footprints (blue). (b) 15-year moving window correlation between the temperature time series. Shaded regions depict 5%, 1% and .1% significance for a two-tailed correlation and n=15.

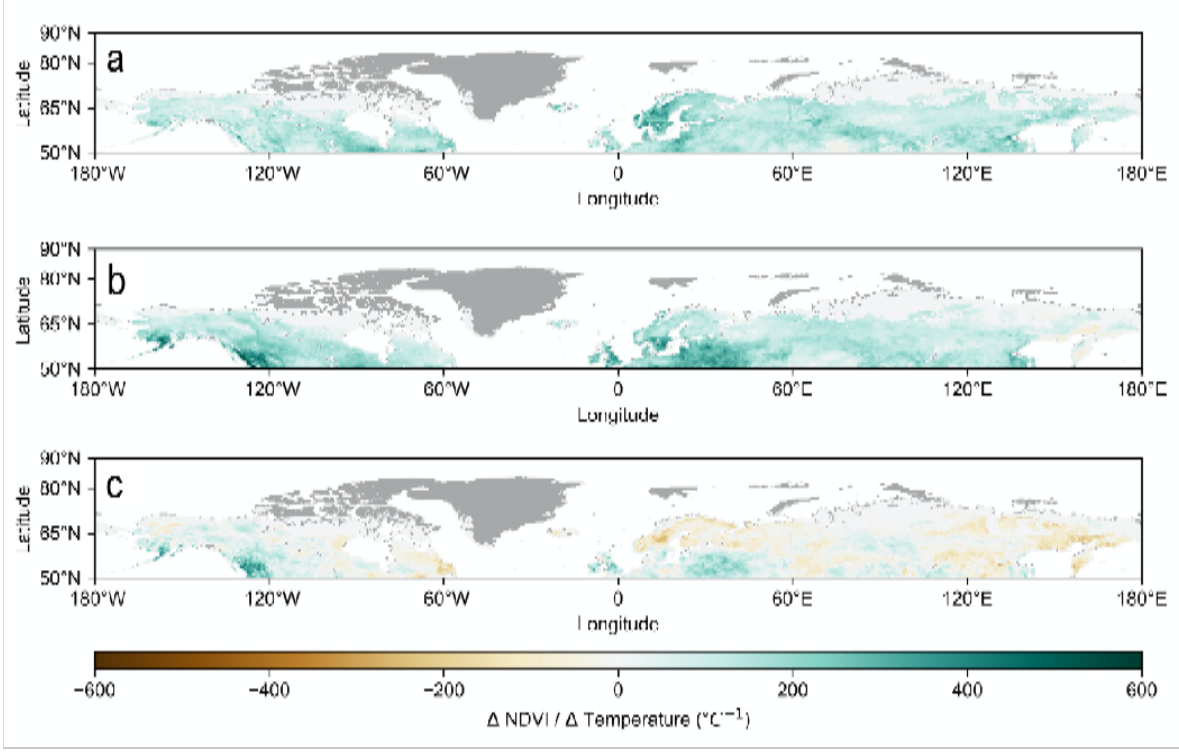

Figure S2.7. Sensitivity of NDVI to temperature derived from the pixel-to-pixel regression slope coefficient between spring NDVI and spring temperature (ST) values for the periods (a)1982-1996 and (b) 1997-2012. Panel (c) depicts values from the panel (a) subtracted from panel (b). Due to the longer time period used in panel (b), values shown were the median regression value after systematically removing each year from the chronology.

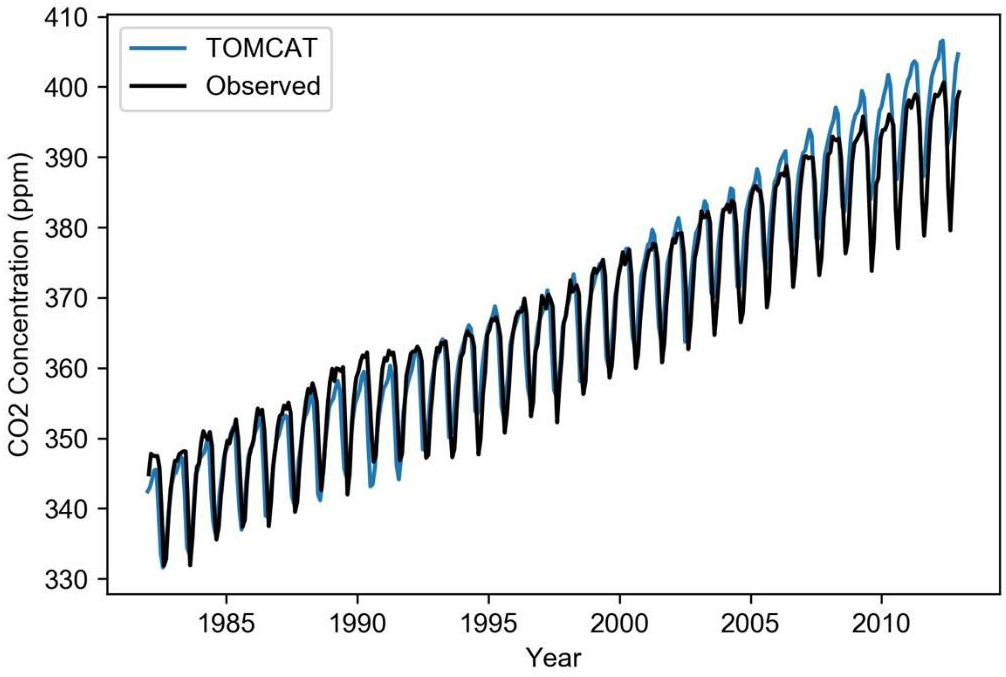

Figure S2.8. Observed values of atmospheric CO_2 concentrations (black) and simulated CO_2 concentrations from CASA-TOMCAT model (blue) at Barrow.

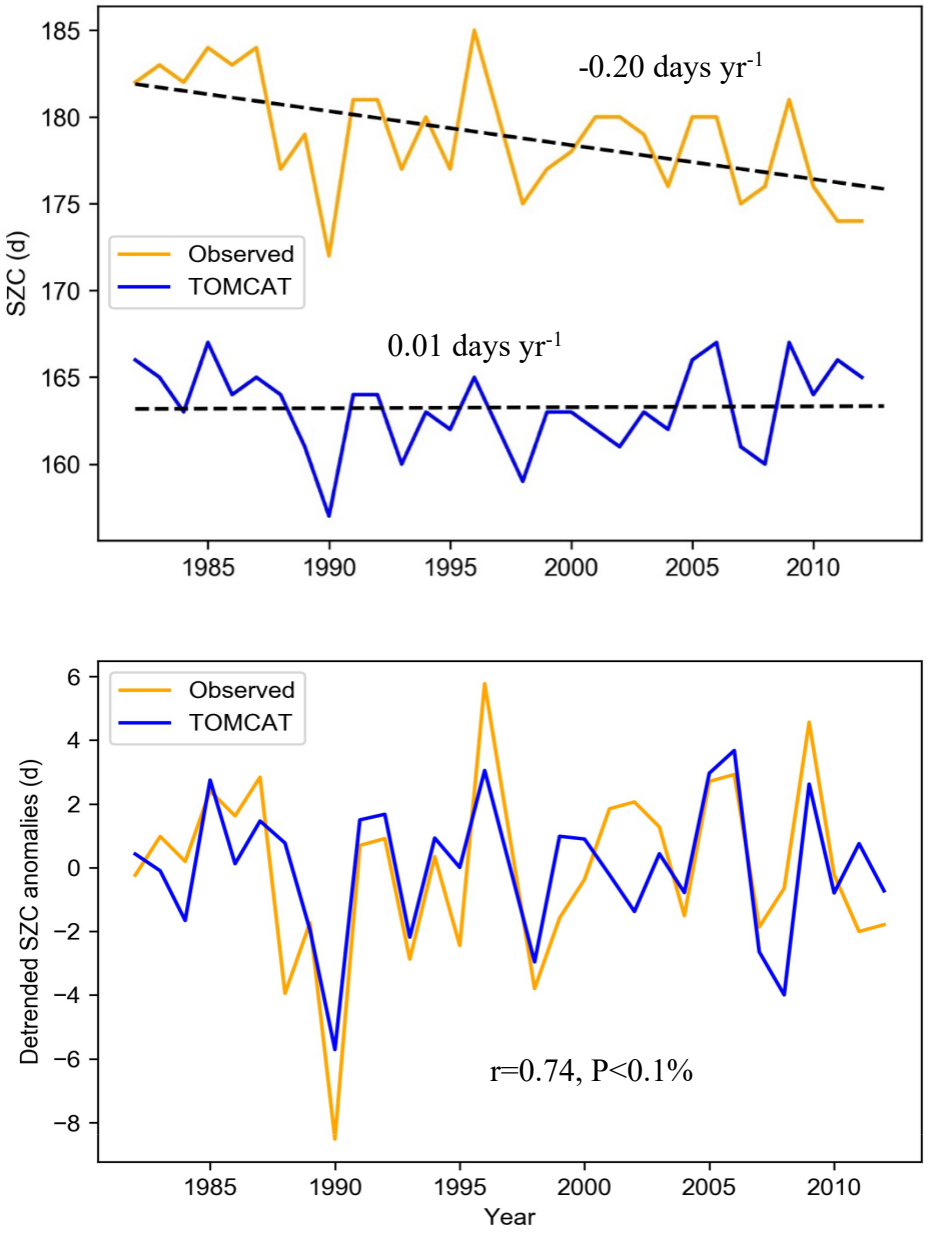

Figure S2.9. (a) Observed values of SZC (orange) and simulated SZC from CASA-TOMCAT (blue). Dashed lines indicate least squares regression, with the rate of change of SZC labelled above lines. (b) Observed and simulated SZC at Barrow, after linearly detrending both time series. The panel shows the Pearson's two-tailed correlation coefficient labelled with significance level.

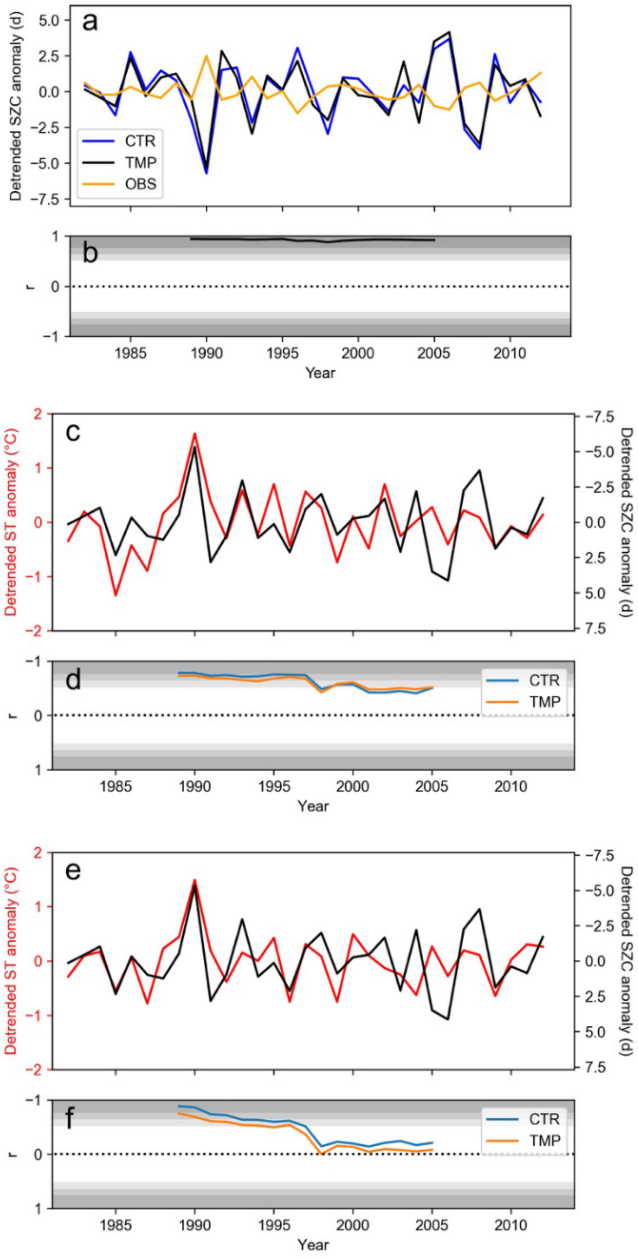

Figure S2.10. (a, c, e) Time series of detrended SZC anomalies from the TMP simulation plotted alongside (a) The CTR simulation and observations of SZC at Barrow, (c) footprint-weighted, detrended spring temperature (ST), (e) detrended spring temperature (ST) averaged over all vegetated land north of 50˚N. (b, d, f) 15-year moving window correlation between (b) the detrended simulated SZC from the TMP and CTR simulations, (d) detrended simulated SZC and footprint-weighted, detrended ST and (f) detrended simulated SZC and spring temperature (ST) averaged over all vegetated land north of 50˚N. Shaded regions depict 5%, 1% and .1% significance for a two-tailed partial correlation and n=15.

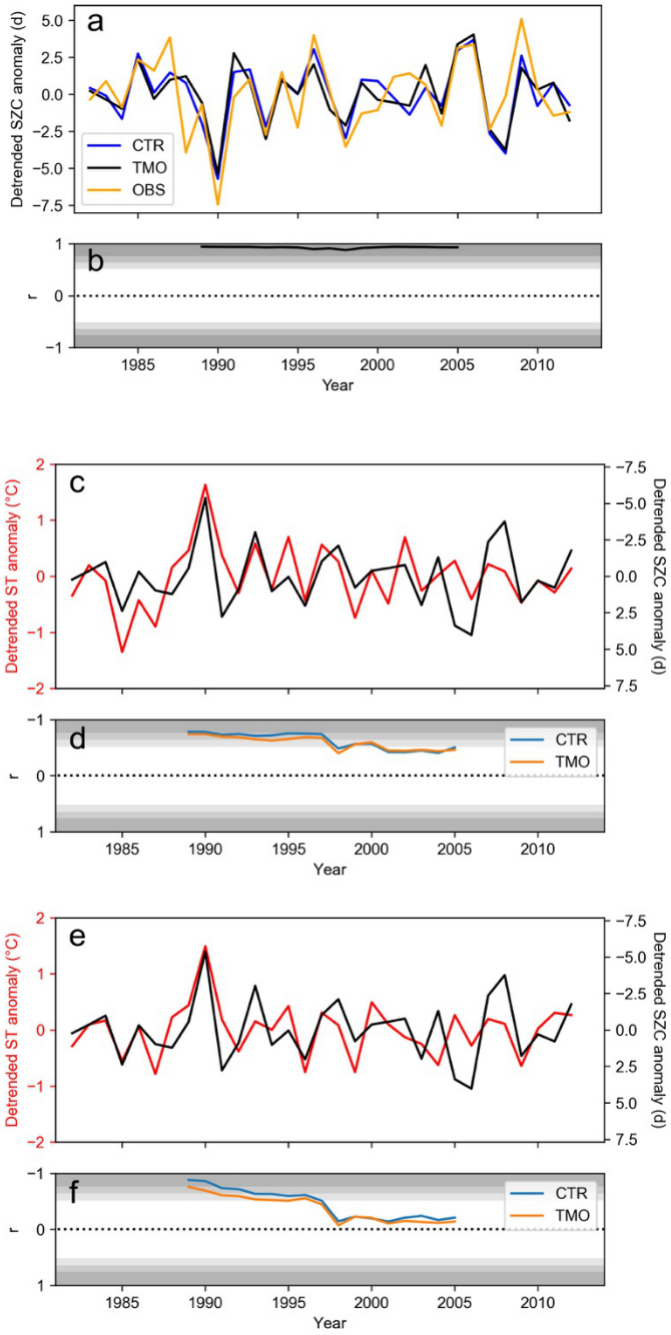

Figure S2.11. As Figure S2.9, but for simulation TMO, in which temperature and moisture scalars are constant.

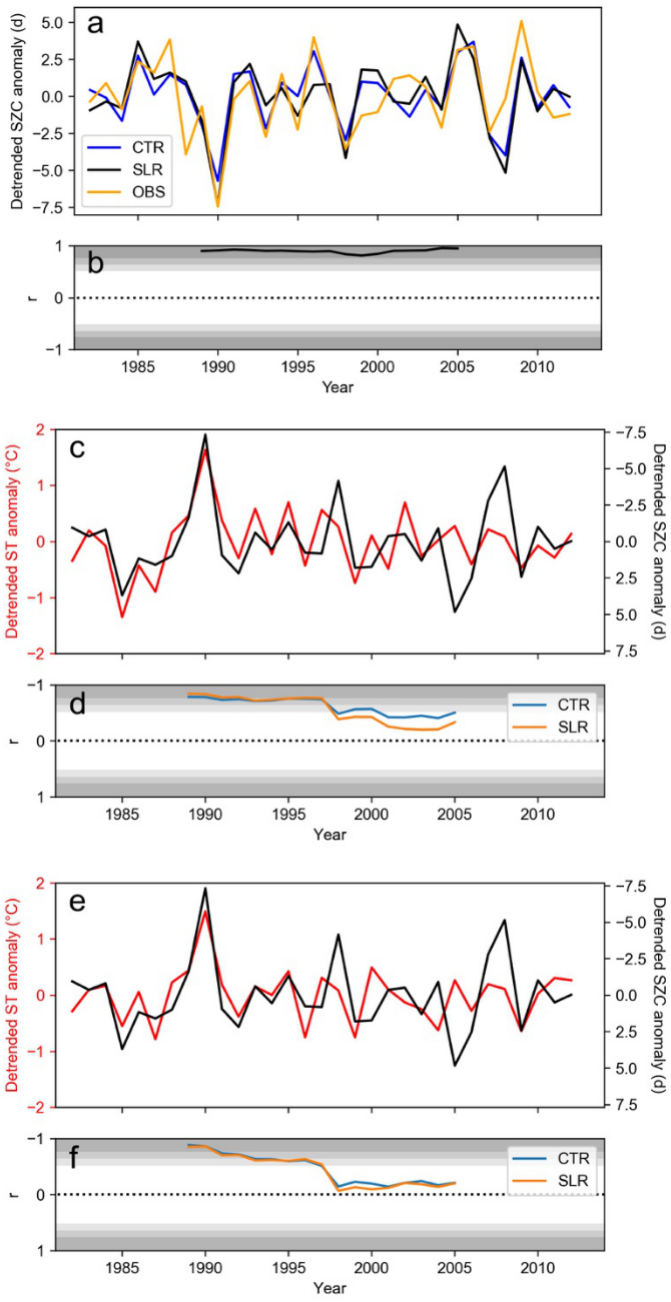

Figure S2.12. As Figure S2.9, but for simulation SLR, in which solar radiation is constant.

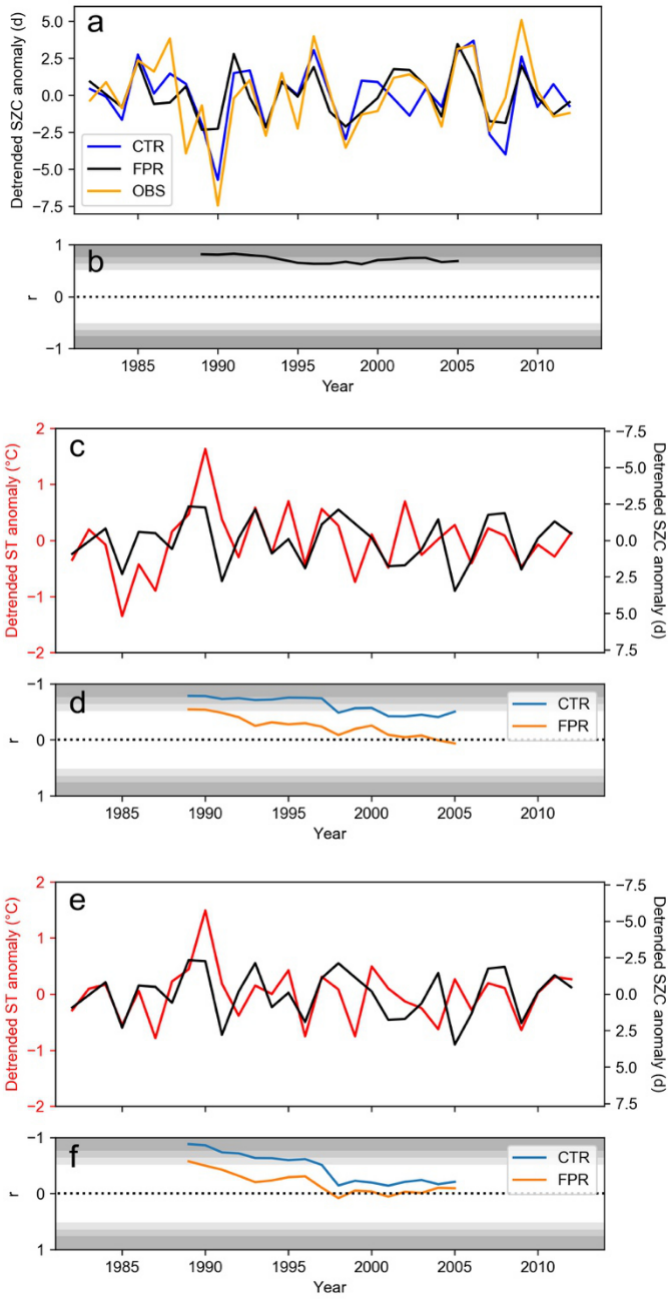

Figure S2.13. As Figure S2.9, but for simulation FPR, in which FPAR is constant.

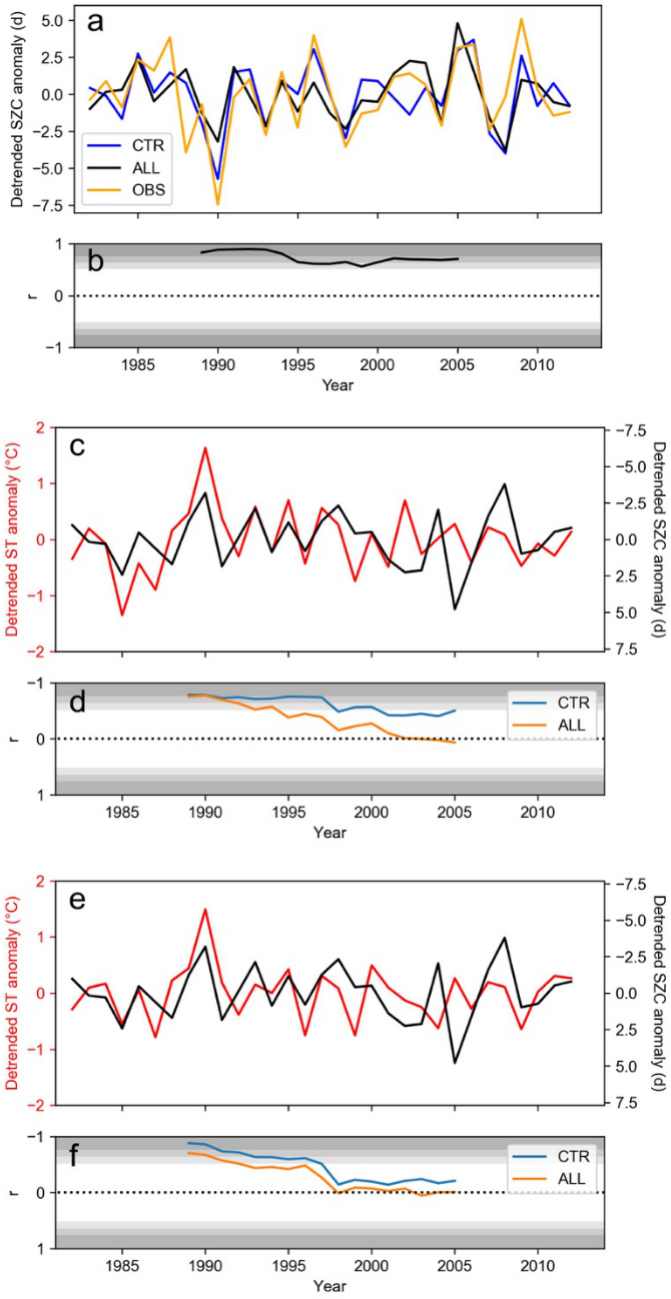

Figure S2.14. As Figure S2.9, but for simulation ALL, in which temperature and moisture scalars, solar radiation, and FPAR are constant.

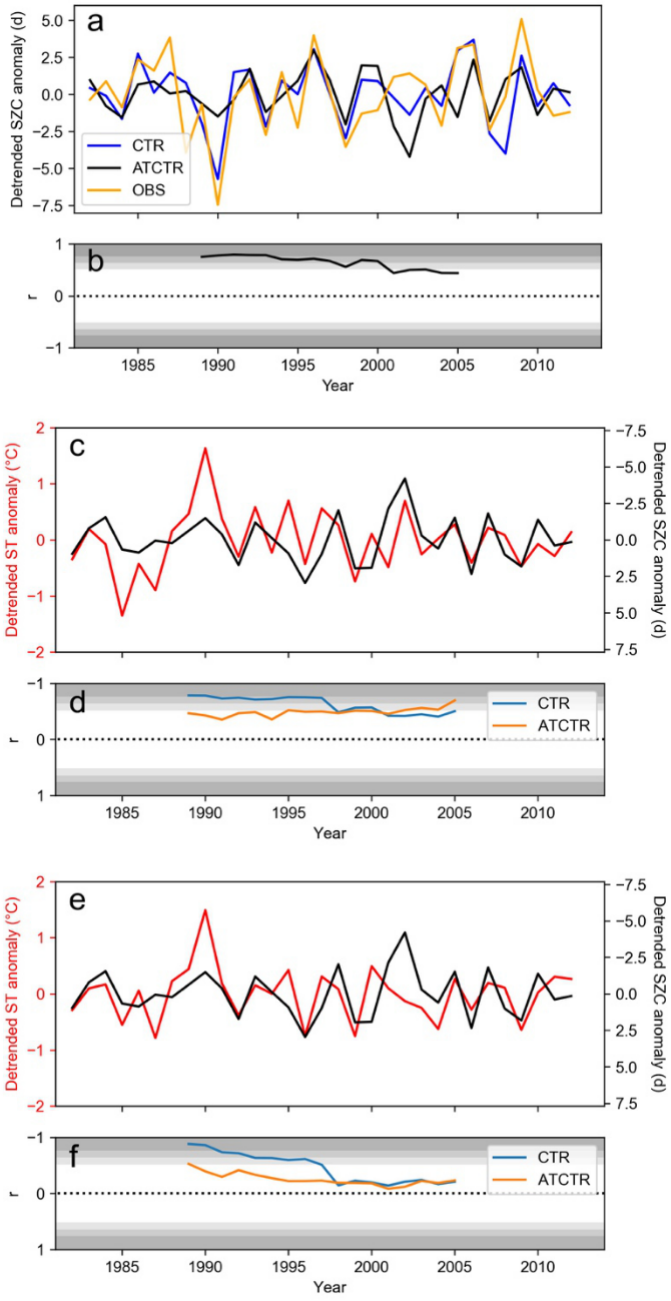

Figure S2.15. As Figure S2.9, but for simulation ATCTR, in which atmospheric transport is constant

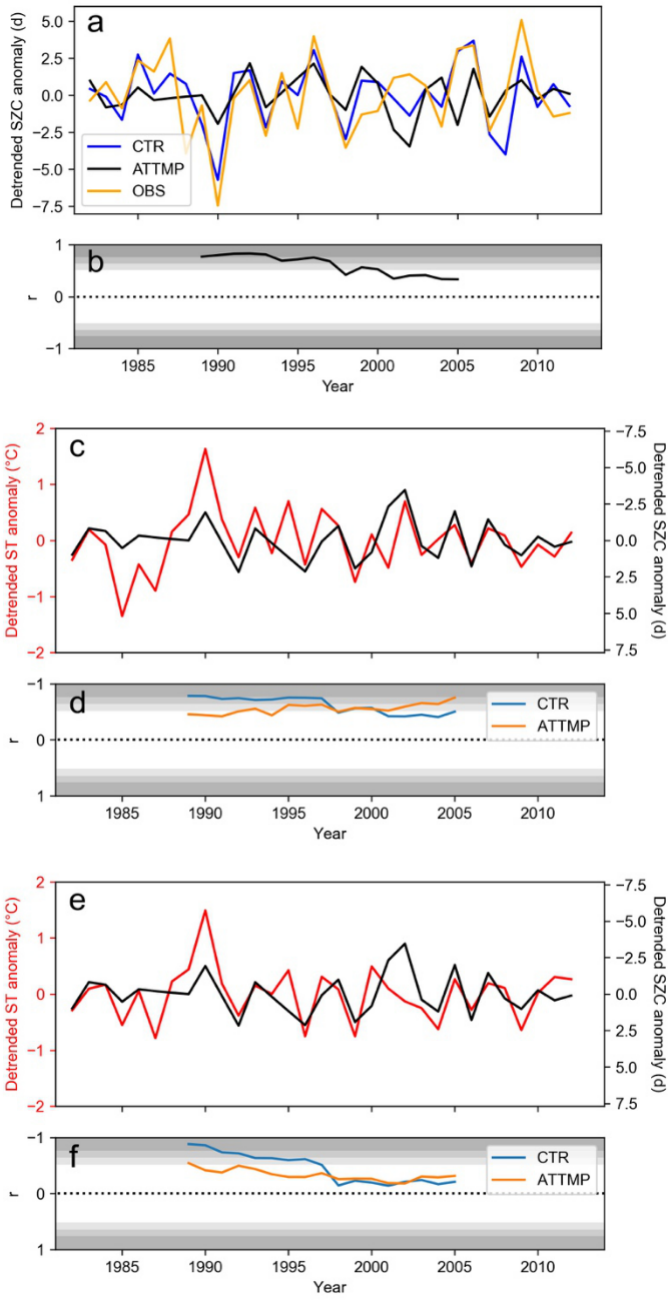

Figure S2.16. As Figure S2.9, but for simulation ATTMP, in which atmospheric transport and the temperature scalar are constant.

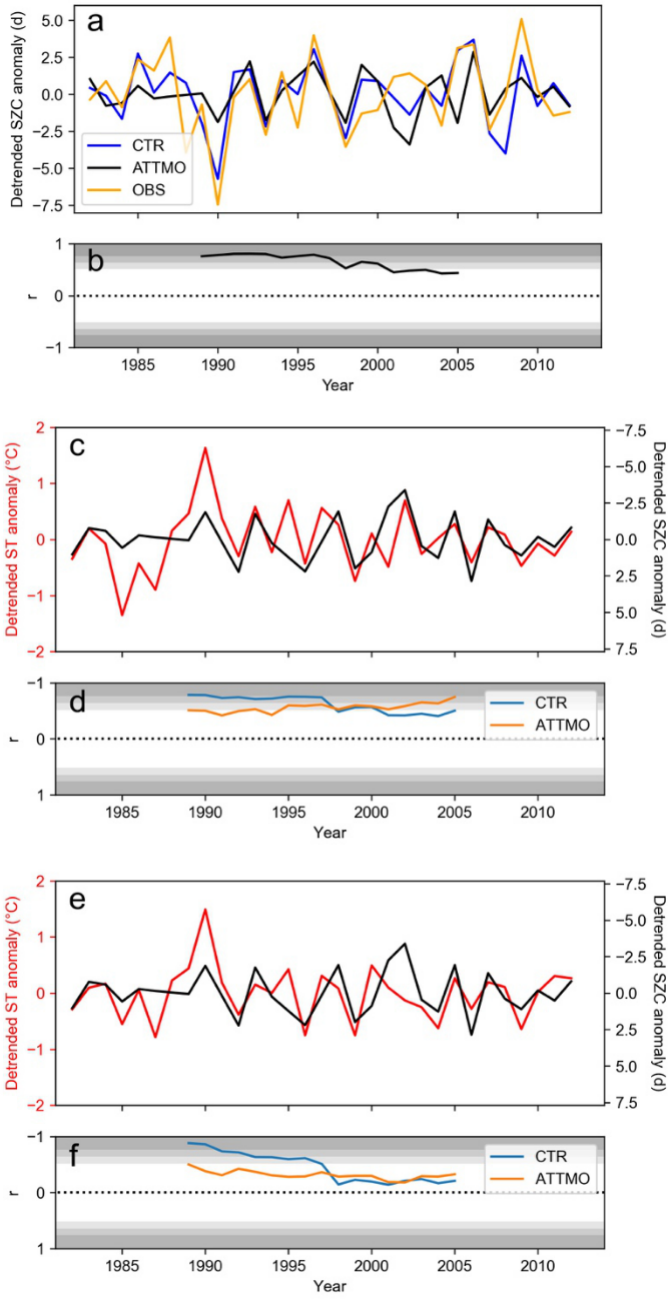

Figure S2.17. As Figure S2.9, but for simulation ATTMO, in which atmospheric transport and the temperature and moisture scalars are constant.

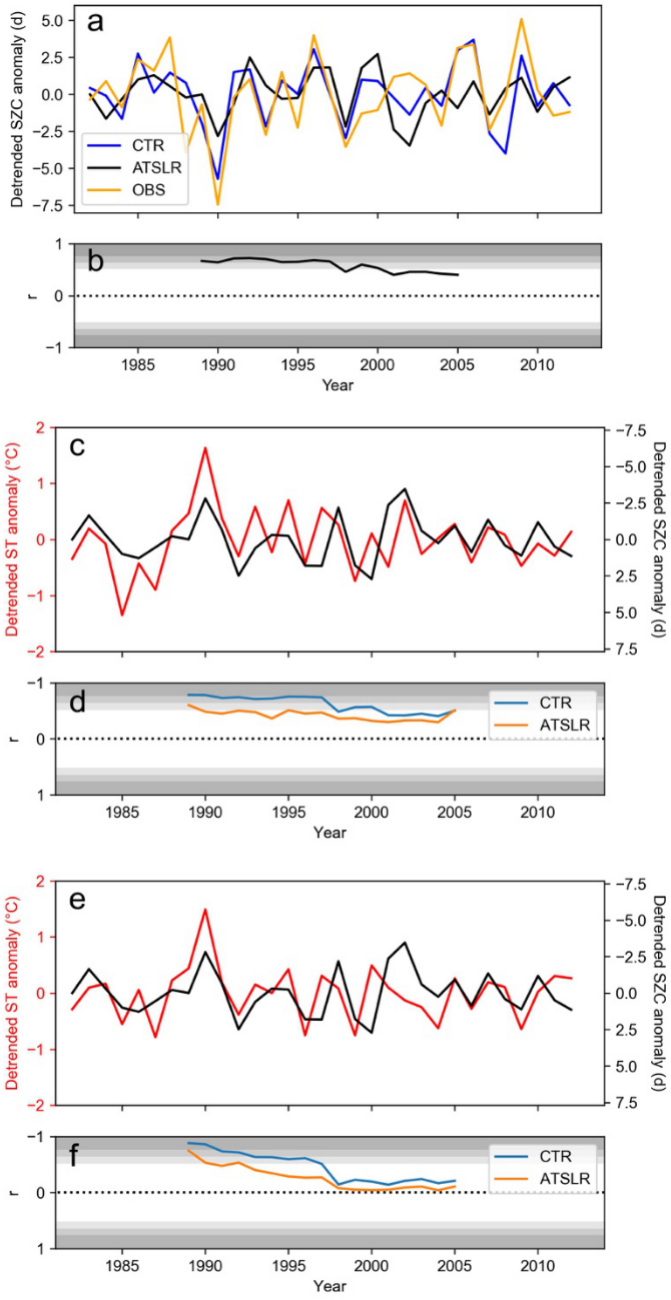

Figure S2.18. As Figure S2.9, but for simulation ATSLR, in which atmospheric transport and solar radiation are constant.

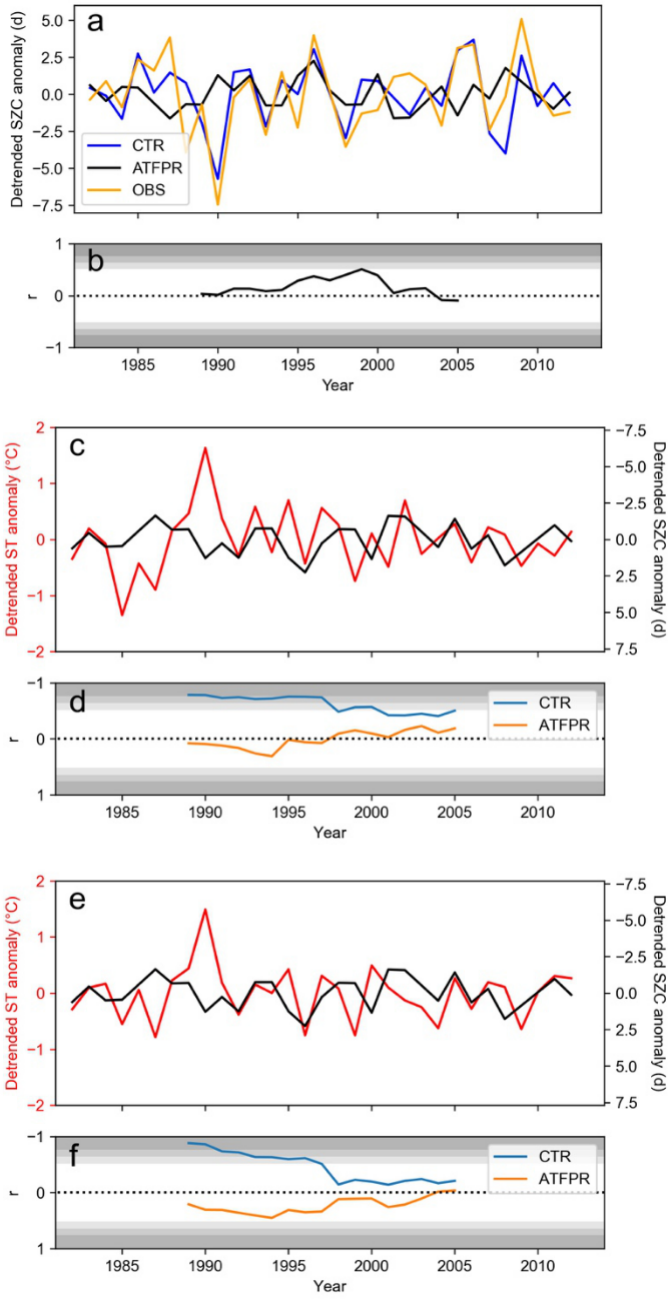

Figure S2.19. As Figure S2.9, but for simulation ATFPR, in which atmospheric transport and FPAR are constant.

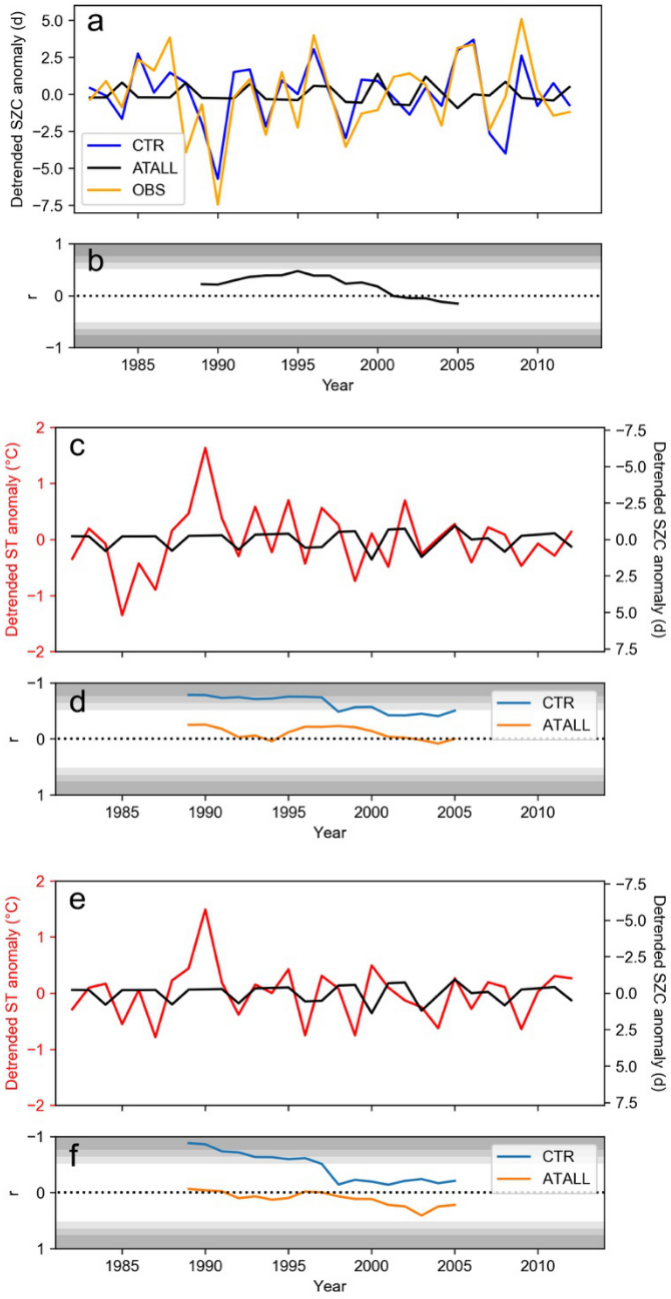

Figure S2.20. As Figure S2.9, but for simulation ATALL, in which atmospheric transport, the temperature and moisture scalars, solar radiation and FPAR are constant.

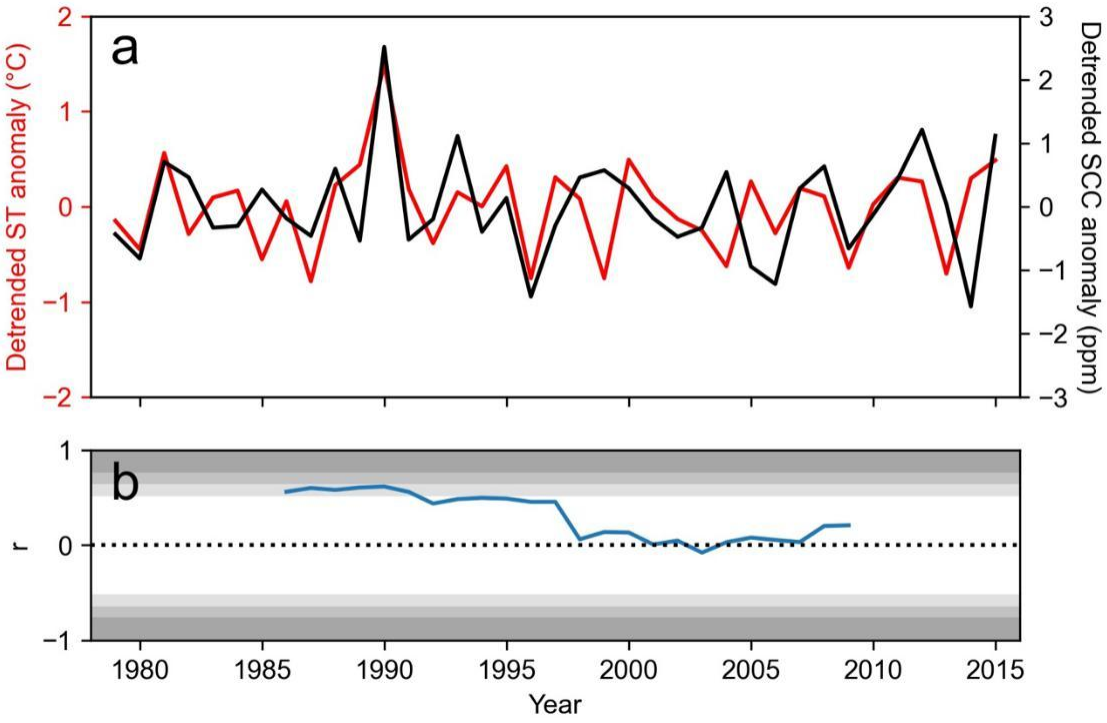

Figure S2.21. Time series of the anomaly (˚C) in detrended spring temperature (ST) averaged across vegetated land north of 50˚N along with detrended SCC (ppm) at barrow. Panel (b) shows corresponding moving window (15 yr) partial correlations (accounting for precipitation and radiation). Shaded regions depict 5%, 1% and 0.1% significance levels (n=15).

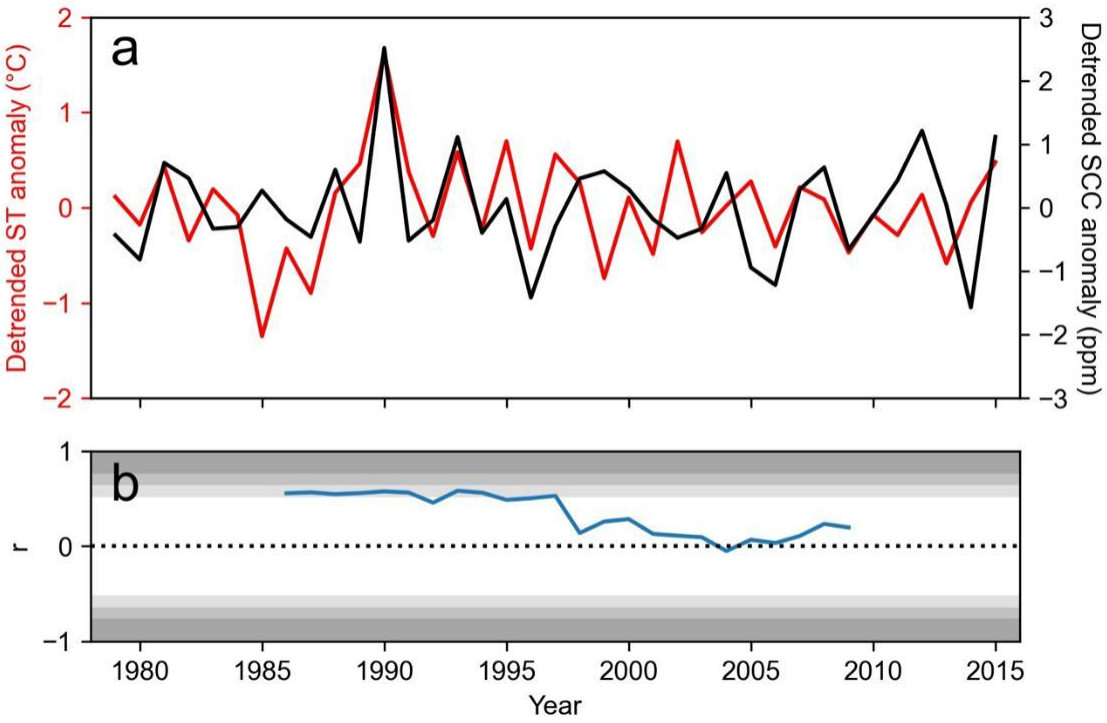

Figure S2.22. Time series of the anomaly (˚C) in detrended spring temperature (ST) weighed by footprints along with detrended SCC (ppm) at barrow. Panel (b) shows corresponding moving window (15 yr) partial correlations (accounting for precipitation and radiation). Shaded regions depict 5%, 1% and 0.1% significance levels (n=15).

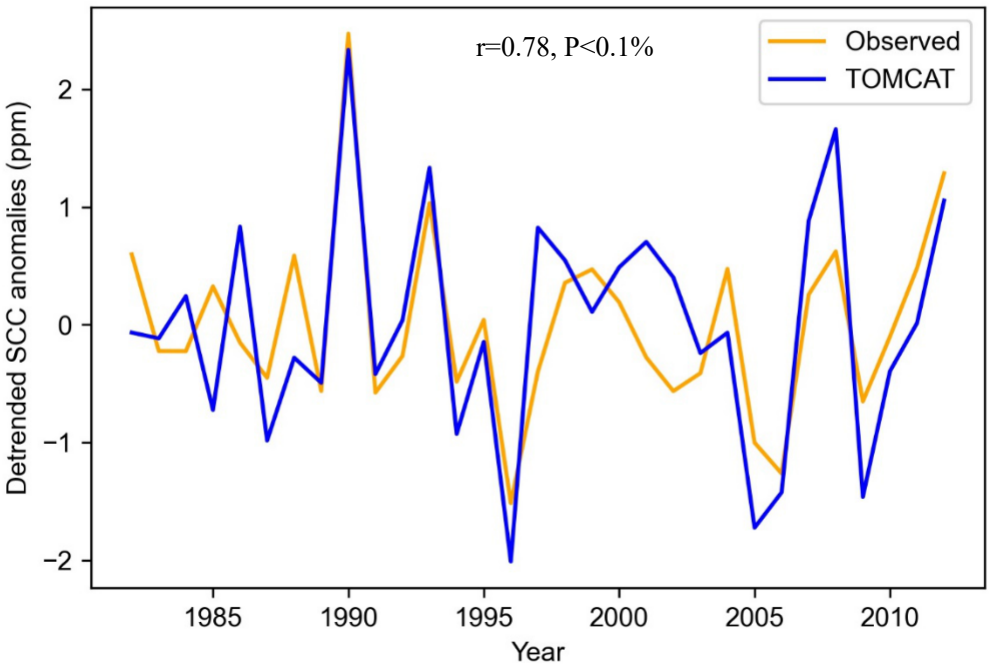

Figure S2.23. Observed and simulated SCC at Barrow, after linearly detrending both time series. The panel shows the Pearson's two-tailed correlation coefficient labelled with significance level.

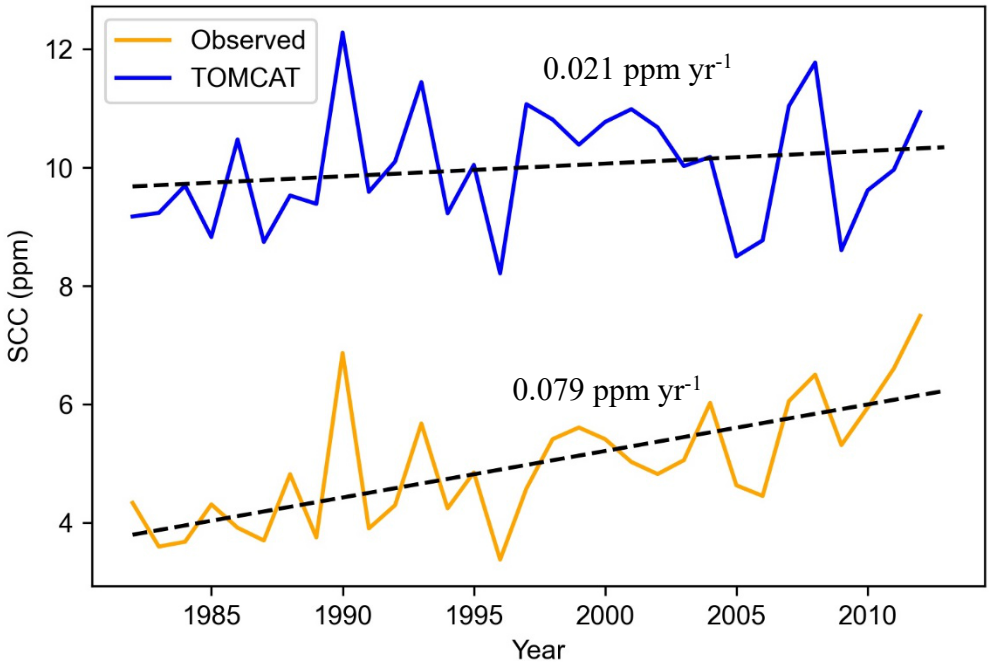

Figure S2.24. Observed values of SCC (orange) and simulated SCC from CASA-TOMCAT (blue). Dashed lines indicate least squares regression, with the rate of change of SCC labelled above lines.

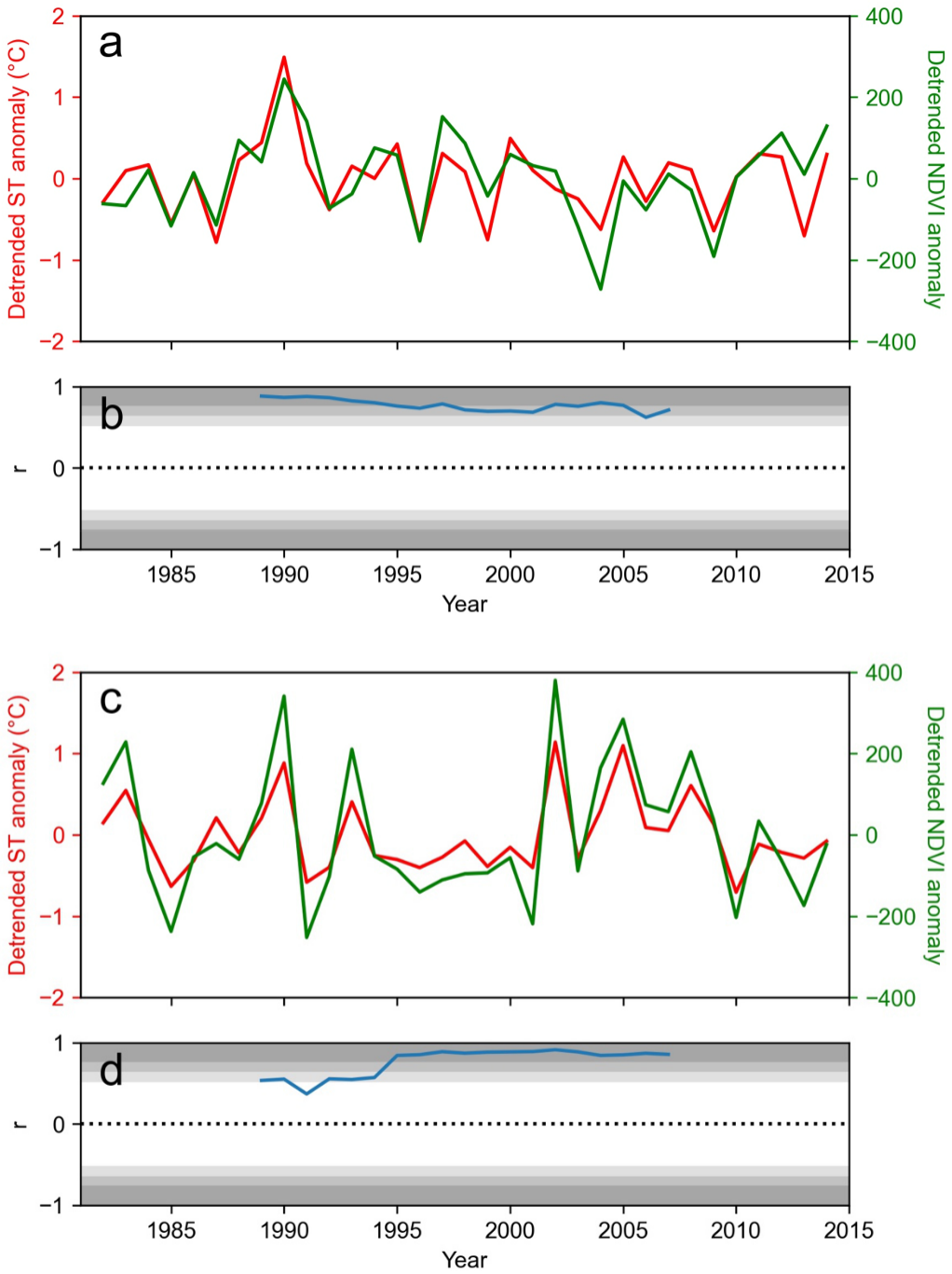

Figure S2.25. Times series of anomalies in detrended spring temperature (ST) and detrended NDVI averaged over (a) all vegetated land north of 50˚N and (b) footprints. Temperature > 0˚C and NDVI > 0.1 masks applied when averaging temperature and NDVI data. Corresponding moving window (15 yr) partial correlations (accounting for precipitation and radiation) are also shown. Shaded regions depict 5%, 1% and .1% significance levels (n=15).

Table S2.1. Correlations between simulated SCC from factorial simulations with observed SCC and spring temperature. The notations *, ** and *** indicate significance at 5%, 1% and 0.1% levels, respectively. Values over the 1997-2012 period are taken from the median correlation value after systematically removing each year from the chronology. Partial correlations take precipitation and cloud cover into account. The constant transport runs are referred to with the 'AT' prefix. To assess the importance of the forcing variables, we compare the correlations for each simulation with those of the CTR run – a large change in correlation indicates a large influence by the variable(s) held constant.

Simulation	**Correlation of simulated SCC with complete model and model with variables held constant**		**Partial correlation of simulated SCC with footprint-averaged observed spring temperature**		**Partial correlation of simulated SCC with 50˚N-averaged observed spring temperature**	
	1982-1996	**1997-2012**	**1982-1996**	**1997-2012**	**1982-1996**	**1997-2012**
Control Run (CTRL)	N/A	N/A	0.75***	0.44	0.70**	0.27
Variable(s) held constant						
Temperature scalar (TMP)	0.97***	0.97***	0.66**	0.37	0.59*	0.19
Temperature and Moisture scalars (TMO)	0.97***	0.96***	0.68**	0.30	0.58*	0.18
Solar Radiation (SLR)	0.95***	0.95***	0.79***	0.35	0.81***	0.36
FPAR (FPAR)	0.87***	0.84**	0.54*	0.1	0.38	0.00
TMO, SLR and FPR (ALL)	0.84***	0.78***	0.52*	-0.05	0.39	-0.05
Transport (AT,CTRL)	0.58*	0.22	0.68**	0.68**	0.66**	0.39
Transport and Temperature scalar (AT,TMP)	0.50	0.22	0.69**	0.61*	0.57*	0.43
Transport and Temperature and Moisture scalars (AT,TMO)	0.50	0.24	0.72**	0.61*	0.57*	0.43
Transport and Solar Radiation (AT,SLR)	0.59*	0.25	0.85***	0.68**	0.83***	0.48
Transport and FPAR (AT,FPAR)	0.57*	-0.01	0.34	0.46	0.16	0.15
Transport, TMO, SLR and FPAR (AT,ALL)	0.30	-0.25	0.23	0.11	0.03	-0.11

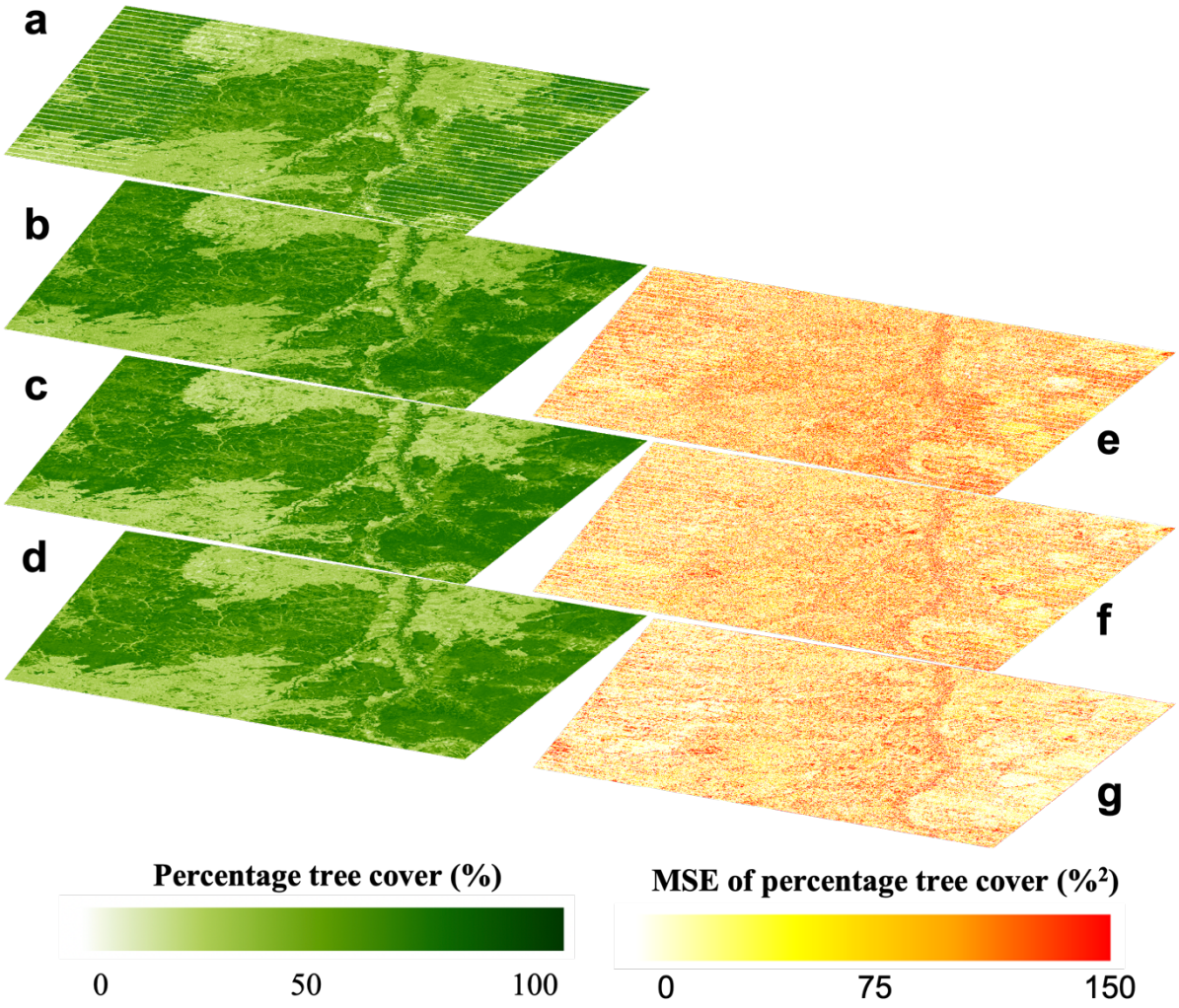

Figure S4.1. (a-d) Estimated percentage tree cover in the study region during 2003 for the (a) L7 image, (b) L5 image, (c) MR-emulated image, (d) DL-emulated image. (e-g) MSE between the L7 image in 2003 and the (e) L5 image, (f) MR-emulated image, (g) DL-emulated image in 2003.

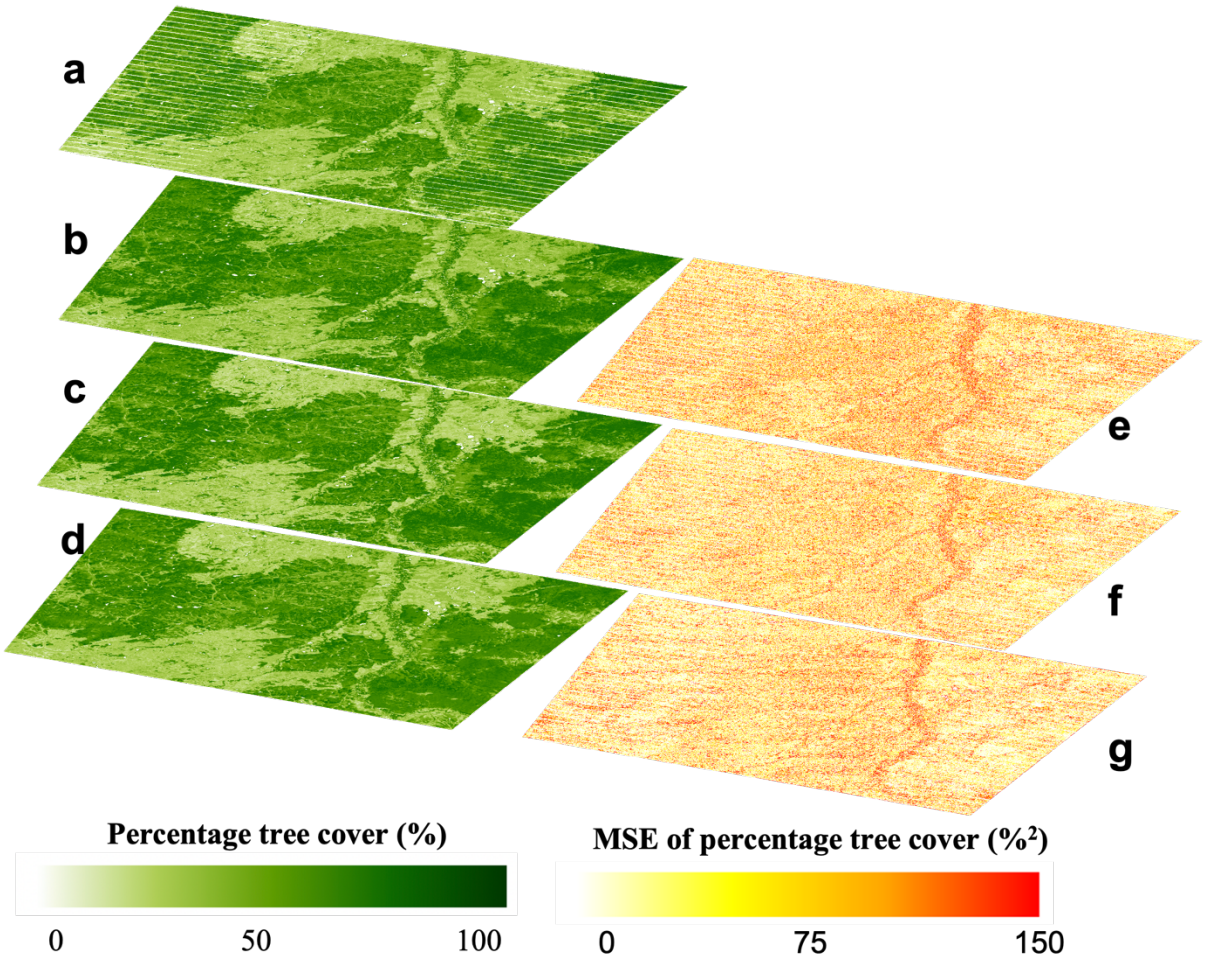

Figure S4.2 As for figure S4.1 but in 2004

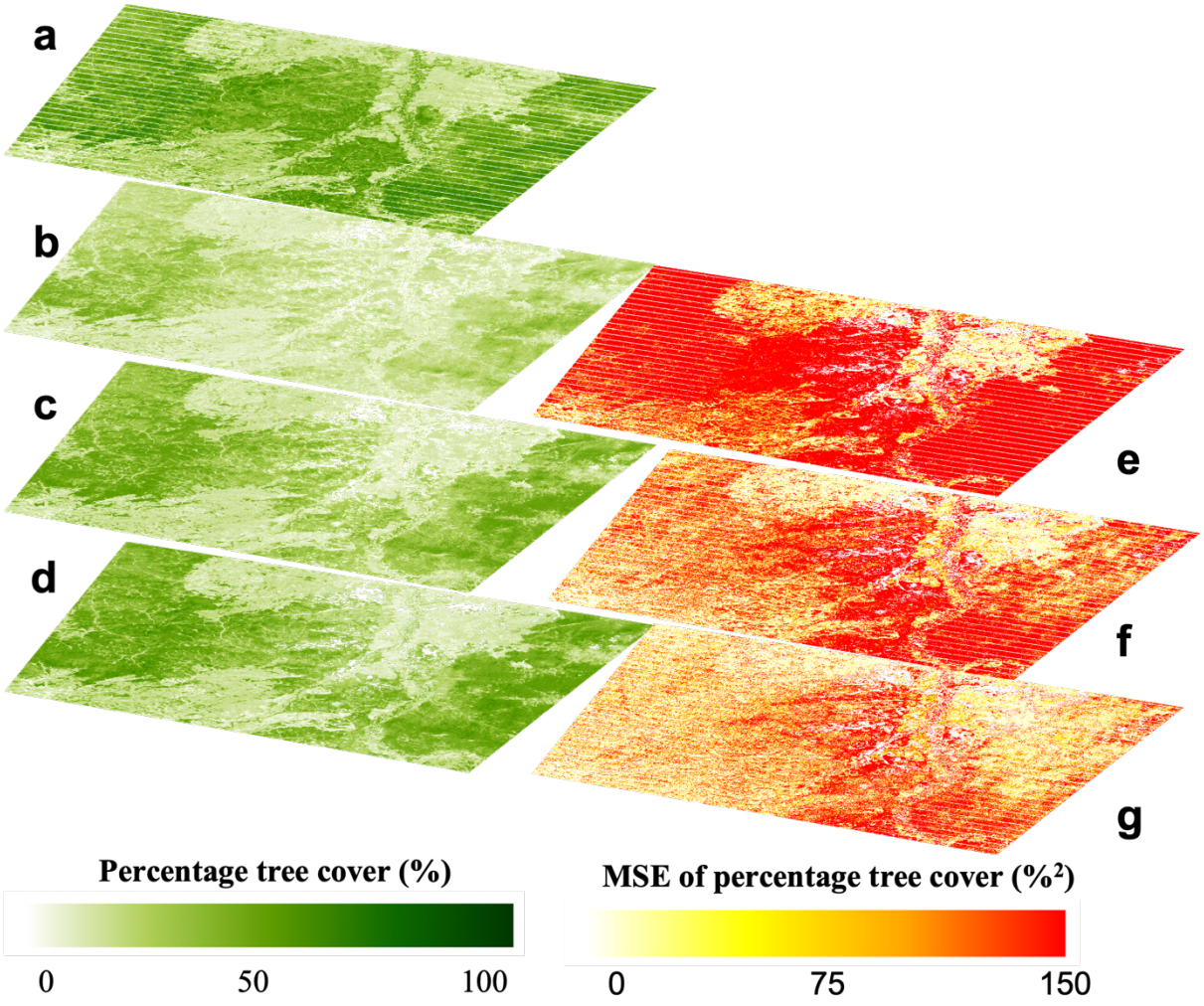

Figure S4.3. As for figure S4.1 but in 2005

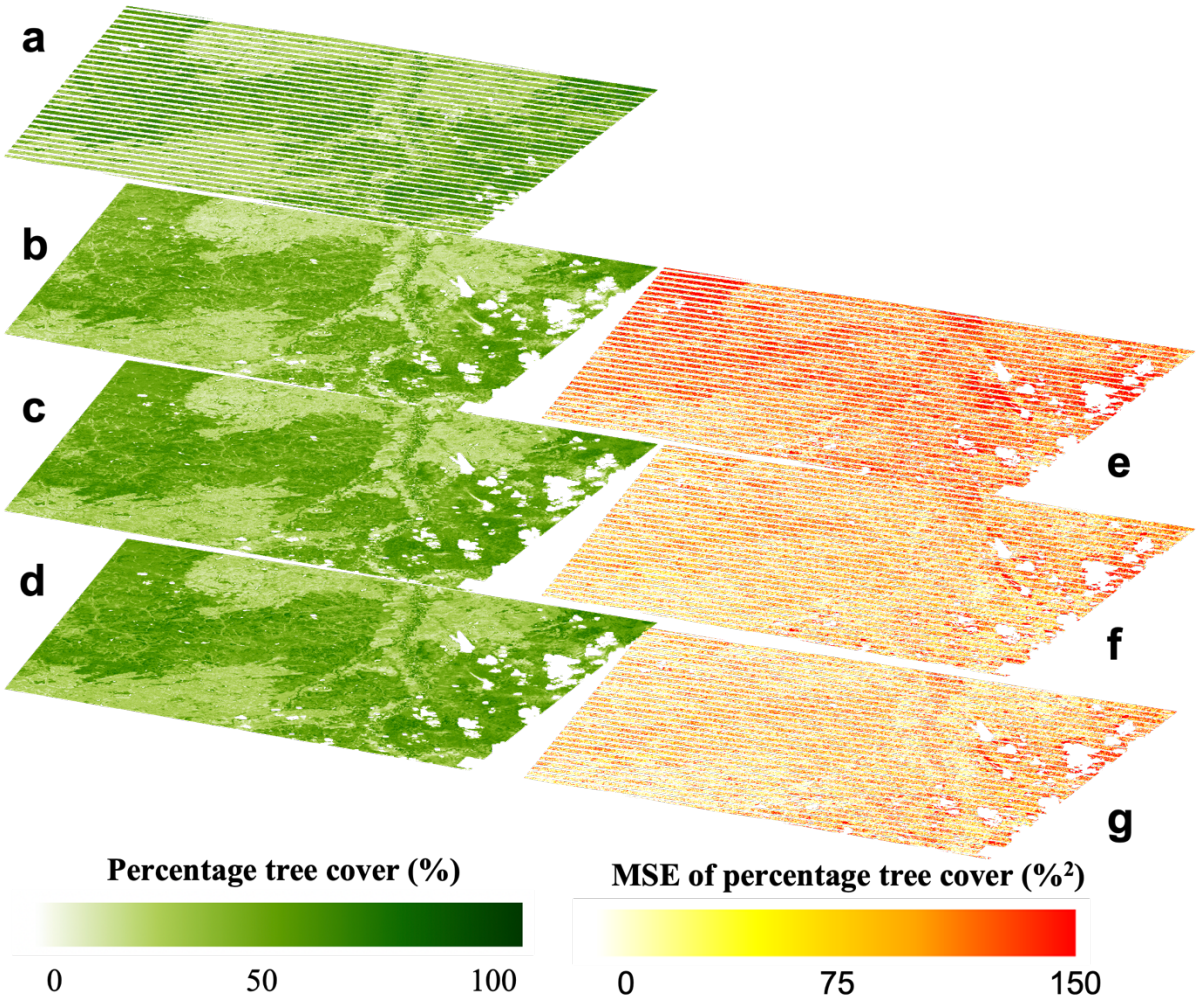

Figure S4.4. As for figure S4.1 but in 2006

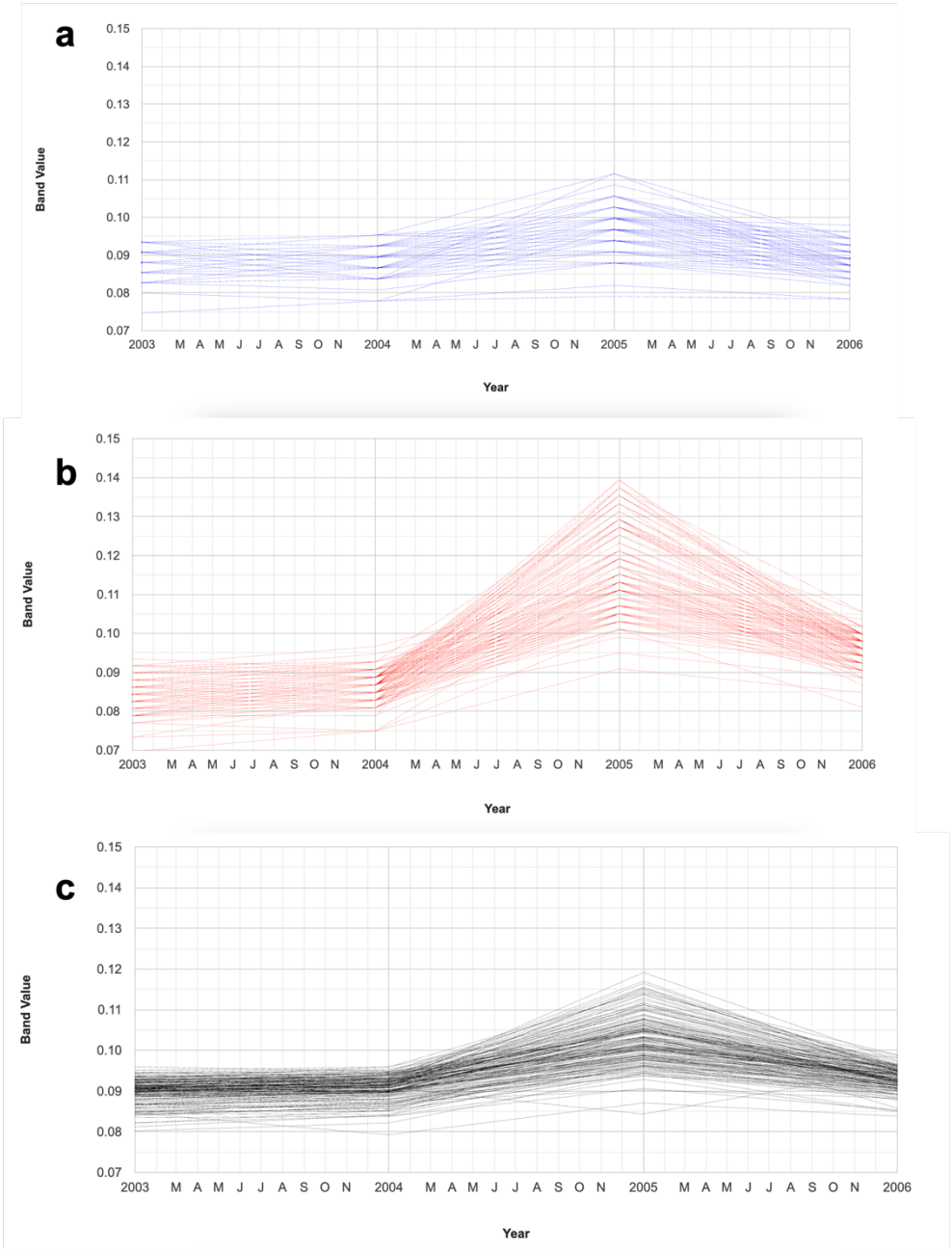

Figure S4.5. Red band values from the (a) L7, (b) L5, and (c) DL-emulated images over 300 random points in the study region during 2003, 2004, 2005, and 2006.

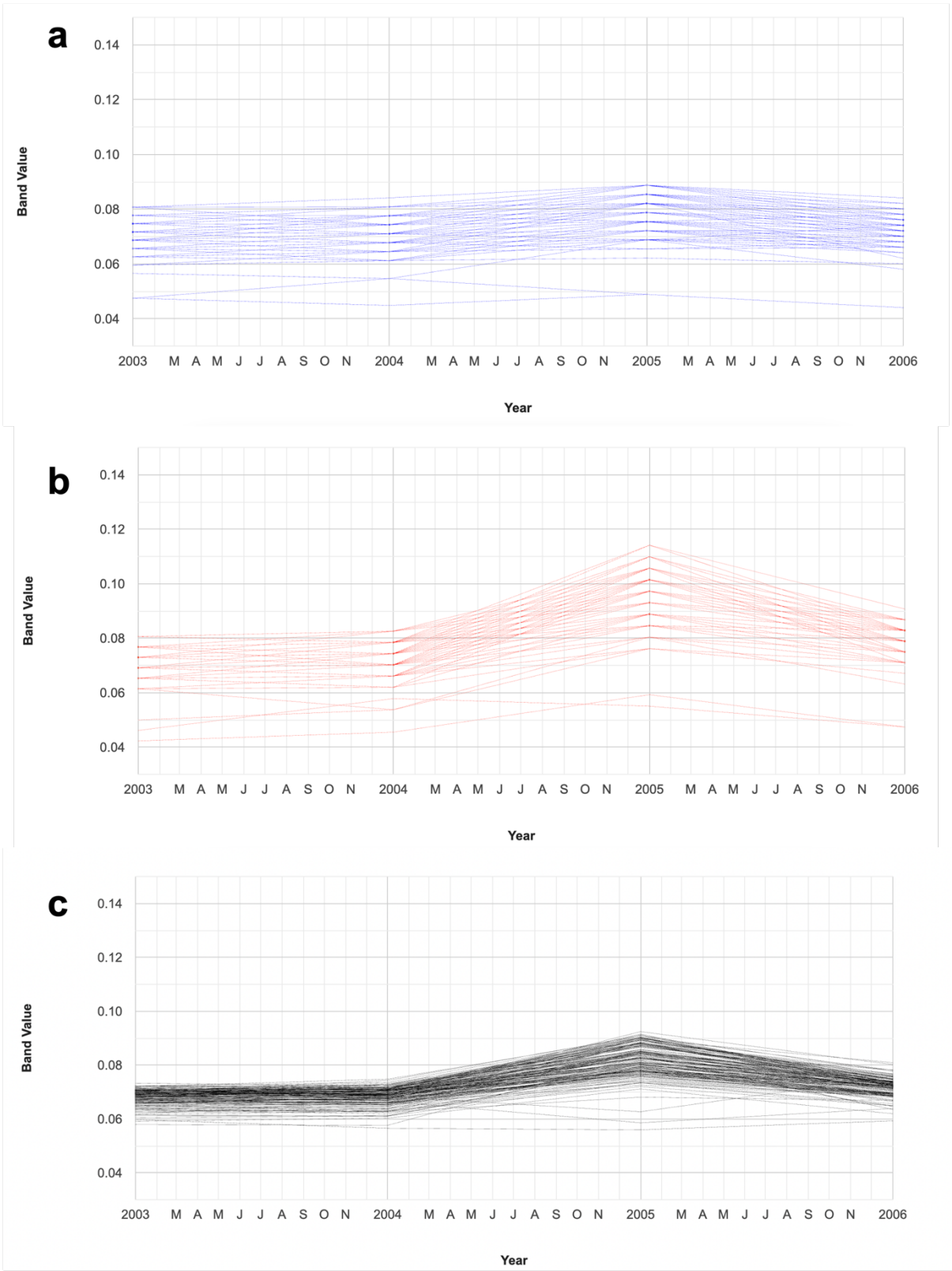

Figure S4.6. As for Figure S4.5 but with the green band.

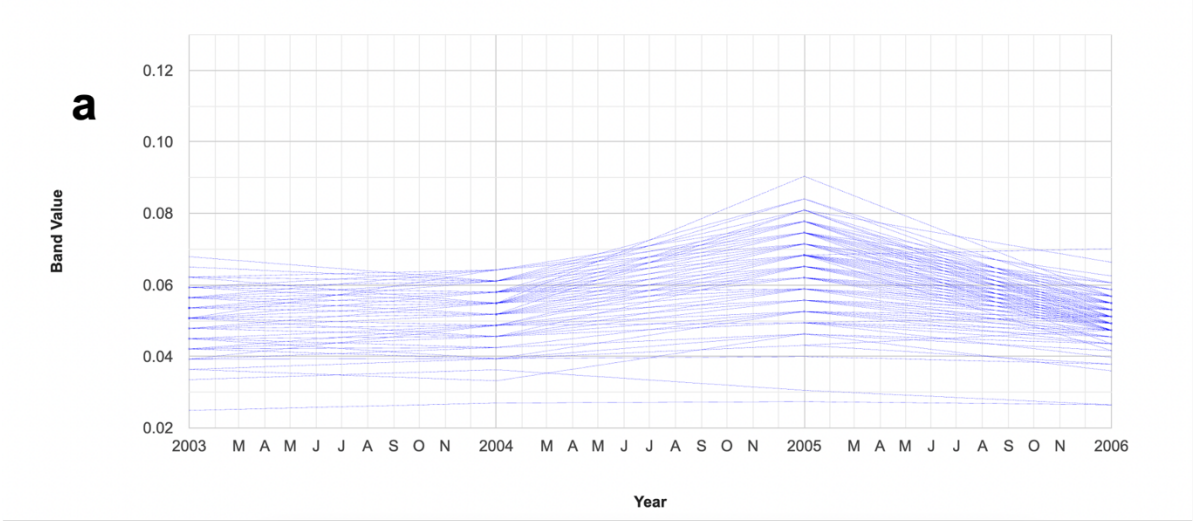

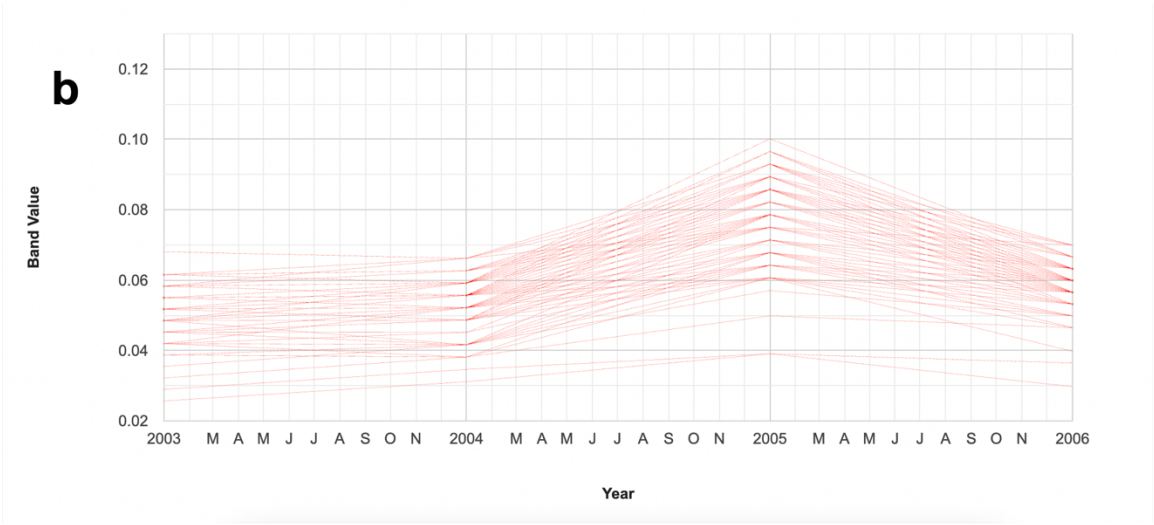

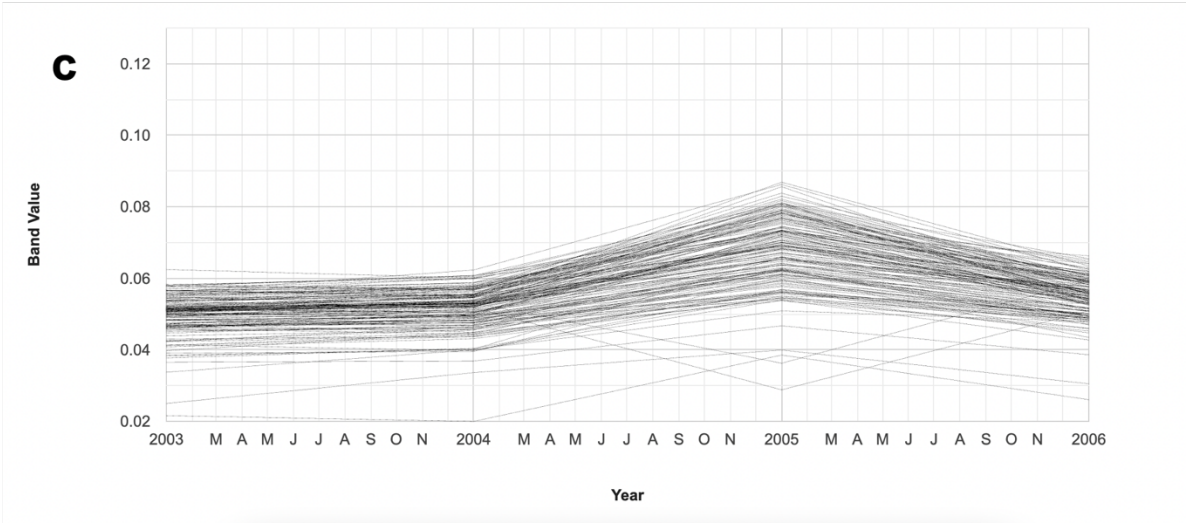

Figure S4.7. As for Figure S4.5 but with the blue band.

Table S4.1: Comprehensive list of L7 and L5 images used to train the models used in this chapter.

L7 code	L5 code
'LE07_073013_19990702'	'1_LT05_072013_19990703'
'LE07_064016_19990804'	'1_LT05_065016_19990803'
'LE07_064016_19990804'	'1_LT05_063016_19990805'
'LE07_061013_19990730'	'1_LT05_060013_19990731'
'LE07_071013_19990805'	'1_LT05_070014_19990806'
'LE07_067014_20030719'	'1_LT05_066014_20030720'
'LE07_067014_20030719'	'1_LT05_066014_20030720'
'LE07_063016_20030808'	'1_LT05_062016_20030809'
'LE07_070014_20030809'	'1_LT05_069014_20030810'
'LE07_070015_20030809'	'1_LT05_069015_20030810'
'LE07_062012_20040702'	'1_LT05_063012_20040701'
'LE07_062013_20040702'	'1_LT05_063013_20040701'
'LE07_067013_20040806'	'1_LT05_068013_20040805'
'LE07_069013_20040804'	'1_LT05_068013_20040805'
'LE07_069014_20040804'	'1_LT05_068014_20040805'
'LE07_069012_20040820'	'1_LT05_068012_20040821'
'LE07_070012_20040827'	'1_LT05_069012_20040828'
'LE07_070013_20040827'	'1_LT05_069013_20040828'
'LE07_065015_20040909'	'1_LT05_066015_20040908'
'LE07_067017_20040907'	'1_LT05_066017_20040908'
'LE07_065015_20040909'	'1_LT05_064015_20040910'
'LE07_078013_20050721'	'1_LT05_077013_20050722'
'LE07_078014_20050721'	'1_LT05_077014_20050722'
'LE07_067015_20050809'	'1_LT05_066015_20050810'
'LE07_067015_20050809'	'1_LT05_066015_20050810'
'LE07_067016_20050809'	'1_LT05_066016_20050810'
'LE07_067017_20050809'	'1_LT05_066017_20050810'
'LE07_077012_20060903'	'1_LT05_076012_20060904'
'LE07_077013_20060903'	'1_LT05_076013_20060904'
'LE07_077013_20060903'	'1_LT05_076013_20060904'
'LE07_065012_20060915'	'1_LT05_064012_20060916'
'LE07_065013_20060915'	'1_LT05_064013_20060916'
'LE07_066014_20070808'	'1_LT05_065014_20070809'
'LE07_066012_20070824'	'1_LT05_065012_20070825'
'LE07_064014_20070826'	'1_LT05_063014_20070827'
'LE07_062014_20070828'	'1_LT05_061014_20070829'

'LE07_072013_20080820'	'1_LT05_071013_20080821'
'LE07_072014_20080820'	'1_LT05_071014_20080821'
'LE07_079014_20080821'	'1_LT05_078014_20080822'
'LE07_062015_20080830'	'1_LT05_061015_20080831'
'LE07_062016_20080830'	'1_LT05_061016_20080831'
'LE07_067013_20080902'	'1_LT05_066013_20080903'
'LE07_075017_20090828'	'1_LT05_074017_20090829'
'LE07_067012_20090905'	'1_LT05_066012_20090906'
'LE07_067013_20090905'	'1_LT05_066013_20090906'
'LE07_074013_20100909'	'1_LT05_073013_20100910'
'LE07_070016_20100913'	'1_LT05_069016_20100914'
'LE07_073013_20100918'	'1_LT05_074013_20100917'
'LE07_073014_20100918'	'1_LT05_074014_20100917'
'LE07_075015_20100916'	'1_LT05_074015_20100917'
'LE07_075016_20100916'	'1_LT05_074016_20100917'
'LE07_073014_20100918'	'1_LT05_072014_20100919'
'LE07_073015_20100918'	'1_LT05_072015_20100919'
'LE07_073016_20100918'	'1_LT05_072016_20100919'
'LE07_064013_20100919'	'1_LT05_063013_20100920'
'LE07_064014_20100919'	'1_LT05_063014_20100920'
'LE07_064015_20100919'	'1_LT05_063015_20100920'
'LE07_064016_20100919'	'1_LT05_063016_20100920'
'LE07_078013_20100921'	'1_LT05_077013_20100922'
'LE07_078014_20100921'	'1_LT05_077014_20100922'
'LE07_076014_20100923'	'1_LT05_075014_20100924'
'LE07_076015_20100923'	'1_LT05_075015_20100924'
'LE07_076016_20100923'	'1_LT05_075016_20100924'
'LE07_076017_20100923'	'1_LT05_075017_20100924'
'LE07_074015_20100925'	'1_LT05_073015_20100926'
'LE07_074016_20100925'	'1_LT05_073016_20100926'
'LE07_074017_20100925'	'1_LT05_073017_20100926'
'LE07_067013_20030719'	'1_LT05_068013_20030718'
'LE07_065012_20030721'	'1_LT05_066012_20030720'
'LE07_069012_20040820'	'1_LT05_068012_20040821'
'LE07_065015_20040909'	'1_LT05_064015_20040910'
'LE07_077012_20060903'	'1_LT05_076012_20060904'
'LE07_065012_20060915'	'1_LT05_064012_20060916'
'LE07_074016_20100925'	'1_LT05_073017_20100926'
'LE07_063015_20030808'	'1_LT05_062016_20030809'

'LE07_063015_20030808'	'1_LT05_062015_20030809'
'LE07_062013_20040702'	'1_LT05_063013_20040701'
'LE07_067013_20040806'	'1_LT05_068012_20040805'
'LE07_069013_20040804'	'1_LT05_068013_20040805'
'LE07_067013_20040806'	'1_LT05_066013_20040807'
'LE07_066013_20110819'	'1_LT05_067013_20110818'
'LE07_065013_20110913'	'1_LT05_064013_20110914'
'LE07_065012_20060915'	'1_LT05_064013_20060916'
'LE07_070012_20040827'	'1_LT05_069012_20040828'
'LE07_065015_20040909'	'1_LT05_066014_20040908'
'LE07_067015_20040907'	'1_LT05_066015_20040908'
'LE07_075016_20090828'	'1_LT05_074016_20090829'
'LE07_074013_20100909'	'1_LT05_073014_20100910'
'LE07_062015_20080830'	'1_LT05_061015_20080831'
'LE07_065015_20040909'	'1_LT05_064016_20040910'
'LE07_078013_20050721'	'1_LT05_077014_20050722'
'LE07_078014_20050721'	'1_LT05_077015_20050722'
'LE07_066013_20070824'	'1_LT05_065014_20070825'
'LE07_071012_20070827'	'1_LT05_070013_20070828'
'LE07_063013_20070904'	'1_LT05_064013_20070903'
'LE07_079012_20080821'	'1_LT05_080012_20080820'
'LE07_072013_20080820'	'1_LT05_071014_20080821'
'LE07_070014_20080822'	'1_LT05_069014_20080823'
'LE07_062016_20080830'	'1_LT05_061017_20080831'
'LE07_071013_20100920'	'1_LT05_072013_20100919'
'LE07_068014_20100915'	'1_LT05_067015_20100916'
'LE07_068015_20100915'	'1_LT05_067015_20100916'
'LE07_069013_20080831'	'1_LT05_068013_20080901'
'LE07_075016_20090828'	'1_LT05_074017_20090829'
'LE07_069014_20080831'	'1_LT05_068014_20080901'
'LE07_067013_20090905'	'1_LT05_068013_20090904'
'LE07_067012_20080902'	'1_LT05_066013_20080903'
'LE07_069014_20090717'	'1_LT05_070014_20090716'
'LE07_067014_20090905'	'1_LT05_068014_20090904'
'LE07_068016_20100915'	'1_LT05_067016_20100916'
'LE07_073014_20100918'	'1_LT05_074013_20100917'
'LE07_066012_20100816'	'1_LT05_067012_20100815'
'LE07_075014_20100916'	'1_LT05_074014_20100917'
'LE07_068013_20060904'	'1_LT05_069013_20060903'

'LE07_075015_20100916'	'1_LT05_074016_20100917'
'LE07_069013_20070829'	'1_LT05_068013_20070830'
'LE07_063012_20070904'	'1_LT05_064012_20070903'
'LE07_070016_20100913'	'1_LT05_071016_20100912'
'LE07_070015_20100913'	'1_LT05_069015_20100914'
'LE07_061016_19990714'	'1_LT05_060016_19990715'
'LE07_065015_19990912'	'1_LT05_066015_19990911'

References

Thoning, K., Tans, P., & Komhyr, W. (1989). Atmospheric carbon dioxide at Mauna Loa Observatory: 2. Analysis of the NOAA GMCC data, 1974-1985. J. Geophys. Res., 94(D6), 8549-8565. doi: 10.1029/jd094id06p08549

Piao, S., Liu, Z., Wang, T., Peng, S., Ciais, P., & Huang, M. et al. (2017). Weakening temperature control on the interannual variations of spring carbon uptake across northern lands. Nat. Clim. Change., 7(5), 359-363. doi: 10.1038/nclimate3277